# An exploratory study of the mechanochemical synthesis of layered double hydroxides


UNIVERSITEIT VAN PRETORIA
UNIVERSITY OF PRETORIA
YUNIBESITHI YA PRETORIA
Denkleiers • Leading Minds • Dikgopolo tša Dihlalefi

**Brenda Antoinette Barnard**

# An exploratory study of the mechanochemical synthesis of layered double hydroxides

**Brenda Antoinette Barnard**


UNIVERSITEIT VAN PRETORIA
UNIVERSITY OF PRETORIA
YUNIBESITHI YA PRETORIA
Denkleiers • Leading Minds • Dikgopolo tša Dihlalefi

Submitted in partial fulfilment of part of the requirements for the degree of Master of Engineering in the Faculty Engineering, the Built Environment and Information Technology, University of Pretoria, Pretoria

**2020**

# An exploratory study of the mechanochemical synthesis of layered double hydroxides

## Synopsis

Layered double hydroxides (LDHs) are clay-like minerals commonly referred to as "anionic clays" with a wide range of physical and chemical properties. LDHs often find application in pharmaceuticals, as polymer additives, as additives in cosmetics, as nanomaterial's and in catalysis. This is due to having variable layer charge density, reactive interlayer space, ion exchange capabilities, a wide range of chemical compositions and rheological properties (Forano et al., 2006).

Various techniques exist for the synthesis of layered double hydroxides. These include co-precipitation, the urea method, induced hydrolysis, sol-gel and hydrothermal methods. Many of these produce environmentally unfriendly effluents or by-products, are energy intensive, make use of metallic salts or require inert synthesis environments (Rives, 2001). Limitations associated with these existing processes make LDH synthesis at an industrial level expensive or difficult to achieve. The need for 'green', affordable and repeatable synthesis methods are therefore often sought after.

Recently the use of mechanochemistry as an alternative synthesis technique has gained wide-spread attention. Mechanochemistry involves the breaking and forming of chemical bonds due to an induced mechanical force. Various mechanochemical techniques for the synthesis of LDH materials exist or have been explored. These include methods such as single-step, two-step and mechano-hydrothermal grinding techniques. Grinding methods can be conducted dry, wet or collectively (Qu, Zhang, et al., 2015a). Mechanochemistry has further been used in conjunction with micro-wave energy and ultrasonic irradiation. The use of mechanochemistry as a synthesis method has proven to be promising with successful and unique LDHs produced. Intercalation of unique or complex anions within the interlayer has further been proven possible. The versatility and robust nature of this synthesis method makes it ideal for industrial application.

Although many studies exist it was noted that limited research has been conducted on single-step wet grinding for LDH synthesis and warrants further investigation (Qu, Zhang, et al., 2015a) (Iwasaki,Yoshii, et al., 2012). This was due to factors such as incomplete conversion, difficulties associated with grinding and morphological imperfections. Single-

step wet milling could be benificial as a synthesis procedure as it eliminates hazards associated with dry powder, contains less process steps and is therefore possibly more cost effective and can be conducted batch, semi-batch or continuosly due to fluid flow. Throughout the literature research conducted it was further noted that not many different milling devices have been explored. Ball mills, mixer mills and manual grinding were the most common methods used to supply mechanical energy to a system. The study therefore aims to expand on single-step wet synthesis of LDH materials by making use of a different milling device, namely a Netzsch LME 1 horizontal bead mill. The selected mill is specifically designed for wet grinding application and can easily be up-scaled to a commercial batch, semi-batch or continous process. Raw materials selected were a combination of oxides, hydroxides and basic carbonates. This would eliminate hazardous salt by-products and effluent, promoting 'green' synthesis of LDH materials. It was noted that the synthesis of LDH with the use of these materials have previously proven to be challenging (Qu, Zhang, et al., 2015a).

Qualitative X-ray diffraction (XRD) analysis was selected as the primary analytical technique for the identification of the LDH phase. Conversion of raw materials to LDH product could not accurately be determined due to the amorphous nature of samples obtained. Rietveld refinement was therefore not conducted and the the exact conversion not calculated. Trends in the conversion of raw materials to LDH product were instead discussed. Fourier transform infrared spectroscopy (FT-IR) analysis was further conducted to support XRD data and trends observed. X-ray fluoresence (XRF) was selected to identify impurities within the system as was expected due to the grinding mechanisms involved. The change in particle size and morphology were further investigated by making use of particle size analysis (PSA) and scanning electron microscopy (SEM).

The study was divided up into two sections namely a 'parameter study' and a 'versatility study'. The 'parameter study' involved exploring the influence of milling and experimental parameters, such as rotational speed, retention time, solids loading, bead size and jacket water temperature, on the synthesis of Mg-Al LDH. The raw materials selected were MgO and $Al(OH)_3$ combined at a $M^{2+}$: $M^{3+}$ ratio of 2:1. The parameters were individually investigated, with the exception of jacket water temperature as it was varied with a change in retention time and a change in rotational speed. Unless stated otherwise or under investigation, parameters were investigated at a set speed of 2000 rpm, jacket water temperature of 30 °C, solids loading of 10 %, retention time of 1 h and with 2 mm yttrium stabilised zirconia beads. Therefore when investigating a specific parameter, the others remained as specified above.

Rotational speed was varied at 1000 rpm, 2000 rpm and 3000 rpm respectively at a jacket water temperature of 30 °C, solids loading of 10 %, retention time of 1 h and with 2 mm

yttrium stabilised zirconia beads. Results indicated a reduction in both the MgO and $Al(OH)_3$ peaks, however LDH peaks were not clearly identifiable. It should be noted that minor quanitites of LDH could still be present within the sample. The presence of $SiO_2$ was observed and peak reduction occured. This implies that peak reduction was likely the result of amorphitisation and grinding activity. Raw material peak reduction increased with an increase in rotational speed. This was expected as the number of collisions and energy added to the system increased with an increase in rotational speed. This was further corroborated with an increase in concentration of degradation contaminants, with an increase in the rotational speed, observed through XRF analysis. Comparatively results obtained for a change in rotational speed, at a jacket water inlet temperature of 50 ℃, indicated a greater decrease in raw material peak intensity with an increase in rotational speed. Minor primary and secondary LDH peaks were observable, however no clear trend identifiable. The rate of LDH formation was expected to increase with an increase in temperature.

The retention time was varied at 1 h, 2 h and 3 h for a jacket water temperature of 30 °C. XRD results indicated a clear reduction in raw material peaks, including that of $SiO_2$, with an increase in retention time. This was expected as extended periods of milling activity result in an increase in the overall amount of collisions to which the sample is exposed. A minor LDH peak was observed to be present after 1 h of milling activity, however decreased and dissapeared after 3 h. This was likely due to amorphitisation or structural degradation of the LDH material. SEM imaging of the sample showed a decrease in sample structure (softening of edges) with an increase in retention time. Comparatively the sample synthesised at a jacket water temperature of 50 °C indicated a more drastic reduction in raw material peaks with an increase in retention time. Minor raw material peaks were observed after 3 h of milling and clear, broad LDH spectra observed. SEM imaging indicated an increase in LDH platelet like structures with an increase in retention time.

Solids loading was varied at 10 %, 20 % and 30 % respectively for a jacket water temperature of 30 °C and conditions described above. No clear LDH pattern was observed for a loading of 10 %, however minor peaks were present for loadings of 20 % and 30 %. Raw material peak reduction was greatest at a loading of 10 %. An increase in the solids loading resulted in a drastic increase in viscosity and therefore a decrease in the grinding activity. LDH peaks present were likely due to the larger concentration of raw materials available for reaction when compared to a lower solids loading. A reduction in grinding activity was corroborated with a reduction in the quanitity of degradation contaminants. Bead size was varied from 2 mm to 0.25 mm at a loading of 10 % and jacket water temperature of 30 °C. The reduction in bead size resulted in a more prominant LDH XRD spectra, with no clear peaks identifiable for a bead size of 2 mm. A decrease in bead size

was expected to result in a increase in the reactive surface area and therefore conversion of raw materials to LDH. A greater decrease in raw material peaks, when compared to the larger bead spectra, could corroborate the increase in conversion expected.

Comparatively the 'versatility' study further explores the synthesis of Mg-Al, Ca-Al, Cu-Al and Zn-Al LDH by adapting optimal synthesis conditions, derived from existing mechanochemical techniques and methods, to the selected process. These were specifically related to the $M^{2+}$:$M^{3+}$ ratio and selected starting materials. Ageing of the samples obtained through the 'versatility study' were further explored to determine if the potential for a two-step commercial process exists. The study was investigated at a set speed of 2000 rpm, jacket water temperature of 30 °C, solids loading of 10 %, retention time of 1 h and with 2 mm yttrium stabilised zirconia beads. Half of the sample collected was subjected to ageing at 80 °C for 24 h under atmospheric conditions. The synthesis of Mg-Al LDH was further explored by making use of a $M^{2+}$:$M^{3+}$ ratio of 3:1 (Tongamp, Zhang & Saito, 2006a). LDH formation was observed to occur more readily than that of a selected 2:1 ratio, however conversion was incomplete with raw material peaks observed in XRD spectra obtained. Ageing of the sample drastically improved conversion with a clear LDH pattern observed for both FTIR and XRD spectra obtained. Raw material peaks were observed to no longer be present after the relevant ageing step, with only minor peaks visible prior to ageing.

The synthesis of Ca-Al LDH was attempted by making use of CaO and $Al(OH)_3$ with and without the addition of a carbonate source, $CaCO_3$. The overall $M^{2+}$:$M^{3+}$ ratio was specified at 2:1 (Qu, Zhong, et al., 2016). Addition of $CaCO_3$ resulted in a clear LDH XRD spectra with minor raw material peaks present prior to ageing. Comparatively, the XRD spectra for the sample without $CaCO_3$ exhibited more prominant raw material peaks with a minor LDH peak present. Ageing of the sample containing $CaCO_3$ resulted in a drastic reduction of the remaining $Al(OH)_3$ and $Ca(OH)_3$ peaks, implying almost complete conversion. Comparitively the sample with no $CaCO_3$ resulted in the formation of the precursor katoite ($Ca_3Al_2(OH)_{12}$).

The synthesis of Zn-Al LDH was conducted with zinc basic carbonate ($Zn_5(CO_3)_2(OH)_6$) as the selected Zn source, at a $M^{2+}$:$M^{3+}$ ratio of 1:1 (Qu, He, M Chen, Huang, et al., 2017). XRD results obtained indicated that LDH formation occured readily during the milling process, however raw material peaks were still present. Ageing of the sample resulted in a high intensity LDH spectra, however, $Al(OH)_3$ peaks were still observed to be present. These synthesis conditions were further adapted to the use of zinc oxide (ZnO) as a Zn source due to ease of availability. Minor XRD LDH peak formation was observed to occur, however, ZnO and $Al(OH)_3$ were still observed to be present. Little difference was observed with further inclusion of the ageing step.

Cu-Al LDH synthesis was attempted, with cupric basic carbonate ($Cu_2(OH)_2CO_3$), at a $M^{2+}$:$M^{3+}$ ratio of 2:1 (Qu, He, M Chen, Q Zhang, et al., 2017). LDH was not easily identifiable prior to ageing due to the similarity between XRD and FTIR spectra for $Cu_2(OH)_2CO_3$ and that of the expected LDH. XRD spectra of the aged sample revealed what could be construed as LDH peaks, however, these were difficult to identify due to the presence of the $Cu_2(OH)_2CO_3$. The selected synthesis conditions were adapted to a $M^{2+}$:$M^{3+}$ ratio of 4:1 to determine if an excess in $Cu_2(OH)_2CO_3$ would drastically influence the synthesis. Little difference was observed in the results obtained.

The wet synthesis of LDH materials with the use of a Netzsch LME 1 horizontal bead mill seems promising for future commercial use. LDH formation was observed to be favoured at higher temperatures and longer retention times. LDH formed was observed to have poor crystallinity with broad LDH peaks in XRD spectra obtained. The use of higher temperatures may result in an increase in the conversion, as well as crystallinity, within the milling chamber. Shorter retention times could be implemented with the addition of the ageing step, as it was observed to improve conversion, as well as crystallinity during the 'versatility study' conducted. The influence of milling parameters on Ca-Al, Cu-Al and Zn-Al LDH should be further explored. The synthesis could be conducted with or without the addition of the ageing step and could be seen as a viable method for commercial scale synthesis of LDH. Optimisation of such a system should be considered in future studies.

Keywords: Mechanochemistry, Layered double hydroxides, Synthesis, Green chemistry, Milling parameters, Netzsch LME 1 horizontal bead mill.

## Acknowledgements

I would like to thank:

- My heavinly father God as he has guided me through this year and provided me with the strength to complete my studies.
- My supervisor, Dr. Johan Labuschagne, for his guidance, support and patience with this project. Through him I have learnt many valuable skills and lessons that I will use throughout my life.
- Mr. Jan Mentz for aiding in the funding and development of this research project.
- TeckSparks Pty Ltd for Project funding.
- Mrs. Wiebke Grote for her extensive help with X-ray diffraction analysis and for always making time for me.
- Ms Jeanette Dykstra for always making time to help me with my XRF analysis and data.
- My family for their love, emotional and financial support.
- My brother Willem Barnard for many sponsored meals and comfort food.
- My friends, Johan Esbach, Frances Seeliger, Louise van Tonder, Hester Oosthuizen, Heidi Marais, Bianca Gevers and Keagan Bester, for their never ending support, guidance and love.
- Robert Charles Webber for his endless love and support, and for picking me up at my lowest points throughout this year.

# Contents

# List of Figures

# List of Tables

# 1 Introduction

Layered double hydroxides (LDHs) have gained attention due to their wide range of physical and chemical properties. LDH materials can be synthesized using various different techniques of which the most common are co-precipitation, reconstruction, hydrothermal methods and urea decomposition-homogenous precipitation (Qu, Zhang, et al., 2015a). These techniques often produce environmentally unfriendly waste product and require high temperatures for synthesis. Novel, "green" synthesis techniques are therefore often sought after.

Recently the use of mechanochemistry as an alternative synthesis procedure has gained wide-spread attention. Various techniques and combinations involving the wet or dry milling of raw materials have been attempted and found to be successful. Three primary mechanochemical synthesis procedures have been identified, namely single-step grinding, mechano-hydrothermal synthesis and two-step grinding (dry grinding followed by wet grinding (Qu, Zhang, et al., 2015a). Single step grinding has predominantly been performed in two ways: (1) the dry grinding of metal salts and hydroxides with small amounts of sodium hydroxide or (2) wet grinding of a metallic salt solution (Qu, Zhang, et al., 2015a). The success associated with the formation of an LDH phase for single step grinding procedures is influenced by the selected starting materials (Qu, Zhang, et al., 2015a). The use of metallic salts of chlorides or nitrates allows for LDH synthesis but introduces a washing step that produces an undesirable waste solution. The use of hydroxides and oxides as starting materials eliminate the production of waste solution, promoting the 'green' synthesis of LDH materials, however has proven to be challenging (Qu, Zhang, et al., 2015a).

Limited research has been conducted on single-step wet grinding and low conversion rates obtained warrant the need for further research (Qu, Zhang, et al., 2015a)(Iwasaki, Yoshii, et al., 2012). The study therefore aims to expand on one-step wet mechanochemical synthesis of LDHs, from oxides, hydroxides and basic carbonates, by making use of a Netzsch LME 1 horizontal bead mill. This included exploring the synthesis of Mg-Al LDH with a change in parameters such as rotational speed, retention time, solids loading, bead size and jacket water inlet temperature. Additionally the synthesis of Mg-Al, Ca-Al, Zn-Al and Cu-Al LDH was further explored by making use of existing synthesis conditions. This was specifically in relation to $M^{2+}$:$M^{3+}$ ratio and selected starting materials associated with existing mechanochemical techniques. The selected mill allows for the continuous, semi batch or batch synthesis of LDH materials. The process could therefore be easily up-scaled to produce large volumes of consistent and commercially viable LDH product. This method of synthesis further allows for the potential for the control of particle size.

The use of LDH materials could therefore be expanded to suit fine-particle application in future studies.

# 2 Literature study

## 2.1 Layered double hydroxides

Layered double hydroxides (LDHs) are clay-like minerals commonly referred to as "anionic clays" with a wide range of physical and chemical properties. These include (Forano et al., 2006):

- Wide range of chemical compositions.
- Variable layer charge density.
- Interlayer space with reactive properties.
- Ion exchange capabilities.
- Swelling in water.
- Rheological properties.
- Colloidal properties.

The layered structure associated with LDH materials is as indicated in Figure 1. The general formula for components classified within the family can be expressed according to Equation 1, representing the layer and interlayer composition respectively. Similarly Equation 2 represents a simpler more commonly used alternative. The general formulae is a combination of the representative divalent and trivalent metal cations associated with an LDH material (Forano et al., 2006).

$$[M^{II}_{1-x}M^{III}_{x}(OH)_2][X^{q-}_{x/q} \cdot nH_2O] \tag{1}$$

$$[M^{II} - M^{III} - X] \tag{2}$$

The general formula can be further extended to multicomponent systems and is described by Equation 3 (Forano et al., 2006).

$$[M^{II} - M'^{II} - M^{III} - M''^{III} - X - Y] \tag{3}$$

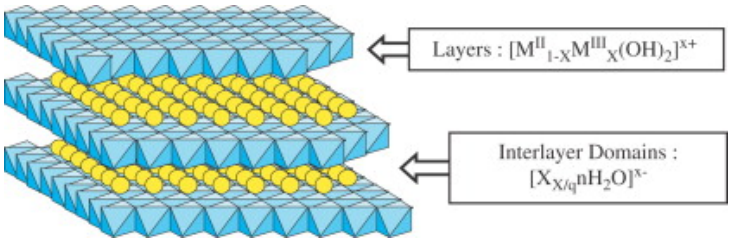


**Figure 1:** Structure associated with layered double hydroxides reproduced with permission from (Forano et al., 2006).

The structural stability and formation of LDH is dependent on the cation radius. The structure becomes unstable when the ionic radius of $M^{2+}$ is smaller than 0.06 nm. Figure 2 depicts the elements that have been reported to enter the composition of natural or synthetic LDH materials (Forano et al., 2006).

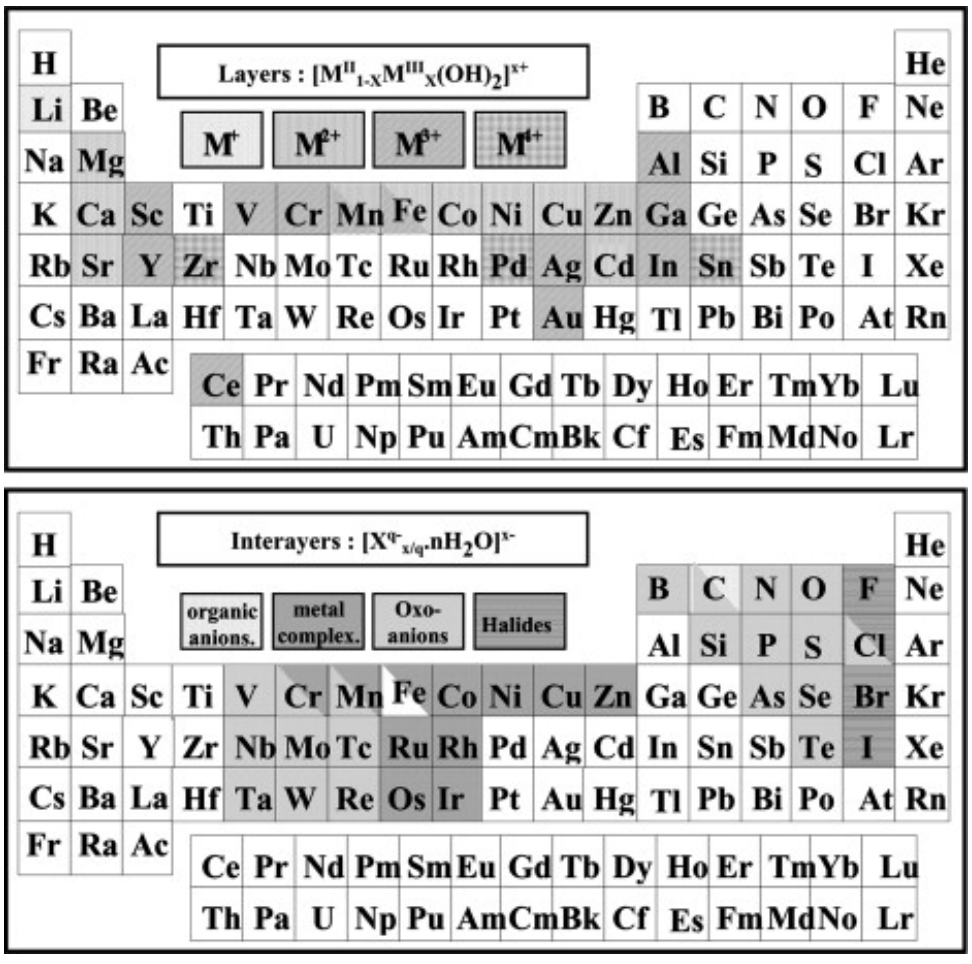


**Figure 2:** Elements that may enter the composition of natural or synthetic LDH materials reproduced with permission from (Forano et al., 2006).

Layered double hydroxides are often synthesised through wet chemical procedures unsuitable for economic large scale production. The aim of the research conducted was to identify possible green synthesis procedures that result in highly crystalline, pure phase LDH products.

### 2.1.1 Preparation of Layered double hydroxides

A variety of preparation techniques exist for the synthesis of LDH phases. Understanding these existing methods and LDH formation mechanisms could be crucial when exploring new synthesis procedures. The most common synthesis techniques are therefore described below.

**co-precipitation** This method is considered to be the most common preparation technique for LDH phases. It involves the slow addition of a mixture of divalent and trivalent metal salts into a reactor filled with water. The pH is then maintained through the addition of a second alkaline solution. This then results in the co-precipitation of the selected metallic salts (Rives, 2001).

The mechanism associated with co-precipitation involves the condensation of hexa-aqua complexes in solution, such that brucite-like layers are built. This structure should then contain the distribution of both selected metallic cations, along with solvated anions within the interlayer. Interlayer anions originate from the same solution into which the metallic salts are added and counter the added metallic cations. If the pH of the system is high, the anion could be a hydroxyl anion from the alkaline solution. Similarly at high pH values, synthesis would need to be conducted under $CO_2$-free conditions to avoid atmospheric carbonate contamination. Intercalation of a desired anion could be achieved through the preparation of a solution containing this anion in the reactor before starting the synthesis (Rives, 2001).

Experimental procedures that influence the crystallinity of the LDH phase obtained are as follows (Rives, 2001):

1. Reactor temperature.
2. pH of selected reaction medium.
3. Metallic salt solution concentration.
4. Alkaline solution concentration.

5. Flow rate of selected reactants.

6. Ageing of the precipitate obtained.

7. Electrolyte accumulation within the reaction medium.

8. Hydro-dynamics associated with stirring mechanisms, reactor geometry and so forth.

9. Complex formation of the metallic cations, which is dependent on the history of the metallic salt solution and can give rise to various different charged monomers or oligomers.

These parameters need to be optimised for the formation of highly crystalline LDH phases. Synthetic LDHs are often microcrystalline platelets that aggregate into a "rose des sables" morphology. Intercalation of certain anions is pH dependent. The pH domain for the selected anion needs to overlap with that of the desired LDH phase, otherwise the selected combination may not be possible.

Thermal treatment is often necessary as optimisation of the pH value, along with ageing time, does not always lead to well crystallised LDH as expected with co-precipitation. Improvement of the the crystallinity is primarily explored with the use of two methods of thermal treatment (Rives, 2001):

1. Temperature adjustment during co-precipitation.

2. Hydrothermal treatment of precipitated material.

Hydrothermal treatment is more commonly used and favours highly crystalline LDH formation when in the presence of water vapour. This is however only if the temperature associated with LDH decomposition is not exceeded. Two methods of hydrothermal treatment are generally followed. The first involves the heating of a closed stainless steel vessel in which an aqueous solution of an LDH precursor is placed. The temperature is set below the critical point at the equilibrium pressure. The second method involves the heating of the selected sample within a gold or silver tube. The pressure is set to be high within the order of 1500 bar for a certain period of time (Rives, 2001).

Other factors such as addition rate and ageing have been known to influence the crystallinity of the LDH phase present. The addition rate can be controlled with the use of a an automatic titration device. Approximately 48 h of ageing is often necessary for high crystallinity. Ageing times should however be tailored towards the specific LDH being synthesised (Rives, 2001).

**The urea method** Urea is considered to have a variety of desirable properties and is used as an agent for precipitation. It has a history of being used to precipitate a selection of metal ions, such as insoluble salts or hydroxides, if in the presence of an appropriate anion (Rives, 2001).

Urea is highly soluble in water and is a weak Brönsted base. Its hydrolysis rate can be controlled through controlling the temperature. The mechanism associated with hydrolysis involves the formation of ammonium cyanate. This is considered to be the rate determining step, followed by the hydrolysis of ammonium cyanate to ammonium carbonate. An increase in temperature from 60 °C to 100 °C increases the rate constant by approximately 200 times its original value. Further hydrolysis of the ammonium to ammonia and the carbonate to hydrogen carbonate results in an overall pH of 9, taking temperature into account. This creates the ideal environment for the precipitation of a variety of metal hydroxides (Rives, 2001).

Urea based homogenous precipitation is known for obtaining well-defined inorganic particles through the decomposition of urea at elevated temperatures. Urea hydrolyses upon heating, producing ammonium and carbonate ions. This results in an increase in the homogenous pH, further contributing to the formation of monodispersed hydroxide and carbonate particles. LDH particles with narrower particle size distributions, than those prepared via titration methods, have been prepared with the urea approach. LDH materials prepared with the use of the urea method have been used for the incorporation of organic anions through ion exchange (Wijitwongwan, Intasa-ard & Ogawa, 2018). A study conducted by (Ogawa & Kaiho, 2001) resulted in the formation of monodispersed and uniform hydrotalcite making use of homogenous precipitation in the presence of urea.

**Induced hydrolysis** This method of LDH preparation involves two steps. Initially the selected trivalent metal hydroxide is precipitated by making use of an alkaline solution. This step is then followed by the slow addition of the precipitate into a solution containing the divalent metal salt. This is done at a constant pH, resulting in the controlled release of the trivalent metal substance and therefore the formation of LDH material (Rives, 2001).

**Sol-Gel** The Sol-Gel method is described as producing LDH materials in a gel-like form from alkoxides. The procedure allows for the control of the $M^{2+}$:$M^{3+}$ ratio through the control of the initial gelling parameters (Lopez et al., 1997). LDH materials prepared through this method have exhibited high thermal stability, however have poorer crystallinity than those prepared through co-precipitation (Rives, 2001).

**Hydrothermal Method** Hydrothermal synthesis commonly refers to heterogenous reactions that occur in an aqueous media at temperatures and pressures greater than 100 °C and 1 bar (Hare, 2001). LDH can therefore be synthesised through the use of oxides and hydroxides as raw materials, rather than salt solutions as used by other methods.

A study conducted by (Xu & Lu, 2005) involved the synthesis of Mg-Al LDH through the use of MgO and $Al_2O_3$. The procedure involved the heating of the oxide mixture to a temperature of 110 °C, upon which LDH formation occurred. It was noted that LDH was the primary phase present, with minor phases resulting due to the initial pH of the oxide suspension, as well as the MgO:$Al_2O_3$ ratio. The alkalinity of the solution resulted in some of the MgO remaining unreacted. It was thus recommended to initially hydrate the oxides to their respective hydroxide phases prior to synthesis.

It was further suggested that the $Mg(OH)_2$ be dissociated as quickly as possible such that $Mg^{2+}$ and $OH^-$ deposit on the surface of the selected $Al(OH)_3/Al_2O_3$, forming an LDH precursor. It is possible for $Al(OH)_4^-$ to ionize from the $Al(OH)_3$ and deposit itself on the surface of the $Mg(OH)_2$/MgO resulting in a similar precursor formation. Further heating results in the crystallisation of the precursor material as a result of the diffusion of metal ions into the solid lattice. This proposed formation mechanism making use of dissociation, deposition and diffusion via two pathways was assumed to be applicable to the general formation of LDH materials. A schematic of the proposed mechanism is depicted in Figure 3 (Xu & Lu, 2005).

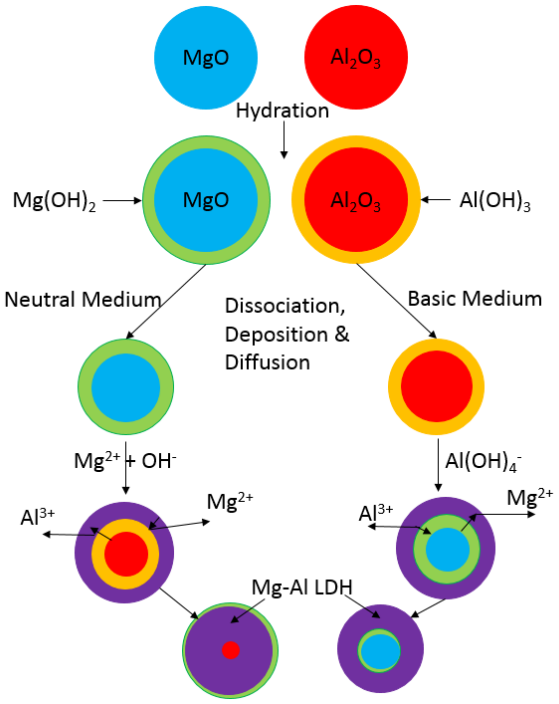


**Figure 3:** Mechanism for LDH formation in the presence of a neutral or basic solution as reproduced with permission from (Xu & Lu, 2005).

**Proposed mechanisms for LDH formation** The mechanisms associated with LDH formation are dependent on the selected synthesis procedure. Understanding existing proposals for formation mechanisms could provide insight into the behavioural changes associated with the selected raw materials when making use of mechanochemistry.

(Xu & Lu, 2005) proposed that three separate view points exist regarding the formation of LDH materials. A study conducted by (Boclair, Braterman, et al., 1999) involved observing the titration behaviour of $M^{2+}$ and $M^{3+}$ against NaOH. Precipitation was noted to occur in two steps, resulting in poorly crystallised LDH material. The addition of a base to a solution containing the mixture of $M^{2+}$ and $M^{3+}$ anions result in the formation of LDH materials. Initially, however, a mixture of hydrous oxides and hydroxides of the $M^{3+}$ anion would precipitate. Continuous addition of the base would allow for the precipitation of the LDH material, rather than just $Mg(OH)_2$.

The mechanism associated with the formation and crystallisation, with a change in temperature, of LDH was investigated by (Eliseev et al., 2002) through co-precipitation. The LDH specifically observed during this study was hydrotalcite. The pH of the system was kept constant at a value of 10. The sample was divided into two separate parts and the temperature controlled either at 20 °C or at 80 °C respectively. Transmission electron microscopy and scanning electron microscopy revealed that initially samples exhibited amorphous filamentary agglomerates when kept at the selected temperatures for short time periods. The agglomerates however were not observed for samples kept at elevated temperatures for 3 days or more. The degree of crystallinity for samples kept at higher temperatures was observed to greater than those kept at lower temperatures for the same period of time.

Crystallisation was determined to be a zero order process. During the initial part of the synthesis the precipitation of agglomerates containing $Al(OH)_3$ or $Mg(OH)_2$ occurs. The $Mg(OH)_2$ precipitated as a layered structure, whereas the $Al(OH)_3$ formed amorphous filamentary agglomerates. The next step involves the crystallisation of the LDH material where diffusion of aluminium atoms into the structure of the $Mg(OH)_2$ occurs. The final stage involves the inclusion of these aluminium atoms into the LDH structure. This was observed through the change of the Aluminium from a tetrahedral coordination to that of an octahedral one, which is characteristic of aluminium located within LDH. The mechanism could therefore be summarised as the initial formation of amorphous agglomerates that gathered in blocks to form a layered structure. The change in coordination of the aluminium atoms from tetrahedral to octahedral was stated to occur simultaneously (Eliseev et al., 2002).

A study conducted by (McLaughlin, White & Hem, 1994) explored the influence that het-

erocoagulation had on the formation of Mg-Al-$CO_3$ LDH, from a suspension of $Mg(OH)_2$ and aluminium hydroxycarbonate. It was observed that when heterocoagulation within the system was prohibited through pH control, hydrotalcite formation rapidly occurred upon exposure of MgO particles to a suspension of aluminium hydroxycarbonate. SEM imaging of the samples indicated that nucleation and growth of the LDH crystal occurred on the surface of formed $Mg(OH)_2$ particles. Mixed suspensions in which heterocoagulation was present resulted in the delayed formation of the LDH material. This was stated to be a result of occlusive coating of the aluminium hydroxycarbonate on the surface of the $Mg(OH)_2$. Hydrotalcite formation occurred sooner in systems that were initially at a higher pH value. This was presumably due to the more rapid ageing of the aluminium hydroxycarbonate coating resulting from early exposure to the surface of the $Mg(OH)_2$ particle. Other aluminium containing hydroxides were mixed with $Mg(OH)_2$ forming suspensions in which heterocoagualtion did not occur. LDH formation was observed to occur rapidly.

A similar study conducted by (Vanderlaan, White & Hem, 1982), investigating the rate at which $Mg(OH)_2$ and aluminium hydroxycarbonate mixtures neutralise acid, observed that the rate was influenced when ageing certain samples. Hydrotalcite formation was stated to occur during the ageing of the gel mixtures and was noted to be present earlier in mixtures with high molar ratios of Mg to Al, a high overall gel concentration, stored at elevated temperatures or had a high initial pH.

## 2.2 Green chemistry

The principle of green chemistry is defined as practising chemical science or manufacturing in a manner that is sustainable, safe, non-polluting, consumes little material and energy and produces no waste product. The incorrect performance of the production, processing, use and disposal of chemical products may result in environmental or human harm (Manahan, 2006). Implementation of green chemistry may result in the total redesign of chemical processes or products such that wastes and the use or production of harmful materials are minimised. It is considered to promote innovation such that profits are increased without detriment to human health and the eco-system. There are various long term benefits that ensure sustainability. These include (Manahan, 2006):

1. Economic: When implemented and maintained at a sophisticated level, green chemistry usually costs less than normal chemistry practices.
2. Materials: Green chemistry is sustainable when efficiently using materials, implementing maximum recycling and using a minimum amount of virgin raw materials.

3. Waste: The reduction or elimination of waste materials and production allows for sustainable green chemistry.

The project aims to find a sustainable synthesis procedure that makes use of the principles surrounding green chemistry. This includes attempting to synthesise layered double hydroxides without the need for harmful solvents such as those used in conventional methods.

## 2.3 Solvent free synthesis of nanoparticles

The synthesis of nanoparticles has been broadly studied due to their versatility in various applications such as catalysis, magnetic materials, semiconductors and pharmaceuticals. The size of the nanoparticles affects the final physical and chemical properties of the product in which they are incorporated and is thus one of the primary manipulated characteristics (Landge, Ghosh & Aiken, 2018).

Typical chemical synthesis methods include mixing of the relevant metal salts or composites in the presence of a solvent or surfactant. Comparatively physical approaches make use of methods such as evaporation condensation, direct heating or laser ablation. Most techniques require an undesirably large amount of solvent to carry out the necessary processes. Solvent-free methods were thus explored, providing a more green and economical approach to the synthesis of the desired particles and products. This could be divided into two main categories, namely mechanochemistry and thermal treatment. Mechanochemistry can be subdivided into ball milling or grinding with a mortar and pestle. Comparatively, thermal treatment is subdivided into decomposition or microwave energy. Decomposition or Thermolysis is further divided into the categories of sublimation thermal heating of metal salts and thermal heating with capping agents(Landge et al., 2018). Figure 4 depicts the methods associated with solvent free synthesis of nanoparticles (Landge et al., 2018).

Advantages associated with solvent free synthesis procedures include (Landge et al., 2018):

1. The conversion of reactants to products is often high.
2. Little to no solvent is incorporated, preventing the use of harmful chemicals.
3. The incorporation of capping agents allows for the prevention of aggregates and particle overgrowth.

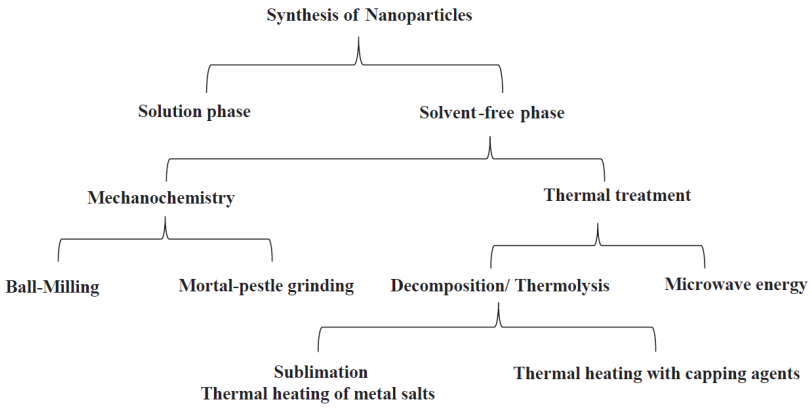


**Figure 4:** Methods associated with the solvent free synthesis of nanomaterials reproduced with permission from (Landge, Ghosh & Aiken, 2018).

4. Clean products are often synthesised with no need for additional purification.

The most well known techniques within the topic of mechanochemistry for nano particles are ball milling and mortar and pestle grinding. The definition of mechanochemistry is further discussed in detail in section 2.5.

## 2.4 Magnesium oxide

Magnesium oxide is a hydroscopic white solid that occurs naturally as "Periclase". Care is often needed to prevent reaction with atmospheric $H_2O$ as seen by Equation 4. It is considered to be stable and slightly soluble in water with a solubility of 0.0086 g·100 $ml^{-1}$ (Ropp, 2013).

$$MgO + H_2O \rightarrow Mg(OH)_2 \tag{4}$$

Several grades of commercial MgO are available and include (Ropp, 2013):

1. Dead-burned: The MgO has been subjected to calcination at temperatures ranging between 1500 °C and 2000 °C. Most if not all for the reactivity is eliminated and is therefore termed 'dead-burned' or refactory grade. Application includes steel production.

2. Hard-burned: Calcination of the MgO conducted at temperatures ranging between 1000 °C and 1500 °C. The reactivity is considered to be low. Application includes fertalisers and animal feeds.

3. Light-burned: The MgO is subjected to calcination at temperatures between 700 °C and 1000 °C. It is termed 'caustic' or 'light burned' magnesia and is considered to have a wide range of reactivity.

Various models have been suggested to describe the hydration of MgO to $Mg(OH)_2$. The hydration reaction can be influenced by factors such as the chemical and phase composition of the magnesia, temperature, time, humidity, particle size and crystallographic orientation. Higher temperatures, pressures and times result in an increase in the hydration rate. The hydration reaction may become faster and easier with a decrease in crystallite size and an increase in the specific surface area and pore volume (Rocha, Mansur & Ciminelli, 2004).

A study was conducted by (Rocha et al., 2004) in which the hydration of caustic magnesia was investigated through reacting high purity MgO with $H_2O$ in a batch reactor. The effects of temperature (35 °C to 90 °C), retention time (0.5 h to 5 h), solids loading (1 % to 25 %) and particle size (-212+75 $\mu$m to -45+38 $\mu$m) on the hydration reaction and kinetics were investigated. Experimentation involved the addition of the solids, at a specified temperature, to a 1000 $dm^3$ borosilicate glass reactor for a set period of time. The slurry was kept under constant agitation at 1220 rpm. Prior to hydration the MgO was calcined at temperatures ranging between 900 °C and 1000 °C. The study suggested that the hydration of caustic MgO in liquid $H_2O$ occurs as follows:

1. The $H_2O$ adsorbs onto the surface of the MgO particle, whilst simultaneously diffusing throught its pores.
2. The MgO undergoes a dissolution reaction with absorbed $H_2O$ resulting in a change in porosity, such that supersaturation of water with $Mg^{2+}$ and $OH^-$ ions is reached.
3. Upon supersaturation, $Mg(OH)_2$ forms on the surface of the MgO, resulting in a further change in porosity. Hydration eventually becomes difficult due to the outer layer of $Mg(OH)_2$.

Primary assumptions for the suggested mechanism included no significant change in the initial particle size and dissolution rate. Higher temperatures were further observed to influence the hydration mechanism, with the mechanism initially governed by the dissolution of the MgO (chemical control). As the reaction progresses, the surface and pores of the MgO are covered with a $Mg(OH)_2$ layer. The reaction rate eventually decreases due to the diffusion of $H_2O$ becoming increasingly more difficult. The reaction scheme is then further controlled by diffusion. Lower temperatures were found to be

only chemically controlled as conversion is low (Rocha et al., 2004). The study however does not include the addition of mechanical energy other than stirring. The addition of milling media and therefore mechanical grinding could result in the removal of the $Mg(OH)_2$ outer layer, creating new reactive sites for further hydration.

Supersaturation was further observed by (Rocha et al., 2004) to occur rapidly within the first few minutes, with initial limits increasing with a decrease in temperature. Figure 5 depicts the transient profile of $Mg^{2+}$ concentration during hydration experiments with a change in hydration temperature. Elevated temperatures resulted in an increase in the rate of hydration, with the kinetics and experimental data depicted in Figure 6. Comparitively the solubility of $Mg(OH)_2$ decreases with an increase in temperature as could be seen in Figure 7. Hydration of MgO is commonly conducted with the use of a water bath and occurs rapidly when making use of of light magnesia. It can however be very slow for dense varieties of magnesia that has been prepared through calcination at high temperatures. Water was observed to hardly attack this form of magnesia. It has been suggested that two types of $Mg(OH)_2$ can exist, one that is more readily soluble (labile) and one that is not (stabile), and is dependent on the how it was synthesised. The labile form can result from the hydration of MgO.

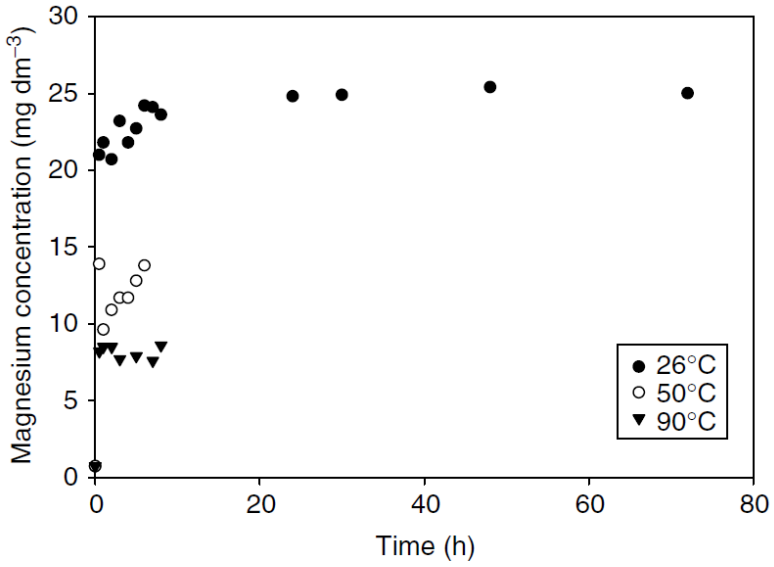


**Figure 5:** Transient profile of $Mg^{2+}$ concentration obtained for hydration experiments reproduced with permission from (Rocha et al., 2004).

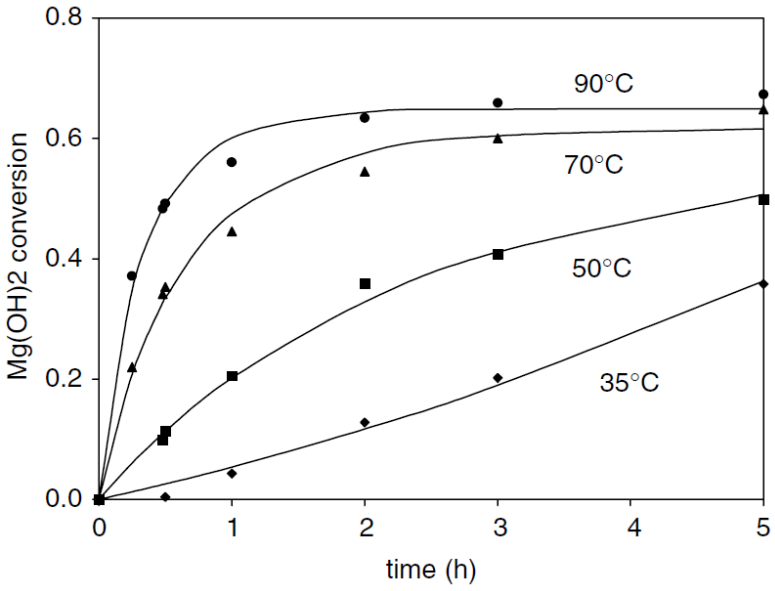


**Figure 6:** Hydration kinetics of MgO with a change in temperature (5% solids, 1220 rpm, -45+35 $\mu$m) reproduced with permission from (Rocha et al., 2004)

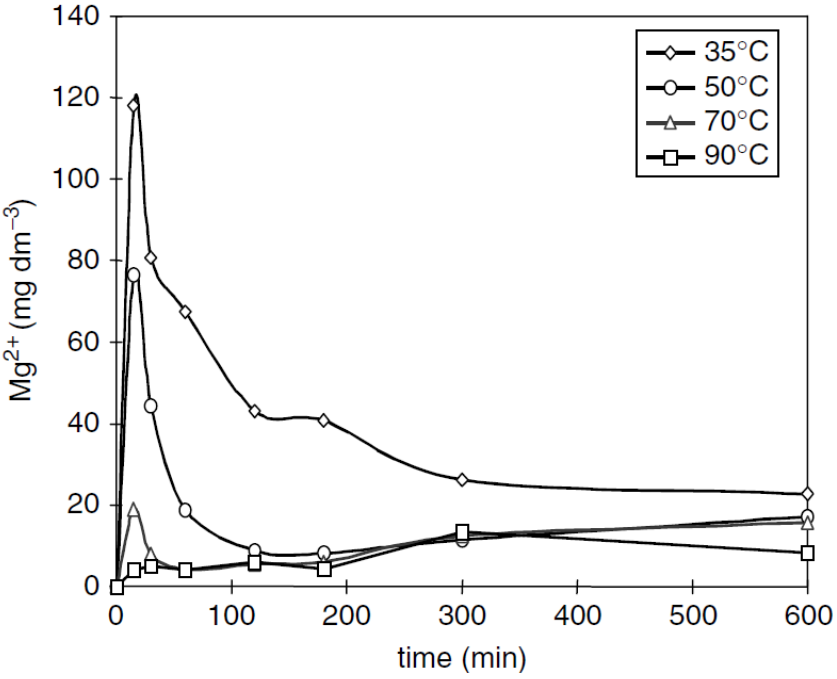


**Figure 7:** The effect of temperature on the solubility of $Mg(OH)_2$ as reproduced with permission from (Rocha et al., 2004).

## 2.5 Mechanochemistry

Various definitions for the term "mechanochemical" exist and the question of which processes are a subject of mechanochemistry is still debatable worldwide. A process could be

considered "mechanochemical" if the initial step results in a primary bond being broken due to an induced mechanical force. Broader definitions include mechanochemistry being primarily concerned with the chemical and physio-chemical changes of components due to mechanical energy (Takacs, 2014).

Reactive surfaces form due to the breaking of bonds which further results in surface reconstruction and reaction with the surrounding medium. Mechanochemical reactions are not limited to the use of solids. Vigorous mixing of liquid mixtures may result in strain and bond breaking due to the induced molecular forces (Takacs, 2014).

The initial step of a "mechanochemical" reaction could incorporate the emission of low energy electrons rather than the breaking of chemical bonds. The electrons could induce negatively charged radicals resulting in a chemical reaction upon absorption. Tribochemical processes primarily make use of this concept due to the main form of mechanical action being attributed to sliding (Takacs, 2014).

Mechanochemistry is considered unique due to the possibility of products differing from compounds and phases produced using conventional chemical techniques. Materials that have difficulty forming traditionally can be synthesised with mechanochemistry. The lack of solubility of certain chemicals can be problematic, however reactions can be induced with the use of a milling process. Thermochemical reactions sometimes requires the use of milling to bring reactants together in the desired configuration (Takacs, 2014).

Organic molecules, unique to mechanical mixing-milling, can be obtained without breaking the covalent bonds in unusual places. This would be achieved using gentle grinding action forcing reactants together that otherwise have difficulty mixing or coming together in the desired configuration. Comparatively, inorganic materials subjected to high energy milling have provided phases and micro-structures that are unique to mechanochemistry. High energy milling results in the destabilisation of complicated crystal structures due to forced mixing and formation of a high defect density. The final result would then be simple metastable crystalline substances or amorphous materials (Takacs, 2014).

## 2.6 Milling technology

The conventional milling technology associated with LDH synthesis include ball mills, mixer mills or planetary ball mills. It was discovered that the properties of the LDH are largely depended on the selected milling process (Intasa-ard et al., 2018). Manual grinding is often performed as an additional comparative test in which a mortar is used. Details regarding these conventional technologies are further discussed in this section.

Unconventional milling technology such as jet milling, knife milling, hammer milling, pin milling and stirred media milling were further considered. Milling technology can be divided according to wet or dry processes.

### 2.6.1 Dry milling technology

Dry milling could refer to the milling of dry solid samples without the addition of solvent or solution. Some technology listed below has further been used for "wet" milling during LDH synthesis in which small amounts of solution are used.

**Manual grinding** Manual grinding has been conducted for centuries with the use of a mortar and pestle for the grinding of drugs or foods. Common designs include a pestle head and mortar consisting of porcelain or heavy stone. Variations of the design have been identified throughout history with some being constructed out of metals rather than stone (Pathak, 2017).

Manual grinding is often conducted with dry solids, however the incorporation of a small amount of liquid is possible. The process involves placing the solid materials into the hollow of the mortar followed by the manual crushing and grinding with the pestle.

**Pin mill** Pin mills form part of a class of high speed mills that contain pin breakers in their grinding circuit. These could be located on a rotor with stator pins situated between the many circular rows of pins on the rotor disk. The pins may otherwise be located on rotors operating in opposite directions resulting in an increase in the differential of speed (Perry & Green, 2008).

**Hammer mill** Hammer mills form part of a class of high speed mills that work for fine pulverising and disintegration. The rotor may be vertical or horizontal which carry hammers commonly referred to as beaters. The hammers can vary between T-shaped elements, stirrups, bars and rings or disks (Perry & Green, 2008).

The grinding action is a result of the impact and attrition between the solid material being ground, the housing and the beaters. The particle size can often be controlled through changing the speed of the rotor, feed rate, the distance between the hammers and the grinding plates and the number or type of hammers used. A screen or grating often encloses a part of or all of the rotor and serves as an internal classifier (Perry & Green, 2008).

The feed is generally non abrasive with a hardness of 1.5 or less. The mill may be operated in conjunction with an external air classifier to produce fine particles. Many machines may contain internal air classifiers.

**Fluid energy or jet mill** Fluid energy mills are classified according to the nature of the milling action. Two major classes exist. The first class makes use of fine high velocity streams that are at an angle around all or a portion of the periphery of a grinding chamber. The other class makes use of high velocity streams that enter the chamber such that two streams impact each other (Perry & Green, 2008).

The mills, despite their class, result in high energy release and turbulence forcing the particles to grind upon themselves. Not all particles end up being fully ground and therefore a classifying action needs to be implemented such that oversized particles are returned for further grinding. Various types of fluid energy mills are available and vary depending on their intended function.

**Knife mill** Knife mills contain a rotor with blades attached such that size reduction and homogenisation of soft, medium or hard particles can occur. The mill is not restricted to dry milling but can also be used for moist or wet materials. Conventional knife mills are used as a household item for food preparation. Common applications include foods, drugs, animal feeds, biology and microbiology (Retsch, 2018).

**Ball mills** Ball mills make use of a propulsion unit which results in the movement of milling balls or media, within a milling chamber or vessel. This results in the creation of frictional forces between the milling media, the milling media and the vessel walls and between the added material and the media. These forces result in wear stresses which ultimately refines the material added to the system, creating a particle size distribution. The mechanisms associated with wear are dependent in the type of mill selected and include impact, friction or shear forces (Ranu & Stolle, 2015).

The processes carried out within ball mills are influenced by different parameters namely the chemical, technological and process parameters. Chemical parameters are those associated with the chemical transformations that occur in the milling chamber and include (Ranu & Stolle, 2015):

1. The type of chemical reaction.
2. Presence of catalysts.

3. Additives.
4. Reagent ratio.
5. Presence of liquids or solvents.

Technological parameters are those that describe the technology used for the reduction of the size of particles and include (Ranu & Stolle, 2015):

1. Type of ball mill.
2. Type of milling media.
3. Number of milling media.
4. Size of milling media.
5. Percentage loading of the milling vessel.

Process parameters are used to control the amount of energy added to the system and include the following (Ranu & Stolle, 2015):

1. Operating frequency (rpm, which is directly related to the kinetic energy associated with the milling media and thus the energy that is given off as heat.
2. Reaction time or milling time: related to the reaction kinetics.
3. Temperature: related to the reaction kinetics.

Three types of ball mills are primarily used for chemical synthesis, namely planetary ball mills (PBM), mixer ball mills (MBM) and vibration ball mills (VBM). Each of these differ in terms of operating principle and the maximum capacity of the vessel.

Planetary ball mills make use of a central disk (sun disk) on which smaller diameter disks are mounted containing the the mechanism that holds the milling vessels. The number of vessels vary between 1, 2 or 4. The disks operate such that they rotate in opposite directions allowing the motion of the milling vessels imitate the rotation of a planet around a central body. The trajectories associated with the milling media have been previously monitored, however specific calculations have been proven difficult to conduct. It has been accepted that the media will follow the rotation of the vessel up to one quarter of its perimeter. The media will then travel through the volume of the vessel such that they collide with the opposite wall (Ranu & Stolle, 2015).

Mixer ball mills (MBM) and vibration ball mills (VBM) operate differently from planetary ball mills (PBM), with the initial force being generated due to oscillations at differing frequencies. The primary difference between MBM and VBM is the plane in which the oscillation occurs and the degree of freedom of the oscillation. Mixing media mills have a vessel mounted on a swing arm which follows a circular arc with oscillation in the horizontal plane. The milling media follow the direction of the container and keep moving despite the oscillation reaching its reversal point. This results in the collision of the media with the ends of the milling vessel. The wear mechanisms associated with this method of milling are friction and impact forces (Ranu & Stolle, 2015).

Comparatively vibration bead mills oscillate on different planes making use of a Cartesian coordinate system. The trajectories are similar to mixer ball mills with two dimensional oscillation taking place. The wear mechanisms were found to be similar to that of mixer ball mills despite the increased complication of the system (Ranu & Stolle, 2015).

Industrial applications often involve the scale up from a ball type mill (laboratory scale) to a stirred media mill. The parameters influencing the processes within the milling chamber, namely chemical reaction and particle size distribution are summarised below (Ranu & Stolle, 2015):

1. Ball mill type: The energy densities within the different systems vary at similar frequencies. Little difference is observed in systems of comparable reaction time and scale in terms of yield and selectivity if operating frequency is varied accordingly. The type of mill selected depends entirely on the desired end function and objective.

2. Grinding material: The properties, such as density, Young's modulus, hardness and abrasiveness influence the nature and outcome of the chemical reactions that occur within the milling vessel and further the final particle size distribution. Kinetic energy generated through torque of the ball mill's propulsion unit is transformed into heat or chemical energy through frictional and impact forces. If chemical reactions result due to the mechanical action of the mill it can be classified as a mechanochemical reaction. Frictional forces may further result in an increase in the bulk temperature of the system, further increasing the rate at which reactions occur. In various cases the product yield of certain reactions has increased by changing the material from lightweight to heavy weight material. If no influence however has been observed, possible product degradation due to high energy could be the cause. The chemical resistance associated with the grinding material is considered important with tungsten carbide and stabilised zirconia identified as the most desirable. This is a result of being chemically inert. The abrasive resistance of zirconia is further considered to be very high. Media with high porosity tend to result in memory

effects which are considered undesirable if not cleaned adequately. Abrasion of the surface of milling tools is undesirable and may result in the interference of induced chemical reactions. Milling balls continuously lose weight during the process and is considered problematic as it decreases the amount of kinetic energy provided to the system.

3. Volume fraction of milling media: The mass of the milling media strongly affects the kinetic energy of the system and can be changed by changing the type of material, size or the number of balls or media. The minimum and maximum number of balls is dependent on the type of mill used, the required trajectories and the wear effects. Increasing the number of grinding bodies within the vessel result in an increase in the energy that is transferred to the system and therefore an increase in the bulk temperature. The relationship, for various organic reactions, between number of bodies and yield are not similar due to different activation energy requirements.

4. Size of milling media: The diameter of the milling balls is dependent on the volume of the milling chamber. The energy transferred to the feed material (stress energy) is proportional to the energy associated with the colliding media bodies (impact energy) and the collision frequency. The impact energy is thus directly proportional to the kinetic energy added to the system. A decrease in the number of grinding bodies (ball-to-powder ratio) results in a decrease in the probability of collisions and therefore product yield. If the overall mass of the media remains constant then the collision frequency and number of stress events within the system is directly proportional to the number of grinding bodies and inversely proportional to their size. The possibility of collision therefore increases for smaller grinding bodies and increases with an increase in the number of grinding bodies. If the diameter of the media is decreased, while keeping the number of grinding bodies constant (mass is not constant) the relevant impact energy will decrease and therefore result in a decrease in product yield.

5. Volume chamber filled: The volume of the vessel that is filled (filling degree) directly influences the trajectory of the grinding media within the vessel. If the vessel is too full with media and feed, no movement and therefore no kinetic energy can be transferred within the system. Efficient energy transfer requires that the milling media have space for acceleration and movement within the milling vessel. Specifications or limits are often provided by the manufacturer.

6. Operating frequency: The operating frequency is directly related to the kinetic energy associated with the milling media. It thus determines the amount of energy that is transferred into heat or chemical energy. It should be noted that an increase in target variables such as conversion, yield and selectivity is expected with an

increase in the operating frequency. It has however been noted that a maximum occurs, after which a decrease in the target variable is observed. This could be due to high energy impacts resulting in the distortion of chemical equilibrium and resulting in unfavourable side reactions. This may also result in different reaction routes which may lower the performance of the desired or specified process. This could further occur in systems which accommodate or result in higher energy densities, such as different types of ball mills.

7. Milling time: Extended periods of milling time result in an increase in the number of collisions between the mill media, mill tools and feed material. The energy density within the system remains constant, however more energy is distributed to the feed material and milling media (the mill charge). Generally an increase in milling time result in an increase in the target variables such as conversion or yield, but prove complicated for selectivity due to the possible promotion of side or parallel reactions.

8. Reaction temperature: The reaction temperature directly influences the rate constant associated with reaction kinetics and therefore influences the rate at which the reactions take place. Commercial ball mills commonly used for laboratory scale experiments do not allow for regulation in system temperature. Individual solutions, such as the installation of a heating mantel, are often employed. When converting to industrial scale, stirred media mills are often selected, making use of a static milling chamber which provide the opportunity to implement heating or cooling. The outlet temperature or final system temperature is highly dependent on the density of the selected grinding media. Common equilibrium temperatures, primarily obtained after 1 h of milling, varies from 40 °C to 80 °C. The bulk system temperature tends to further increase with an increase in milling time, milling frequency and the filling volume of the chamber.

### 2.6.2 Wet milling technology

Wet milling involves the use of a large amount of solvent or carrier liquid resulting in the grinding of a slurry.

**Stirred media mills** Stirred media mills are primarily used for the dispersion processes and soft grinding of materials such as dyes, clays, calcium carbonate and biological cells. Stirred mills commonly use media smaller than or equal to 6 mm and may be restricted to wet milling. The design of stirred mills commonly include a central paddle wheel with

stirrer speeds ranging between 100 rpm and 1500 rpm. The milling media rotates slowly while oscillating in one or more plane (Perry & Green, 2008).

Discs mounted onto a central shaft allow for the stirring of milling media. The feed material enters at one end and is discharged at the other. Horizontal machinery eliminates gravity segregation of the entering slurry feed. Milling media is retained with the use of a screen or stacked flat discs that are closely spaced. The use of discs are useful for slurries with viscosities that range up to 50 Pa·s. Screens that have been hydronamically shaped can operate with media with diameters as low as 0.2 mm. Centrifugal force predominantly aids in the seperation of milling media from milled product (Perry & Green, 2008).

Cooling water is often necessary and continuously circulated through the jacket, and at times through the central shaft, to allow for temperature control. A series of mills are sometimes implemented with a decreasing size in media and increasing rotary speed. This allows for product to reach the desired fine particle size (Perry & Green, 2008).

The performance of bead mills are affected by the following process variables (Perry & Green, 2008):

- Agitator speed.
- Feed rate.
- Bead size.
- Bead charge.
- Bead density.
- Temperature.
- Blade design.
- Shape of mill chamber.
- Residence time.

Stirred media mills were otherwise described by (Wills & Finch, 2016) as a mill making use of "an agitator and spherical grinding media". Stirred milling is primarily used in grinding applications producing fine to ultrafine particles. Sand mills or bead mills are included when referring to stirred mills despite not conforming to the above mentioned criterion. Comparatively ball mills can be categorised as tumbling mills. The primary difference between stirred and tumbling mills is the way in which the grinding energy is transferred

to the material being milled. Tumbling mills make use of both impact (abrasion) and shear (attrition) energy in roughly equal measure. Stirred mills predominantly make use of shear energy which is more effective for fine grinding application (Wills & Finch, 2016).

Stirred milling is described as being more energy efficient which is speculated to be a result of a "splash out" effect. This involves the expulsion of fine particles with the slurry rather than breakage of the particle (Wills & Finch, 2016).

Rod shaped media has been proven to be more efficient than spherical media in ultra fine grinding application. It is recommended to operate the mill at maximum media loading during operation. Note a too high water content the number of contact events between particles and media drops therefore less grinding. If the solids content is too high, loose fluidisation of the mill and media moves only due to impeller. (Edit this, it is important) (Wills & Finch, 2016).

**Bead or sand mills** An alternative grinding process to that of ball milling involved the use of a bead or sand mill. Bead milling is described as a two stage process consisting of an essential premixing followed by grinding. The premixing should preferably be carried out with the use of a high speed disperser. The greater the degree of dispersion achieved prior to grinding, the shorter the dwell time within the bead mill (McKay, 1994).

Figure 8 depicts the typical schematic of a continous bead mill. The process involves the use of a motor that drives the central shaft at high speeds. The shaft is typically fitted with a series of disks consisting of abrasion resistant material, primarily hard steel, for the agiation of the beads. A feed pump forces the millbase slurry throught the chamber. The pumping rate influences the retention time along with the desired degree of dispersion. The vessel contains a jacket for cooling during the grinding process. Grinding media is retained within the vessel with the use of a separator or screen. The velocity of the milling media and the material is higher in the following areas:

- Between the rims of the blades or disks.
- Between the wall of the vessel and the shaft.

This results in the formation of velocity gradients which form a "double-doughnut" configuration between the disks. This further promotes the development of shear forces which break down agglomerates. This is then combined with the normal shear forces produced by the rotation of the milling media (McKay, 1994).

Similar to other forms of milling making use of media, the charge to voids ratio, along with the bead size are considered to be important. Typical bead sizes vary between 1 mm to 3 mm with lower bead sizes being dependant on the type of separator employed. Variations in the bead mill design include vertical open top, closed top or horizontal chambers, along with variations in disk shape and number (McKay, 1994).

Horizontal mills are advantageous when compared to vertical mills as they do not result in start up problems when the milling media settles. The grinding media further remains uniformly distributed throughout the chamber allowing for the use of high density media. The medium-to-charge ratio can also be further increased resulting in a higher output (McKay, 1994).

Additional advantages of sandmills include high throughput rates, less costly and easier cleanup, along with reproducibility of product quality. Batch to Batch inconsistencies are eliminated (Nass, 1992).

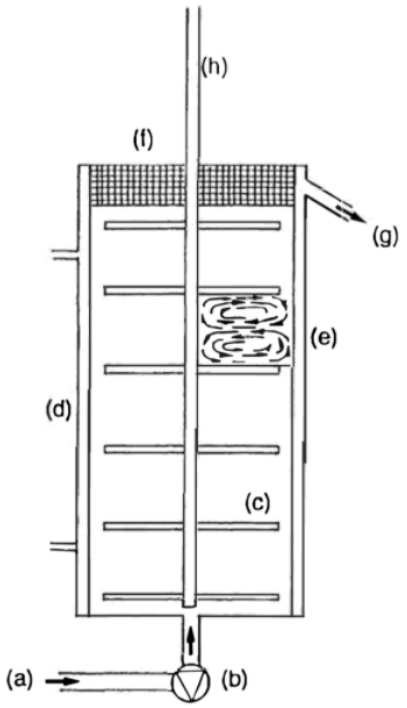


**Figure 8:** Schematic of a continuous bead or sand mill as reproduced with permission from (McKay, 1994). (a) Entry of premixed material; (b) Pump; (c) Impeller disks or blades; (d) Jacketed vessel for cooling/heating; (e) Expected flow pattern; (f) Separator for retention of grinding media; (g) Exit port; (h) Drive shaft to the motor.

**Media wet mills** Media wet mills are similar in principle to stirred media mills and are further described as mills that operate through mechanically moving media with the selected material in a liquid (Williams, Watts & Miller, 2012).

The performance of the milling process is influenced by the characteristics of the milling media used. Various different geometries associated with milling media are available, however spherical geometry was found to be the most effective shape. Bead diameters ranging from 0.05 mm to 130 mm are commercially available, however beads 6 mm and smaller are commonly used. Bead materials include various types of steels, annealed glass, polystyrene derivatives, polytetrafluoroethylene, $ZrO_2$, $ZrSiO_4$, $Al_2O_3$ and $SiO_2$ (Williams et al., 2012). The performance of media wet mills are affected by the physical and technological parameters mentioned in Table 1.

**Table 1:** The effect of milling process parameters on the performance of a media (bead) wet mill (Williams et al., 2012).

| Process variable | Effect on particle size |
|---|---|
| Bead size | A decrease in bead size results in a decrease in the steady-state average particle-size. |
| Intrinsic bead denity | Changes in bead density may have varying results and are dependent on the materials milled. Some cases, higher density beads have resulted in a more coarse product. |
| Bead loading | Bead charges greater than or equal to 50 % generally result in a satisfactory milling efficiency. |
| Agitator speed | An increase in the linear velocity of the agitator results in an increase in the milling rate. |
| Temperature | An increase in temperature may result in a small average particle sizes along with an increase in product dispersion. The physical characteristics and chemical stability of the material may degenerate. Smaller particles may further dissolve. |
| Residence time | Increase in residence time results in a decrease in average particle size. |

## 2.7 Mechanochemical Synthesis of layered double hydroxides

Mechanochemistry is a novel approach for the synthesis and intercalation of LDH materials. Various advantages, such as ease of operation and elimination of solution operation

have made the use of mechanochemical techniques desirable. Most LDH materials up until recently have been synthesised with the use of co-precipitation, hydrothermal methods or urea decomposition-homogeneous precipitation. The primary principle associated with each of these methods include the precipitation of various types of metal ions (solution operation) which make large scale production difficult. Difficulties associated with solution operation include (Qu, Zhang, et al., 2015a):

- Differing precipitation rates of metal ions in multicomponent systems.
- The formation of impurities and intermediate phases.
- The need for inert environments ($N_2$) for the synthesis of carbonate free LDH materials.
- The application of heat during synthesis procedures.
- The production of waste effluent.
- High production costs.

Previously mechanochemistry was used as a method of modification in material science to ensure particles were dispersed and obtained a high surface energy. A review paper constructed by (Qu, Zhang, et al., 2015a) identified three primary mechanochemical synthesis procedures for the production of LDH, namely:

- Single-step grinding.
- Mechano-hydrothermal.
- Two-step grinding (dry grinding followed by wet grinding).

Similarly the mechanochemical intercalation of LDH materials make use of the following three methods (Qu, Zhang, et al., 2015a):

- Grinding of LDH and intercalation compound with the assistance of a liquid.
- The grinding of raw materials and intercalation compound together, followed by hydrothermal treatment when in the liquid phase.
- The collective grinding of water, amorphous raw materials and the intercalation compounds during the second step of the aforementioned two-step grinding method.

Mechanochemistry is considered important due to the promise of synthesising LDH with new elemental combinations and the insertion of new compounds into the LDH structure (Qu, Zhang, et al., 2015a). It was discovered that additional methods have been developed since the release of the review paper by (Qu, Zhang, et al., 2015a) and are further discussed in Section 2.9. It should further be noted that authors, at times, combine the different mechanochemical techniques for the purpose of gaining insight.

### 2.7.1 Mechano-hydrothermal synthesis

Mechano-hydrothermal synthesis makes use of grinding for chemical activation of starting materials, followed by the process of hydrothermal crystallisation. This procedure is advantageous due to the formation of highly crystalline LDH at low temperatures and shorter reactions times. Studies on the use of ball-milling and manual grinding, depending on the use of metallic salts, oxides, or hydroxides, as a pretreatment for hydrothermal processing has been conducted. This was done to obtain the necessary uniform mixtures for the hydrothermal treatment step. The use of manual grinding was primarily associated with metallic salts as raw materials, rather than hydroxides or oxides which are more chemically stable (Qu, Zhang, et al., 2015a).

Hydrothermal treatment and its effects have been studied extensively. It is generally speculated that during hydrothermal treatment disaggregation of particles occur first, followed by particle growth. This considered to be of great importance as LDH particles easily aggregate especially when in a solution. The growth of individual LDH crystallites takes place followed by the growth of the particles. The surface energies associated with large and small particles differ. This results in the dissolution and redeposition of smaller particles and therefore the growth of larger particles (Ostwald ripening). Improved crystallinity in the LDH products are thus observed (Zhang & Li, 2013).

A mechanochemical approach making use of manual grinding of solid salts, specifically $Na_2CO_3$, NaOH, $Al(NO_3)_3{\cdot}9H_2O$ and $Mg(NO_3)_2{\cdot}H_2O$, followed by a peptisation process was conducted by (Zhang et al., 2012) in the synthesis of Mg-Al-LDH. LDH with poor crystallinity and thermal stability was obtained after the grinding process. Peptisation further resulted in the improvement of thermal stability with the formation of regular highly crystalline particles.

The study varied parameters such as grinding time, molar ratio of Mg to Al and water content were manipulated such that the morphology of the LDH was controlled. The molar ratios were varied between 2:1, 3:1 and 4:1, exhibiting a maximum in crystallinity at 3:1. The morphology was observed to change from regular hexagonal shape to coagulated

spheres with an increase in molar ratio. It is speculated that the stability of the LDH phase is strongly dependent on the molar ratios of $M^{2+}$:$M^{3+}$ added to the system. The most stable LDH phases are expected to form between a ratio of 2:1 and 3:1 (Zhang et al., 2012).

Grinding results in the chemical activation of reagents added to the system. Sufficient grinding results in the regular arrangement of particles, however prolonged grinding may result in structural imperfections. The crystallinity was found to pass through a maximum at 60 min when varying grinding time between 30, 60 and 90 min. Enough energy must therefore be supplied to the system for LDH formation and particle arrangement (Zhang et al., 2012).

The addition of water to the system is expected to reduce the degree of supersaturation which negatively influences the particle morphology and degree of crystallinity. It was observed that the addition of water resulted in an increase in the aggregation of particles and a decrease in particle size and crystallinity (Zhang et al., 2012).

The method of mechanochemical LDH synthesis was extended to the production of Zn-Al, Mg-Fe and Ni-Al LDH. The process involved the manual grinding of $Na_2CO_3$, NaOH, $M^{3+}(NO_3)_3.mH_2O$ and $M^{2+}(NO_3)_2{\cdot}nH_2O$. The ground powder mixtures obtained were then hydrothermally treated at 100 °C for 24 h. The primary findings indicated that the grinding process results in the incomplete formation of LDH phases. Hydrothermal treatment was found to result in high degrees of crystallinity and regular LDH formation. It was also noted that the degree of reaction associated with the LDH formation was dependent on the the melting point of the precursor salts. Lower melting points were found to result in more LDH phase in samples after grinding (Zhang & Li, 2013).

Comparatively, ball milling provides higher activation energy than manual grinding and can therefore be used in the synthesis of LDH from hydroxides or oxides. The synthesis of Mg-Al-$NO_3$ LDH was successfully conducted through a novel route involving a pre-milling step followed by hydrothermal treatment. The initial step includes the milling of MgO and $Al_2O_3$ in a ball mill. The milled mixture was further placed in an autoclave with $NaNO_3$ solution and hydrothermally treated (Zhang, Du, Song, Liu, et al., 2013). A similar procedure was used for the successful synthesis of Mg-Al-Fe-$NO_3$ LDH. It was further noted that Li-Al-Cl LDH could be synthesised by grinding gibbsite for short and long periods of time, followed by hydrothermal treatment in a Lithium chloride (LiCl) solution (Qu, Zhang, et al., 2015a).

### 2.7.2 Single-step grinding

Single-step grinding has predominantly been performed in two ways (Qu, Zhang, et al., 2015a):

- Dry grinding of metal salts and hydroxides, with small amount of NaOH.
- Wet grinding, making use of a ball mill, of a metallic salt solution.

The dry grinding process makes use of either a ball mill or manual grinding methods. The grinding allows for the chemical activation of the hydroxides and metal salts such that the crystal structure is weakened. The necessary crystal water for LDH formation is provided during the washing step of the process. The formation of Mg-Al-$HCO_3$, Mg-Al-$NO_3$ and Mg-Al-Cl LDH has been successful with this method (Qu, Zhang, et al., 2015a).

The synthesis process involving the formation of Mg-Al-Cl LDH, from $Mg(OH)_2$ and $AlCl_2{\cdot}6H_2O$, required the addition of an inert that reduced the hygroscopic nature of the starting materials. It was speculated that unreacted $Mg(OH)_2$ in the system was due to particles slinking to the bottom as a result of the hygroscopicity of $AlCl_2{\cdot}6H_2O$. The addition of KCl resulted in pure phase LDH formation (Khusnutdinov & Isupov, 2007).

Single step wet grinding has reportedly resulted in the synthesis of highly crystalline iron based LDH (Co-Fe-Cl) using an iron free cobalt chloride solution milled at room temperature in a tumbling mill making use of carbon steel balls. The one-step synthesis method required no additional pH control and heating. Iron ions were obtained were found to gradually elute from the balls during the milling process. The pH of the system was further controlled by hydroxide formation from the decomposition of water molecules within the system. Oxidation of $Co^{2+}$ was prevented through limiting the oxygen content within the system, argon gas was used to create the desired inert conditions prior to milling (Iwasaki, Shimizu, et al., 2012).

A similar synthesis procedure was conducted with the use of $NiCl_2$ solution resulting in the production of Ni-Fe-Cl LDH. This synthesis method was deemed suitable for large scale production due to the ease of up-scaling the milling process. The grinding process was deemed important as vigorous stirring of Fe(0) powder with $NiCl_2$ did not result in LDH formation. Further pH adjustment of a $NiCl_2$ and $FeCl_3$ solution with NaOH addition did not result in the formation of an LDH phase. The large amounts of mechanical energy produced through milling was thus deemed necessary for LDH formation (Iwasaki,Yoshii, et al., 2012).

The success associated with the formation of LDH, for single step grinding procedures, has been noted to be dependent on the selected starting materials used. The use of metallic salts of chlorides or nitrates allow for possible LDH synthesis, however the ground sample may require washing, producing undesirable waste solution. The use of hydroxides or oxides eliminate the generation of waste solution, however LDH synthesis becomes challenging. The effects of mechanochemical activation were found to increase when reactants were subjected to an initial dry milling step, avoiding initial water addition (Qu, Zhang, et al., 2015a).

### 2.7.3 Two-step dry and wet grinding

The two-step dry and wet grinding process makes use of an initial dry grinding step, followed by the addition of the stoicheometrically correct amount of water for LDH synthesis. The initial step allows for the production of an amorphous mixture with active sites necessary for chemical reactions to occur. Water addition was determined to be necessary for crystallisation (Tongamp, Zhang & Saito, 2006b).

A single step operation was conducted, for comparison with the two step operating procedure, in which $Mg(OH)_2$ and $Al(OH)_2$ was milled with the use of a planetary ball mill. The amount of water added to the system was varied. It was determined that the addition of water in the one step synthesis procedure prevents the reduction of starting materials to the required amorphous phase. The two step milling procedure prevents interference and therefore LDH formation was more prominent (Tongamp, Zhang & Saito, 2006b).

Results indicated that more water than the stoicheometrically correct amount was required for the reaction to reach completion. This was deemed necessary due to water absorbing on sample surfaces and difficulties associated with introducing the added water into the formed crystal structures. Excessive water addition resulted in wet milling and therefore a reduction in the LDH phase. An increase in milling time further promoted LDH formation reaching a maximum. This process allows for little carbonate contamination due to little amounts of solution involved within the process (Tongamp, Zhang & Saito, 2006b). The two-step process is as depicted by Figure 9.

The two-step process provides a simple procedure for intercalation. Compounds selected for intercalation can be added to the second step of the process. This eliminates the need for ion-exchange and regeneration procedures (Qu, Zhang, et al., 2015a). The synthesis of Mg-Al-$NO_3$ was successfully conducted through the initial milling of $Mg(OH)_2$ and $Al(OH)_3$, followed by milling with $Mg(NO_3)_2{\cdot}H_2O$. Synthesis was conducted in a planetary ball mill. A one step milling process in which all raw materials were added at

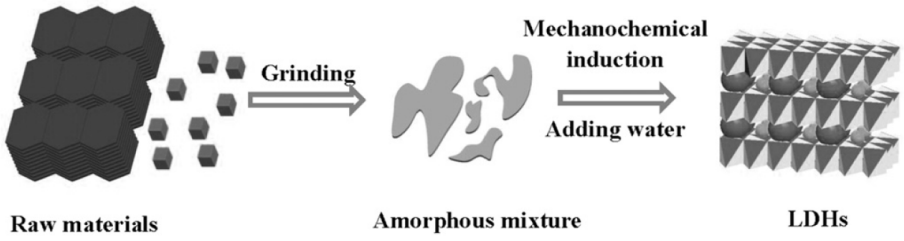


**Figure 9:** Two-step dry and wet grinding procedure reproduced with permission from (Qu, Zhang, et al., 2015a).

once was conducted for comparative purposes. The formation of Mg-Al-$NO_3$ did occur however the reaction did not reach completion (Tongamp, Zhang & Saito, 2008).

A super-paramagnetic $Fe_3O_4$ (Mg-Al-OH-LDH) has been synthesised through a two step milling procedure. The initial step was conducted through the dry milling of $Mg(OH)_2$, $Al(OH)_3$ and $Fe_3O_4$ for 1 h. This was followed by the wet milling, with water, of the products for 5 h. The final product was found to contain homogeneously dispersed $Fe_3O_4$ cores within the LDH matrix (Zhang, Du, Zhang, et al., 2012).

The mechanochemical approach was found to successfully synthesise LDH compounds that could not be produced with conventional methods. A Ca-Sn-LDH was synthesised using a two step mechanochemical approach. The method was further extended to incorporate the intercalation of amino acids (cystine and valine) such that an organic-inorganic nano-composite could be produced. Three experimental procedures were followed for comparative purposes (Ferencz, Szabados, Adok-Sipiczki, et al., 2014):

1. Co-precipitation of $CaCl_2$ or $CoCl_2$ and $SnCl_4$ in a NaOH solution.
2. One step dry grinding of precursor materials: $CaCl_2$, $CoCl_2{\cdot}6H_2O$, $Ca(OH)_2$ and $SnCl_4{\cdot}6H_2O$.
3. Two step grinding of precursor materials: $CaCl_2$, $CoCl_2{\cdot}6H_2O$, $SnCl_4{\cdot}6H_2O$ and $Ca(OH)_2$. This included 1 h dry grinding followed by 2 h wet grinding.

Milling procedures were conducted using a mixer mill and experiments were then replicated using a agate mortar and pestle. Results indicated that the two step mechanochemical procedure successfully resulted in Ca(II)-Sn(IV)-LDH synthesis. Intercalation of amino acids into the LDH structure was further found to occur. The one step procedure could not generate enough hydroxides for the formation of the LDH structure. Similarly the co-precipitation method was found to be unsuccessful with no LDH phase being

identified in the final product. It was noted that the agate mortar and pestle were sufficient for LDH synthesis and that the mixer mill was not necessary (Ferencz, Szabados, Adok-Sipiczki, et al., 2014).

A similar two step procedure was conducted for the synthesis of Ca-Al-LDH making use of $Ca(OH)_2$, $Al(OH)_3$ and NaOH or water. Experimental grinding procedures were conducted on a mixer mill and with a mortar for comparison. Grinding with a mortar resulted in incomplete reaction, with little LDH formation. This could be due to insufficient production of mechanical energy for product formation when making use of hydroxides as raw materials. Results obtained using the mixer mill indicated near complete conversion of reactants to pure phase LDH, making use of optimised milling conditions. It was observed that the ball to sample ratio had a large effect on the synthesis process. It was further noted that as the milling frequency increases, a maximum occurs after which the concentration LDH decreases. This could be due to the complete destruction of the LDH crystal with an increase in mechanical energy (Ferencz, Kukovecz, et al., 2015).

### 2.7.4 Comparison of different mechanochemical synthesis methods

A summary of the advantages and disadvantages of the mechanochemical techniques available for LDH synthesis is depicted in Table 2. Among all the processes listed the two-step grinding procedure was recommended for further studies (Qu, Zhang, et al., 2015a). Novel techniques discussed in Section 2.9 were not included in this comparative summary.

**Table 2:** The advantages and disadvantages of the various types of mechanochemical approaches as reproduced with permission from (Qu, Zhang, et al., 2015a).

| Approach | | Advantages | Disadvantages |
|---|---|---|---|
| Mechano-hydrothermal | Manual grinding | Regular hexagonal crystals | Solvent involvement |
| | | Highly Dispersed | Starting materials limited to soluble salts |
| | | | Waste of energy |
| | Ball-milling | Regular hexagonal crystals | Solvent involvement |
| | | Raw materials include the use of salts, hydroxides and oxides | Waste of energy |
| Direct mechanochemical synthesis | Single step wet grinding | Ease of operation | Solvent involvement |
| | | Saving energy | Seemingly limited to Fe based LDH |
| | Single step dry grinding | Ease of operation | LDH crystallinity is low |
| | | Free of any solvent | |
| | Two-step grinding | Ease of operation | Agglomeration of particles |
| | | Free of any solvent | |
| | | Raw materials include the use of salts, hydroxides and oxides | |

## 2.8 Mechanochemical intercalation

Four major mechanochemical processes were identified by (Qu, Zhang, et al., 2015a) for the intercalation of LDH:

1. Liquid assisted grinding of LDH with intercalation compounds.
2. Manual grinding of selected raw materials with compounds needed for intercalation. This is followed by hydrothermal treatment in water.
3. Ball milling starting materials such that an amorphous mixture is produced followed by hydrothermal treatment in a solution containing intercalation compounds.
4. Two-step grinding process.

The identified processes can be further divided into two categories namely solvent-free intercalation or solvent-involved intercalation. Solvent free intercalation was described by (Qu, Zhang, et al., 2015a) to make use of solid state reactions in which little or no solution is used for the desired reaction. It should be noted that washing of the product is still applicable. A summary of the previously mentioned processes are as depicted in Figure 10 according to solvent involved and solvent free intercalation.

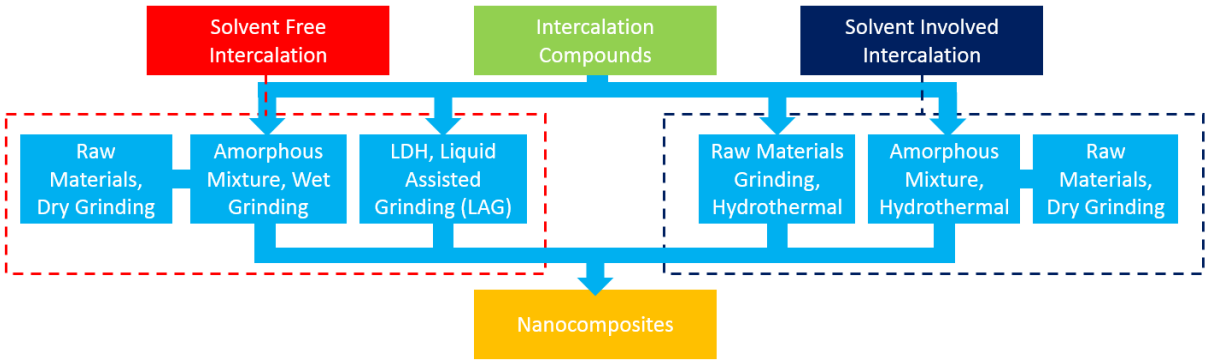


**Figure 10:** Summary of mechanochemical intercalation procedures as reproduced with permission from (Qu, Zhang, et al., 2015a).

Novel intercalation procedures are further identified and discussed in Section 2.9.

### 2.8.1 Solvent-involved intercalation

The synthesis of Mg-Al-LDH intercalated with methotrexatum (MTX), for application in drug delivery, was successfully conducted making use of a mechano-hydrothermal process. The starting materials $Mg(NO_3)_2{\cdot}6H_2O$ $Al(NO_3)_3{\cdot}9H_2O$ and NaOH were manually

ground after which MTX powder was added and the grinding proceeded. The final powder product was washed with deionised water and further peptised. The crystallinity, morphology and release properties of the product was compared to MTX-LDHs obtained with the use of the co-precipitation method (Qi, Zhang & Li, 2012).

The results obtained from this study indicated that the LDH synthesised through mechano-hydrothermal methods displayed superior properties to LDH synthesised via co-precipitation. The particles were found to be more monodispersed and regular. The release property of the LDH was found to be slower and thus ideal for drug delivery application. Energy conservation was not considered (Qi et al., 2012). The synthesis of MTX LDH was optimised by (Qu, Zhang, et al., 2015b) in in which the addition of NaOH, grinding duration, hydrothermal time and the temperature were investigated. Results indicated that the addition of NaOH improved the LDH morphology, monodispersity and loading capacity.

Sodium dodecyl sulfate (SDS) intercalated Mg-Al LDH was successfully synthesised by (Zhang, Du, Song & Hou, 2015). The process involved the milling of $Mg(OH)_2$ and $Al(OH)_2$ in a planetary ball mill, followed by hydrothermal treatment in an SDS solution. The LDH synthesised was to absorb 2,4-dichlorophenoxyacetic acid and was found to have a high absorption efficiency and capacity. The structure and morphology of the LDH was found to be similar to those synthesised by traditional methods. It was further determined that the milling step was vital for the formation of the LDH structure.

### 2.8.2 Solvent-free intercalation

Solvent-free intercalation makes use of solid state reactions in which no or little solution is used (Qu, Zhang, et al., 2015a). The synthesis of Ca-Sn-cystine and Ca-Sn-valine LDH, as described in Section 2.7.3, followed a two-step dry and wet grinding intercalation procedure. The versatility associated with mechanochemical intercalation is noted when exploring the use of organic anions and pharmaceutical applications.

The intercalation of bioactive molecules, namely Eusolex or 2-phenylbenzimidazol-5-sulfonic acid (EUS), was conducted by (Milanesio et al., 2010). The synthesis procedure made use of a mixture of Zn-Al-$NO_3$ LDH and EUS which was manually ground with a small amount of NaOH solvent. The aim was to determine whether EUS could be exchanged with $NO_3$ within the LDH layer using mechanochemical techniques.

Analysis was conducted on the sample after drying and again after washing. Results indicated that the composition and crystallinity of the LDH obtained within the samples were comparable to those obtained through traditional methods. It was further found

that the addition of a washing step removed co-product formed ($NaNO_3$ and improved the LDH crystallinity. It was observed that ionic exchange starts instantaneously after the addition of the solvent and occurs mainly in the solid state as no dissolution of the Zn-Al-$NO_3$ LDH was noted. The small amount of solvent was thus concluded to result in the creation of an active surface between the LDH and the EUS by deprotonation of EUS (Milanesio et al., 2010).

A similar mechanochemical method was followed for the intercalation of a series of non-steroidal anti-inflammatory drugs, specifically ketoprofen (KET), flurbiprofen (FLUR), ibuprofen (IBU), indomethacin (INDO), triprofenic acid (TIAP), along with the two dyes 3-carboxy coumarin (COUM) and fluorescein (FLUO). The analytical procedure used was fast *in situ* X-ray powder diffraction (XRPD) such that the intercalation of the bioactive molecules could be observed. Results obtained implied that the intercalation of the organic anion takes place in the solid state. It was further noted that reaction conditions were optimised such that the reaction could be completed in minutes rather than days or hours (Conterosito et al., 2013).

Although a total of 8 experiments were conducted by (Conterosito et al., 2013), it was found that only 5 were successful, namely EUS, KET, TIAP, IBU and FLUR. The reactions for TIAP and IBU were found to have reached completion. No reaction was observed for analysis conducted after dry grinding, however the addition of a small amount of solvent was found to promote LDH formation. The unsuccessful reactions associated with INDO and FLUO were speculated to be due to their bulky nature and may require more extreme reaction conditions. It was further noted that reaction yields could be improved through increasing the polarity or pH of the solution.

## 2.9 Recent developments for the mechanochemical synthesis of layered double hydroxides

A summary paper was recently constructed by (Intasa-ard et al., 2018) in which many novel accomplishments associated with LDH and mechanochemistry were summarised or mentioned. A brief description regarding the methods used for LDH synthesis and intercalation were provided. Although some methods have remained the same as those previously described, new methods making use of post synthetic treatments, such as agitation or ultrasound irradiation have been developed. Well crystallised, homogeneous LDH was found to result from these new methods obtained (Intasa-ard et al., 2018).

### 2.9.1 Mg-Al Layered double hydroxides

The most representative mineral of the LDH group is referred to as "hydrotalcite", a white hydrous mineral, with the chemical formula $Mg_6Al(OH)_{16}(CO_3)\cdot 4H_2O$ (Mg-Al-$CO_3$). Its properties consist of a rhombohedral crystalline system, low hardness of 2.00 and low density of 2.06. Hydrotalcite and hydrotalcite-like minerals are rare in nature (Forano et al., 2006).

Hydrotalcite is commonly synthesised with the use of the co-precipitation method and is widely used for catalysis. A route for the synthesis of meixnerite (Mg-Al-OH) was developed by (Tongamp et al., 2006a) through a two-step mechanochemical synthesis route. A mixture of $Mg(OH)_2$ and $Al(OH)_3$ (ratio 3:1) was initially dry milled for 1 h followed by 2 h of milling with water. All experiments were conducted in a planetary ball mill (45 $cm^3$ inner volume) with 7 stainless-steel balls of 15 mm diameter.

Recently (Bester, 2016) did a study on the mechanochemical synthesis of LDH compounds with the use of a horizontal bead mill. The study was aimed at the viability of mechanochemical LDH synthesis rather than the optimisation. The synthesised product was to be used as a flame retardant in PVC (poly vinyl chloride). The material would thus require properties that allow for the prevention of PVC breakdown and are not detrimental to the processing of the polymer. The synthesis of Mg-Al-OH was studied and results obtained indicated the formation of both Mg-Al-OH and Mg-Al-$CO_3$ LDH. Products were thermally aged and found to be outside the desired particle size range for polymer matrix incorporation. The product was found to reach the desired particle size after 60 min, however it was unclear whether the reaction reached completion at that point (Bester, 2016).

Another solvent free technique includes dry grinding of raw materials followed by hydrothermal treatment. A study was conducted by (Du et al., 2016) in which plate-like Ni-Mg-Al LDH was synthesised and its properties compared to that of LDH synthesised using traditional co-precipitation. Results obtained indicated that the mechano-hydrothermal method resulted in more highly crystalline, hexagonal LDH, whereas that produced by co-precipitation contained a flower like structure more prone to agglomeration. The dry grinding step used within this study was that of manual grinding.

The synthesis and stability of Mg-Al-acetate LDH for thin film ion exchange applications, was investigated, with the use of a 2 step mechanochemical procedure, by (Kuramoto et al., 2017). The raw materials, $Mg(OH)_2$and $Al(OH)_3$ were initially dry milled. Magnesium acetate, $Mg(CH_3COO_2)\cdot 4H_2O$, was then added to the process and the milling continued. All grinding procedures were conducted with the use of a planetary ball mill

and no washing step was included. The results obtained indicated that the synthesis of pure phase LDH was successful and would further be subjected to stability and hydration tests. Stability tests were conducted to ensure that the sample could be stored under different conditions for elongated time periods. The LDH product was thus subjected to the following test conditions:

1. Dry air: The sample was exposed to dry air at room temperature. It was noted that dehydration of the sample occurred through a reduction in the LDH basal spacing.
2. High humidity: Exposure to high humidity allowed for the decomposition of intercalated acetate ions into carbonate anions. The exchange of anions could also have occurred due to the adsorption of atmospheric carbon dioxide during storage of the sample.
3. Closed container: The sample was stored within a closed container for approximately one month. No anion exchange or decomposition of acetate was observed under these storage conditions.
4. Hydration: Although not specifically related to storage, the dehydration and swelling of the LDH product was investigated. The sample, once mixed with water and then dried, was found to have an increased basal spacing attributed to hydration. No decomposition of acetate or adsorption of carbon dioxide occurred during the hydration and drying procedures conducted.
5. Aqueous suspension: A highly transparent aqueous suspension was obtained and stored under nitrogen atmosphere. No precipitation was observed after a few days of storage.
6. Ambient conditions without nitrogen: The interlayer acetate was found to decompose and undergo exchange with carbonate anions when an aqueous sample was stored under atmospheric conditions.

The results obtained were comparable with those of LDH prepared via traditional methods. It was further interesting to note that the acetate intercalated LDH could successfully be transformed into a thin film. The advantage of this LDH was demonstrated by subjecting the film to a solid-state ion exchange with coumarin-3-carboxylic acid (C3C). Intercalation of C3C was successful and was advantageous as thin films constructed using C3C as a starting material were often of poor quality or not possible (Kuramoto et al., 2017).

A study conducted by (Fahami & Beall, 2016) indicated the successful synthesis of Mg-Al-$SO_4$ LDH through the use of a one step milling procedure, followed by washing and ageing.

Results indicated that high purity, round platelet, LDH was obtained after approximately 60 min of milling with the use of a high energy ball mill (8000 M Mixer/Mill).

Recently a CdS/Mg-Al LDH composite was synthesised by dry milling the respective hydroxides along with $CdCl_2$ and $Na_2S$ in a high energy ball mill. The ground product was then agitated in water such that LDH formation could occur. Analysis indicated that the CdS was uniformly distributed within the LDH matrix rather than the intercalation thereof (Li, Chen, et al., 2018).

Many of the studies conducted have indicated that mechanochemistry gives rise to complex LDH structures that are not possible with conventional methods. It has also been noted that at times additives are required when making use of traditional methods, to allow for intercalation into the LDH or stability thereof. Mechanochemistry is also useful in other areas such as the intercalation of an LDH into a polymer matrix without the need for compatibilsers or organic modifiers (Zhang & Chen, 2018).

### 2.9.2 Ca-Al Layered double hydroxides

Hydrocalumite is a subgroup related to hydrotalcite, with the representative formula $Ca_2Al(OH)_6Cl{\cdot}3h_2O$. It is considered a rare, hydrated Calcium aluminate that occurs naturally as bladed crystals. The structure consists of an ordered arrangement of $Ca^{2+}$ and $metal^{3+}$ cations. A general representation is described by Equation 5 (Forano et al., 2006).

$$[Ca_2M^{III}(OH)_6]^{x+}[X^{q-}_{x/q} \cdot nH_2O] \tag{5}$$

The synthesis of hexagonal-shaped hydrocalumite via a one-pot mechanochemical approach was successfully conducted by (Fahami, Beall, et al., 2016). The method was found to produce the LDH within 30 minutes. Well crystallised hydrocalumite was further found to form at 60 min of milling. A decrease in XRD peak intensity and sharpness with an increase in milling time was noted. This was considered to be due to mechanically induced amorphisation. The method involved the milling of $CaCl_2$, $AlCl_3$ and NaOH, at different times, using a high energy ball mill (8000 M) at atmospheric conditions. It should be noted that NaCl is produced as a side product that was disposed of through washing the LDH product (Fahami, Beall, et al., 2016).

A study was conducted by (Fahami, Duraia, et al., 2017), using similar reaction conditions to (Fahami, Beall, et al., 2016), in which the effect of ion content on composition and

structural features of Ca-Al-Cl LDH was investigated. The mechanochemical method included the one-pot milling $CaCl_2$, $Al(OH)_3$ and NaOH, using a high energy ball mill (8000M mixer mill) at atmospheric conditions. The degree of substitution (x) of chlorine was varied between 0.1 and 0.4 using the general formula $Ca_{1-x}Al_x(OH)_2Cl^-_x$. The chlorine content however was noted to be controlled by the amount of aluminium substitution that occurred within the LDH lattice. The final composition was thus acquired with the use of Equation 6.

$$(1-x)CaCl_2 + xAl(OH)_3 + (2-3x)NaOH \rightarrow Ca_{1-x}Al_x(OH)_2Cl_x + (2-3x)NaCl \quad (6)$$

Results obtained from this study indicated that highly crystalline, pure phase, Ca-Al-Cl LDH was obtained at degree of substitution of 0.2, with no side product formation. Low levels of Al substitution yielded portlandite as a by product, whereas high levels resulted in gibbsite as an additional phase. Calcite formation was detected in samples at high and low degrees of substitution. It was further noted that the substitution of chlorine affected the size of the crystallites and the degree of crystallinity (Fahami, Duraia, et al., 2017).

Comparatively Ca-Al LDH was successfully synthesised with a two-step mechanochemical process in which the addition of a third phase was considered. Initially the milling of only the relevant hydroxides, namely $Ca(OH)_2$ and $Al(OH)_3$, resulted in the formation of katoite as a main phase. The further addition of carbonate ($CaCO_{3)}$ or chloride ($CaCl_2{\cdot}2H_2O$) during the operation allowed for the formation of Ca-Al-LDH. The addition of a third phase for the stabilisation of the desired LDH compounds is considered important for future synthesis procedures (Qu, Zhong, et al., 2016).

The grinding procedure was conducted with the use of a planetary ball mill at 600 rpm. The operation involved the dry grinding of the respective starting materials followed by the addition of a small amount of water. Nearly pure phase Ca-Al-$CO_3$ and Ca-Al-Cl LDH was obtained. It was however noted that at certain molar ratios the reaction did not run to completion. It was further observed that the synthesis of the Ca-Al-Cl LDH occurred more easily than that of the Ca-Al-$CO_3$ LDH. This could be due to the possibility that the reactivity of water soluble $CaCl_2{\cdot}2H_2O$ being higher than that of $CaCO_3$, which is water insoluble. It was noted that the synthesis of different types of LDH could be possible with a variation in the anion (third phase) added to the system (Qu, Zhong, et al., 2016).

A study conducted by (Zhong et al., 2017) presented interesting results regarding the

incorporation of a third phase during LDH synthesis for the absorption of Cr(VI). The method involved the dry grinding of hydroxides ($Al(OH)_3$ and $Ca(OH)_2$) and a mixture of hydroxides with chlorides ($CaCl_2$ and $MgCl_2$), forming a precursor. These mixtures were then agitated in solutions of deionised water and $K_2CrO_4$, $CaCl_2$ or $MgCl_2$, or a mixture of both chlorides and Cr(VI). Results indicated the successful formation of Ca-Al-Cr(VI) LDH for mixtures containing only the Cr(VI) source and those containing Cr(VI) along with chlorides (Zhong et al., 2017).

The objective was to remove toxic Cr(VI) from the environment, despite the presence of other anions, through the formation of LDH, rather than using already synthesised LDH. The absorption potential was found to be excellent in the presence of only a Cr(VI) source and good for a mixture of chlorides and Cr(VI). This indicated that the formation of Ca-Al-Cr LDH as the main phase occurred despite the presence of Cl anions. It was noted that when only agitating in the presence of a Cr(VI) source ($k_2CrO_4$) that one type of Ca-Al-Cr LDH was synthesised, namely $3CaO{\cdot}Al_2O_3{\cdot}CaCrO_4{\cdot}12H_2O$. Comparatively, when Cl was present during the agitation step, a second stable Ca-Al-Cr LDH phase was identified along with the first, specifically $3CaO{\cdot}Al_2O_3{\cdot}CaCrO_4{\cdot}14H_2O$. This suggested that incorporation of more water molecules into the LDH structure was possible with the coexistence of chlorides in solution (Zhong et al., 2017).

It was further noted that the Cr(VI) absorption efficiency increased with an increase in the concentration of $MgCl_2$. This was however believed to be due to the formation of the stable $3CaO{\cdot}Al_2O_3{\cdot}CaCrO_4{\cdot}12H_2O$ and $3CaO{\cdot}Al_2O_3{\cdot}CaCrO_4{\cdot}14H_2O$ phases rather than the concentration of the $MgCl_2$. A stable phase of Ca-Al-$CrO_4$ LDH was observed to result, indicating the preferred incorporation of Cr(VI) into the LDH structure, despite the presence of chloride ions. The LDH formed were irregular, spherical particles with very poor crystallinity. The study further confirmed that when milling only hydroxides, and using only deionised water, a stable phase of katoite would form rather than LDH. A third phase such as chlorides, chromate or carbonate was thus necessary to transform the katoite phase into an LDH phase (Ca-Al-X) (Zhong et al., 2017).

The synthesis of Ca-Al-$CO_3$ LDH, along with halogen intercalated Ca-Al LDH, through a mechanochemical pre-treatment, followed by ultrasonic irradiation, was successfully conducted by (Szabados, Meszaros, et al., 2016). Milling was conducted using a mixer mill with stainless steel grinding balls. Key observations made during this study were:

1. Pre-milling was essential for the formation of the desired LDH phase. No LDH formation occurred otherwise.
2. Increasing the milling time resulted in an increase in LDH peak intensity and reflections obtained during XRD analysis.

3. An increase in the milling time resulted in the formation of secondary products, namely hydrated tricalcium-aluminate (TCA-$Ca_3[Al(OH)_6]_2$) and calcium aluminium oxide hydrate ($Ca_2Al_2O_5 \cdot 8H_2O$).

4. It was speculated that an increase in the carbonate concentration would result in a decrease in TCA formation, and a further increase in LDH formation. A sodium carbonate solution was thus added to the milled hydroxides and its concentration varied. It was found that upon increasing the carbonate concentration, the LDH concentrations increased considerably. The solubility of the TCA was believed to increase with an increase in carbonate concentration, further resulting in the decomposition of its precursors to calcium carbonate ($CaCO_3$). Excess carbonate within the system was found to reduce the LDH and $Ca(OH)_2$ to $CaCO_3$.

Similarly, the synthesis of the LDH Ca-Al-Fe, intercalated with carbonate or chloride anions, was possible when combining mechanochemistry and ultrasonic irradiation. Nearly pure phase, highly crystalline, LDH was obtained during this process. It was noted that during ultrasonic treatment, intense mechanochemical effects were provided due to cavitation in the liquid, occurring near the surface of the already-milled solids. The collapse of the cavities resulted in the production of high speed jets of liquid, forming reactive surfaces and thus close-to phase pure LDH (Szabados, Pasztor, et al., 2016).

Boron containing LDH was synthesised using dehydration-rehydration, anion exchange and mechanochemistry for application as catalysts in the Beckmann rearrangement reaction of cyclohexanone oxime. The type of borate ion varies according to the system pH. The mechanochemical process yielded LDH with monoborate ($B(OH)_4^-$ within the layers. Comparatively, LDH synthesised via dehydration-rehydration methods contained triborate ($B_3O_3(OH)_4^-$) anions within its layered structure. The catalytic activity of the two borate containing LDHs were thus found to vary, with that produced via mechanochemistry having no activity. The LDH obtained through anion exchange did not have borate intercalated within its structure, but rather contained borate anions on the outer surface only (Varga et al., 2017).

### 2.9.3 Cu-Al Layered double hydroxides

A study was conducted by (Qu, He, Chen, Zhang, et al., 2017) in which $Cu_2(OH)_2CO_3$ and $Al(OH)_3$ was initially dry milled and then agitated in water or methyl orange. The milling method made use of a zirconium dioxide, two-pot planetary ball mill. Results obtained indicated that the dry milling step allowed for the formation of an amorphous precursor, which readily formed highly crystalline LDH when agitated in the selected

solution. The amorphous phase, and thus LDH phase, was found to be dependent on the selected milling speed. Higher operating speeds, in this case greater than 400 rpm, were necessary for the precursor formation. Pure phase Cu-Al LDH, with no impurities, was found to form when milled at 600 rpm and then agitated in water. The ratio of Cu:Al was further varied during the study and the optimum was found at a ratio of 2:1. A too low ratio resulted in no LDH formation, whereas larger ratios resulted in the presence of unreacted cupric carbonate.

The study further aimed to synthesise methyl orange (MO) intercalated LDH through the dry milling of raw materials followed by agitation in methyl orange. Pure, highly crystalline, Cu-Al-MO LDH was obtained. The presence of crystalline LDH was thought to be a result of the inclusion of an agitation step rather than a wet milling step. LDH obtained through dry milling followed by wet milling is often observed to be large agglomerates. It was further noted throughout the study that the formation of a precursor was more effective than direct anion exchange (Qu, He, Chen, Zhang, et al., 2017).

A similar method was used in the syntheses of dodecyl sulfate ($DS^-$) intercalated Cu-Al LDH, for 2,4-dichlorophenoxyacetic acid (2,4-D) adsorption, by (Qu, He, Lei, et al., 2017). Pure phase, pillared, Cu-Al-DS LDH was successfully synthesised with the use of ball milling. A comparative study was conducted on the mechanochemically synthesised LDH and that obtained through ion exchange, more specifically, Cu-Al LDH stirred within a SDS solution. Results indicated that LDH synthesised via mechanochemical means was superior in terms of $DS^-$ intercalation. This was thought to be due to the difficulty of the bulky $DS^-$ entering the LDH layers. Phase pure DS-LDH was not synthesised through ion exchange methods. The adsorption capability of 2,4-D was found to be quite similar in both studies conducted (Qu, He, Lei, et al., 2017).

### 2.9.4 Zn-Al layered double hydroxides

A Zn-Al LDH was synthesised by (Qu, He, Chen, Huang, et al., 2017) with a similar method to that described in section 2.9.3 by (Qu, He, Chen, Zhang, et al., 2017). The study involved the dry milling of Zn basic carbonate ($Zn_4CO_3(OH)_6{\cdot}H_2O$) and $Al(OH)_3$, with the use of a planetary ball mill, followed by agitation in water. A comparative study was further conducted between the above-mentioned method and the two step mechanochemical route, in which dry milling followed by wet milling of raw materials, is conducted. It was noted that replacing the wet milling step with agitation produced LDH with higher crystallinity and good dispersion. The LDH produced by wet milling exhibited low crystallinity and agglomerates. It was also noted that various types, specifically low and high Zn content LDH, could be synthesised when making use of a grinding

procedure and varying the molar ratios between 1:1 and 3:1. Nearly phase pure LDH was obtained, making use of agitation, at a rotational speed of 600 rpm. This was interesting as reaction conditions were similar to that for Cu-Al LDH synthesis conducted by (Qu, He, Chen, Zhang, et al., 2017) and (Qu, He, Lei, et al., 2017).

Recently (Li, Zhang, He, et al., 2017) successfully synthesised $Zn_xCd_{(1-x)}S$ and Zn-Al LDH along with the LDH precursors with the use of a one-step mechanochemical procedure. The LDH structures were synthesised after the grinding operation by washing the formed precursors in distilled water. A similar study was conducted by (Li, Zhang, Liu, Wu, et al., 2018) when synthesising Ag/Zn-Al LDH. It was noted that no evidence for Ag entering the Zn-Al LDH was obtained, but instead it was uniformly distributed on the surface of the LDH. This was found to assist in the photo-catalytic degradation of methyl orange under visible light. The presence of Ag thus did not destroy the LDH structure formed, successfully synthesising a composite material.

Rose shaped, highly crystalline Zn-Al LDH was synthesised by (Szabados, Bus, et al., 2016) with the use of a ultrasonically-aided milling procedure, followed by rinsing with aqueous ammonia. The synthesis procedure was compared to that making use of agitation rather than ultrasonic irradiation. The process of irradiation was found to yield superior results. This was speculated to be a result of cavitation that occurs in sonicated systems. Energy is released through the collapse of bubbles at crevices within the solids. This results in the further breakdown of larger particles to smaller ones.

Recently (Li, Zhang, Liu, Chen, et al., 2018) successfully synthesised a $Bi_2S_3$/Zn-Al LDH composite with the use of a planetary ball mill. Products were synthesised by grinding zinc carbonate hydroxide hydrate ($Zn_4CO_3(OH)_6$·H textsubscript2O), $Al(OH)_3$ and $Bi_2S_3$ followed by stirring in water. It was understood that the $Bi_2S_3$ particles were distributed among the LDH matrix and not intercalated between the layers.

### 2.9.5 Li-Al layered double hydroxides

The mechanochemical synthesis of Li-Al LDH was first conducted, using a two-step grinding procedure, by (Qu, He, Wang, et al., 2016). The process involved the dry milling of Li(OH) and $Al(OH)_3$, followed by the addition of water and further milling. The amount of water added to the system was varied between 1 and 5 mol. Product obtained was described as being somewhat caked or nearly dry powders. No further treatment or drying was conducted on the samples obtained. Experiments were conducted with the use of a planetary ball mill.

The study was further aimed at determining the effect of the wet grinding time, specifically between 0.5 and 4 h, on the synthesis and crystallinity of the LDH. Prolonged wet grinding was reported to result in the successful formation of highly crystalline, pure phase LDH. Additionally, the Li/Al ratio was varied, with pure phase LDH being synthesised for a ratio of 1:2. Most synthesis routes require an excess of raw material which is inevitably washed away. Comparatively, a mechanochemical route requires the exact stoichiometric amount, otherwise excess reactant will be observed with the product. Poor dispersion and agglomeration of particles was noted in the final LDH products obtained (Qu, He, Wang, et al., 2016).

Pure phase tetraborate pillared Li-Al LDH was synthesised for the first time by (Qu, Li, et al., 2016), using a mechano-hydrothermal procedure. Aluminium hydroxide was first activated with the use of a planetary ball mill and then hydrothermally treated in $Li_2B_4O_7$ and water. Samples were compared to Li-Al LDH synthesised via the traditional two-step mechanochemical method and were found to be more crystalline, with little agglomeration. A similar study was conducted by (Zhang & Hou, 2018) in which pure phase, highly crystalline, well dispersed hexagonal Li-Al-OH was synthesised using the mechano-hydrothermal method. The crystallinity was found to be dependent on the temperature at which hydrothermal treatment was conducted, increasing with an increase in temperature. The Li-Al-OH LDH synthesised via a comparative two-step mechanochemical procedure was found to exhibit irregular stone-like particles. Interestingly when increasing the Li:Al ratio of the starting materials from 0.5 through to 5, the Li:Al ratio within the LDH was found to remain constant at 0.5. This was speculated to be due to the vacancy content in the crystalline $Al(OH)_3$.

### 2.9.6 Synthesis of layered double hydroxides consisting of Cobalt

Various types of LDH comprising of cobalt have been synthesised with the use of conventional means. It was however noted that little information regarding the mechanochemical synthesis of Co-LDH was available.

Previously synthesised layered double hydroxides include Co-Fe-Cl (Iwasaki, Shimizu, et al., 2012) as described in Section 2.7.1 and Co-Fe(II)-Fe(II) with the use of a modified colloid mill reactor (Xu et al., 2011).

### 2.9.7 Synthesis of layered double hydroxides consisting of Nickel

Little information regarding recent developments in the mechanochemical synthesis of Nickel based layered double hydroxides was found to be available

### 2.9.8 Non-conventional layered double hydroxides

Various interesting LDH have been synthesised via mechanochemical means. A study conducted by (Ferencz, Szabados, Varga, et al., 2016) indicated that Ca(II)-Fe(III)-LDH was successfully synthesised with the use of dry grinding followed by further grinding with small amounts of water or NaOH solution. The water and NaOH solution was added such that a sufficient amount of hydroxide groups were present for the respective LDH to form. The process was conducted with the use of a mixer mill. The study as aimed at producing pure phase LDH through varying the Ca:Fe molar ratio, the dry grinding time (without water addition) and the amount of water added to the system. Pristine LDH along with cystinate and tyrosinate intercalated LDH was successfully synthesised.

The study revealed that no grinding was necessary for LDH formation, however that increasing the dry milling time increased the conversion of the reactants to LDH. This was considered to be a result of mechanical activation of the particle surfaces. The activation is speculated to be a result of the increase in surface area, decrease in the coherence energy of the particles and an increase in both the internal and surface energy. The effects of the grinding frequency were further investigated. Low frequencies resulted in smaller XRD intensities with a maximum being observed with an increase in frequency. A further increase resulted in a reduction in LDH crystallinity and eventual destruction of the LDH. Changing the molar ratios further revealed that a ratio of 2:1 (Ca:Fe) was optimal to avoid excess reactant within the system and minuscule $CaCO_3$ formation (Ferencz, Szabados, Varga, et al., 2016).

Similarly, an ultrasonically-enhanced mechanochemical procedure for the synthesis of Ca-Fe LDH was developed by (Szabados, Varga, et al., 2018). The process included a pre-milling step followed by ultrasonic irradiation. The halides $F^-$, $Cl^-$, $Br^-$ and $I^-$, azide and the oxo anions $CO_3^{2-}$,$NO_3^-$ and $ClO_4^-$ were successfully intercalated into the synthesised Ca-Fe LDH.

Research was conducted in an effort to identify whether $Ti^{4+}$ and $Mn^{2+}$ have been successfully incorporated into an LDH structure through a mechanochemical route. Little information was found to be available regarding the use of grinding for synthesis purposes.

## 2.10 The effects of grinding on the final properties of layered double hydroxides

The final properties of LDH synthesised through mechanochemical techniques may need to conform to certain standards before they can be incorporated into certain products

or manufacturing processes. The type of milling may not only affect synthesis, but may result in LDH that does not have the correct particle size, morphology or characteristics for the intended use. It was thus considered important to investigate the effect of certain grinding techniques on the final properties of already synthesised LDH.

The effects of three different grinding procedures, namely knife milling, ball milling and jet milling, on the final properties of layered double hydroxides was studied by (Pagano et al., 2018). The particle size, morphology, specific surface area, crystallinity and flow character were investigated. It was noted that one of the most important characteristics is the final particle size as it affects the characteristics of the formulations in which it is incorporated. These include the homogeneity, stability and flow properties of the final product and is considered further important if incorporated semi-solid blends. The search for synthesis methods in which the dimensions of the final LDH product can be controlled, for industrial scale application, is open. A solution to this could be the use of grinding methods such as those mentioned (Pagano et al., 2018).

The selected grinding technique is dependent on the type of material to be milled. It is further important to maintain the desired product features such as crystallinity and morphology. The study conducted made use of Mg-Al-$NO_3$ LDH due to its broad use and versatility, however the study was specifically aimed at pharmaceutical application. Results obtained indicated that ball milling resulted in the largest particle size, whereas jet milling produced the finest particles of the techniques used. The morphology of the LDH crystal was found to be altered for ball milling and knife milling in which agglomerates and aggregates were the final result. Comparatively, particles obtained from jet milling maintained their crystal structure with no breakage and slight flattening (Pagano et al., 2018).

The specific surface area for ball and knife milled particles were found to have decreased, whereas for those that were jet milled the specific surface area increased. The decrease of surface area was said to be attributed to agglomeration. Similar to the trends associated with morphology, a loss of crystallinity was observed for both ball and knife milled samples. Comparatively the crystallinity for the jet milled samples remained acceptable and no carbonate contamination was noted (Pagano et al., 2018).

The flow properties of the LDH is considered to be one of the most important characteristics for product manufacture and quality. High flow-ability was found to ensure reproducible filling of dies or capsule shells for tablet and capsule manufacturing for pharmaceuticals. Samples obtained from ball milling contained very low flow character with low homogeneity. Knife milling samples indicated acceptable flow character however was considered inhomogeneous. Finally, the jet milled product was found to exhibit

good homogeneity and a fair flow character. It was thus concluded that for industrial manufacture of LDH for pharmaceutical application, jet milling would be the best of the presented methods to follow (Pagano et al., 2018).

## 2.11 Commercial Milling

Particle size reduction occurs through factors such as pressure, friction, attrition, impact or shear via particle-particle, particle-media or particle-mill interactions. Dry milling and wet milling differ, with both processes having their own unique limitations. Dry grinding may result in issues such as powder accumulation, electrostatic agglomeration, and considerable amounts of frictional heat and upon scale-up the flow properties may affect the uniformity of the product being delivered. Milled and partially milled product may be very cohesive and may accumulate. This would result in the reduction of the overall process yield. The removal of product from areas with low flow periodically, such as in pipe elbows, cyclones or any bends, may increase processing times and costs. Blockages associated with accumulated powders could further result in overheating and equipment failure. Additional environmental limitations associated with dry grinding include the production of fines that may be hazardous to operators and impact the environment. The formation of explosive dust also requires consideration hot sources such as heated surfaces or electrical sources need to be carefully maintained. The production cost associated with dry milling increases with the need for safety equipment and safety procedures for operating personnel (Williams et al., 2012).

Wet milling, commonly referred to as slurry milling, has multiple benefits over its dry milling counterpart. This includes thermal control, safer operation and particle distribution. Thermal control allows for more versatile operation in which more complex or thermally sensitive compounds can be processed. The prevention of chemical decomposition, solid phase transitions or product melting is increasingly valuable. A concern with wet milling, however, is the dissolution of submicron or fine particles within the system. Additionally, the production of larger particles through Ostwald ripening poses a challenge. When scaling the process to a commercial level, it is of importance to consider the effects of surface area to batch volume, which affects the heat transfer. Sealing of the wet milling equipment is necessary to prevent contamination and prolong the seal lifetime. The final particle size distribution is dependent on the type of wet milling equipment selected, however is largely dependent on the residence time of the system. This can be controlled through single or multi-passes (Williams et al., 2012).

Ball milling is one of the most commonly used methods for LDH synthesis and is likely due the amorphitization ability of the equipment through impact. The process of commercial

grinding requires a significant amount of electrical energy, as well as increased quantities of steel due to machine and media wear. Communition efficiency is therefore of importance. Energy efficiencies associated with tumbling mills can be as low as 1 % or less. It has been reported that for ball milling, the theoretical energy required for size reduction is approximately 0.6 % of the energy supplied to the machine set-up. Additionally, the surface free energy related to solid materials is within the order of $10^2$ to $10^3$ $mJ \cdot m^{-2}/$. Studies have indicated that the specific energy required to produce a particle with a specific surface area of 0.3 $m^2 \cdot g^{-1}$ should only require 0.1 $kWh \cdot t^{-1}$. Real grinding systems, however, require 10 to 100 $kWh \cdot t^{-1}$ resulting in a calculated efficiency between 0.1 % and 1 %. (Fuerstenau & Abouzeid, 2002).

Agitator bead mills produced by Netzsch are designed for a wide range of applications such as homogenization of solids, deagglomeration and dispersing. They are designed to handle some of the most demanding grinding processes such as the comminution of quartz or boron carbide, and can process solids concentrations of up to 80 %. The comminution energy within agitator bead mills is transferred via the grinding media. Each comminution stage can be described through the specific energy input and differs for every selected product. Studies have attempted to correlate the grinding performance and the energy input into the system. Smaller grinding media, the energy utilized is deemed to be better initially. This is however only true for up to a certain bead size, after which the energy required to achieve a certain particle size can rise substantially. A wide range of Netzsch grinding systems exist and models used within laboratory trials can be scaled up to a commercial level. (Netzsch, 2009)

## 2.12 Standard Mill operation

A NETZSCH LME 1 Horizontal mill for continuous grinding and dispersion of the solids in liquid, with the use of a disc agitator, was used for all experimental procedures followed. The disc agitator, commonly used for processing products related to the paint and varnish fields, can be exchanged with a peg agitator used for difficult products. This includes highly abrasive media or highly viscous and temperature sensitive products.

The principle of use is similar to that of agitator bead mills in which the grinding media is accelerated with the use of an agitator shaft. The energy supplied to the media is then transferred to the solids via collisions and de-accelaration. The vessel is placed in a horizontal position such that even activation of the grinding media is provided.

Figure 11 depicts a schematic of the mill as provided by NETZSCH.

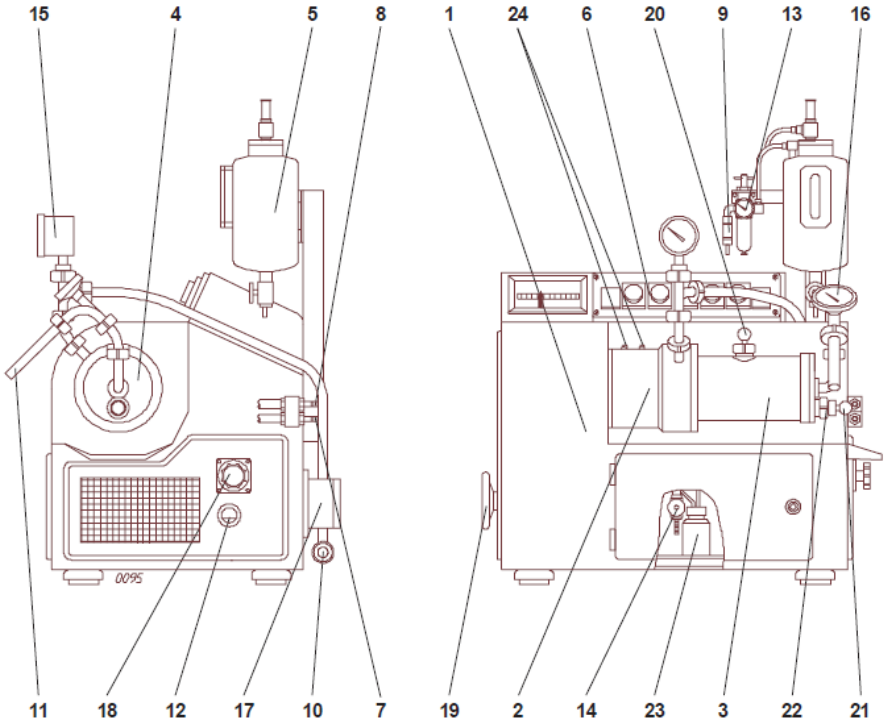


**Figure 11:** Technical schematic of a horizontal mill as provided by NETZSCH.

The numerical references are as follows:

1. Machine stand.
2. Bearing housing.
3. Grinding vessel.
4. Tank floor.
5. Liquid vessel for sealing during grinding.
6. Control panel.
7. Cooling/heating water inlet.
8. Cooling/heating water outlet.
9. Compressed air connection.
10. Product inlet.
11. Product outlet.
12. Oil level of pump gear.
13. Pressure reducing valve.
14. Discharge valve for sealing liquid.
15. Manometer.
16. Thermometer.
17. Pump.
18. Speed adjustment of pump.
19. Speed adjustment of agitator shaft.
20. Bead filling connection.
21. Product discharge.
22. Grinding media discharge.
23. Leakage vessel.
24. Grease nipple.

The relevant control panel is as depicted in Figure 12 where the numerical references are as follows:

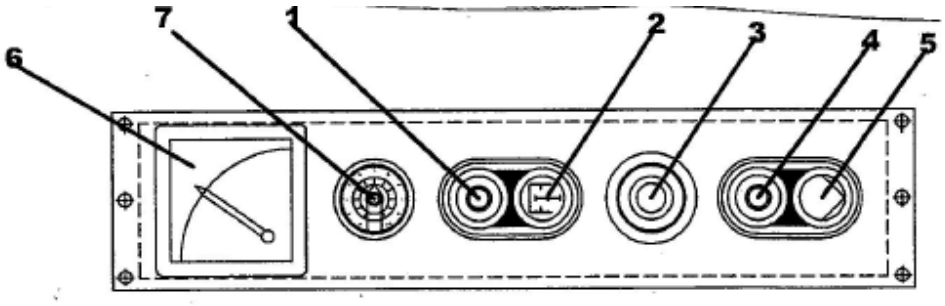


**Figure 12:** Technical schematic of the control panel as provided by NETZSCH.

1. Off switch to agitator.
2. On switch to agitator.
3. Emergency off switch.
4. Off switch to pump.
5. On switch to pump.
6. Agitator ammeter.
7. Speed rheostat.

The selected mill is desirable due to the following advantages:

- High grinding capacity.
- Closer grain distribution.
- The grinding system undergoes less strain.

The pump setup provided by NETSCH was not used. Standard mill operation consisted of the following steps:

- Check the level of the sealing liquid and adjust the sealing pressure accordingly by opening of the compressed air line.
- Charge the grinding vessel with the selected media, fill up if required. Only use media of the same type and size.

- Open cooling water valves.
- Switch on mill and adjust agitator speed to minimum 1000 rpm.
- Switch on pump.
- The desired product is to be fed in suspension and thus processed in one passage into the vessel. The flowrate of the product and thus the residence time in the mill is adjusted by the selected feed pump.
- The product can be either cooled or heated depending on its temperature behaviour.

## 2.13 Selection of milling media

NETSCH provides a guideline for the selection of grinding media. The media selected is dependent on the following criteria:

- Contamination.
- Material density.
- Efficiency.

Contamination refers to selected products restricting the type of grinding media that may be used due to the following:

- Colour change .
- Chemical incompatibility.
- Separation of the broken grinding media is extremely difficult or costly.
- Regulations such as those found in the food industry.

The specific gravity of the grinding media is an indication of the amount of energy that can be transferred during collisions to the product particles. At a constant agitator speed and with satisfactory product suspension the energy released is only dependent on the mass of the milling media. If the energy released during the grinding operation is not sufficient, media with a higher specific gravity would have to be selected. It should however be noted that grinding media with a larger diameter, providing the same mass, could reach

the desired similar effect. This however results in a reduced number of grinding media within the system and therefore reduce the number of contact points.

The efficiency of the selected grinding media are dependent on the following factors:

- Media charge.
- Wear behaviour.
- Grinding capacity.

The wear behaviour is dependent on the combination of grinding media and the suspension. The grinding capacity is further influenced by the mass of the selected grinding media. The size of the selected grinding media should be within the range of 20 to 50 times the size of the initial grain size. Grinding may require a two step procedure if the energy requirement is high or the initial grain size of the product is too high.

## 2.14 Analytical techniques

### 2.14.1 X-ray differaction analysis (XRD)

X-ray differaction analysis involves exposing a sample with X-rays such that they interact with any crystalline phase present. This interaction results in the production of a unique differaction pattern. XRD patterns act like fingerprints that allow for the charicterisation of phases present within crystalline samples (Cullity, 1956).

XRD analysis is the primary analytical technique used for the characterisation of LDH materials. Phases within the sample are generally identified through comparison with existing stadards. Peak intensity is indicative of the total amount of scattering from each crystal plane (Connoly, 2019). Samples with poor crystallinity and disordered stacking of the layers result in difficulties associated with the interpretation of the XRD data. Diffraction lines are often broad and asymmetric as a a result (Cavani, Trifiro & Vaccari, 1991).

The interlayer spacing of the LDH can be calculated with the use of Braggs law as described in Equation 7.

$$n\lambda = 2dsin(\theta) \tag{7}$$

where d refers to the distance between the atomic layers within the LDH crystal. The variable $\lambda$ refers to the wavelength of the incident X-ray beam. The variable n further refers to an intiger, typically selected to be 1 and $\theta$ describes the angle of deflection.

Reaction products of powdered samples were identified using a PANalytical X'Pert Pro powder diffractometer in $\theta$-$\theta$ configuration fitted with an X'Celerator detector and variable divergence- and fixed receiving slits. The system made use of Fe filtered Co-K$\alpha$ ($\lambda$=1.789 $\mathring{A}$). Samples were prepared using the standardized PANalytical backloading system, providing a random distribution of particles. Samples were scanned from 5°to 90°2$\theta$ with a step size of 0.008. Sample mineralogy was determined using the ICSD database in correlation with X'Pert Highscore plus software.

### 2.14.2 Fourier transform infrared spectroscopy (FT-IR)

FT-IR analysis can be conducted to determine the qualitative presence of chemical compounds that are present within a sample. An IR-spectrometer ill be used to pass infrared radiation through a sample and will make use of a detector to plot the transmittance or absorbance as a function of the wavenumber of the radiation. A downward peak is indicative of the absorption at a select wavenumber. IR spectroscopy allows for the identification of functional groups and bonds within a molecule. The spectrum obtained typically extends from radiation at 4000 $cm^{-1}$ to 600 $cm^{-1}$ and can be seperated into a functional group region as well as a fingerprint region (1450 $cm^{-1}$-400 $cm^{-1}$). The fingerprint region, however, is unique to each sample but may be complex. Stretching vibrations typically occur within the functional group region whereas bending vibrations occur typically within the fingerprint region (Harding, 2019).

The intensity associated with absorption bands are dependent on the change in dipole moment of a bond as well as the specific number of bonds present. Two different atoms result in a difference in electronegativity and therefore allow for photon absorption. No electronegativity results in no absorption and therefore no peaks will be observed. Bigger electronegativities result in more intense absorption (Harding, 2019). Table 3 depicts the characteristic bonds associated with each of the LDH materials synthesised, as obtained from literature. FT-IR spectra were obtained using a Perkin Elmer 100 Spectrophotometer. Analysis was conducted over a range of 550 $cm^{-1}$ to 4000 $cm^{-1}$ and represent an average of a total of 32 scans, at a selected resolution of 2 $cm^{-1}$.

**Table 3:** Possible bands present within FT-IR spectra for LDH materials.

| Wavenumber ($cm^{-1}$) | Type of Bond | Reference |
|---|---|---|
| 430 | O-M-O | (Aisawa et al., 2002) |
| 900-300 (str) | M-O | (Socrates, 2001) |
| 3000 | Adsorbed water | (Aisawa et al., 2002) |
| 1620 | | (Aisawa et al., 2002) |
| 1400 | C-H stretching vibration | (Aisawa et al., 2002) |
| 2850 | | (Aisawa et al., 2002) |
| 2925 | | (Aisawa et al., 2002) |
| 1360 | Carbonate in interlayer | (Dudeka et al., 2012) |
| 3000 | | (Dudeka et al., 2012) |
| 1366 | | (Labuschagne et al., 2015) |
| | | (Qu, Zhong, et al., 2016) |
| 3022 | | (Qu, Zhong, et al., 2016) |
| 1420 | Carbonate on surface | (Qu, Zhong, et al., 2016) |
| 875 | | (Qu, Zhong, et al., 2016) |
| 1530-1320 | $CO_3^{2-}$ | (Socrates, 2001) |
| 1160 | | (Socrates, 2001) |
| 1100-1020 | | (Socrates, 2001) |
| 890-800 | | (Socrates, 2001) |
| 745-670 | | (Socrates, 2001) |
| 3250-3600 | Bonded O-H | (Nicolet, 2019) |
| | | (Tongamp et al., 2006a) |
| 3500-3700 | Free O-H | (Nicolet, 2019) |
| | | (Tongamp et al., 2006a) |
| 1100-900 | Silicate | (Socrates, 2001) |
| 770-700 | $ZrO_3^{2-}$ | (Socrates, 2001) |
| 600-450 | | (Socrates, 2001) |
| 500-300 | | (Socrates, 2001) |
| 240-230 | | (Socrates, 2001) |
| 3800-3000 (str) | M-OH | (Socrates, 2001) |
| 3700-3300 (str) | | (Qu, Zhong, et al., 2016) |
| 1200-690 (def) | | (Socrates, 2001) |

### 2.14.3 Particle size analysis (PSA)

Particle size analysis is an analytical technique that determines the size range of the particles present within a sample. Particle size is considered to be important as it influences the properties of particulate matter and can be an indicator of quality and performance. This is considered to be true for powders, suspensions, aerosols and emulsions. The flow and compact properties of powders are influenced by its shape and size. Larger particls with spherical shape flow readily and more easily than particles that are smaller with high aspect ratios. Dissolution occurs more readily for small particles and will result in greater suspension viscosities when compared with larger particles (Horiba Scientific, 2019).

Many existing techniques make the assumption that particles being analysed are spherical. This is due to the complexity associated with multi dimensional particles. This approach is considered to be simplistic, as well as innacurate, however does not cause serious problems for particles generated with most industrial applications. The assumption is considered to be problematic only for particles with large aspect ratios such as fibres or needles (Horiba Scientific, 2019).

Samples collected were analysed wet and fully dispersed, before the respective filtration and drying steps, with the use of a Mastersizer 3000 (Malvern Instruments, UK). A Hydro LV solids unit was used for addition and distribution of solid particles. The mastersizer 3000 makes use of laser differction analysis to determine the particle size range for a select wet or dry sample. A laser beam, is passed through the dispersed sample and the intensity of the scattered light is measured (Malvern Panalytical, 2019).

A typical system consists of three main configurations (Malvern Panalytical, 2019):

1. An optical bench through which the dispersed sample passes. This is where the particles are illuminated with the laser beam. Multiple detectors would then measure the scattered light making use of both blue and red light wavelengths.
2. Sample dispersion units ensure that the sample is delivered to the bench at the correct concentration and suitably dispersed.
3. Instrument software analyses the scattered data obtained and calculated the desired particle size distribution.

### 2.14.4 Scanning electron microscopy (SEM)

Scanning electron microscopy makes use of an electron microscope. Images are produced through scanning the surface of the sample, which is mounted on a stage, with a concentrated beam of electrons. The column and chamber of the microscope is evacuated with the use of pumps. The level at which the vacuum is maintained is dependent on the type of microscope in use. A multitude of signals (backscatterd electrons, secondary electrons and charactersitic X-rays) are produced due to the electron-sample interaction which are then detected by a set of detectors. An image of the topography of the sample can then be generated. The electron beam can penetrate the sample to a certain depth (few microns) and is dependant on the accelerating voltage and the sample density.

Sample morphology was examined with the use of SEM imaging. A Zeiss Gemini 1 cross beam 540 FEG SEM (Oberkochen, Germany) was used for all selected samples. Dry powdered samples were secured onto an aluminium sample holder and graphite coated 5 times with a Polaron Equipment E5400 SEM auto-coating sputter system (Quorum, East Sussex, UK).

### 2.14.5 X-ray fluoresence (XRF)

X-ray fluoresence is a non-destructive analytical technique used to determine the exact elemental composition of a sample. This is done through the measurement of the fluorescent X-ray that is emmited from the sample upon excitation with the use of a primary X-ray source. Each element present emmits a unique set of fluorescent X-rays (ThermoFischer, 2019).

The XRF process is as follows (ThermoFischer, 2019):

1. The sample, solid or liquid, is irradiated with the use of high energy X-rays from a select X-ray tube.
2. Upon irradiation an electron from the inner orbital of an atom is dislodged.
3. An electron from a higher energy orbital will fill the vacancy and release a fluorescent X-ray. This is then measured and analysed.

Samples were dried at 100 °C and roasted at 100 °C to determine mass loss upon ignition. 1 g of the sample was mixed with 6 g Lithumtetraborate flux and fused at 1050 °C to form a stable fused glass bead. Analysis was conducted using a Thermo Fisher ARL Perform ‘X Sequential instrument. Samples were characterized using UNIQUANT software.

The estimated error is given as the highest value from three selected sources. These include (1) Counting statistical error, (2) systematic errors in corrections for background and line overlaps and, (3) error based on the K factor equation. A standard material is analysed for each smple batch under the same analytical conditions and was prepared under the same conditions as each sample. Table 4 depicts the estimated error and calculated percentage error associated with an analysed standard. The percentage error can increase drastically for smaller measurements and should be considered when looking at select components.

**Table 4:** An example of an analysed standard as presented by the Department of Geology, University of Pretoria (UP)

| Component | BHVO-1 Certified | BHVO-1 Analysed | BHVO-1 Est. Error | Percent Err. |
|---|---|---|---|---|
| SiO2 | 49.94 | 48.59 | 0.25 | 0.514 |
| Al2O3 | 13.8 | 13.79 | 0.17 | 1.23 |
| MgO | 7.23 | 8.16 | 0.14 | 1.72 |
| Na2O | 2.26 | 1.98 | 0.07 | 3.54 |
| P2O5 | 0.273 | 0.321 | 0.016 | 4.98 |
| Fe2O3 | 12.23 | 11.62 | 0.16 | 1.38 |
| K2O | 0.52 | 0.534 | 0.027 | 5.056 |
| CaO | 11.4 | 10.62 | 0.15 | 1.41 |
| TiO2 | 2.71 | 2.48 | 0.08 | 3.23 |
| V2O5 | 0.0566 | 0.0538 | 0.0027 | 5.018 |
| Cr2O3 | 0.0422 | 0.0379 | 0.0019 | 5.013 |
| MnO | 0.168 | 0.17 | 0.0085 | 5 |
| NiO | 0.0154 | 0.0168 | 0.0013 | 7.74 |
| CuO | 0.017 | 0.0192 | 0.0014 | 7.29 |
| ZrO2 | 0.0242 | 0.103 | 0.0068 | 6.601 |
| SO3 | | 0.0352 | 0.0024 | 6.82 |
| Co3O4 | | 0.0162 | 0.0012 | 7.41 |
| BaO | | 0.562 | 0.16 | 28.47 |
| ZnO | | 0.0173 | 0.0012 | 6.94 |
| SrO | | 0.121 | 0.006 | 4.96 |
| Y2O3 | - | 0.0171 | 0.0056 | 32.75 |

# 3 Experimental design

The aim of the study was to expand on the synthesis of LDH materials through mechanochemical means. Many mechanochemical techniques were found to exist, however little research has been conducted on one-step wet mechanochemical synthesis of LDH. An exploratory approach was therefore used for the experimental design and research conducted.

## 3.1 Apparatus

A NETZSCH LME Horizontal mill for continuous grinding of solids in liquid, with a disc agitator, modified for batch synthesis was used for all experimental runs conducted. Figure 13 depicts a general schematic of the modified set-up. Modification of the system allowed for no inlet or product flow to occur. The system was therefore sealed at both the inlet and outlet to the milling chamber. Batch modification allowed for the conservation of raw materials. The instrument was selected as it is primarily designed for wet milling and allows for ease of upscaling to a commercial level.

Steel head 10k NTC temperature (MicroRobotics) sensors were placed directly into the jacket water line at the entrance and exit of the cooling water jacket. Similarly a Fs400A G1 flow meter (MicroRobotics) was placed in the inlet line at the entrance to the jacket, in sequence with the temperature sensor. The internal temperature of the vessel could not be measured directly as a result of the grinding activity. A temperature sensor was therefore placed on the front plate of the mill, such that the temperature associated with the jacket was excluded. A detailed schematic depicting the location of each sensor is indicated in Figure 13.

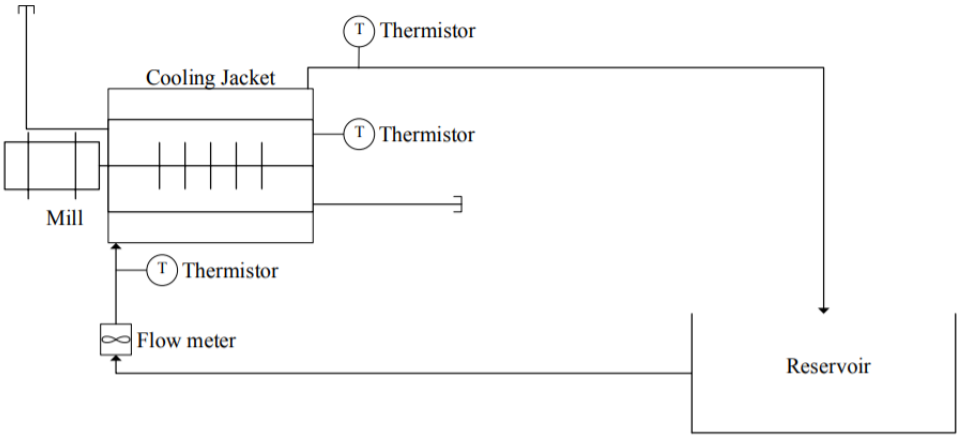


**Figure 13:** Process flow diagram of batch mill set-up.

## 3.2 Synthesis conditions

The selection of synthesis conditions were divided up into two seperate subsections, namely a parameter study and a versatility study.

**Parameter study** The influence of milling parameters on the synthesis of Mg-Al layered double hydroxide was investigated making use of batch operation under atmospheric

conditions. The following milling and synthesis parameters were selected to be kept constant throughout each experimental run:

1. Media shape: The optimum shape for grinding has been reported to be spherical (Williams et al., 2012), however for fine grinding application rod shaped media has proven to produce desirable results (Wills & Finch, 2016). Due to availability spherical media was selected for all grinding experiments conducted.

2. Media loading: Studies recommend operation be conducted at maximum loading for efficient grinding (Wills & Finch, 2016). The media loading was therefore selected to remain constant at 60 % occupying a volume of 0.735 L.

3. Media material: The selected material for all grinding purposes was yttrium stabilised zirconia due to its highly inert nature, hardness and availability.

4. Starting materials: The starting materials selected were commercial grade MgO (86 %, Chamotte Holdings) and $Al(OH)_3$ (99.2 %, Belguam Indal). The selection of raw materials are further discussed in Section 4.

5. Metal ratio: The selected $M^{2+}$:$M^{3+}$ ratio was kept constant at 2:1.

6. Cooling water flow rate: The flow rate remained constant at 525 $L{\cdot}h^{-1}$. This was selected at as an intermediate flow rate, with the maximum observed to be 800 $L{\cdot}h^{-1}$ without modification.

Unless stated otherwise, the following milling parameters were kept constant for each experimental run:

1. Jacket water inlet temperature was set to 30 °C. This was observed to be the lowest constant temperature available from the surroundings without the need for refrigeration. Temperatures naturally fluctuate throughout the seasons, with the highest temperature observed to be 30 °C in summer. This was therefore selected to be the lowest controllable temperature throughout the year.

2. Bead size was kept constant at 2 mm due to availability and ease of use.

3. Rotational speed was kept constant at 2000 rpm as this was deemed to be an intermediate speed between the maximum (3000 rpm) and minimum (1000 rpm) operational speeds available. It was observed that 1000 rpm was the minimum operational speed at which runs were deemed to be successful. Experimental runs were unsuccessful at lower speeds for the selected synthesis conditions and loading, as

the system would automatically shut down. Similarly the maxmimum operational speed was determined to be 3000 rpm, with greater speeds not possible without modification.

4. Retention time was selected to be 1 h.

5. Solids loading was set at 10 % raw materials in water.

The milling parameters investigated were therefore as follows:

1. Rotational speed: The rotational speed was varied at 1000 rpm, 2000 rpm and 3000 rpm, for 1 h at a jacket water inlet temperature of 30 °C. A change in the rotational speed should result in an increase in the milling rate, increasing the number of collisions in a set time frame. It was therefore of interest to determine the influence of rotational speed on the formation of LDH product (Ranu & Stolle, 2015).

2. Residence time: The residence time was varied for 1 h, 2 h and 3 h, at a cooling water inlet temperature of 30 °C and rotational speed of 2000 rpm. An increase in milling time could influence the conversion of raw materials to LDH product as an increase in the residence time result in an increase in the number of collisions (Ranu & Stolle, 2015).

3. Solids loading: The solids loading was varied at 10 %, 20 % and 30 %. Greater solids loading should result in an increase in the particle-particle collisions within the milling time frame. It was further expected that the viscosity of the slurry change drastically with an increase in solids loading, which may reduce the overall number of collisions (Ranu & Stolle, 2015).

4. Bead size: The bead size was varied from 2 mm to a size of 0.25 mm, at a cooling water inlet temperature of 30 °and rotational speed of 2000 rpm. It was speculated that decreasing the milling media size will result in an increase in the amount of reactive surface area, therefore increasing the conversion of reactants to LDH (Ranu & Stolle, 2015).

5. Jacket water temperature: The jacket water temperature was increased from 30 °C to a maximum of 50 °C. Greater jacket water temperatures were not available without further modification to the system. The increase in temperature was investigated for a change in rotational speed at 1000 rpm, 2000 rpm and 3000 rpm. Similarly the change in temperature was further investigate for a change in retention time for 1 h, 2 h and 3 h, at a rotational speed of 2000 rpm. Higher temperature

was expected to influence the rate of reaction within the system (Ranu & Stolle, 2015).

**Versatility study** The synthesis of Mg-Al, Ca-Al, Zn-Al and Cu-Al layered double hydroxides were further investigated. Synthesis conditions such as the $M^{2+}$:$M^{3+}$ ratio's as well as selected raw materials were adapted from existing literature that make use of other mechanochemical techniques. The following milling and synthesis conditions were kept constant for each experimental run:

1. Rotational speed was set at 2000 rpm, this was selected as an intermediate speed between 1000 rpm and 3000 rpm, which correspond to the minimum an maximum speeds of the mill.
2. Jacket water inlet temperature was set at 30 °C, with a flow rate of 525 $L{\cdot}h^{-1}$. It was of interest to determine the extent at which the sysnthesis occurs at the lowest natural temperature for each of the selected LDH materials, before synthesising at higher temperatures.
3. Retention time was selected to be 1 h.
4. Bead size and type were selected to be 2 mm yttrium stabilised zirconia due to its durability and inert nature.
5. Solids loading was selected to be 10 %.
6. Bead loading remained constant at 60 % by volume.

Intermediate milling conditions were selected to determine the versatility of the synthesis procedure. The synthesis conditions specific to each of the LDH materials were adapted from literature. These were found to be the optimal conditions specified for mechanochemical techniques making use of either a ball mill or mixer mill. These were determined to be:

1. Mg-Al: The raw materials selected were MgO and $Al(OH)_3$ added at a 3:1 $M^{2+}$:$M^{3+}$ ratio to $H_2O$ (Tongamp et al., 2006a).
2. Ca-Al: The synthesis as conducted in two ways, with or without the addition of a carbonate source. Raw materials selected were therefore CaO, $Al(OH)_3$ and $CaCO_3$, added according to a 2:1:0 or a 3:2:1 ratio $M^{2+}$:$M^{3+}$:$CaCO_3$ to $H_2O$ (Qu, Zhong, et al., 2016).

3. Zn-Al: Two zinc sources were seperately investigated at a $M^{2+}$:$M^{3+}$ ratio of 1:1 with $Al(OH)_3$. These were selected to be ZnO and $Zn_5(CO_3)_2(OH)_6$ to be added to $H_2O$ (Qu, He, M Chen, Huang, et al., 2017).

4. Cu-Al: The selected raw materials were $Cu_2(OH)_2CO_3$ added at a 2:1 and 4:1 $M^{2+}$:$M^{3+}$ ratio to $H_2O$. The selected 2:1 ratio was initially adapted from literature. The selected 4:1 ratio was only tested once results were analysed for the 2:1 ratio. This was done to determine the effect an excess of $Cu^{2+}$ would have on the formation of Cu-AL LDH.

Limited research has been conducted on single-step wet grinding procedures with excess water and warrants further investigation. Synthesis techniques may have limitations on the type of LDH materials that could be synthesised. It is therefore necessary to determine whether such limitations are prevalent for the selected mechanochemical procedure. The selection of optimal conditions, specifically in relation to $M^{2+}$:$M^{3+}$ relevant to conventional mechanochemical techniques provide insight on the performance on the selected milling technique. Samples were subjected to ageing for 24 h at 80 °C to determine whether the selected mill allowed for sufficient mecanochemical activation of the sample such that LDH formation would commence. It was of interest further investigate the effect ageing would have on the milled mixture.

**Summary of synthesis conditions** Table 5 summarises the selected synthesis conditions for both the defined parameter and versatility studies. It should be noted that S2 and S16 are the same sample, however have been listed twice for ease of understanding.

**Table 5:** The synthesis conditions selected for each experimental run conducted, as well as the sample reference. *The metal ratio for Ca-Al LDH refers to $M^{2+}$:$M^{3+}$:$CaCO_3$.

| Sample | LDH type | Metal ratio | Rotational speed [rpm] | Jacket water [°C] | Solids loading [%] | Residence time [h] | Bead size [mm] |
|---|---|---|---|---|---|---|---|
| S1 | Mg-Al | 2:1 | 1000 | 30 | 10 | 1 | 2 |
| S2 | Mg-Al | 2:1 | 2000 | 30 | 10 | 1 | 2 |
| S3 | Mg-Al | 2:1 | 3000 | 30 | 10 | 1 | 2 |
| S4 | Mg-Al | 2:1 | 2000 | 30 | 10 | 1 | 2 |
| S5 | Mg-Al | 2:1 | 2000 | 30 | 10 | 2 | 2 |
| S6 | Mg-Al | 2:1 | 2000 | 30 | 10 | 3 | 2 |
| S7 | Mg-Al | 2:1 | 2000 | 30 | 20 | 1 | 2 |
| S8 | Mg-Al | 2:1 | 2000 | 30 | 30 | 1 | 2 |
| S9 | Mg-Al | 2:1 | 2000 | 30 | 10 | 1 | 0.25 |
| S10 | Mg-Al | 2:1 | 1000 | 50 | 10 | 1 | 2 |
| S11 | Mg-Al | 2:1 | 2000 | 50 | 10 | 1 | 2 |
| S12 | Mg-Al | 2:1 | 3000 | 50 | 10 | 1 | 2 |
| S13 | Mg-Al | 2:1 | 2000 | 50 | 10 | 1 | 2 |
| S14 | Mg-Al | 2:1 | 2000 | 50 | 10 | 2 | 2 |
| S15 | Mg-Al | 2:1 | 2000 | 50 | 10 | 3 | 2 |
| S16 | Mg-Al | 2:1 | 2000 | 30 | 10 | 1 | 2 |
| S17 | Mg-Al | 3:1 | 2000 | 30 | 10 | 1 | 2 |
| S18 | Ca-Al* | 3:2:1 | 2000 | 30 | 10 | 1 | 2 |
| S19 | Ca-Al* | 2:1:0 | 2000 | 30 | 10 | 1 | 2 |
| S20 | Zn-Al | 1:1 | 2000 | 30 | 10 | 1 | 2 |
| S21 | Zn-Al | 1:1 | 2000 | 30 | 10 | 1 | 2 |
| S22 | Cu-Al | 2:1 | 2000 | 30 | 10 | 1 | 2 |
| S23 | Cu-Al | 4:1 | 2000 | 30 | 10 | 1 | 2 |

# 4 Materials

The selected raw materials were a mixture of oxides and hydroxides such that the production of harmful salt effluent could be avoided. This would allow for a 'greener' method of LDH synthesis.

**Aluminium hydroxide** Commercial grade Aluminium hydroxide ($Al(OH)_3$)(99.2%, Belguam Indal) was used as the primary source of $M^{3+}$ for all LDH materials synthesised.

**Magnesium oxide** Commercial grade Magnesium Oxide (MgO) (86%, Chamotte Holdings) was used for all experiments involving the synthesis of Mg-Al LDH. The MgO was initially calcined at a temperature of 800 °C for 1 h to produce light burned Magnesia (Ropp, 2013). This allowed for the elimination of $MgCO_3$ and possible $Mg(OH)_2$ from the starting material.

The selected MgO had been calcined at a temperature of 950 °C prior to purchase, with a reported reactivity of 65 % (Chamotte, 2018). It was noted that minor quantities of forsterite ($Mg_2SiO_4$) were naturally present within the sample prior to use. SEM imaging of the MgO, after calcination is depicted in Figure 14.

**Calcium oxide** Commercial grade calcium hydroxide ($Ca(OH)_2$) was initially calcined for 1 h at a temperature of 900 °C to form Calcium oxide (CaO) (66 %, Lime co.). This allowed for the elimination of hydroxide and carbonate impurities present within the starting material. The CaO was then reacted with water for 15 min to form $Ca(OH)_2$ prior to milling. XRF analysis on the $Ca(OH)_2$ indicated that approximately 66 % of the sample was CaO. SEM imaging of the CaO is depicted in Figures 17.

**Calcium carbonate** Commercial grade Calcium carbonate ($CaCO_3$) (96.5 %, Idwala Carbonates) was used as the primary carbonate source for the synthesis of Ca-Al LDH. SEM imaging of the raw material is depicted in Figure 16

**Zinc basic carbonate** Zinc basic carbonate ($Zn_5(CO_3)_2(OH)_6$ ( $\geq$ 58 % Zn, Sigma-Aldridge)) was used for the synthesis of Zn-Al LDH. SEM imaging prior to milling is depicted in Figure 18.

**Zinc oxide** Paint grade Zinc oxide (ZnO) (99 %, Zinchem) was selected as the second zinc source to be explored in the synthesis of Zn-Al LDH. SEM imaging of the selected raw material is as depicted in Figure 19.

**Cupric basic carbonate** Commercial grade Cupric basic carbonate ($Cu_2(OH)_2CO_3$) (96 %, Adchem) was milled according to a 2:1 (Qu, He, M Chen, Q Zhang, et al., 2017) and 4:1 (Excess $Cu_2(OH)_2CO_3$) $M^{2+}$:$M^{3+}$ metal ratio. SEM imaging for the $Cu_2(OH)_2CO_3$ is depicted in both Figures 20 and 21. The sample primarily consisted of rectangular platelets.

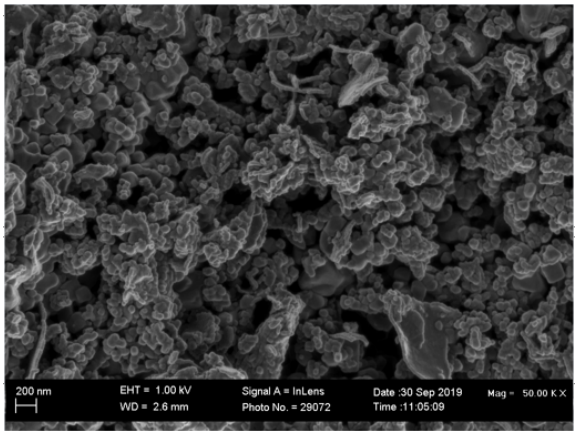


**Figure 14:** SEM imaging of calcined MgO.

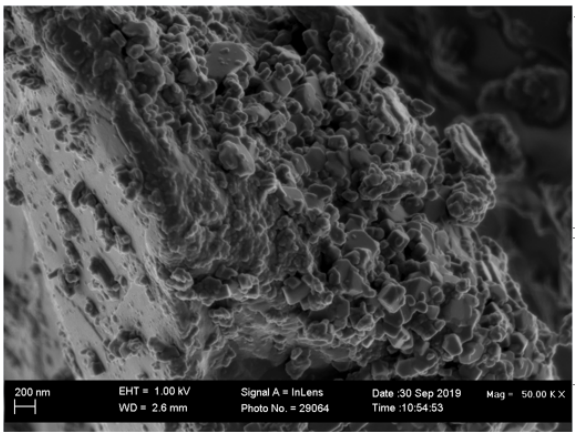


**Figure 15:** SEM imaging of $Al(OH)_3$.

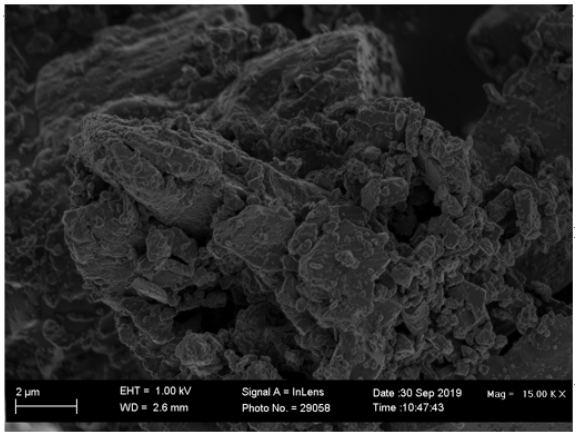


**Figure 16:** SEM imaging of $CaCO_3$.

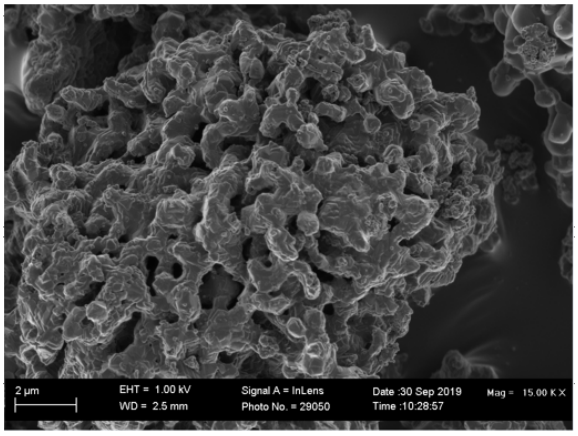


**Figure 17:** SEM imaging of CaO.

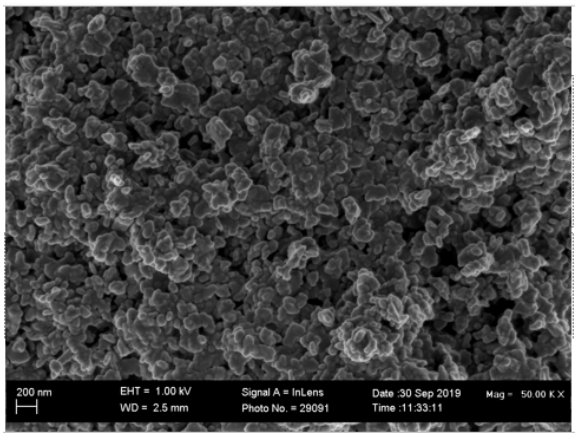


**Figure 18:** SEM imaging of $Zn_5(CO_3)_2(OH)_6$.

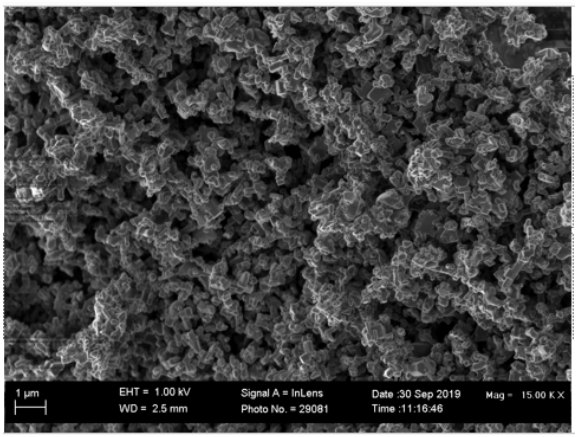


**Figure 19:** SEM imaging of ZnO.

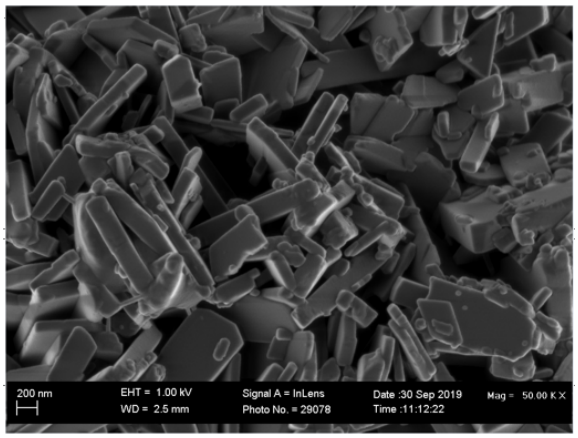


**Figure 20:** SEM imaging of $Cu_2(OH)_2CO_3$.

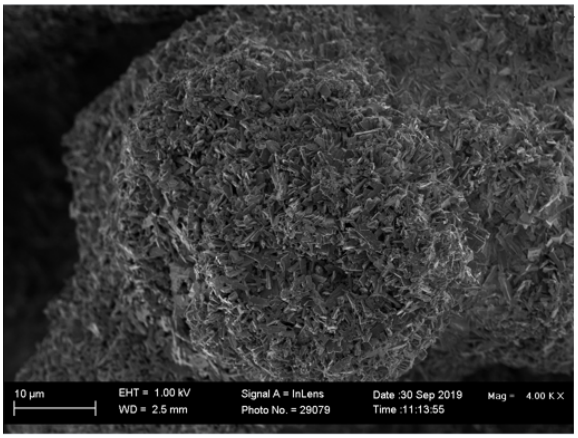


**Figure 21:** SEM imaging of $Cu_2(OH)_2CO_3$.

# 5 Experimental method

## 5.1 Mill set-up

Prior to each experimental run the following steps were implemented for the start up of the mill:

1. The level of the sealing liquid was checked to be within the correct operational limitations.
2. Air pressure line was opened and pressure kept constant at 400 kPa.
3. Milling vessel was fully assembled.

4. The milling vessel was charged with 2 mm yttrium stabilised zirconia beads to 60 % by volume. Bead size remained consistent for each experimental run, unless stated otherwise.
5. Cooling water valves were opened and jacket water flow rate was set at 525 $L{\cdot}.h^{-1}$.
6. Jacket water inlet temperature was set at 30 °C unless specified otherwise.
7. Data logging commenced upon the start of each experimental run.

## 5.2 Parameter Study

### Rotational Speed

1. Approximately 28.63 g of MgO and 23.83 g of $Al(OH)_3$ were weighed and placed in seperate beakers.
2. The two dry powders were mixed together and added to the milling chamber with the use of a funnel.
3. 472 g of water was measured from the cooling water line set a temperature of 30 °C. This was then added to the milling chamber.
4. The chamber was sealed and milling commenced at the selected rotational speed. Milling speeds were varied at 1000 rpm, 2000 rpm and 3000 rpm
5. Milling commenced for the duration of 1 h.

### Retention time

1. Approximately 28.63 g of MgO and 23.83 g of $Al(OH)_3$ were weighed and placed in seperate beakers.
2. The two dry powders were mixed together and added to the milling chamber with the use of a funnel.
3. 472 g of water was measured from the cooling water line. This was then added to the milling chamber. The cooling water inlet was set at a temperature of 30 °C.
4. The chamber was sealed and milling commenced at the selected rotational speed of 2000 rpm.
5. Milling commenced for the selected durations of 1 h, 2 h and 3 h.

**Solids Loading**

1. The raw material solids loading was varied at 20 % and 30 % for each experimental run.
2. The two dry powders were mixed together and added to the milling chamber with the use of a funnel.
3. The required water was measured from the cooling water line. This was then added to the milling chamber. The cooling water inlet was set at a temperature of 30 °C.
4. The chamber was sealed and milling commenced at the selected rotational speed of 2000 rpm.
5. Milling commenced for the duration of 1 h.

**Bead Size**

1. The milling chamber was loaded to a capacity of 60 % by volume with 250 $\mu$m yttrium stabilised zirconia beads.
2. Approximately 28.63 g of MgO and 23.83 g of $Al(OH)_3$ were weighed and placed in seperate beakers.
3. The two dry powders were mixed together and added to the milling chamber with the use of a funnel.
4. 472 g of water was measured from the cooling water line set a the selected inlet temperature of 30 °C.
5. The chamber was sealed and milling commenced at each of the selected rotational speeds. The milling speed was set at 2000 rpm.
6. Milling commenced for the duration of 1 h.

**Cooling water inlet temperature** The cooling water inlet temperature was varied for a change in the rotational speed as well as a change in the retention time. The method associated with a change in rotational speed was as follows:

1. Approximately 28.63 g of MgO and 23.83 g of $Al(OH)_3$ were weighed and placed in seperate beakers.

2. The two dry powders were mixed together and added to the milling chamber with the use of a funnel.
3. 472 g of water was measured from the cooling water line set a the selected inlet temperature of 50 °C.
4. The chamber was sealed and milling commenced at each of the selected rotational speeds. The milling speed was varied at 1000 rpm, 2000 rpm and 3000 rpm.
5. Milling commenced for the duration of 1 h.

Similarly the method associated with a change in retention time was as follows:

1. Approximately 28.63 g of MgO and 23.83 g of $Al(OH)_3$ were weighed and placed in seperate beakers.
2. The two dry powders were mixed together and added to the milling chamber with the use of a funnel.
3. 472 g of water was measured from the cooling water line set a the selected inlet temperature of 50 °C.
4. The chamber was sealed and milling commenced at a rotational speed of 2000 rpm.
5. Milling commenced for the durations of 1 h, 2 h and 3 h.

**Sample collection, Filtering and Drying** All samples obtained for the duration of the parameter study were subjected to the following sample collection, filtration and drying steps:

1. The front cap of the milling chamber was removed upon completion of the experimental run. Sample and beads were collected in a 5 L plastic beaker.
2. The sample and beads were stirred briefly to prevent settling. The sample was then decanted into a 350 ml plastic container and sealed.
3. The obtained sample was filtered with the use of a gravity filtration set-up.
4. The filtercake was placed on a watch glass and dried at a temperature of 60 °C under atmospheric conditions.
5. Drying commenced for the duration of 12 h.
6. Samples were reduced to powder form with the use of a mortar and pestle and stored for analysis.

## 5.3 Versatility Study

1. Masses for each of the selected LDH materials, namely Mg-Al, Ca-Al, Zn-Al and Cu-Al, are summarised in Table 6. Seperate experimental runs were conducted for each of the LDH materials specified.

2. The two dry powders associated with their respective LDHs were mixed together and added to the milling chamber with the use of a funnel.

3. The respective mass of $H_2O$ associated with each of the selected LDH materials was measured from the cooling water line. The inlet temperature was set at 30 °C.

4. The chamber was sealed and milling commenced at a rotational speed of 2000 rpm for the duration of 1 h.

5. The front cap of the milling chamber was removed upon completion of the experimental run. Sample and beads were collected in a 5 L plastic beaker.

6. The sample and beads were stirred briefly to prevent settling. The sample was then decanted into a 350 ml container and sealed.

7. Approximately 175 ml of sample was aged in a 250 ml beaker, at 80 °C for 24 h under atmospheric conditions. The rotational speed was kept constant at 400 rpm.

8. The remaining, as well as the aged sample were filtered with the use of a gravity filtration set-up conducted under atmospheric conditions.

9. The filtercake was placed on a watch glass and dried at a temperature of 60 °C under atmospheric conditions for 12 h.

10. Samples were reduced to powder form with the use of a mortar and pestle.

**Table 6:** Mass quantities [grams] of raw materials associated with LDH materials selected for versatility study at their respective $M^{2+}$:$M^{3+}$ ratio

| | Mg:Al | Ca:Al | Ca:Al | Zn:Al | Zn:Al | Cu:Al | Cu:Al |
|---|---|---|---|---|---|---|---|
| | 3:1 | 3:2:1 | 2:1:0 | 1:1 | 1:1 | 2:1 | 4:1 |
| MgO | 33.79 | - | - | - | - | - | - |
| CaO | - | 25.93 | 35.89 | - | - | - | - |
| $CaCO_3$ | - | 10.58 | - | - | - | - | - |
| ZnO | - | - | - | - | 26.99 | - | - |
| $Zn_5(CO_3)_2(OH)_6$ | - | - | - | 30.69 | - | - | - |
| $Cu_2(OH)_2CO_3$ | - | - | - | - | - | 38.97 | 44.91 |
| $Al(OH)_3$ | 18.75 | 15.91 | 16.60 | 21.77 | 25.78 | 13.75 | 7.92 |
| $H_2O$ | 472.82 | 471.76 | 472.39 | 472.23 | 474.53 | 474.57 | 475.49 |

## 5.4 Cleaning Procedure

The selected cleaning procedure was conducted at the end of each experimental run.

1. Beads were rinsed repeatedly with water after collection. The water was decanted at the end of each rinse until the water was observed to be clear.
2. The milling chamber was rinsed and scrubbed with a brush, however was not dissasembled. Deconstruction of the milling chamber was observed to result in damage to the vessel and components.
3. The front cap was washed and reassembled to the milling chamber. The mill was reloaded with the rinsed beads and filled with water. Milling commenced for 15 min at a speed of 2000 rpm.
4. The media was collected and water decanted. The milling chamber was then reloaded for the next experimental run.

# 6 Results and Discussion

Qualitative X-ray diffraction (XRD) analysis was selected as the primary analytical technique for the identification of the LDH phase. Primary peaks associated with the LDH material as well as that of the raw materials were indicated with the use of a dashed line as well as the relevant label. Fourier transform infrared spectroscopy (FT-IR) analysis was conducted to support XRD data obtained. X-ray fluoresence (XRF) was selected to identify impurities within the system. The change in particle size and morphology were observed making use of particle size analysis (PSA) and scanning electron microscopy (SEM).

## 6.1 Parameter study

### 6.1.1 Rotational speed

**XRD analysis** The rotational speed was varied between 1000 rpm, 2000 rpm and 3000 rpm for a cooling water inlet temperature of approximately 30 °C. Figure 22 depicts the XRD spectra obtained for samples synthesised at each of the selected rotational speeds.

The primary observations made were as follows:

1. The peak intensity for MgO and $Al(OH)_3$ decreased with an increase in rotational speed. It was noted that the decrease for $Al(OH)_3$ was more pronounced than that of MgO, with no $Mg(OH)_2$ peaks identified. This could be attributed to the exposure of the MgO to high temperatures prior to purchase, as well as the selected calcination step. The reactivity of MgO is strongly influenced by calcination temperature and time (Ropp, 2013). Similarly the hydration rate for MgO to $Mg(OH)_2$ is low at low temperatures (Rocha et al., 2004). It should be noted that the dissolution of the raw materials could be influenced by the selected synthesis conditions. Factors such as solubility, dissolution rate and mixing kinetics could contribute to the discrepencies observed.

   The pH of the system, in combination with factors such as temperature, concentration and pressure, influence the raw material phases present within the sample. Although not measured, the pH of the system was expected to be alkaline due to pH values of MgO (10-11) and $Al(OH)_3$ (7). It has been reported that the only stable form of aluminium in alkaline solution are aluminates (Zorn & Kaminski, 2015). The $Al(OH)_3$ reacts with $OH^-$ to form the $Al(OH)_4^-$ phase, which could then wash out of the system. This would therefore contribute to the decrease in $Al(OH)_3$ peak intensity observed. More research should be conducted, through pH measurements, to determine the extent at which these factors influence the results obtained. This is true for all experiments conducted.

   Higher rotational speeds may directly influence the amount of energy available for transfer to heat or chemical energy (Ranu & Stolle, 2015). Similarly the chemical activation of raw materials may increase with an overall increase in the impact energy and number of collisions. This could therefore result in the increase in conversion of raw materials to an amorphous LDH precursor or mixed metal oxides, with an increase in the rotational speed.

2. The peak intensity of the inert material $SiO_2$ decreased with an increase in rotational speed. This implies that the overall decrease in peak intensity observed for all materials could be due to an increase in amorphitisation. Higher operational speeds directly influence the kinetic energy associated with the media and particles within the system. This results in a greater amount of high energy impacts within a set time frame (Ranu & Stolle, 2015). Particle degradation should therefore increase with an increase in the rotational speed, resulting in a greater degree of amorphitisation.

   The physical properties associated with the individual solid raw materials may also influence their individual rate of amorphitisation. The hardness associated with

$Al(OH)_3$ varies between 2.5 and 3 on the Moh's hardness scale (Mindat, 2019a). Comparitively periclase (MgO) has a recorded hardness of 5.5 (Mindat, 2019b). It should be noted that the hardness of caustic MgO was expected to vary from that of periclase, however data was not readily available to confirm the exact numerical measurement. Grinding of the $Al(OH)_3$ could therefore occur from both the milling media and that of MgO.

3. Minor primary LDH peaks could be construed as being present for each of the selected rotational speeds. No clear trend was observed and LDH peaks were not clearly identifiable. It is possible that amorphous LDH precursor formation occurs due to the changes in raw material peaks observed, however could not be identified through XRD analysis. Similarly minor quantities of LDH or amorphous mixed metal hydroxides could be present within the sample, however difficult to identify through XRD analysis.

Measured system temperatures are summarised in Table 9. The power input varied at measured values of 0.49 kW, 1.09 kW and 1.57 kW for speeds of 1000 rpm, 2000 rpm and 3000 rpm respectively. Assuming a steady flow system the total energy removed through cooling water was calculated from Equation 8, where $\dot{Q}$ represents the rate of net heat transfer in and out of the control volume ($kJ \cdot s^{-1}$), $\dot{m}$ the mass flowrate ($kg \cdot s^{-1}$), $\Delta T$ the difference in temperature (K) and Cp is the heat capacity ($kJ \cdot kg^{-1} \cdot K^{-1}$) (Cengel & Ghajar, 2015). Heat capacity is a function of temperature and can be described by Equation 9 (Perry & Green, 2008), where Cp represents the heat capacity of a liquid ($J \cdot kmol^{-1} \cdot K^{-1}$), $C_1$ through to $C_5$ are constants summarised in Table 8 and T is the temperature (K). The difference in calculated heat capacity values for the maximum and minimum measured jacket water temperatures, for all experiments conducted, equated to approximately 0.1 %. Heat capacity was therefore assumed to remain relatively constant and calculated with the use of the measured inlet temperature. A constant density of water of 1 $kg \cdot l^{-1}$ was assumed. Assumptions were true for all heat related calculations throughout the study. Calculated values are as summarised in Table 7.Heat removed by the cooling water was calculated to be 0.19 kW, 0.52 kW and 0.62 kW for each of the selected speeds. System temperature was observed to increase with an increase in the rotational speed. This was expected due to an increase in kinetic energy, friction and grinding activity. The changes in temperature may influence raw material solubility as well as increase the rate of conversion of raw materials to reaction products.

$$\dot{Q} = \dot{m} Cp \Delta T \tag{8}$$

$$Cp(liquid) = C_1 + C_2 T + C_3 T^2 + C_4 T^3 + C_5 T^4 \tag{9}$$

**Table 7:** Summary of calculated parameters associated with the heat removed by jacket water with a change in rotational speed. Samples were synthesised at a jacket water inlet temperature of approximately 30 °C

| Speed [rpm] | T1 [K] | T2 [K] | Molar Flow [kmol·h$^{-1}$] | Cp [J·kmol$^{-1}$·K$^{-1}$] | Cp [kJ·kmol$^{-1}$·K$^{-1}$] | Q [kJ·h$^{-1}$] | Q [kJ·s$^{-1}$] |
|---|---|---|---|---|---|---|---|
| 1000 | 303.73 | 304.04 | 28.89 | 75308.45 | 75.31 | 674.46 | 0.18 |
| 2000 | 302.98 | 303.84 | 28.96 | 75316.94 | 75.32 | 1875.71 | 0.52 |
| 3000 | 303.79 | 304.81 | 29.09 | 75307.79 | 75.31 | 2234.39 | 0.62 |

**Table 8:** Heat capacity constants as described by (Perry & Green, 2008)

| Constant | Numeric Value |
|---|---|
| $C_1$ | 276370 |
| $C_2$ | -2090.1 |
| $C_3$ | 8.125 |
| $C_4$ | -0.014116 |
| $C_5$ | 9.3701E-06 |

**Table 9:** Average temperature and flowrate measurements obtained for Mg-Al LDH samples synthesised with a change in rotational speed, at a cooling water inlet temperature of 30 °C.

| Rotational Speed [rpm] | Flow rate [L·h$^{-1}$] | Inlet [°C] | Outlet [°C] | Reactor [°C] |
|---|---|---|---|---|
| 1000 | 520.01 | 30.58 | 30.89 | 31.17 |
| 2000 | 521.25 | 29.83 | 30.69 | 33.07 |
| 3000 | 523.59 | 30.64 | 31.66 | 37.49 |

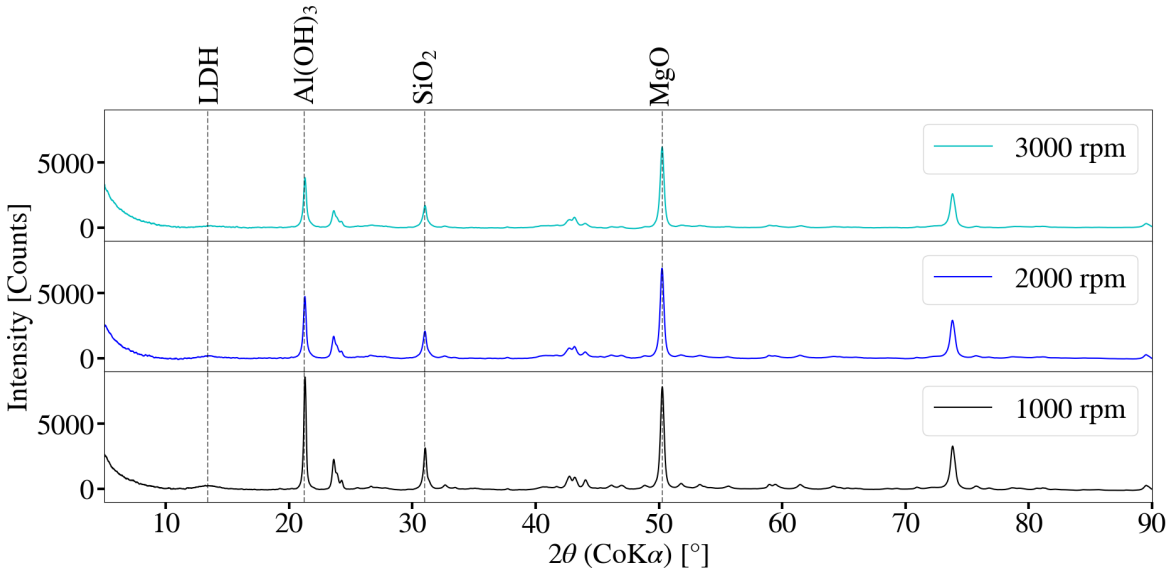


**Figure 22:** XRD spectra for Mg-Al LDH samples synthesised at a cooling water inlet temperature of 30 °C, with a change in rotational speed.

**FT-IR analysis** Figure 23 depicts the FT-IR spectra for each of the selected rotational speeds. Minor differences were observed between samples synthesised with a change in rotational speed. Peaks were observed between 3300 cm$^{-1}$ and 3700 cm$^{-1}$. These could be attributed to bonded and free -OH within each sample (Nicolet, 2019). This was expected as the samples were a mixture of oxides, hydroxides and possibly minor quantities of LDH. Carbonate contamination was observed with sharp peaks at 1366 cm$^{-1}$. This is possibly indicative of the $CO_3^{2-}$ v3 antisymmetric vibrations (Labuschagne et al., 2015) commonly identified within LDH structures. Atmospheric carbonate contamination was expected as synthesis, as well as drying, was conducted under atmospheric conditions. The peaks observed at 1099 cm$^{-1}$ could be attributed to a Si-O interaction (Socrates, 2001) (Nicolet, 2019) as a result of $SiO_2$ present within the starting MgO. The peaks observed at 1020 cm$^{-1}$ could further corroborate carbonate present within the sample (Socrates, 2001). Peak intensity was observed to decrease with an increase in the rotational speed. Peak intensity is indicitive of the amount of a specific bonds present within

the sample (Harding, 2019). A possible suggestion for the observed increase in transmittance (decrease in peak intensity) could be that an increase in rotational speed results in an increase in the degree of amorphitisation aswell as the destruction of chemical bonds.

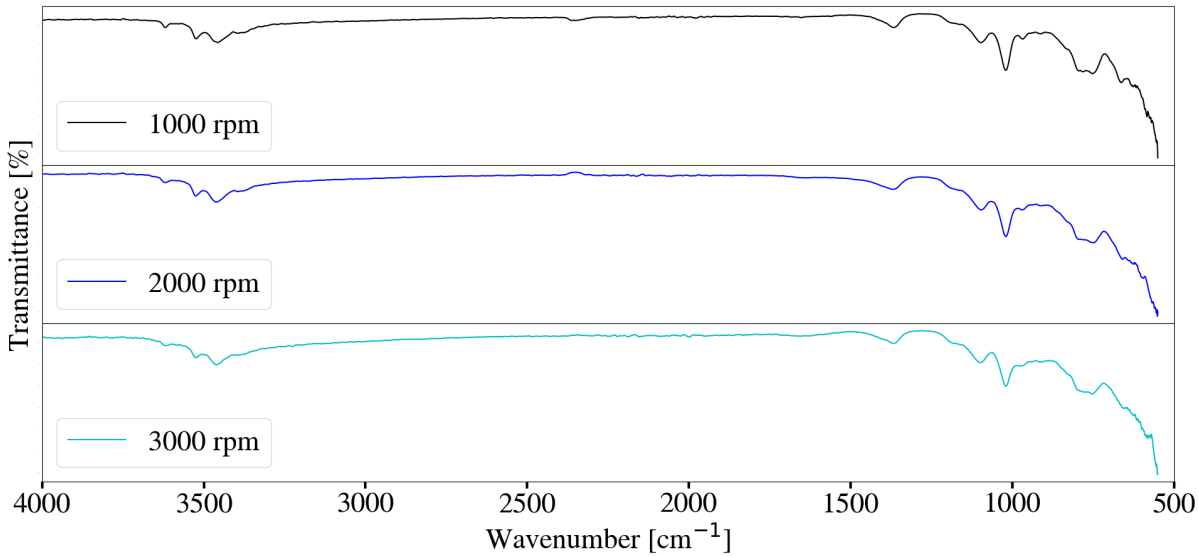


**Figure 23:** FT-IR spectra for Mg-Al LDH samples synthesised at a cooling water inlet temperature of 30 °C, with a change in rotational speed.

**XRF analysis** Table A.31 depicts the mass composition of each sample obtained at a selected rotational speed. Degradation of the milling media and chamber was observed to occur with an increase in the operational speed. The chemical composition of any LDH samples within the system could not be estimated through XRF analysis due to the presence of amorphous material.

Impurities within the mill could be a result of various differing factors such as mill degradation, bead degradation and the retention of chemical compounds from any previous run conducted. Although washing of the mill was conducted after each experimental run, it was deemed impossible to ensure that no additional chemical impurities were retained after each run, without excessive stripping of the milling chamber and components. Cross contamination was therefore possible for each run conducted throughout this study. Mass percentages obtained coincide with the selected $M^{2+}$:$M^{3+}$ ratio of 2:1.

It was observed that the impurities such as $Fe_2O_3$, $Cr_2O_3$, NiO, $ZrO_2$, $MoO_3$ and $Y_2O_3$ were present within each sample. This was expected as sample discolouration increased from a light to a dark grey. The estimated error for impurities should be taken into consideration when attempting to identify trends within the system ith regards to impurities.

LDH formation results in the presence of crystal water as well as $OH^-$ anions within the interlayer. This is lost upon ignition forming part of the LOI value. The overall amount

of volatiles (OH groups) within the system could increase upon the formation of LDH ($Mg_4Al_2(OH)_{12}CO_3{\cdot}4H_2O$ and $Mg_4Al_2(OH)_{14}{\cdot}XH_2O$ ), when compared to the starting MgO and $Al(OH)_3$ mixture.

**Particle Size analysis** Particle size analysis was conducted at the end of each of the experimental runs to determine whether a change in the milling speed would have a drastic effect on the measured $D_{90}$, $D_{50}$ and $D_{10}$ values obtained. Table 10 summarises the particle sizes obtained after 1 h of milling for a change in rotational speed. Similarly the distributions obtained are indicated in Figure 24. The distribution was observed to be bi-modal, with primary modes between 1 $\mu$m and 10 $\mu$m and a smaller secondary mode between 0.1 $\mu$m and 1 $\mu$m. Bi-modal distributions could indicate the existence of two distinct populations that result from a different source (Bunte & Abt, 2001). It was hypothesised that the formation of minor quantities of LDH could contribute to the phenomenom observed. This is corroborated by the results obtained in Section 6.1.5. Raw materials exhibited a multimodal distribution with dominant mode between 1 $\mu$m and 10 $\mu$m, which should be true for all samples throughout the study. Although synthesis conditions differ between experimental sets, the formation of LDH was observibly clear at elevated temperatures and retention times. The particle size distribution was observed to change from a bi-modal distribution, with a primary mode between 1 $\mu$m and 10 $\mu$m to that with a primary mode between 0.1 $\mu$m and 1 $\mu$m. This was noted to coincide with changes observed in XRD patterns depicted in Figure 40. Although LDH synthesis was unclear for the relevant samples as seen by XRD patterns in Figure 22, the presence of amorphous precursor or minor quantities of poorly crystalline LDH could contribute to the relevant distributions. No obvious trends were observed, other than minor differences in the bi-modal distributions obtained.

It should be noted that greater rotational speeds resulted in an increase in the concentration of $Fe_2O_3$ and $ZrO_2$ contaminants within the system. This is evident by the XRF results depicted in Table A.31. This supports the notion that more grinding action is present when increasing the operational speed. The increase in contaminants present could influence the particle size distributions obtained and could therefore contribute in the discrepancies observed.

It could further be true that the with an increase in rotational speed, results an increase in reactor temperature as seen by Table 9, resulting in possible particle growth. The larger particle sizes for a speed 1000 rpm could also be the result of agglomeration, as observed by the agglomeration tail present in Figure 24. Reaction schemes, although not clear in the XRD spectra obtained in Figure 22, could further contribute to discrepancies observed as a result of the formation of new chemical species.

**Table 10:** Particle size measured for Mg-Al samples synthesised at a cooling water inlet temperature of 30 °C, with a change in rotational speed

| Rotational speed [rpm] | $D_{10}$ [$\mu$m] | $D_{50}$ [$\mu$m] | $D_{90}$ [$\mu$m] |
|---|---|---|---|
| 1000 | 0.924 | 3.84 | 8.63 |
| 2000 | 0.962 | 3.39 | 6.21 |
| 3000 | 1.99 | 4.12 | 7.33 |

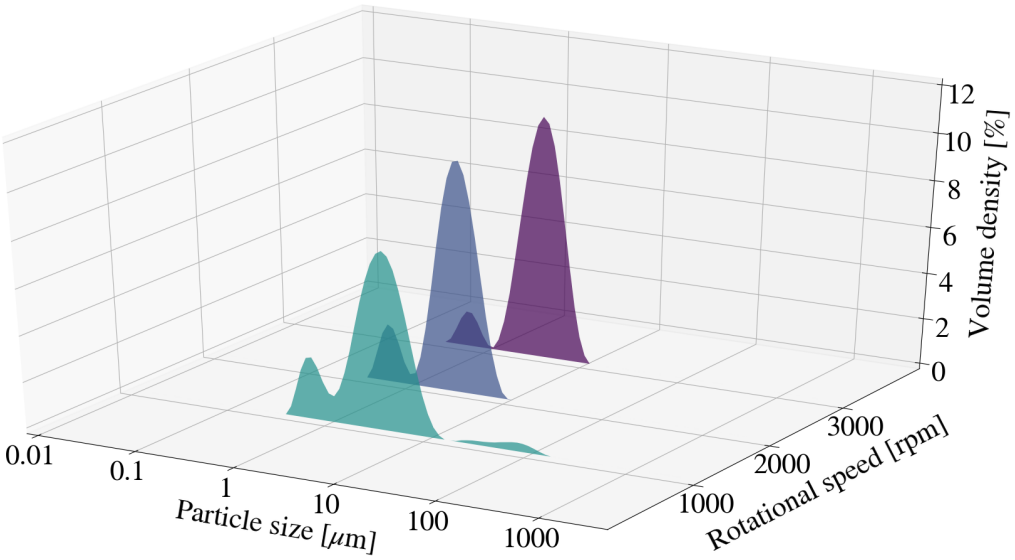


**Figure 24:** Particle size distribution for Mg-Al LDH samples synthesised at a cooling water inlet temperature of 30 °C, with a change in rotational speed.

### 6.1.2 Retention time

The XRD spectra for samples synthesised with a change in retention time, at a cooling water inlet temperature of 30 °C and rotational speed of 2000 rpm, is depicted in Figure 25. Key observations made were as follows:

1. The peak intensity of $Al(OH)_3$ and MgO decreased with an increase in retention time. The peak intensity of $Al(OH)_3$ was further observed to decrease at a greater rate than that of MgO, with no $Mg(OH)_2$ peaks observed. This likely attributed to the reactivity of the MgO as described in Section 6.1.1.

   The increase in retention time increases the amount of particle-particle and particle-media collisions that occur (Ranu & Stolle, 2015), increasing the amount of reactive sites available. The decrease in peak intensity for both raw materials could therefore further be a result of conversion to amorphous mixed metal hydroxides/oxides, a amorphous LDH precursor or minor quantities of LDH within the sample.

2. The $SiO_2$ peaks were found to decrease with an increase in retention time. This could once-again be due to an increase in the degree of amorphitisation. Extended perods of milling activity result in an increase in the amount of collisions that occur within the chamber (Ranu & Stolle, 2015), reducing the crystallinity of the $SiO_2$. The rate of amorphitisation for each of the individual raw materials could once-again be influenced by their physical properties, as described in Section 6.1.1.

3. A decreasing trend in the primary LDH peak intensity was observed with an increase in retention time. Minor peaks were present at retention times of 1 h and 2 h of milling activity at $2\theta$ values of 13.50° and 13.54° respectively. No clear LDH peak was observed after a retention time of 3 h. This is likely due to an increase in the degree of amorphitisation or possible destruction of the LDH structure. This is corroborated by the reduction in peak intensity of the inert $SiO_2$.

4. A $CaCO_3$ peak was identified to be present after 3 h of milling. This is likely due to contamination within the milling chamber. The milling process was observed to be 'dirty', with limitations associated with the cleaning of the milling chamber and components.

Temperature and flowrate measurements associated with each experimental run is depicted in Table 11. The energy transferred to the cooling water was calculated as described in Section 6.1.1, using Equations 8 and 9, to be 0.38 kW, 0.44 kW and 0.46 kW for retention times of 1 h, 2 h and 3 h respectively. Calculated values associated with heat removed from the system is as summarised in Table 12.

**Table 11:** Average temperature and flowrate measurements obtained for Mg-Al LDH samples synthesised with a change in retention time, at a cooling water inlet temperature of 30 °C.

| Retention Time [h] | Flow rate [L·s$^{-1}$] | Inlet [°C] | Outlet [°C] | Reactor [°C] |
|---|---|---|---|---|
| 1 | 521.73 | 29.30 | 29.93 | 31.79 |
| 2 | 518.33 | 29.16 | 29.89 | 32.14 |
| 3 | 519.32 | 29.05 | 29.82 | 32.25 |

**Table 12:** Summary of calculated parameters associated with the heat removed by jacket water for a change in retention time. Samples were synthesised at a jacket water inlet temperature of approximately 30 °C

| Time [h] | T1 [K] | T2 [K] | Molar Flow [kmol·h$^{-1}$] | Cp [J·kmol$^{-1}$·K$^{-1}$] | Cp [kJ·kmol$^{-1}$·K$^{-1}$] | Q [kJ·h$^{-1}$] | Q [kJ·s$^{-1}$] |
|---|---|---|---|---|---|---|---|
| 1 | 302.45 | 303.08 | 28.99 | 75323.25 | 75.32 | 1374.44 | 0.38 |
| 2 | 302.31 | 303.04 | 28.80 | 75324.96 | 75.32 | 1583.42 | 0.44 |
| 3 | 302.20 | 302.97 | 28.85 | 75326.32 | 75.33 | 1673.43 | 0.46 |

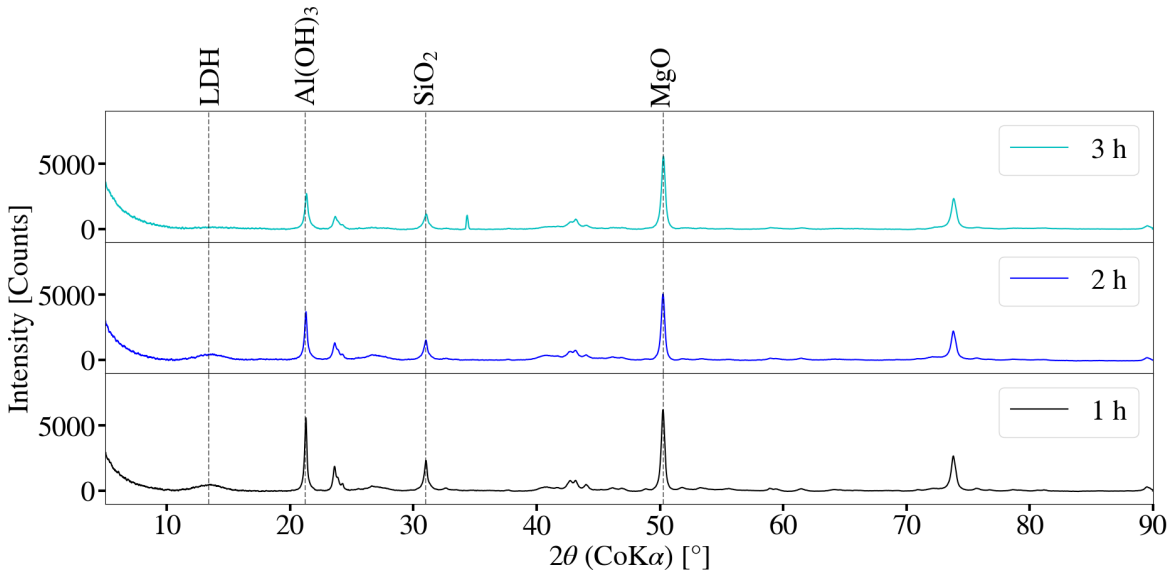


**Figure 25:** XRD spectra for Mg-Al LDH samples synthesised for retention times of 1 h, 2 h and 3 h, at a cooling water inlet of temperature 30°C and a rotational speed of 2000 rpm.

**FT-IR analysis** Figure 26 depicts the FT-IR spectra for each sample with a change in retention time. The spectra were observed to be similar to those with a change in rotational speed. The percentage transmittance was observed to increase (peak intensity decreased) with an increase in the retention time for the overall spectra. This could once-again be due to the possible destruction of chemical bonds, as described in Section 6.1.1, with an increase in retention time. Peaks observed between 3300 $cm^{-1}$ and 3700 $cm^{-1}$ are likely due to bonded and free -OH within the sample (Nicolet, 2019). Carbonate interactions were visible with peaks at approximately 1366 $cm^{-1}$ for all samples obtained (Dudeka et al., 2012) (Labuschagne et al., 2015). The Si-O interaction was once-again noted with a peak around 1099 $cm^{-1}$.

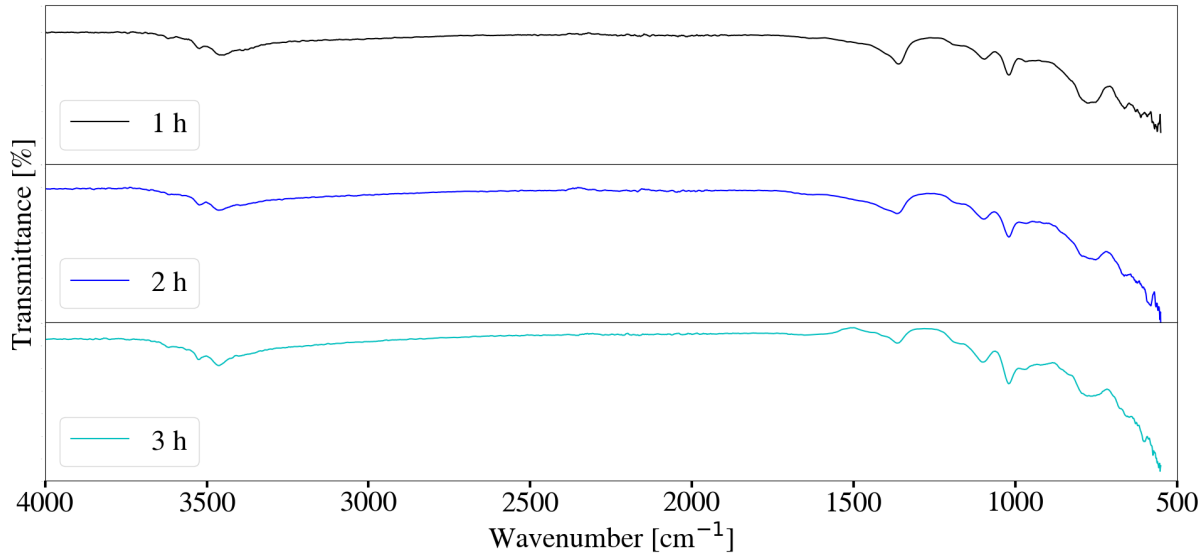


**Figure 26:** FT-IR spectra for Mg-Al LDH samples synthesised for retention times of 1 h, 2 h and 3 h, at a cooling water inlet of temperature 30°C and a rotational speed of 2000 rpm.

**XRF analysis** An increase in retention time implies an increase in milling activity with time (Ranu & Stolle, 2015). This was therefore expected to result in an increase in the concentration of impurities associated with both mill degradation and trapped chemical species. Sample discolouration was observed from a light grey to that of a dark metallic grey with an increase in residence time.

Data obtained through XRF analysis for a change in retention time is depicted in Table A.32. The concentrations for impurities associated with bead and mill degradation such as $Fe_2O_3$, $Cr_2O_3$, $ZrO_2$, $MoO_3$ and $Y_2O_3$ were once again noted to be present for each sample. This was expected as increased retention time results in an increase in the amount of grinding activity, therefore a further increase in the amount of degradation.

**Particle Size analysis** Figure 27 depicts the change in particle size with time. The $D_{90}$, $D_{50}$ and $D_{10}$ values of the original MgO and $Al(OH)_3$ mixture were measured to be 17.20 $\mu$m, 7.10 $\mu$m and 1.96 $\mu$m respectively. It was noted that the $D_{50}$ and $D_{10}$ values seemingly plateaued after approximately 40 min of milling activity, below 3 $\mu$m and 0.80 $\mu$m respectively. Comparatively the $D_{90}$ value remained relatively constant, below a value of 5 $\mu$m, after 50 min of milling with little change observed for the remainder of the experimental run. The final numerical values obtained after 3 h of milling for the relevant $D_{90}$, $D_{50}$ and $D_{10}$ were 4.48 $\mu$m, 2.51 $\mu$m and 0.757 $\mu$m.

The particle size distribution with time for 3 h of milling activity is depicted in Figure 28. The raw material distribution was observed to be multimodal, with a dominant mode between 1 $\mu$m and 10$\mu$m. Raw materials were added to the milling chamber as dry powders. They were then dispersed for 60 s at the selected synthesis conditions before a sample was taken. The mode located between 10 $\mu$m and 100 $\mu$m was likely the result of agglomeration. Comparatively, the minor mode between 0.1 $\mu$m and 1 $\mu$m appears to have just started to develop. This mode continues to develop with time, however seems to slow down after 30 min of milling activity. As described in Section 6.1.1, this fine particle distribution could be the result of LDH formation within the system. Little change was observed in the shape of the bi-modal distribution after 40 min with the exception of minor agglomeration tails between 10 $\mu$m and 100 $\mu$m. Agglomerates could result from the collected sample being stagnant for a short time period. The distributions became more narrow and sharp with an increase in milling time. This was expected as particle size reduction was noted to occur in Figure 27. It is further possible for the presence of contaminants such as $Fe_2O_3$ and $ZrO_2$ to influence the particle size distributions obtained.

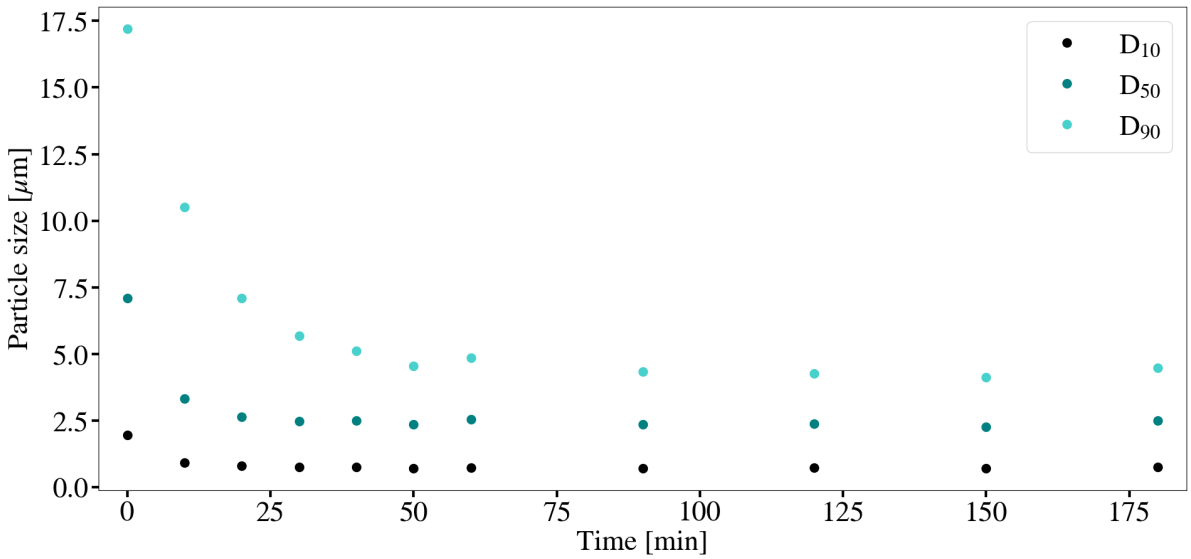


**Figure 27:** The change in particle size with time for Mg-Al LDH samples synthesised at a cooling water inlet temperature of 30 °C, with a change in retention time.

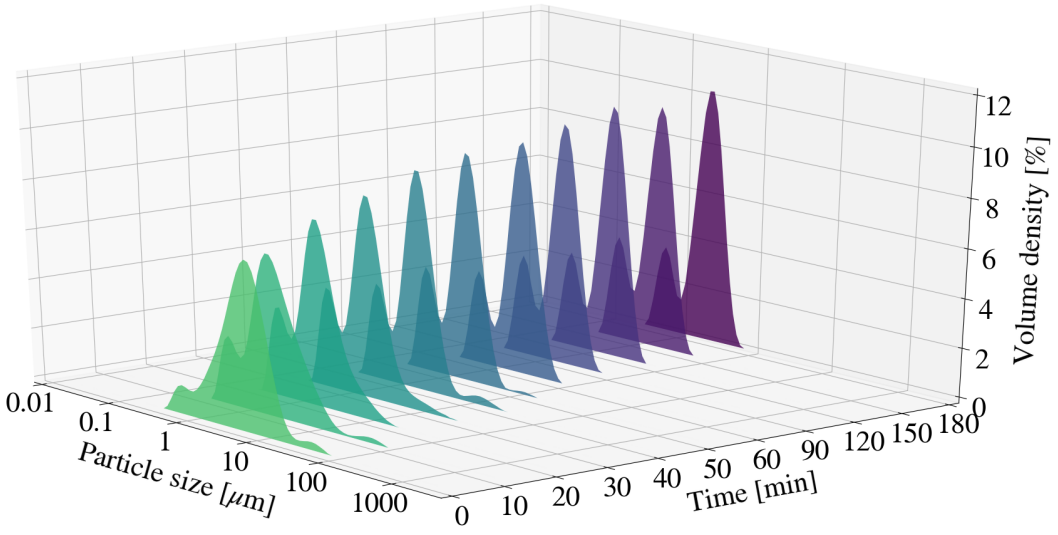


**Figure 28:** Particle size distribution for Mg-Al LDH samples synthesised at a cooling water inlet temperature of 30 °C, with a change in retention time.

**SEM imaging** SEM imaging, depicted in Figures 29, 30 and 31, was conducted to provide insight on the change in morphology of the sample with a change in retention time. It was noted that the samples became increasingly more amorphous with an increase in the retention time. This is supported by the loss of structure, i.e softening of edges, of the particles with time.

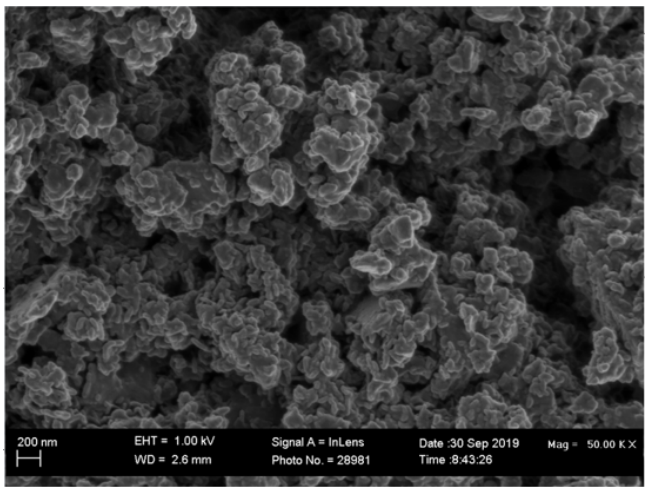


**Figure 29:** SEM imaging of Mg-Al LDH sample after 1 h of milling at a cooling water inlet temperature of 30 °C and rotational speed of 2000 rpm.

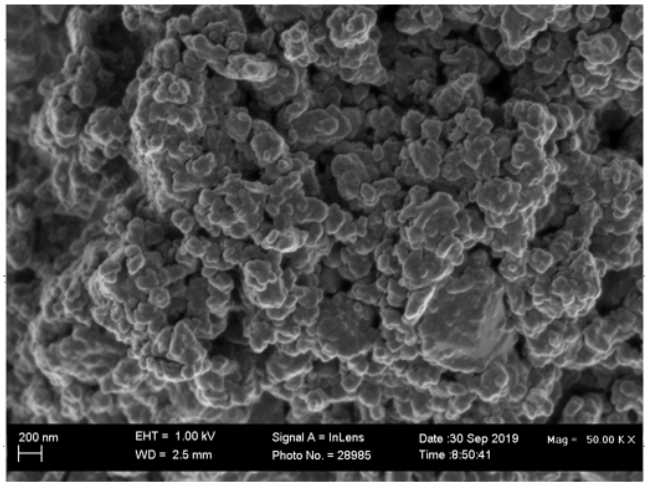


**Figure 30:** SEM imaging of Mg-Al LDH sample after 2 h of milling at a cooling water inlet temperature of 30 °C and rotational speed of 2000 rpm.

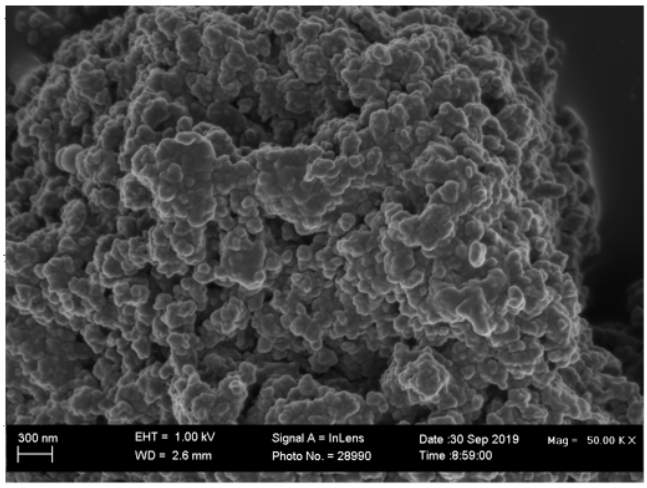


**Figure 31:** SEM imaging of Mg-Al LDH sample after 3 h of milling at a cooling water inlet temperature of 30 °C and rotational speed of 2000 rpm.

### 6.1.3 Solids loading

**XRD analysis** Figure 32 depicts the XRD spectra for samples synthesised at solids loadings of 10 %, 20 % and 30 %, at a cooling water inlet temperature of 30 °C and operational speed of 2000 rpm. The primary observations were as follows:

1. The $SiO_2$ peaks were found to be smallest for a 10 % solids loading, with little difference observed between samples synthesised at a 20 % and 30 % loading. This could be due to the change in solids loading directly influencing the volume of solids within the vessel. Higher solids loading's could result in a greater amount of solid-solid interaction and collisions. Similarly too high a solids loading could result in no

movement and therefore no transfer of kinetic energy (Ranu & Stolle, 2015). The grinding action therefore decreases with an increase in the solids loading. Figure 33 depicts a photograph of the sample for a solids loading of 30 %. The slurry was observed to be thick and viscous supporting the notion that grinding efficiency reduces if the solids loading is too great. The implied trend, although not obvious here, would be that the grinding efficiency passes through a maximum, after which grinding activity reduces drastically.

2. No obvious trend was observed for MgO peaks present within the sample. The peaks associated with $Al(OH)_3$ was lowest for a loading of 10 % and and greatest for that of 20 %. Little change in the MgO could be attributed to its reactivity, as well as a decrease in the grinding efficiency with an increase in solids loading. This could be further be true for the differences observed in peak intensity of $Al(OH)_3$, with grinding of the raw material being greatest at the lower solids loading (10 %).

3. Minor LDH peaks were observed to be present for solids loadings of 20 % and 30 % at $2\theta$ values of 13.40° and 13.33° respectively. No obvious peak was observed for the sample synthesised at a 10 % solids loading and no clear trend was evident. Due to the possible decrease in grinding efficiency with an increase in solids loading, the degree of amorphitisation and structural degradation could therefore be greater at the lower solids loadings. This could result in amorphous LDH precursor material, minor quantities of LDH, or an amorphous mixture of oxides and hydroxides present within the sample that are not easily identifiable through XRD analysis. It should be worth noting that the concentration of LDH in samples synthesised at higher solids loadings could be higher than the 10 % sample due to a higher concentration of raw materials available for reaction.

Average temperatures measured for each of the selected solids loading's are summarised in Table 13. Table 14 summarises the relevant calculated values associated with heat removed by the jacket water. The total energy removed from the system through cooling water was therefore calculated to be 0.37 kW and 0.36 kW for a loading of 20 % and 30 % respectively.

**Table 13:** Average temperature and flowrate measurements obtained for Mg-Al LDH samples synthesised with a change in solids loading, at a cooling water inlet temperature of 30 °C.

| Solids Loading [%] | Flow rate [$L \cdot h^{-1}$] | Inlet [°C] | Outlet [°C] | Reactor [°C] |
|---|---|---|---|---|
| 10 | 521.25 | 29.83 | 30.69 | 33.07 |
| 20 | 520.52 | 29.74 | 30.35 | 33.05 |
| 30 | 527.62 | 30.35 | 30.94 | 33.47 |

**Table 14:** Summary of calculated parameters associated with the heat removed by jacket water for a change in solids loading. Samples were synthesised at a jacket water inlet temperature of approximately 30 °C.

| Solids Loading [%] | T1 [K] | T2 [K] | Molar Flow [kmol·h$^{-1}$] | Cp [J·kmol$^{-1}$·K$^{-1}$] | Cp [kJ·kmol$^{-1}$·K$^{-1}$] | Q [kJ·h$^{-1}$] | Q [kJ·s$^{-1}$] |
|---|---|---|---|---|---|---|---|
| 10 | 302.98 | 303.84 | 28.96 | 75316.94 | 75.32 | 1857.71 | 0.52 |
| 20 | 302.89 | 303.50 | 28.92 | 75317.99 | 75.32 | 1328.56 | 0.37 |
| 30 | 303.50 | 304.09 | 29.31 | 75311.00 | 75.31 | 1302.44 | 0.36 |

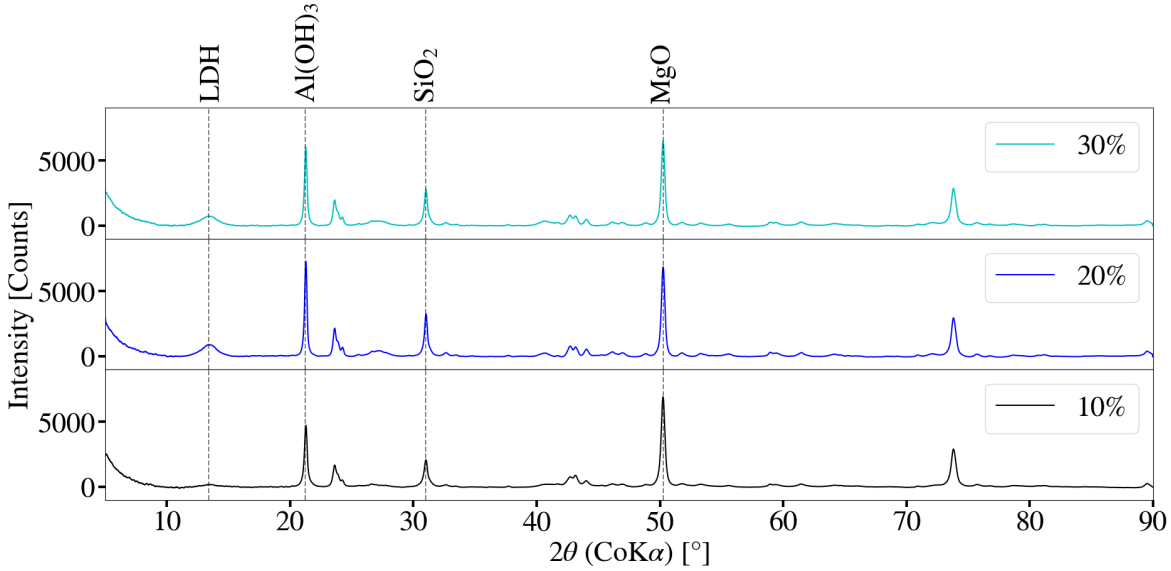


**Figure 32:** XRD spectra for Mg-Al LDH samples synthesised for solids loadings of 10 %,20 % and 30 %, at a cooling water inlet temperature of 30 °C at a rotational speed of 2000 rpm.

**Figure 33:** Photograph of Mg-Al LDH sample slurry with 30 % solids loading, post milling.

**FT-IR analysis** Figure 34 depicts the FT-IR spectra for samples synthesised with a change in solids loading. Differences between spectra were observed to be minor. As with previous samples analysed, peaks between 3300 $cm^{-1}$ to 3700 $cm^{-1}$ could be attributed to free and bonded -OH groups within the sample (Nicolet, 2019). This was expected as the sample contained unreacted raw materials, and possibly amorphous hydroxides and oxides. Similarly carbonate contamination was once again noted at 1366 $cm^{-1}$ (Dudeka et al., 2012) (Labuschagne et al., 2015).

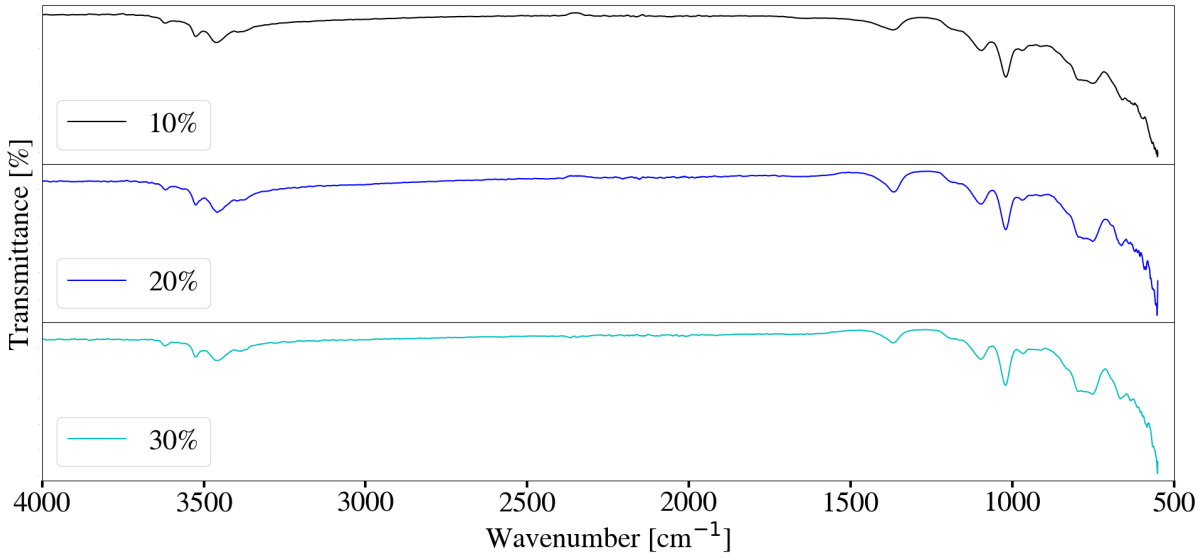


**Figure 34:** FT-IR spectra for Mg-Al LDH samples synthesised for solids loadings of 10 %,20 % and 30 %, for a cooling water inlet temperature of 30 °C at a rotational speed of 2000 rpm.

**Particle size analysis** The change in particle size associated with an increase in the solids loading is summarised in Table 15, similarly the change in distribution is depicted in Figure 35. A dominant mode was observed for eeach sample between 1 $\mu$m and 10 $\mu$m. A smaller mode was observed to occure between 0.1 $\mu$m and 1 $\mu$m and likely the result of LDH within the samples. Samples synthesised with a 20 % and 30 % solids loading depicted small modes between 10 $\mu$m and 100 $\mu$m, skewing the distributions and particle sizes obtained. These were likely the result of agglomerate formation and high sample viscosities. It is further possible that insufficient particle dispersion occured due to restricted movement within the milling chamber. Trends associated with the relevant $D_{90}$, $D_{50}$ and $D_{10}$ and distributions were therefore unclear. Particle size reduction could however be influenced by the increase in solids loading due to the decrease in grinding activity. This would result in little to no miling activity and therefore no drastic decrease in particle size. The particle size was observed to be smallest at a solids loading of 10 % and could be due to increased mobility and grinding efficiency.

**Table 15:** Particle size measured for Mg-Al samples synthesised at a cooling water inlet temperature of 30 °C, with a change in solids loading

| Solids Loading [%] | $D_{10}$ [$\mu$m] | $D_{50}$ [$\mu$m] | $D_{90}$ [$\mu$m] |
|---|---|---|---|
| 10 | 0.962 | 3.39 | 6.21 |
| 20 | 1.44 | 4.34 | 12.8 |
| 30 | 1.15 | 4.19 | 9.56 |

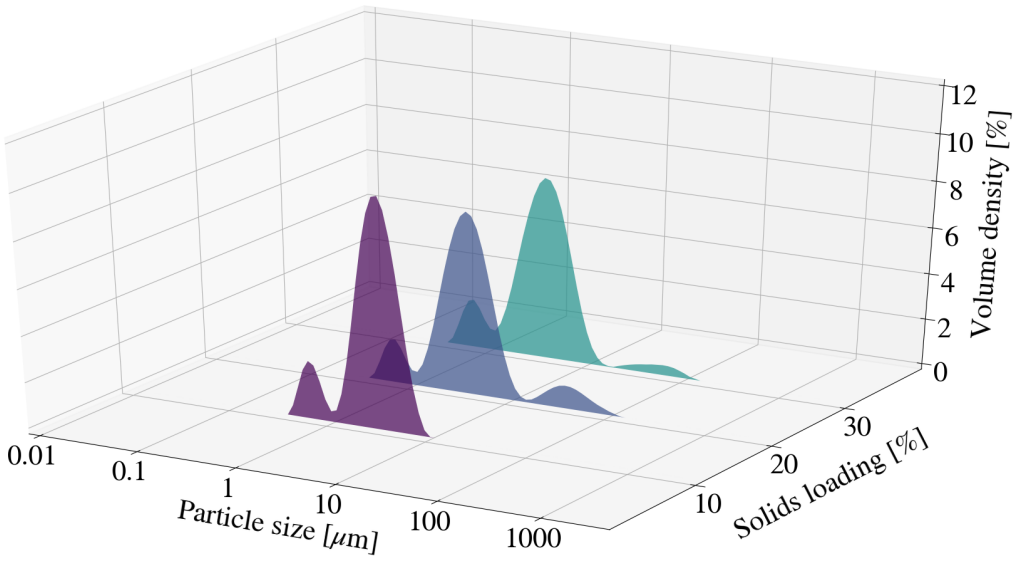


**Figure 35:** Particle size distribution for Mg-Al LDH samples synthesised for solids loadings of 10 %,20 % and 30 %, at a cooling water inlet temperature of 30 °C and a rotational speed of 2000 rpm

**XRF analysis** Table A.33 depicts the mass composition of samples obtained at different solids loadings. Concentrations of impurities associated with mill and bead degradation were expected to exhibited a decreasing trend with an increase in the solids loading. This could be due to a decrease in milling activity as movement of the media becomes restricted with an increase in the viscosity of the slurry. The impurities $P_2O_5$, MnO and $K_2O$. were likely attributed to retained chemical species within the milling chamber.

### 6.1.4 Bead Size

**XRD analysis** The XRD spectra for the Mg-Al LDH sample synthesised with a bead size of 0.25 mm, at a cooling water inlet temperature of 30 °C and rotational speed of 2000 rpm, is depicted in Figure 36. This was plotted along side that of a Mg-Al LDH sample synthesised at the same conditions, however making use of the 2 mm beads. Key observations were as follows:

1. Little difference was observed when comparing peak intensities associated with $Al(OH)_3$ for the selected media sizes. Comparatively the peak intensity for MgO decreased with a decrease in the media size.

   The volume of the bead loading was kept constant at approximately 60 % by volume, with masses of 2.57 kg and 2.52 kg measured for the 2 mm and 0.25 mm beads, respectively. Masses were observed to be similar with 2 mm beads having a greater mass than that of the 0.25 mm beads. The energy (stress energy) transferred to the mixed oxide-hydroxide slurry is proportional to the impact energy and the collision frequency. For a constant media mass the collision frequency and number of stress events is directly proportional to the number of grinding bodies and inversly proportional to their size. The probability for collisions therefore increases with a decrease in the media size (Ranu & Stolle, 2015). The reactive surface area would therefore have increased with a decrease in particle and bead size. The hydration of MgO to $Mg(OH)_2$ would therefore occur more readily. This would then further result in LDH formation as seen by a minor LDH peak observed at a 2 $\theta$ value of 13.51°. No obvious peak was present for the sample synthesised using 2 mm beads. Possible factors that could influence the change observed is the change in grinding mechanism, mixing kinetics and solubility. More research should be conducted to determine the effect these factors have on the LDH formation reaction mechanism. An increase in the number of collisions could result in a

greater degree of amorphitisation. This is supported by the decrease in $SiO_2$ peak intensity observed.

Measured flowrates and temperatures for the system is as summarised in Table 17. The energy transferred was calculated to be 0.55 kW for a bead size of 0.25 mm and 0.52 kW for a size of 2 mm. Calculated parameters associated with the heat removed through jacket water is summarised in Table 16.

**Table 16:** Summary of calculated parameters associated with the heat removed by jacket water for a change in bead size. Samples were synthesised at a jacket water inlet temperature of approximately 30 °C

| Bead Size [mm] | T1 [K] | T2 [K] | Molar Flow [kmol·h$^{-1}$] | Cp [J·kmol$^{-1}$·K$^{-1}$] | Cp [kJ·kmol$^{-1}$·K$^{-1}$] | Q [kJ·h$^{-1}$] | Q [kJ·s$^{-1}$] |
|---|---|---|---|---|---|---|---|
| 0.25 | 303.88 | 304.78 | 29.34 | 75306.81 | 75.31 | 1988.55 | 0.55 |
| 2.00 | 302.98 | 303.84 | 28.96 | 75316.94 | 75.32 | 1857.71 | 0.52 |



**Table 17:** Average temperature and flowrate measurements obtained for Mg-Al LDH samples synthesised with a change in bead size, at a cooling water inlet temperature of 30 °C.

| Bead size [mm] | Flowrate [L·s$^{-1}$] | Inlet [°C] | Outlet [°C] | Reactor [°C] |
|---|---|---|---|---|
| 0.25 | 528.12 | 30.73 | 31.63 | 32.23 |
| 2.00 | 521.25 | 29.83 | 30.69 | 33.07 |

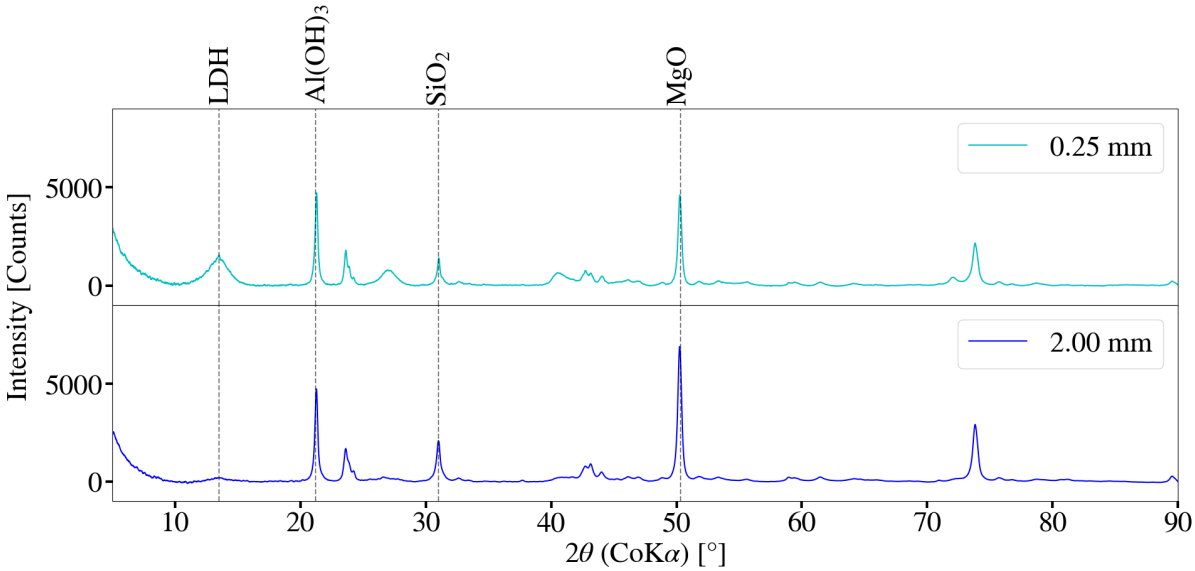


**Figure 36:** XRD spectra for Mg-Al LDH synthesised with a bead size of 0.25 mm, at a cooling water inlet temperature of 30 °C and rotational speed of 2000 rpm.

**FT-IR analysis** Figure 37 depicts the FT-IR spectra for samples synthesised with a change in media size. Both samples exhibited similar spectra. Peaks associated with free and bonded -OH stretching vibrations were once-again prevalent between 3300 $cm^{-1}$ to 3700 $cm^{-1}$ (Nicolet, 2019) (Tongamp, Zhang & Saito, 2007). It was noted that these peaks were broader, with a lower transmittance, for the sample synthesised using 0.25 mm beads. As could be seen by the XRD spectra, LDH peaks were more clearly identifiable than with that of the sample synthesised with 2 mm beads. The presence of LDH (Tongamp, Zhang & Saito, 2007) could have resulted in the discrepencies observed. Similarly carbonate contamination was once-again observed and to be expected at peaks around 1366 $cm^{-1}$ (Dudeka et al., 2012) (Labuschagne et al., 2015) and 1020 $cm^{-1}$ (Socrates, 2001) for both samples.

**Particle size analysis** The change in particle size with time is depicted in Figure 38. Prior to milling the $D_{90}$, $D_{50}$ and $D_{10}$ values of the solids mixture was measured to be 18.40 $\mu$m, 7.95 $\mu$m and 2.44 $\mu$m. Particle size degradation occured steadily with time reaching final values of 5.91 $\mu$m, 2.84 $\mu$m and 0.724 $\mu$m after 60 min of milling activity. This was observed to be smaller than final particle size measurements for the sample synthesised making use of 2 mm beads, with values measured at 6.21 $\mu$m, 3.39 $\mu$m and 0.962 $\mu$m. A decrease in media size should result in the decrease in steady-state average particle size (Williams et al., 2012) and would corroborate the differences observed.

The particle size distribution with a change in time is as depicted in Figure 39. A bi-modal distribution was observed to form after 10 min of milling activity, with raw materials

exhibiting a predominantly uni-modal distribution. A minor mode between 0.1 $\mu$m and 1 $\mu$m exists after raw materials were dispersed for 60 s within the milling chamber. The reduction in size from 2 mm to 0.25 mm results in an increase in the quantity of milling beads and therefore a substantial increase in the number of stress events within a set volume (Netzsch, 2009). This should subsiquently result in an increase in reactive surface area, ultimately resulting an in an increase in conversion of raw materials to reaction products. XRD analysis depicted in Figure 36 indicates that LDH synthesis was more prominant for samples synthesised with the use of a smaller media size. This would corroborate the notion that the formation of modes between 0.1 $\mu$m and 1 $\mu$m are the likely result of LDH formation as described in Section 6.1.1. It was further worth noting that the particle size measurements depicted in Figure 27 were similar to those depicted for a change in media size. Coupled with the formation of new chemical species, the presence of minor agglomeration tails make it difficult to determine the isolated effect of 0.25 mm beads on final particle size.

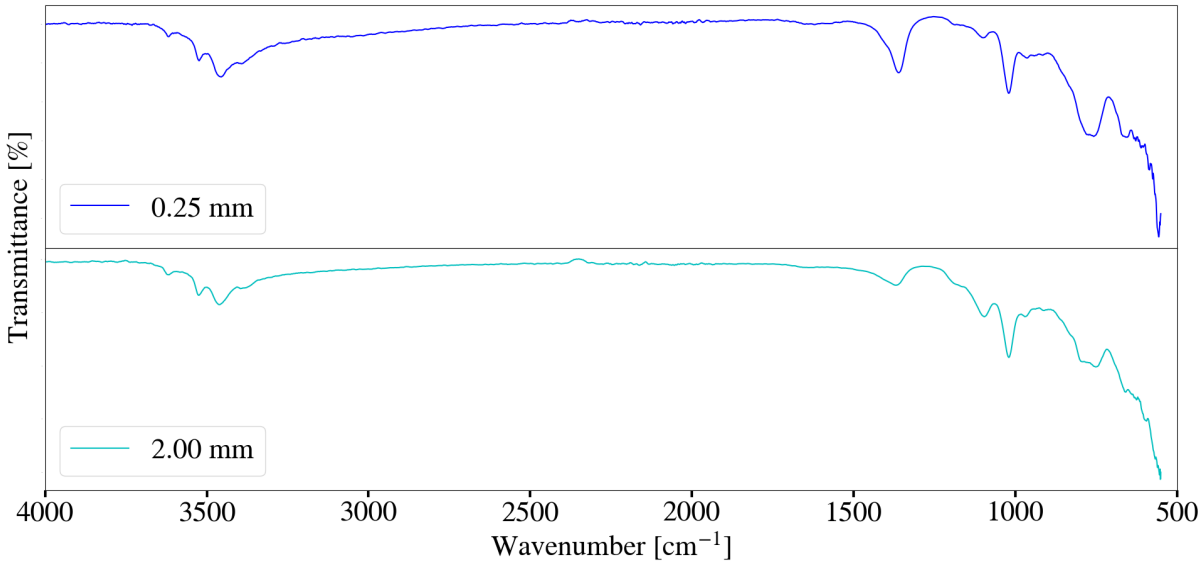


**Figure 37:** FT-IR spectra for Mg-Al LDH synthesised with a bead size of 0.25 mm, at a cooling water inlet temperature of 30 °C and rotational speed of 2000 rpm.

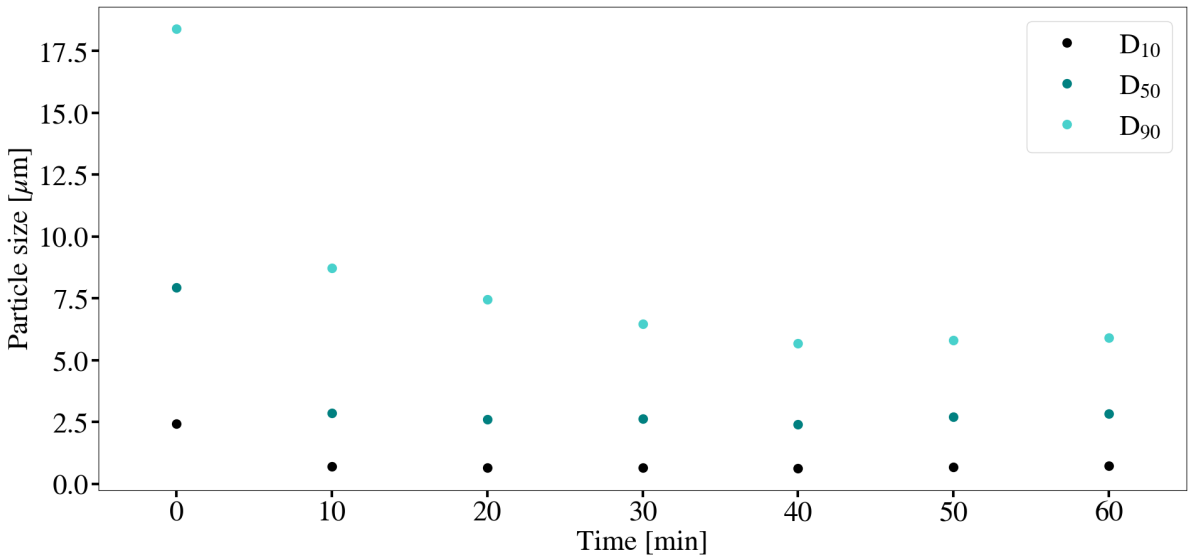


**Figure 38:** The change in particle size with time for Mg-Al LDH sample synthesised with a bead size of 0.25 mm, at a cooling water inlet temperature of 30 °C and rotational speed of 2000 rpm.

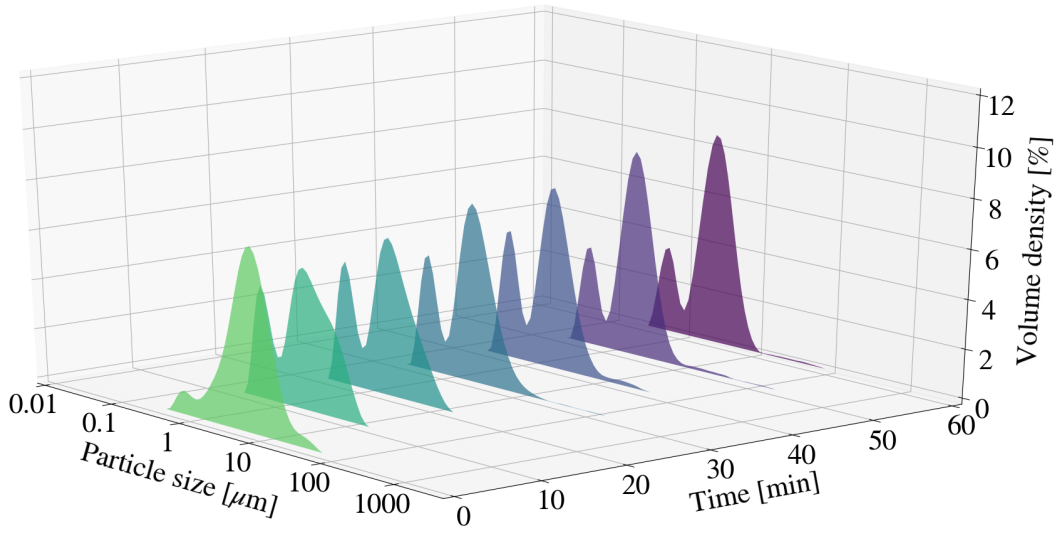


**Figure 39:** Particle size distribution for Mg-Al LDH sample synthesised with a bead size of 0.25 mm, at a cooling water inlet temperature of 30 °C, at a rotational speed of 2000 rpm.

**XRF analysis** The XRF data for the Mg-Al LDH sample synthesised with a bead size of 0.25 mm is summarised in Table A.34. The calculated $M^{2+}$:$M^{3+}$ ratio was determined to be 2.00:1.1 which coincides with the masses depicted in Section 5.2.

Bead and Mill degradation could once again be the result of impurities such as $Fe_2O_3$, $Cr_2O_3$, NiO, $ZrO_2$, $Y_2O_3$ and $MoO_3$. Other impurities present could further be attributed

to the retention of unwanted chemical species within the system as well as impurities within the selected raw materials. It was further noted that the recorded LOI value was approximately 32.71. Comparitively that of S2 was observed to lower at 22.33. This could once again be attributed to the quanitity of LDH present within the sample, with a more prominant LDH XRD spectra observed for the sample synthesised with the use of 0.25 mm beads.

### 6.1.5 Cooling water inlet temperature

The cooling water inlet temperature was varied, from 30 °C to that of 50 °C, for a change in retention time, at a set rotational speed of 2000 rpm. Similarly the increase in temperature was applied to a change in the rotational speed, for a set time of 1 h.

#### Retention time

**XRD analysis** The XRD spectra for samples synthesised with a change in retention time, at cooling water inlet temperature of 50 °C, is depicted in Figure 40. The primary observations made were as follows:

1. The peak intensity for MgO and $Al(OH)_3$ decreased with an increase in retention time. The decreasing trend was observed to be more drastic than for samples synthesised at a cooling water inlet temperature of 30 °C. Higher reactor temperatures result in an increase in the rate of reaction. The conversion of raw materials to LDH product would therefore occur more rapidly than with samples synthesised at lower temperatures. A study conducted by (Rocha et al., 2004) has indicated that higher temperatures for caustic MgO result in higher hydration rates, thus reaching equilibrium faster. The degree of supersaturation decreases with an increase in temperature. Once supersaturation has occured $Mg(OH)_2$ would precipitate at the surface of the MgO particle (Rocha et al., 2004). Hydration therefore becomes difficult due to the formation of a $Mg(OH)_2$ layer on the surface of the MgO particle, preventing further dissolution. This does however not include the addition of mechanical energy other than stirring. The grinding activity provided with the addition of milling media could result in the removal of the outer layer of $Mg(OH)_2$. This would expose the hidden MgO surface to allow for further reaction to $Mg(OH)_2$ and eventually LDH. This would also be true for experiments conducted at lower temperatures, however the rate of hydration is slow (Rocha et al., 2004), leading to low conversion despite continuous exposure of the MgO surface.

It could be possible that upon formation the $Mg(OH)_2$ immediately reacts to form the LDH phase. This could further explain the lack of $Mg(OH)_2$ peaks observed.

2. Broad primary LDH peaks were present for all samples synthesised at a jacket water inlet temperature of 50 °C. The peak intensity was observed to be greatest, at a $2\theta$ value of 13.80°, after 3 h of milling activity. The XRD spectra was observed to be more prominent than with samples synthesised at a cooling water inlet temperature of 30 °C. Longer retention times allow for an increase in the overall amount of collisions and therefore the amount of reactive sites. This would therefore result in an increase in the conversion of raw materials to LDH product. This is supported by the observed decrease in raw material peaks with an increase in retention time. The rate of LDH formation would be greater due to the elevated temperature. Furthermore studies associated with conventional synthesis methods have indicated that higher temperatures favor LDH formation (Rives, 2001). This would support the observed differences between samples synthesised at a greater jacket water inlet temperature and those at a lower temperature. A decrease in $SiO_2$ was observed

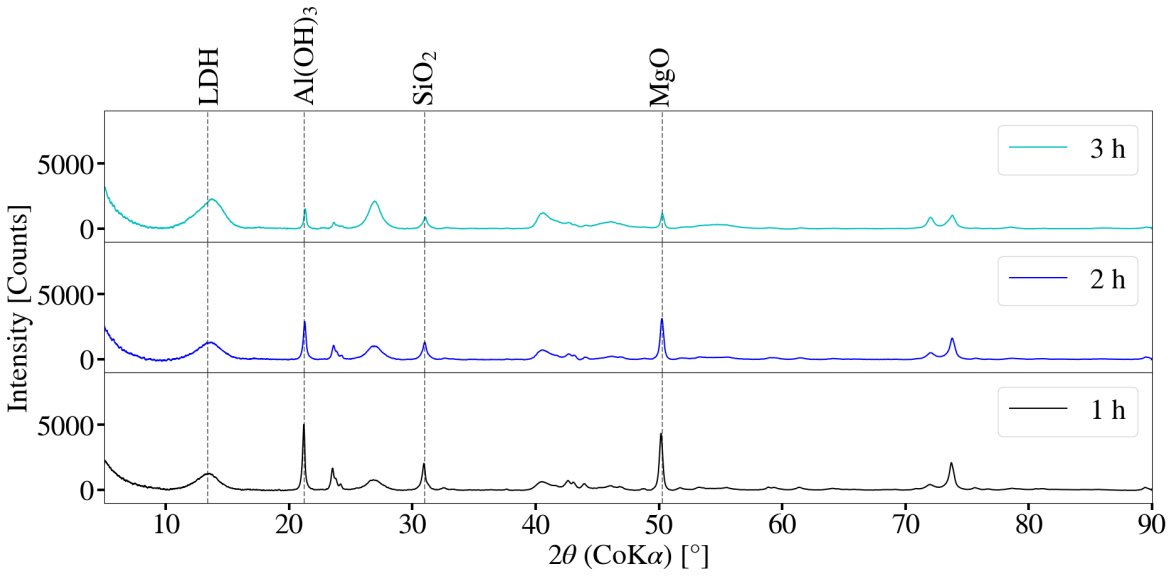


**Figure 40:** XRD spectra for Mg-Al LDH samples synthesised for retention times of 1 h, 2 h and 3 h, at a cooling water inlet of temperature 50°C and a rotational speed of 2000 rpm.

with an increase in milling time. This could once again be due to the increase in amorphitisation as described in Section 6.1.2.

Average temperature and flowrate measurements are summarised in Table 19. The calculated energy transferred to the jacket water was approximately 0.073 kW, 0.17 kW and 0.18 kW for retention times of 1 h, 2 h and 3 h respectively. Calculated parameters associated with heat transfer to the jacket water are summarised in Table 18.

**Table 18:** Summary of calculated parameters associated with the heat removed by jacket water with a change in retention time. Samples were synthesised at a jacket water inlet temperature of 50 °C

| Retention Time [h] | T1 [K] | T2 [K] | Molar Flow [kmol·h$^{-1}$] | Cp [J·kmol$^{-1}$·K$^{-1}$] | Cp [kJ·kmol$^{-1}$·K$^{-1}$] | Q [kJ·h$^{-1}$] | Q [kJ·s$^{-1}$] |
|---|---|---|---|---|---|---|---|
| 1 | 324.75 | 324.87 | 28.98 | 75252.48 | 75.25 | 261.68 | 0.073 |
| 2 | 324.84 | 325.13 | 29.03 | 75252.89 | 75.25 | 633.49 | 0.17 |
| 3 | 324.88 | 325.18 | 29.05 | 75253.08 | 75.25 | 655.81 | 0.18 |



**Table 19:** Average temperature and flowrate measurements obtained for Mg-Al LDH samples synthesised with a change in retention time, at a cooling water inlet temperature of 50 °C.

| Retention Time [h] | Flow rate [L·h] | Inlet [°C] | Outlet [°C] | Reactor [°C] |
|---|---|---|---|---|
| 1 | 521.60 | 51.60 | 51.72 | 52.26 |
| 2 | 522.51 | 51.69 | 51.98 | 52.76 |
| 3 | 522.89 | 51.73 | 52.03 | 52.91 |

**FT-IR analysis** Figure 41 depicts the FT-IR spectra for Mg-Al LDH samples synthesised with a change in retention time, at a cooling water inlet temperature of 50 °C. An increase in retention time at an elevated temperature resulted in clear LDH formation as could be seen by XRD spectra in Figure 40. The increase in conversion could be seen with the change in FT-IR spectra observed. Peaks located between 3300 $cm^{-1}$ and 3700 $cm^{-1}$, typically associated with free and bonded -OH, became broader with an increase in retention time. This could be due to a decrease in free -OH within the sample as a result of the increase in conversion of raw materials ($Al(OH)_3$ and MgO) to LDH. This could therefore be the result of water within the LDH stucture containing strong -OH bonds (Tongamp, Zhang & Saito, 2007). Similarly the peak at approximately 1366 $cm^{-1}$ decreased in percentage transmittance (increased in intensity) with an increase in the retention time. This is likely due to an increase in carbonate interactions ($CO_3^{2-}$ v3 antisymmetric vibrations) (Dudeka et al., 2012) (Labuschagne et al., 2015) within the sample and LDH. The consistent peak observed at 1100 $cm^{-1}$ could once again be due to the Si-O interaction from the selected MgO (Socrates, 2001). The FT-IR spectra obtained after 3 h of milling resembled that of Mg-Al LDH mechanochemically synthesised with the use of $Mg(OH)_2$ and $Al(OH)_3$ (Tongamp, Zhang & Saito, 2007).

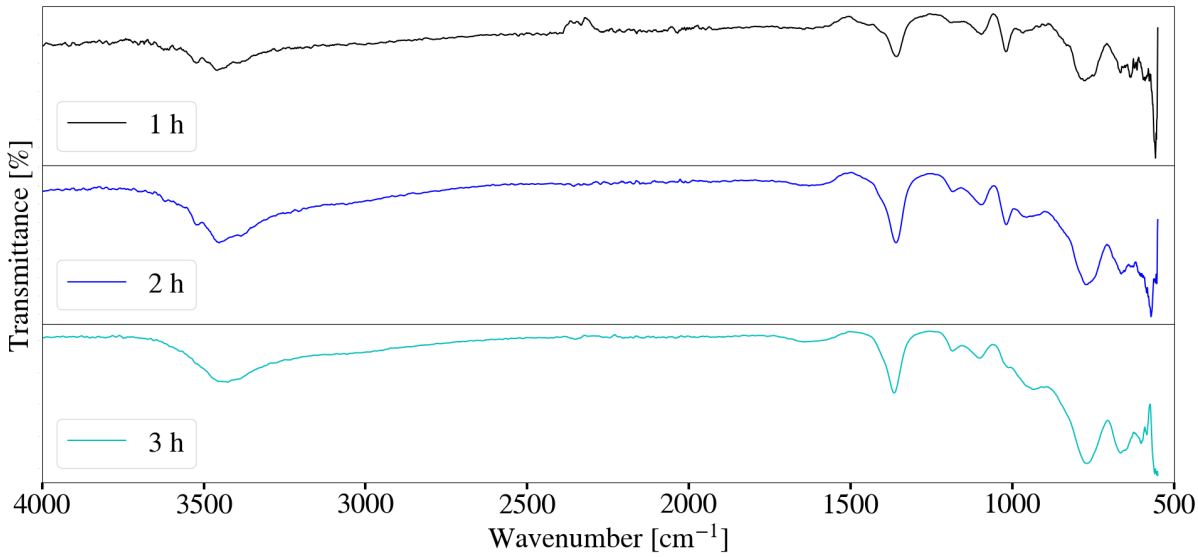


**Figure 41:** FT-IR spectra for Mg-Al LDH samples synthesised for retention times of 1 h, 2 h and 3 h, at a cooling water inlet of temperature 50°C and a rotational speed of 2000 rpm.

**Particle size analysis** The change in particle size with time for Mg-Al LDH synthesised with a change in retention time, at a jacket water inlet temperature of 50 °C, is depicted in Figure 42. The $D_{90}$, $D_{50}$ and $D_{10}$ values for the original raw material mixture was measured to be 17.3 $\mu$m , 6.89 $\mu$m and 1.81 $\mu$m respectively. It was noted that the $D_{10}$ values plateaued to below 0.6 $\mu$m only after 60 min of milling. Slight fluctuations were

observed for the $D_{50}$ values present, however remained relatively consistent after 60 min of milling, below a particle size of 2 $\mu$m. Comparatively the $D_{90}$ values stabilised after a retention time of approximately 60 min, below a value of 4 $\mu$m. The final $D_{90}$, $D_{50}$ and $D_{10}$ values measured after 3 h of milling were 3.41 $\mu$m, 1.18 $\mu$m and 0.52 $\mu$m respectively. The distribution associated with samples synthesised at 50 °C exhibited fluctuations, with a formation and change in the size of the bi-modal distribution. Raw materials exhibited a dominant mode between 1 $\mu$m and 10 $\mu$m with minor modes between 0.1 $\mu$m and 1 $\mu$m, and 10 $\mu$m and 100 $\mu$m. The mode between 0.1 $\mu$m and 1 $\mu$m increased in size with an increase in retention time. This was observed to correlate with the formation of LDH as could be seen in Figure 40. Agglomeration tails were further observed to be consistently present. The particle size distribution present within the system is directly influenced by the formation and types of compounds present. The distributions depicted in Figure 28 varied drastically from that observed in Figure 43. The reaction rate associated with LDH formation could be lower at 30 °C, therefore the change in particle size with time would be less drastic due to a lower conversion within the selected time intervals. It is possible that the mode located between 1 $\mu$m and 10 $\mu$m represent the unreacted raw materials present within the sample (population 1), decreasing with size as a result of converting to LDH (population 2). Conversion was incomplete after 3 h of milling activity. It is unclear if the bi-modal distribution would eventually converge into a uni-modal distribution located between 0.1 $\mu$m and 1 $\mu$m.

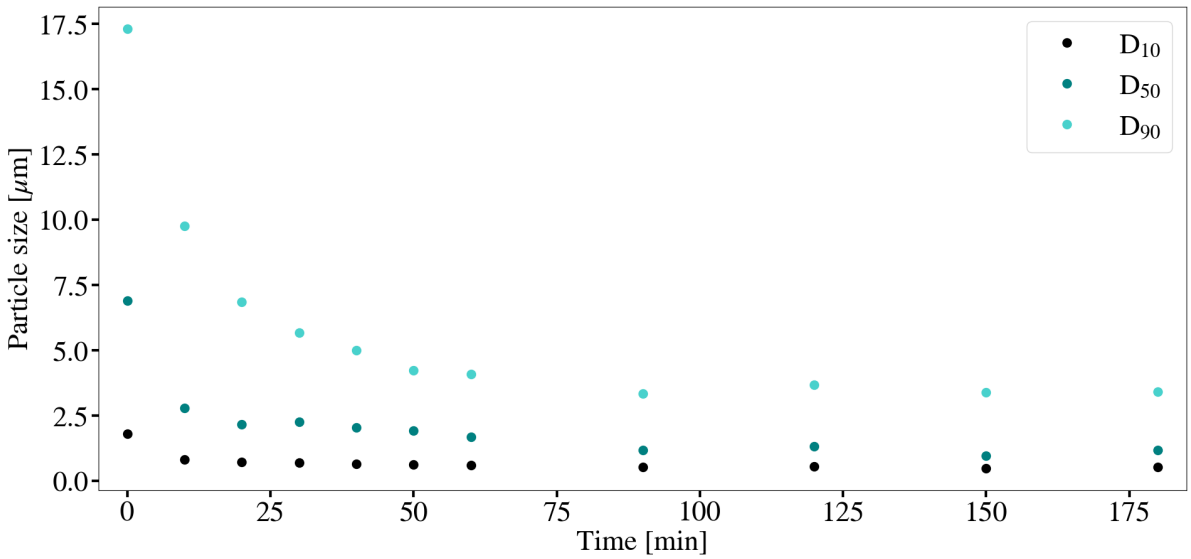


**Figure 42:** The change in particle size with time for Mg-Al LDH samples synthesised at a cooling water inlet temperature of 50 °C, with a change in retention time.

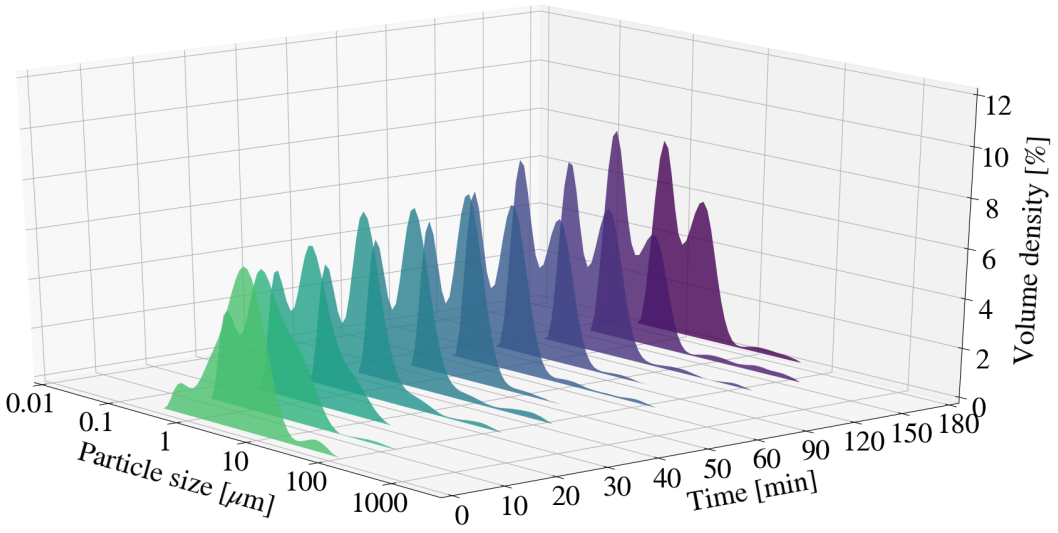


**Figure 43:** Particle size distribution for Mg-Al LDH samples synthesised at a cooling water inlet temperature of 50 °C, with a change in retention time.

**XRF analysis** Table A.35 depicts the mass composition of all samples synthesised, with a change in retention time, at a jacket water inlet of 50 °C. Impurities attributed to mill degradation, such as $Fe_2O_3$, $Cr_2O_3$, $ZrO_2$, $MoO_3$ and $Y_2O_3$ were once again present. This was expected as sample discolouration from a light grey to a dark metallic grey occured with an increase in residence time. Minor differences were observed when compared to data obtained for samples synthesised at a cooling water inlet of 30 °C.

**SEM imaging** Figures 44, 45 and 46 depict the SEM imaging for samples synthesised at a cooling water inlet temperature of 50 °C. The morphology of the sample seems to change drastically with an increase in retention time. The presence of small platelet-like structures increases with an increase in the retention time. These platelets were observed to be absent for samples synthesised at 30 °C and could possibly be the formation of LDH platelets as supported by the XRD spectra in Figure 40.

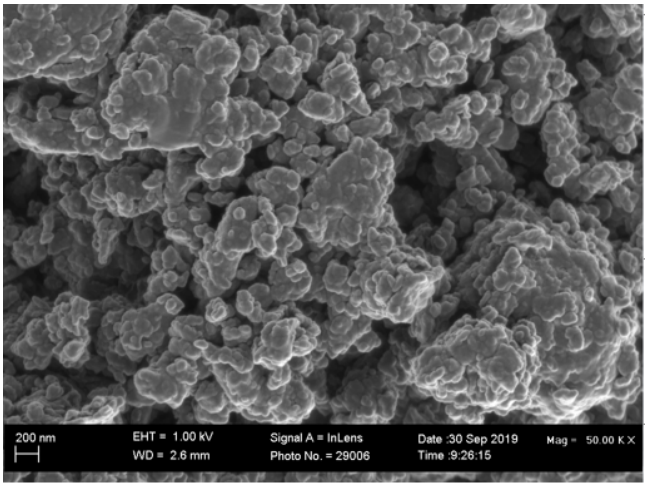


**Figure 44:** SEM imaging of Mg-Al LDH sample after 1 h of milling at a cooling water inlet temperature of 50 °C and rotational speed of 2000 rpm.

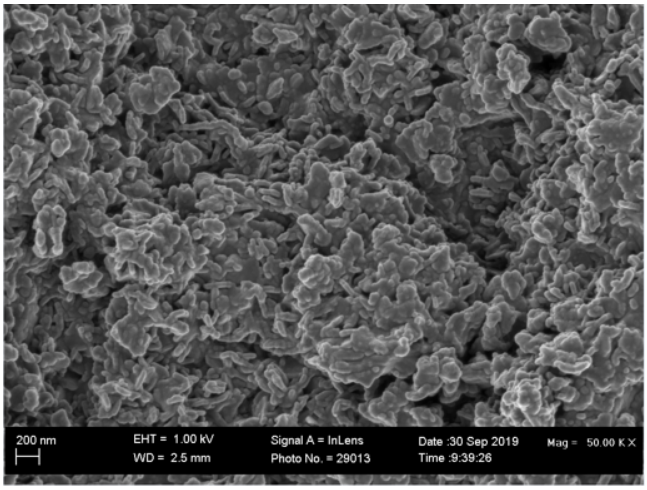


**Figure 45:** SEM imaging of Mg-Al LDH sample after 2 h of milling at a cooling water inlet temperature of 50 °C and rotational speed of 2000 rpm.

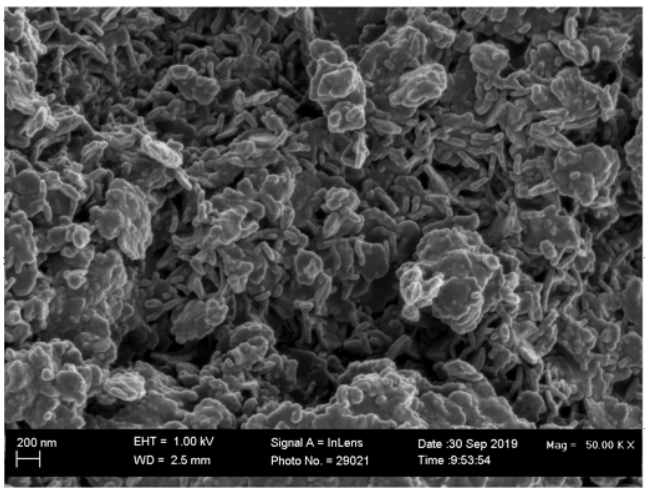


**Figure 46:** SEM imaging of Mg-Al LDH sample after 3 h of milling at a cooling water inlet temperature of 50 °C and rotational speed of 2000 rpm.

**Rotational speed**

**XRD analysis** In attempt to determine the influence of temperature during the milling process, the cooling water inlet temperature was increased from 30 ℃ to approximately 50 degree C for each of the selected rotational speeds. The XRD spectra for the obtained samples are depicted in Figure 47. The primary observations were as follows:

1. The MgO and $Al(OH)_3$ peaks decreased with an increase in rotational speed. The peak reduction associated with $Al(OH)_3$ was more drastic than that of MgO. The overall decrease in peak intensity for the selected raw materials was found to be slightly greater than those synthesised at lower temperatures. The slight change could once-again be attributed to the influence of temperature on the rate of reaction and hydration as described in Section 6.1.5. Despite the increase in temperature and change in kinetic energy, the difference observed from samples synthesised at lower temperatures is small. The selected retention time of 1 h could therefore not clearly demonstrate the affect temperature may have with a change in rotational speed. Trends may therefore become more obvious with an increase in the retention time as seen in Figure 40.

2. The reduction in $SiO_2$ peak intensity was found to be similar to that of samples synthesised at lower temperatures, as seen in Section 6.1.1.

3. Minor primary LDH peaks were present, overall these peaks were more pronounced than those observed for samples synthesised at a cooling water inlet temperature of 30 ℃. The rate of LDH formation was expercted to be greater at higher temperatures and could therefore explain the difference in peak intensity observed.

4. No noticeable trend was associated with the primary LDH peaks. This could be a result of both the degree of amorphitisation and structural degradation, aswell as the selected retention time being too short.

Average flowrates and temperatures are summarised in Table 21. The power input remained the same as that described in Section 6.1.1. The total energy removed for each of the selected rotational speeds was calculated to be 0.36 kW, 0.61 kW and 1.21 kW respectively. Table 20 summarises the relevant parameters associated with the energy transferred to the jacket water.

**Table 20:** Summary of calculated parameters associated with the heat removed by jacket water with a change in rotational speed. Samples were synthesised at jacket water temperatures of approximately 50 °C

| Rotational Speed [rpm] | T1 [K] | T2 [K] | Molar Flow [kmol·h$^{-1}$] | Cp [J·kmol$^{-1}$·K$^{-1}$] | Cp [kJ·kmol$^{-1}$·K$^{-1}$] | Q [kJ·h$^{-1}$] | Q [kJ·s$^{-1}$] |
|---|---|---|---|---|---|---|---|
| 1000 | 322.41 | 323.00 | 29.02 | 75243.33 | 75.24 | 1288.25 | 0.36 |
| 2000 | 323.72 | 324.73 | 29.07 | 75248.04 | 75.25 | 2209.29 | 0.61 |
| 3000 | 323.33 | 325.32 | 29.11 | 75246.52 | 75.25 | 4360.28 | 1.21 |

**Table 21:** Average temperature and flowrate measurements obtained for Mg-Al LDH samples synthesised with a change in rotational speed, at a cooling water inlet temperature of 50 °C.

| Rotational Speed [rpm] | Flow rate [°C] | Inlet [°C] | Outlet [°C] | Reactor [] |
|---|---|---|---|---|
| 1000 | 522.34 | 49.26 | 49.85 | 47.70 |
| 2000 | 523.25 | 50.57 | 51.58 | 48.28 |
| 3000 | 524.14 | 50.18 | 52.17 | 54.45 |

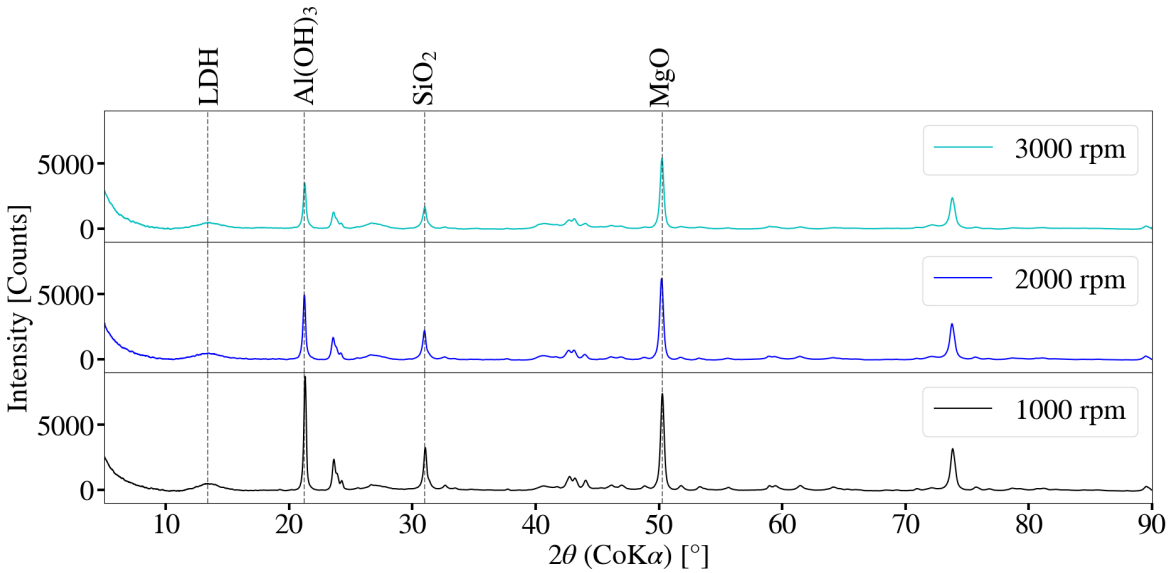


**Figure 47:** XRD spectra for Mg-Al LDH samples synthesised at a cooling water inlet temperature of 50 °C, with a change in a rotational speed.

**FT-IR analysis** Figure 48 depicts the FT-IR spectra for Mg-Al LDH samples synthesised at a cooling water inlet temperature of 50 °C, with a change in rotational speed. Little difference was observed between spectra obtained. Peaks that could be attributed to free and bonded -OH were observed to be present between 3300 $cm^{-1}$ and 3700 $cm^{-1}$ (Nicolet, 2019). Similarly carbonate contamination was noted at a prominant peak observed for all samples around 1366 $cm^{-1}$ (Dudeka et al., 2012) (Labuschagne et al., 2015). Little difference was observed for samples synthesised at 30 °C when compared to that synthesised at 50 °C.

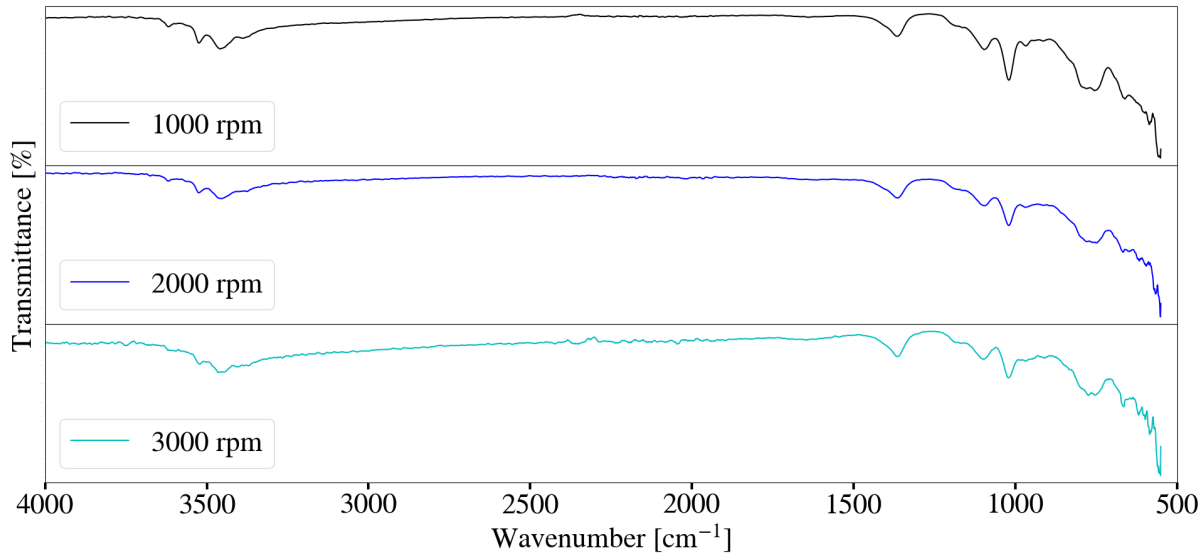


**Figure 48:** FT-IR spectra for Mg-Al LDH samples synthesised at a cooling water inlet temperature of 50 °C, with a change in rotational speed.

**Particle size analysis** Particle size analysis was conducted on the obtained samples to determine whether a change in temperature would result in a change in the final particle size distributions obtained. The measured $D_{90}$, $D_{50}$ and $D_{10}$ values are as summarised in Table 22. Similarly the distributions obtained are depicted in Figure 49. Little difference was observed for the $D_{50}$ and $D_{10}$ values obtained for all three samples. This was further true for the $D_{90}$ values obtained for both samples synthesised at speeds of 2000 rpm and 3000 rpm. Comparatively the $D_{90}$ value at 1000 rpm was observed to be greater at a value of 9.45 $\mu$m. The distribution for the sample at 1000 rpm exhibits an agglomeration tail, with a dominant bi-modal distribution present between a particle size of 10 $\mu$m to 0.1 $\mu$m. This could be the result of the discrepancies observed, however it should one again be noted that lower rotational speeds result in an overall decrease in the kinetic energy transferred to the particles and system. The degree of amorphitisation as well as grinding activity would therefore decrease. The reduction in particle size would therefore be less drastic than that of samples synthesised at greater speeds. Minor secondary modes were once again observed between 0.1 $\mu$m and 1 $\mu$m and could be attributed to the formation of LDH as described previously.

No obvious differences, apart from the $D_{90}$ for the sample at 1000 rpm, were observed for the particle sizes obtained when compared to that of samples synthesised at a cooling water inlet temperature of 30 °C. This however does not conclude that temperature has no effect, as factors such as contamination from mill degradation and the overall reaction scheme influence the final particle sizes measured. Greater temperatures have been proven to promote LDH synthesis as seen by the ageing experiments conducted during the versatility study. The differences in reaction schemes could further be seen by the differences in the LDH peak intensities observed between the XRD spectra depicted in Figures 22 and 47.

**Table 22:** Particle size measured for samples S11, S12 and S13 at the end of a 1 h milling period

| Rotational speed [rpm] | $D_{10}$ [$\mu$m] | $D_{50}$ [$\mu$m] | $D_{90}$ [$\mu$m] |
|---|---|---|---|
| 1000 | 0.734 | 2.62 | 9.45 |
| 2000 | 0.806 | 3.44 | 6.57 |
| 3000 | 0.805 | 3.42 | 6.78 |

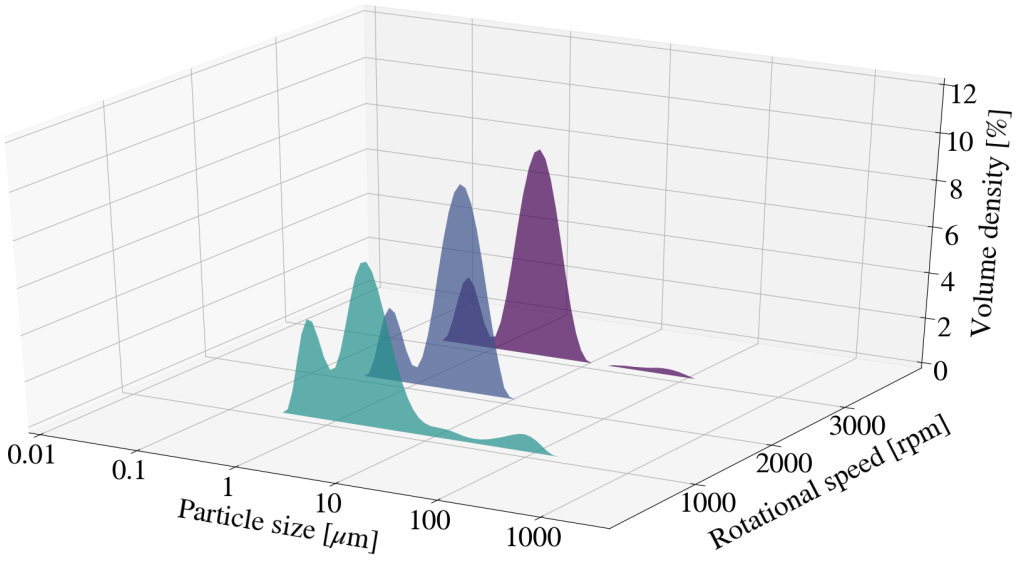


**Figure 49:** Particle size distribution for Mg-Al LDH samples at a cooling water inlet temperature of 50 °C, with a change in rotational speed.

**XRF analysis** The mass composition for each sample, as obtained through XRF analysis, is depicted in Table A.36. Sample discolouration with an increase in rotational speed was once again observed. Indicating that the concentration of milling and media degradation contaminants increased. Impurities such as $K_2O$, MnO and CuO were likely due to retained chemical species within the milling chamber.

## 6.2 Versatility study

### 6.2.1 Mg-Al LDH

**XRD analysis** The XRD spectra for the Mg-Al LDH sample synthesised with a 2:1 $M^{2+}$:$M^{3+}$ ratio, before and after ageing, is depicted in Figure 50. The sample will be reffered to as S16, as summarised in Table 5, for ease of reference. It was observed that LDH peaks prior to ageing were difficult to identify, with MgO and $Al(OH)_3$ peaks still largely present. Ageing for 24 h at 80 °C resulted in a prominent LDH pattern with diminished MgO and $Al(OH)_3$ peaks.

Although LDH peaks were noted to be mostly absent before ageing, the presence of an amorphous LDH precursor, small LDH crystallites or polymorphs within the sample could have acted as a catalyst for further LDH formation during the ageing step. Higher temperatures should increase the rate of LDH formation, ageing of the sample at the

selected conditions would therefore have prompted further LDH formation and a greater conversion of raw materials to product. This could be tested in future by agitating the selected raw materials, with no milling activity, at 80 °C and analysing the sample for the presence of LDH.

The primary and secondary LDH peaks observed for S16 after ageing correspond to $2\theta$ values of 13.49° and 27.22°. The d-spacing was therefore calculated from Equation 7 to be 0.759 nm. This was found to be smaller than values obtained in literature involving mechanochemical methods (0.781 nm) (Zhang et al., 2012). Lattice imperfections as a result of mechanically induced amorphitisation could contribute to changes in d-spacing values observed (Fahami, W Beall, et al., 2016). Basal spacing has been found to further be influenced by factors such as the amount of water present and carbonate contamination (Zhang et al., 2012). The addition of water has been known to decrease the degree of supersaturation which could negatively impact morphology and crystallinity of the synthesised LDHs. It has further been observed that the crystallinity of LDHs can pass through a maximum, with lattice imperfections increasing with an increase in milling time (Tongamp, Zhang & Saito, 2007).

MgO peaks were no longer visible after the selected ageing step, with a small $Al(OH)_3$ peak still visible at a $2\theta$ value of 21.22°. The rate of hydration for caustic MgO increases drastically with an increase in temperature as seen in Figure 6. Milling was conducted at a jacket water inlet temperature of 30 °C, whereas ageing as conducted at 80 °C. This would corroborate the large MgO peaks present within the sample prior to ageing.

Comparatively the XRD spectra for the Mg-Al LDH sample synthesised using a 3:1 $M^{2+}$:$M^{3+}$ ratio, before and after ageing, is depicted in Figure 51. The sample was labelled S17 for ease of reference.

LDH was observed to have formed more readily than S16, after 1 h of milling. LDH synthesised with a 3:1 $M^{2+}$:$M^{3+}$ is considered to be the most stable form of LDH, as it occurs in this state naturally (Forano et al., 2006). The reaction scheme was however incomplete with raw material peaks clearly visible.

Ageing resulted in further conversion to LDH product, with a substantial decrease in $Al(OH)_3$ and MgO peak intensity. A minor peak for $Al(OH)_3$ was still present after ageing, with no clear MgO peak observed. The primary and secondary peaks for the LDH formed prior to ageing were broad and corresponded to $2\theta$ values of 13.37° and

26.99° respectively. The d-spacing associated with this was calculated to be approximately 0.767 $\mu$m. A slight shift in the LDH spectra was noted to have occurred after ageing, with a primary and secondary peak at 13.48°and 27.10°. This was found to correlate with a d-spacing of 0.760 $\mu$m.

Average flowrate and temperature measurements are summarised in Table 24. The energy input to the system at 2000 rpm was measured to be approximately 1.09 kW. Similarly the overall energy removed from the system for both samples S16 and S17 was estimated to be 0.52 kW and 0.37 kW respectively. Table 23 summarises the calculated parameters associated with the heat transferred to the jacket water.

**Table 23:** Summary of calculated parameters associated with the heat removed by jacket water for Mg-Al samples synthesised with a change in $M^{2+}$:$M^{3+}$ ratio.

| $M^{2+}$:$M^{3+}$ | T1 [K] | T2 [K] | Molar Flow [kmol·h$^{-1}$] | Cp [J·kmol$^{-1}$·K$^{-1}$] | Cp [kJ·kmol$^{-1}$·K$^{-1}$] | Q [kJ·h$^{-1}$] | Q [kJ·s$^{-1}$] |
|---|---|---|---|---|---|---|---|
| 2:1 | 302.98 | 303.84 | 28.96 | 75316.94 | 75.32 | 1857.71 | 0.52 |
| 3:1 | 303.75 | 304.36 | 29.20 | 75308.23 | 75.31 | 1341.59 | 0.37 |

**Table 24:** Average temperature and flowrate measurements obtained for Mg-Al LDH samples synthesised with a change in $M^{2+}$:$M^{3+}$ ratio.

| $M^{2+}$:$M^{3+}$ | Flow rate [L·h$^{-1}$] | Inlet [°C] | Outlet [°C] | Reactor [°C] |
|---|---|---|---|---|
| 2:1 | 521.25 | 29.83 | 30.69 | 33.07 |
| 3:1 | 525.68 | 30.60 | 31.21 | 33.29 |

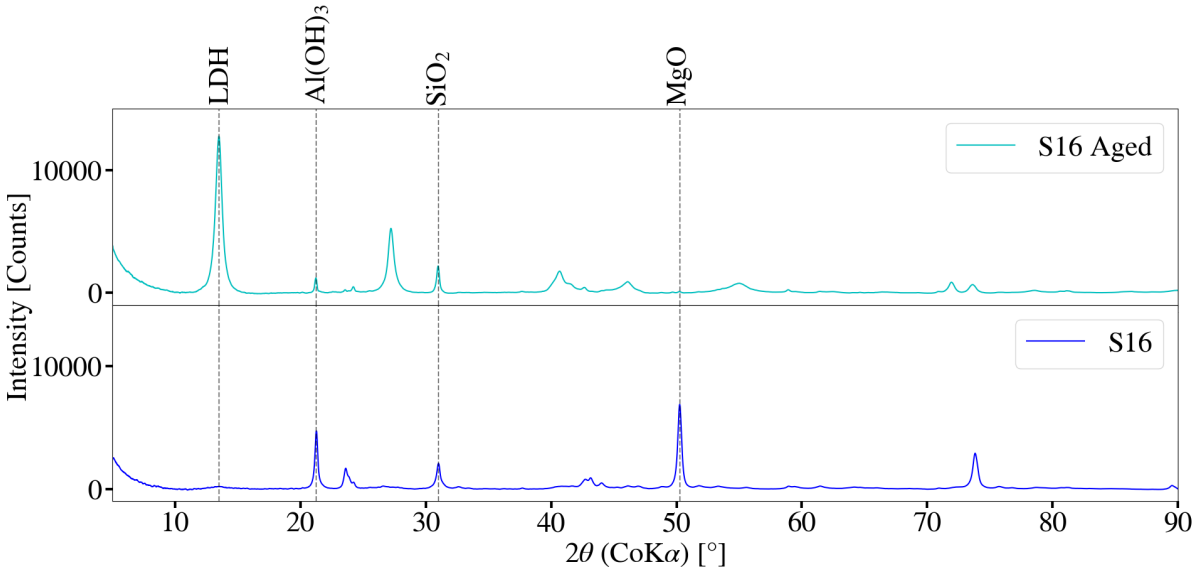


**Figure 50:** XRD spectra for Mg-Al LDH sample, before and after ageing, synthesised using a $M^{2+}$:$M^{3+}$ ratio of 2:1.

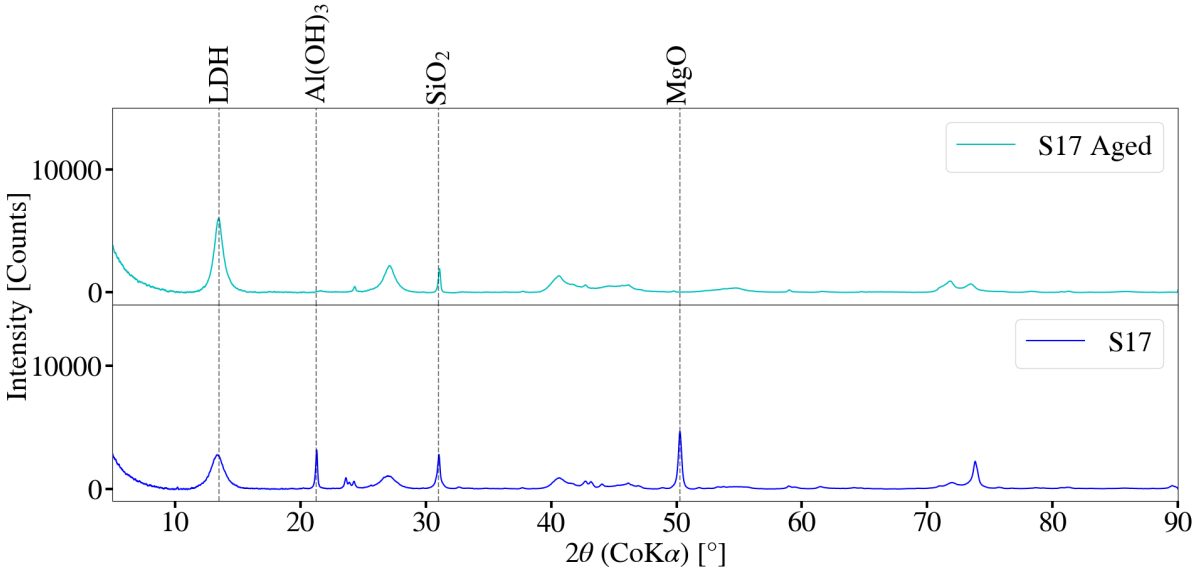


**Figure 51:** XRD spectra for Mg-Al LDH sample, before and after ageing, synthesised using a $M^{2+}$:$M^{3+}$ ratio of 3:1.

**FT-IR analysis** The FT-IR spectra for S16 and S17 is depicted in Figure 52. Prior to ageing peaks observed between 3500 $cm^{-1}$-3700 $cm^{-1}$ can be attributed to the stretching vibrations of free -OH groups (Nicolet, 2019) (Tongamp, Zhang & Saito, 2007). Similarly peaks located between 3250 $cm^{-1}$-3600 $cm^{-1}$, specifically those located at 3462 $cm^{-1}$ (S16) and 3454 $cm^{-1}$ (S17), are further attributed to bonded –OH groups (Nicolet, 2019) (Tongamp, Zhang & Saito, 2007). Broadening of peaks could be due to water molecules with -OH bonding (Tongamp, Zhang & Saito, 2007). Carbonate interactions ($CO_3^{2-}$ v3 vibrations) are present within the samples and is indicative of peaks located at 1367 $cm^{-1}$

(S16) and 1365 $cm^{-1}$ (S17) (Tongamp, Zhang & Saito, 2007) (Nicolet, 2019). Ageing of both S16 and S17 resulted in the intensification of these peaks. This could be the result of carbonate contamination as the synthesis, filtering and ageing was conducted under atmospheric conditions. A broad peak between 3250 $cm^{-1}$ and 3700 $cm^{-1}$ was observed to form upon ageing. This could be assigned to the O-H stretching vibrations that occur within layered brucite like structure of the LDH as well as water molecules within the interlayer (F Zhang, N Du, Song & Hou, 2015).

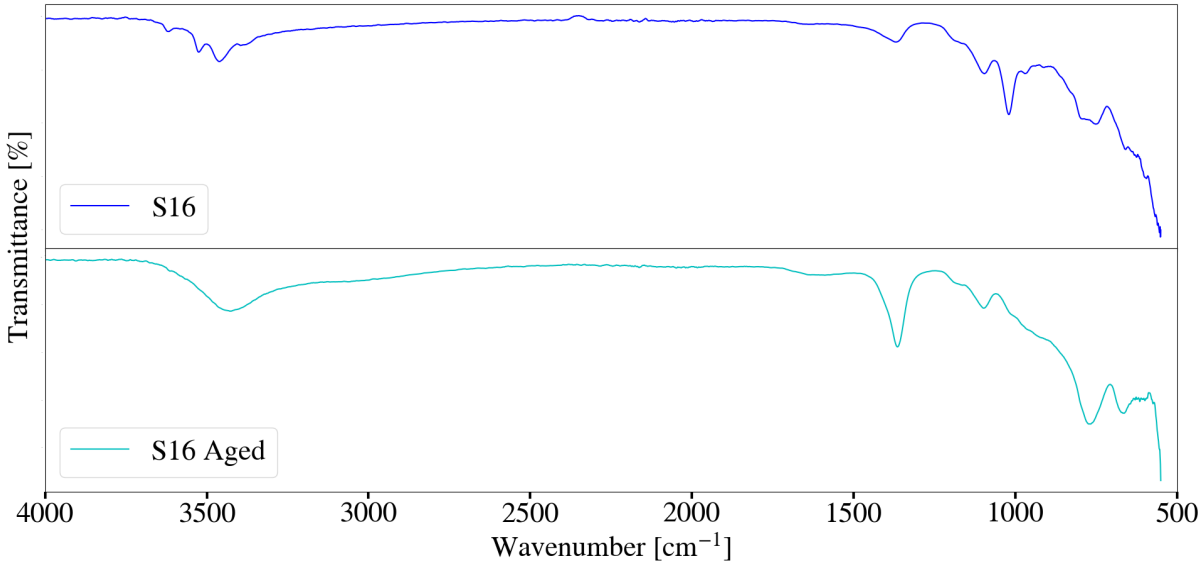


**Figure 52:** FT-IR spectra for Mg-Al LDH sample, before and after ageing, synthesised using a $M^{2+}$:$M^{3+}$ ratio of 2:1.

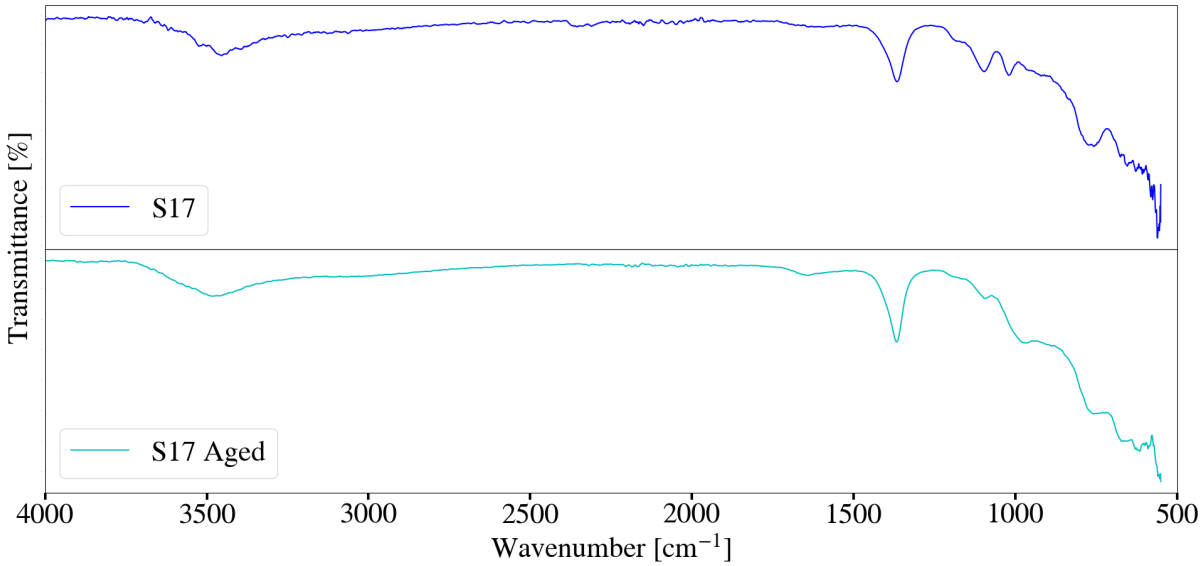


**Figure 53:** FT-IR spectra for Mg-Al LDH sample, before and after ageing, synthesised using a $M^{2+}$:$M^{3+}$ ratio of 3:1.

**Particle size analysis** The particle size distribution with a change in time for S16 is as depicted in Figure 54. Prior to milling the numerical values for the $D_{90}$, $D_{50}$ and $D_{10}$ of the MgO and $Al(OH)_3$ mixture were 17.60 $\mu$m, 7.79 $\mu$m and 2.35 $\mu$m respectively. The change associated with these values for 1 h of milling activity is indicated in Figure 55. It was observed that after approximately 10 min of milling the $D_{10}$ values stabilised at approximately 1 $\mu$m. Comparatively the average particle size seemingly plateaued after 10 min of milling to below 4 $\mu$m. It was noted that the $D_{90}$ values continued to follow a decreasing trend for the entire 1 h milling period. The final numerical distribution for the relevant $D_{90}$, $D_{50}$ and $D_{10}$ were measured to be 6.21 $\mu$m , 3.39 $\mu$m and 0.962 $\mu$m respectively.

Figure 54 exhibits little change in the shape of the bi-modal distribution after 30 min of milling activity. The little change observed in the distributions could be an indication that the conversion to LDH product is relatively low and that the primary action occurring within the mill is particle size reduction. Ageing of the sample resulted in a drastic change in the bi-modal distribution, having become broader. This could be attributed to the conversion of the raw materials to LDH product. Particle formation as well as crystal growth due to high temperatures, was expected to influence the distribution and overall size. Particle agglomeration could further contribute to the observed changes, with final $D_{90}$, $D_{50}$ and $D_{10}$ values of 31.60 $\mu$m, 7.32 $\mu$m and 1.65 $\mu$m.

Figure 57 refers to the change in particle size with time for S17. The measured $D_{90}$, $D_{50}$ and $D_{10}$ values of the original raw material mixture were 18.80 $\mu$m , 7.22 $\mu$m and 1.66 $\mu$m respectively. This was noted to be larger than the distribution for S16 and was likely a result of the difference in $M^{2+}$ to $M^{3+}$ ratio selected. After approximately 10 min of milling activity the relevant $D_{50}$ and $D_{10}$ values stabilised to below 3 $\mu$m and 0.80 $\mu$m respectively. The $D_{90}$ particle size followed a decreasing trend to a final value of 4.94 $\mu$m.

The change in the particle size distribution with time is represented by Figure 56. It was noted that the distribution varied to that of S16, with a more prominent secondary node on the bi-modal distributions obtained. The changes observed could be a result of metal ratio selected, as well as the conversion to of raw materials to LDH product. The formation of LDH was observed to have occurred more readily for S17 as seen by the XRD spectra depicted in Figure 51. The formation of new chemical compounds could directly influence the particle size and shape obtained. It is however unclear when LDH formation occurs during the 1 h milling period and can not be inferred from the distribution obtained. Ageing of the sample resulted in a a broad tri-modal distribution. This could once again be attributed to factors such as LDH product formation, particle agglomeration and particle growth. The final $D_{90}$, $D_{50}$ and $D_{10}$ values were measured to be 50.20 $\mu$m, 9.65 $\mu$m and 1.47 $\mu$m. It was noted that inclusion of the ageing step

resulted in a more viscous claylike slurry.

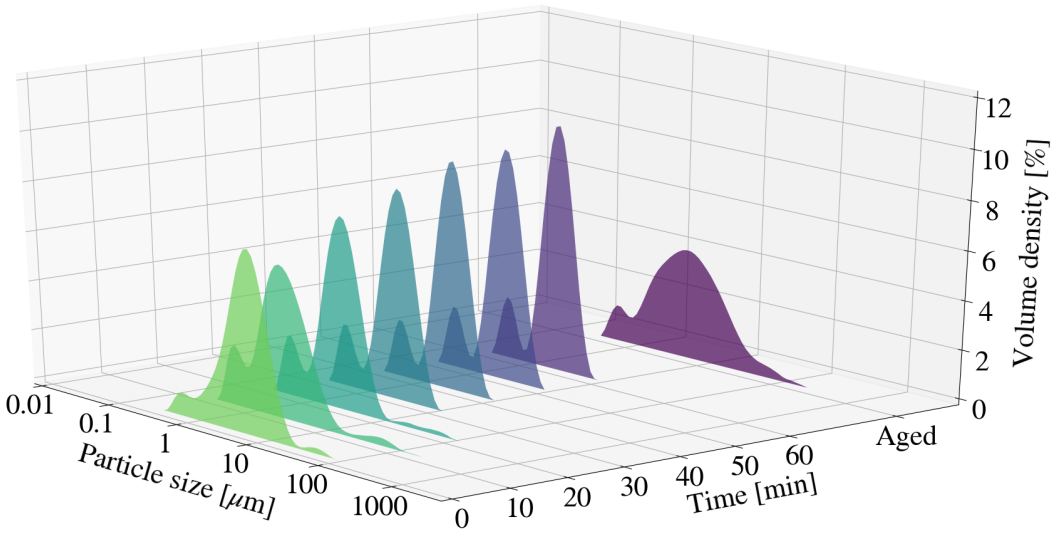


**Figure 54:** Particle size distribution with a change in time for Mg-Al LDH sample, before and after ageing, synthesised using a $M^{2+}$:$M^{3+}$ ratio of 2:1.

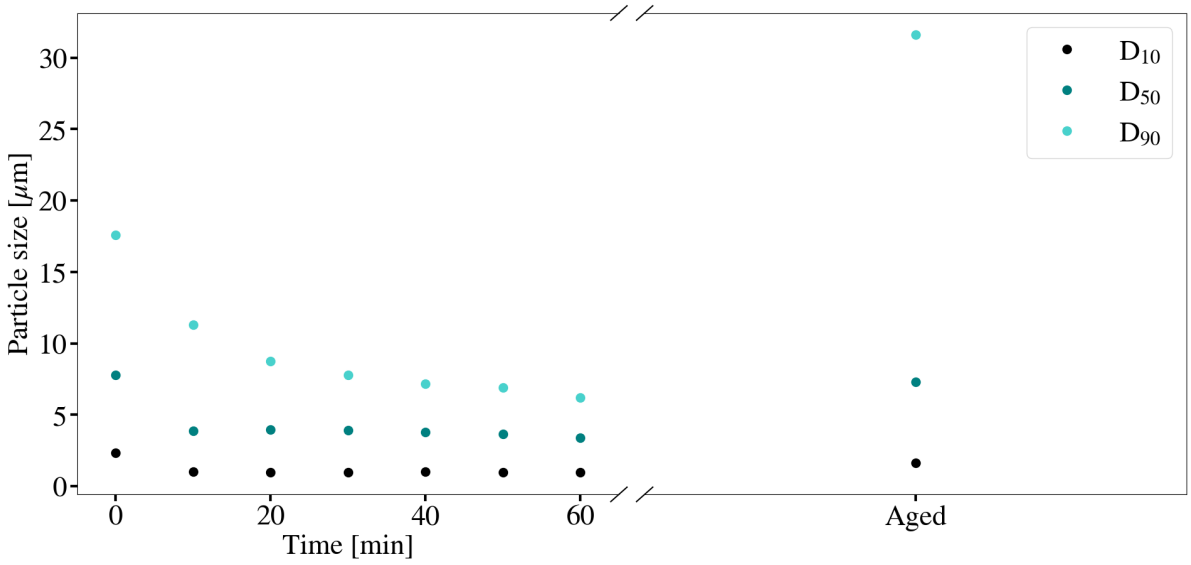


**Figure 55:** The change in particle size with time for Mg-Al LDH sample, before and after ageing, synthesised using a $M^{2+}$:$M^{3+}$ ratio of 2:1.

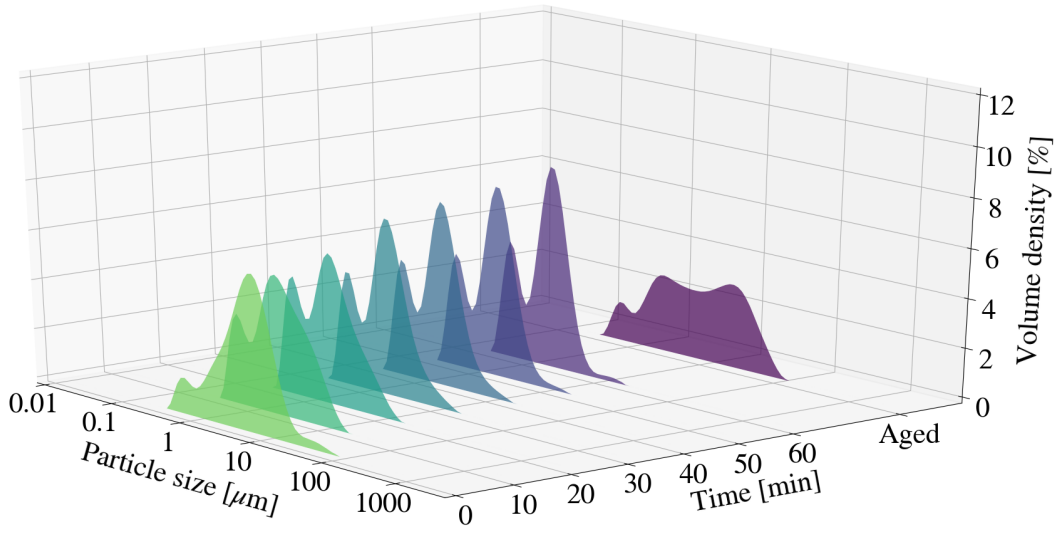


**Figure 56:** Particle size distribution with a change in time for Mg-Al LDH sample, before and after ageing, synthesised using a $M^{2+}$:$M^{3+}$ ratio of 3:1.

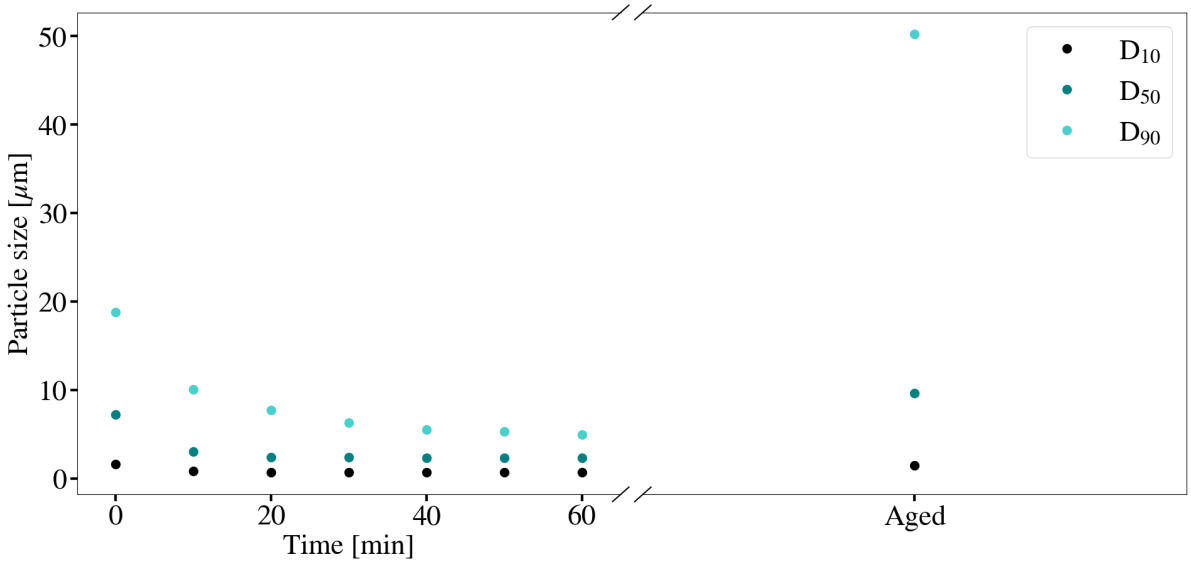


**Figure 57:** The change in particle size with time for Mg-Al LDH sample, before and after ageing, synthesised using a $M^{2+}$:$M^{3+}$ ratio of 3:1.

**XRF analysis** XRF analysis was conducted on samples S16 and S17 to ensure that the selected $M^{2+}$:$M^{3+}$ ratios were stoicheometrically correct for each sample. Table A.37 summarises the mass percentage of primary components and impurities present with each sample. The actual $M^{2+}$:$M^{3+}$ ratios for S16 and S17 were calculated to be approximately 2.00:1.04 and 3.00:1.04. This confirms that the selected masses for the desired experiments conducted were accurate as described in Table 6.

The observed presence of CuO and ZnO could be attributed to retained chemical species within the milling chamber. Contamination from the degradation of the mill likely resulted in the presence of $Fe_2O_3$, $Cr_2O_3$, NiO and $MoO_3$. Similarly the degradation of milling media contributed to the presence of $ZrO_2$ and $Y_2O_3$. Components such as MnO and $K_2O$ are likely a result of contaminant retention within the mill from previous runs conducted through its lifetime.

The measured LOI (loss upon ignition) values were observed to differ between samples. This is likely due to the structural difference between the samples synthesised with different metal ratios. Variation in both crystal water as well as the amount of intercalated $OH^-$ in LDH product could account for the difference observed in these values. Similarly the amount of LDH present within each sample may vary and further contribute to the observed differences. It should further be noted that the XRF data is associated with the sample prior to ageing.

**SEM imaging** SEM imaging of both samples, before ageing, is depicted in Figures 58 ando 59. No obvious morphological differences were observed between samples prior to ageing. Comparitively, Figures 60 and 61, depict the samples after ageing for 24 h at 80 °C. Thin platelet like structures were present in both samples. These are likely the result of LDH formation as supported by the XRD spectra in Figures 50 and 51.

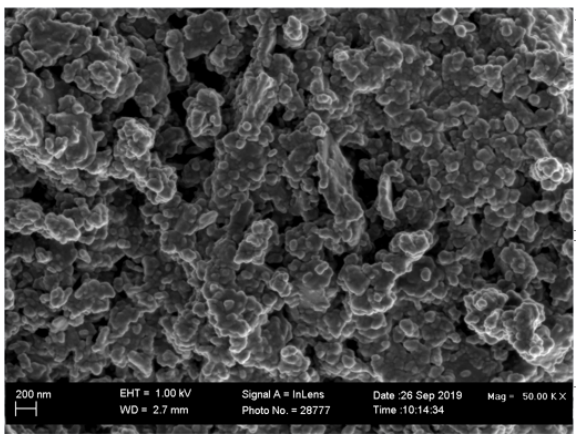


**Figure 58:** SEM imaging of Mg-Al LDH sample synthesised using a $M^{2+}$:$M^{3+}$ ratio of 2:1, prior to ageing.

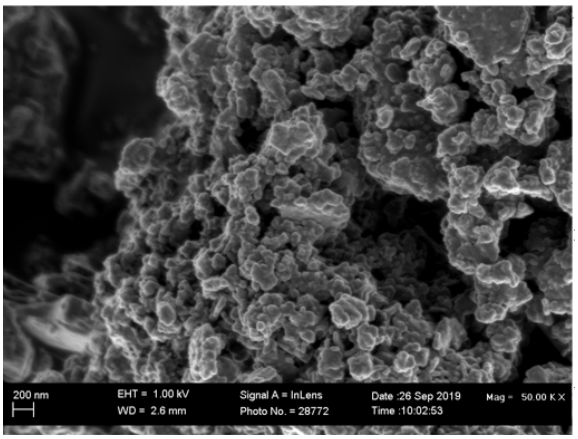


**Figure 59:** SEM imaging of Mg-Al LDH sample synthesised using a $M^{2+}$:$M^{3+}$ ratio of 3:1, prior to ageing.

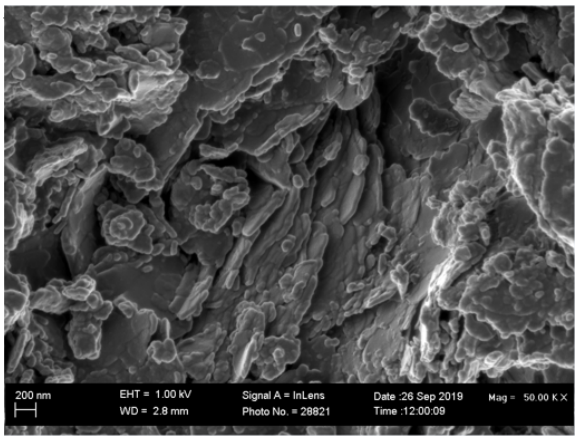


**Figure 60:** SEM imaging of Mg-Al LDH sample synthesised using a $M^{2+}$:$M^{3+}$ ratio of 2:1, after ageing.

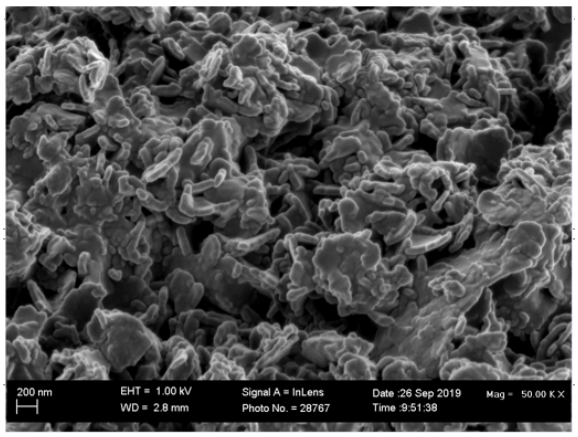


**Figure 61:** SEM imaging of Mg-Al LDH sample synthesised using a $M^{2+}$:$M^{3+}$ ratio of 3:1, after ageing.

### 6.2.2 Ca-Al LDH

**XRD analysis** The synthesis of Ca-Al LDH was attempted by making use of commercial grade CaO, $Al(OH)_3$ and $CaCO_3$ as raw materials. Samples were synthesised according to a 3:2:1 and 2:1:0 ratio of $M^{2+}$:$M^{3+}$:$CaCO_3$ and will be referred to S18 and S19 for ease of reference. XRD spectra for both samples, before and after ageing, are as depicted in Figures 62 and 63. Samples were aged for 24 h at 80 °C under atmospheric conditions.

The XRD spectra associated with S18 indicated that LDH was present prior to ageing, with the primary peak located at a $2\theta$ value of 13.50°. The respective d-spacing calculated with the use of Equation 7 was therefore determined to be 0.759 nm. Prior to ageing it was noted that conversion was incomplete with $Al(OH)_3$ and $Ca(OH)_2$ peaks observed at $2\theta$ values of 21.28°and 39.82°respectively. Ageing of sample resulted in more complete conversion with a minor $Al(OH)_3$ peak observed. The $Ca(OH)_2$ peaks were no longer visible. It was noted that a more defined and prominent $CaCO_3$ peak was present after the ageing process. Twinning LDH peaks were observed at $2\theta$ values of 13.54° and 13.2°, corresponding to d-spacing values of 0.757 nm and 0.776 nm respectively. This could possibly be due to the formation of different LDH phases and orientations.

Comparatively the XRD spectra for S19 is depicted in Figure 63. An LDH peak was observed to be present at a $2\theta$ value of 13.47°, corresponding to a d-spacing of 0.761 nm. No direct carbonate source was available for LDH formation, however the synthesis was not conducted under inert conditions. Rendering the formation of $CO_3^{2-}$ intercalated LDH material possible. The presence of atmospheric carbonate could possibly be identified through the formation of $CaCO_3$ peak.

The peaks associated with $Al(OH)_3$ and $Ca(OH)_2$ were observed to be more prominent than those for S18. Ageing of S19 resulted in the formation of the LDH precursor katoite ($Ca_3Al_2(OH)_{12}$) as a by-product. Conversion remained incomplete implying that the addition of a carbonate source or third phase was necessary for the successful synthesis of Ca-Al LDH as stated by (Qu, Zhong, et al., 2016). Twinning primary peaks were again observed after ageing was implemented at $2\theta$ values of 13.27° and 13.58°. The relevant d-spacing values associated with these were calculated to be 0.772 nm and 0.754 nm.

The average temperatures associated with samples S18 and S19 are depicted in Table 26. The estimated energy removed by the cooling jacket was determined to be 0.45 kW and 0.37 kW for S18 and S19 respectively. Table 25 depicts the calculated parameters associated with the heat transferred to the jacket water.

**Table 25:** Summary of calculated parameters associated with the heat removed by jacket water for Ca-Al samples synthesised with a change in $M^{2+}$:$M^{3+}$:$CaCO_3$ ratio.

| $M^{2+}$:$M^{3+}$:$CaCO_3$ | T1 [K] | T2 [K] | Molar Flow [kmol·h$^{-1}$] | Cp [J·kmol$^{-1}$·K$^{-1}$] | Cp [kJ·kmol$^{-1}$·K$^{-1}$] | Q [kJ·h$^{-1}$] | Q [kJ·s$^{-1}$] |
|---|---|---|---|---|---|---|---|
| 3:2:1 | 303.38 | 302.64 | 28.93 | 75320.96 | 75.32 | 1612.24 | 0.45 |
| 2:1:0 | 305.19 | 304.58 | 29.11 | 75299.44 | 75.30 | 1337.13 | 0.37 |

**Table 26:** Average temperature and flowrate measurements obtained for Ca-Al LDH samples synthesised, with and without the addition of $CaCO_3$, using a $M^{2+}$:$M^{3+}$ ratio of 2:1.

| $M^{2+}$:$M^{3+}$:$CaCO_3$ | Flow rate [L·h$^{-1}$] | Inlet [°C] | Outlet [°C] | Reactor [°C] |
|---|---|---|---|---|
| 3:2:1 | 520.66 | 29.49 | 30.23 | 32.75 |
| 2:1:0 | 523.99 | 31.43 | 32.04 | 33.94 |

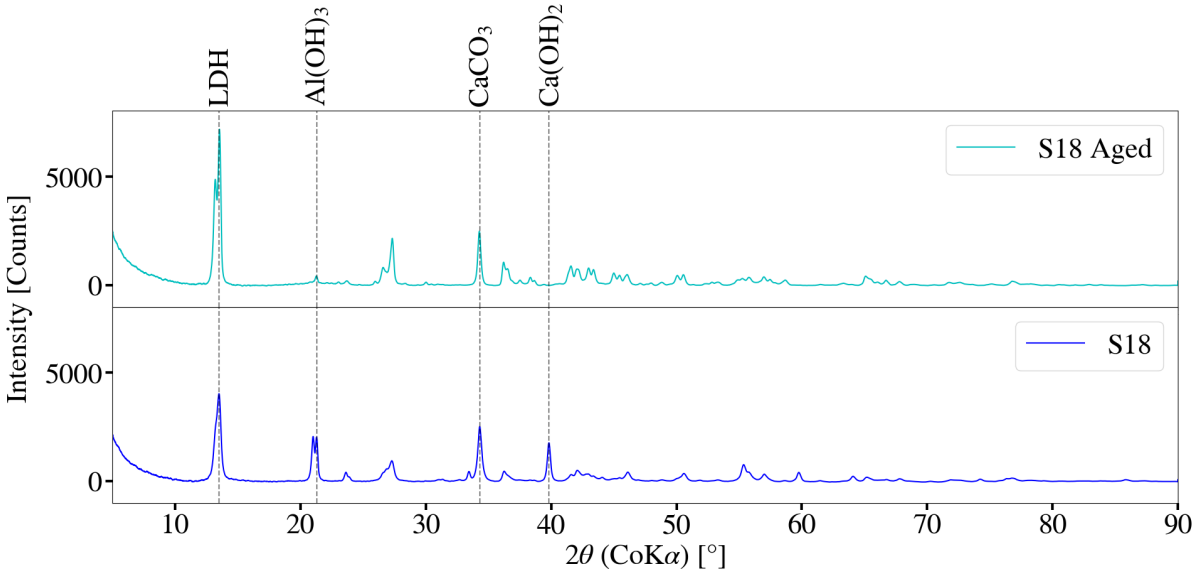


**Figure 62:** XRD spectra for Ca-Al LDH sample, before and after ageing, synthesised with the addition of $CaCO_3$ using a $M^{2+}$:$M^{3+}$ ratio of 2:1.

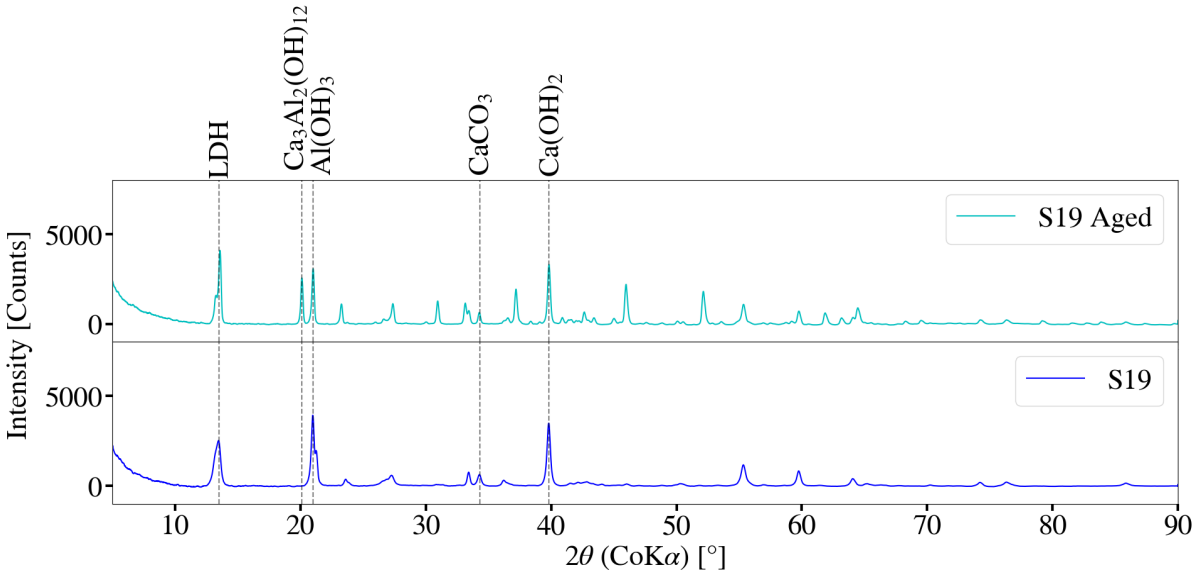


**Figure 63:** XRD spectra for Ca-Al LDH sample, before and after ageing, synthesised without the addition of $CaCO_3$ using $M^{2+}$:$M^{3+}$ ratio of 2:1.

**FT-IR analysis** The FT-IR spectra for S18 is depicted in Figure 64. Prior to ageing, peaks between 3700 $cm^{-1}$ and 3300 $cm^{-1}$ were observed and could be due to free M-OH vibrations within the sample (Qu, Zhong, et al., 2016). This was to be expected as conversion was observed to be incomplete, with $Al(OH)_3$ and $CaOH_2$ still present. The peak observed at 3465 $cm^{-1}$ could be due to free water and bonded water molecules within the interlayer, as well as -OH vibrations within the octahedral layer (Labuschagne et al., 2015). Peaks observed at 1418 $cm^{-1}$ and 876 $cm^{-1}$ could be due to the vibrations of carbonate on the surface of the LDH (Qu, Zhong, et al., 2016). Similarly peaks observed

at 1370 $cm^{-1}$ and 3527 $cm^{-1}$ could be attributed to the vibrations of carbonate ($CO_3^{2-}$ v3 vibrations) within the interlayer of the LDH structure (Fahami, W Beall, et al., 2016) (Nicolet, 2019). The spectra for the S18 after ageing was similar to that prior to ageing. It was however noted that the peak at 1022 $cm^{-1}$ dissapeared once ageing was complete and could be attributed to the reaction of raw materials to LDH.

The FT-IR spectra for S19 is depicted in Figure 65. The spectra prior to ageing was once again similar to that of S18. Prior to ageing peaks were observed between 3300 $cm^{-1}$ and 3700 $cm^{-1}$. These could be attributed to bonded and free -OH within the sample (Nicolet, 2019). A broad peak at 1414 $cm^{-1}$ could be due to carbonate within the system (Socrates, 2001). This was expected as synthesis and drying were conducted under atmospheric conditions, despite no direct carbonate source being present. Peaks observed between 900 $cm^{-1}$ and 500 $cm^{-1}$ could further be a result of M-O (Aisawa et al., 2002) and M-OH (Socrates, 2001) interactions within the sample. Ageing of the sample resulted in a drastic change of the specra with twinning peaks at 1366 $cm^{-1}$ and 1415 $cm^{-1}$. These could once-again be attributed $CO_3^{-2}$ v3 antisymmetric vibrations (Labuschagne et al., 2015) as a result of the LDH formed prior to ageing, as well as carbonate interactions on the surface (Qu, Zhong, et al., 2016).

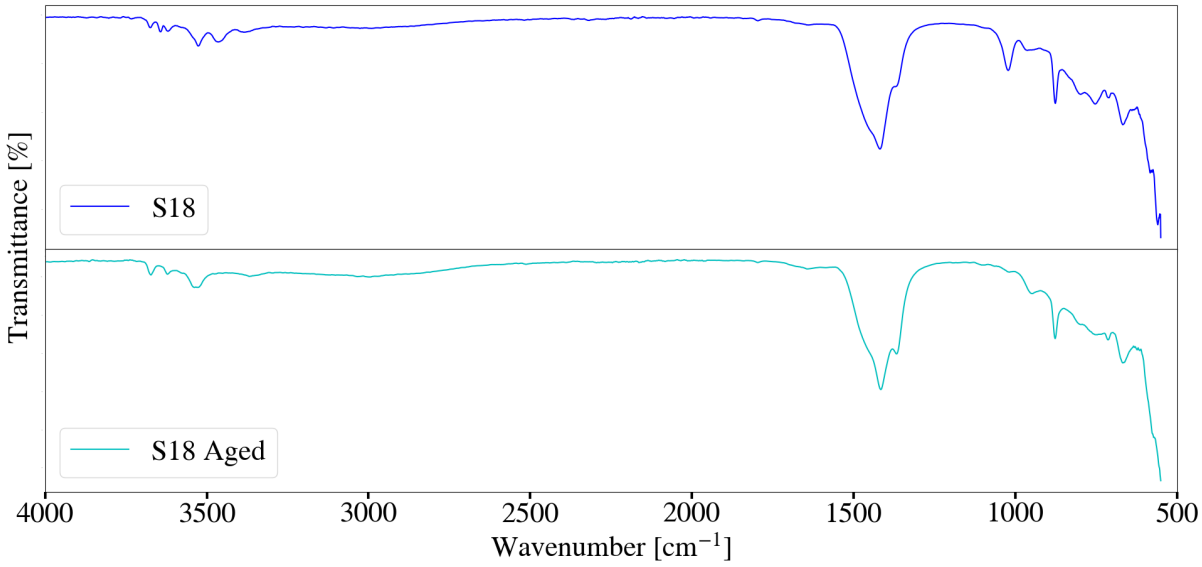


**Figure 64:** FT-IRspectra for Ca-Al LDH sample, before and after ageing, synthesised with the addition of $CaCO_3$ using a $M^{2+}$:$M^{3+}$ ratio of 2:1.

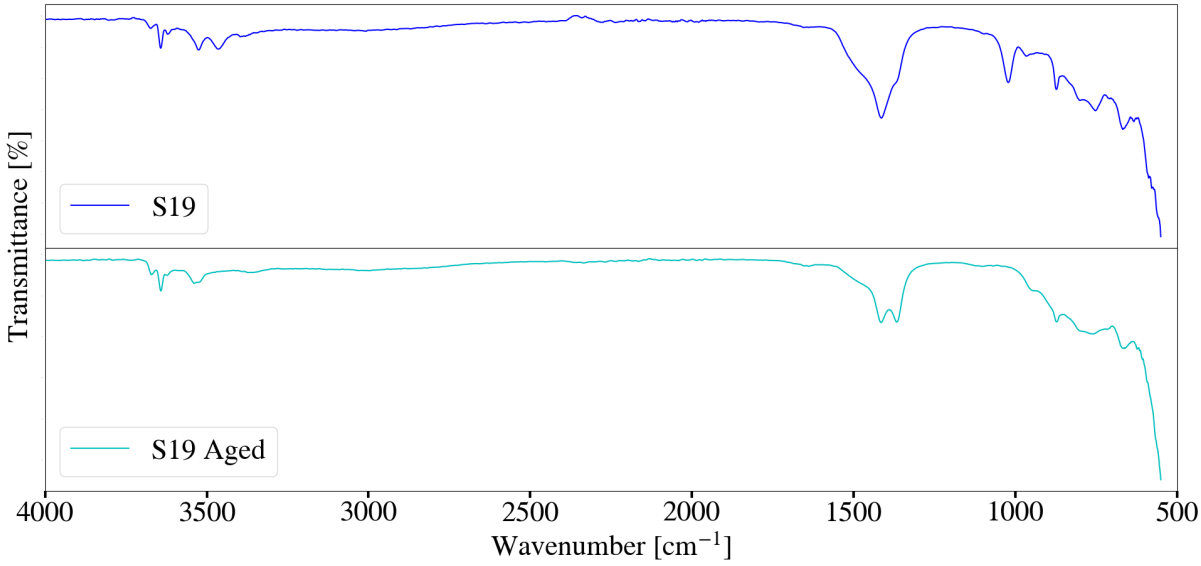


**Figure 65:** FT-IR spectra for Ca-Al LDH sample, before and after ageing, synthesised without the addition of $CaCO_3$ using a $M^{2+}$:$M^{3+}$ ratio of 2:1.

**Particle size analysis** The change in particle size with time for S18 is depicted in Figure 67. The relevant $D_{90}$, $D_{50}$ and $D_{10}$ values for the initial $Ca(OH)_2$, $CaCO_3$ and $Al(OH)_3$ mixture were 23.6 $\mu$m, 7.84 $\mu$m and 1.98 $\mu$m respectively. The large $D_{90}$ value observed at 20 min of milling could be a result of agglomeration as supported by the agglomeration tail seen in Figure 66. It was noted that after approximately 20 min of milling activity the $D_{10}$ value stabilised to below 0.70 $\mu$m at approximately 0.594 $\mu$m. Although not clearly depicted in Figure 67 the average particle size continued to decrease slightly to a final value of 1.7 $\mu$m, whereas the $D_{90}$ values fluctuated slightly to a final value of 36.9 $\mu$m.

Fluctuations in the particle size measurements could be due to the formation of LDH product within the sample. Figure 66 depicts the change in particle size distribution with time. The distributions observed varied with each time measurement and could therefore be indicative of the ongoing reaction to the desired LDH product, as seen by Figure 62. As new compounds form the distribution is predicted to continuously change until the reaction has eventually reached completion. It is unclear whether the reaction would have continued after 60 min of milling activity and can not be inferred from the distribution obtained.

Ageing of the sample resulted in the conversion of the remaining raw materials into LDH product. The particle size distribution therefore changed from a broad multi-modal distribution to that of a narrow tri-modal distribution. The final $D_{90}$, $D_{50}$ and $D_{10}$ values obtained were 24.5 $\mu$m, 3.64 $\mu$m and 1.06 $\mu$m respectively.

Comparatively the change in particle size with time for S19 is indicated in Figure 69. The original hydroxide mixture exhibited $D_{90}$, $D_{50}$ and $D_{10}$ values of 686 $\mu$m, 9.17 $\mu$m and 2.29 $\mu$m. These were observed to be higher than that of S18 and likely due to agglomeration of the raw materials. The $D_{10}$ values seemingly plateaued after 40 min of milling to below 0.70 $\mu$m, exhibiting a final value of 0.661 $\mu$m for the mixture. Comparatively the average particle size continued to decrease slightly to a final value of 2.71 $\mu$m. Overall the $D_{90}$ values fluctuated and followed an increasing trend to a final measurement of 86 $\mu$m. Although LDH formation was not as complete as that observed for S18, it did occur as could be seen by the XRD spectra in Figure 63. The increase in particle size could be a result of the extent of reaction within the system.

The distribution for S19, as seen in Figure 68, differs to that of S18 and could be attributed to the difference in reaction schemes for both systems. LDH formation for S19 did not occur as readily as that of S18 as could be seen from the XRD spectra depicted in Figures 62 and 63. The formation of chemical species directly influences the particle size distribution as they will contain differing particle sizes to that of the selected raw materials. In this case ageing of the sample did not lead to complete LDH formation, but rather the formation of the precursor katoite. The distribution therefore changed to that of a bi-modal distribution with final $D_{90}$, $D_{50}$ and $D_{10}$ values of 6.40 $\mu$m, 3.01 $\mu$m and 0.849 $\mu$m respectively.

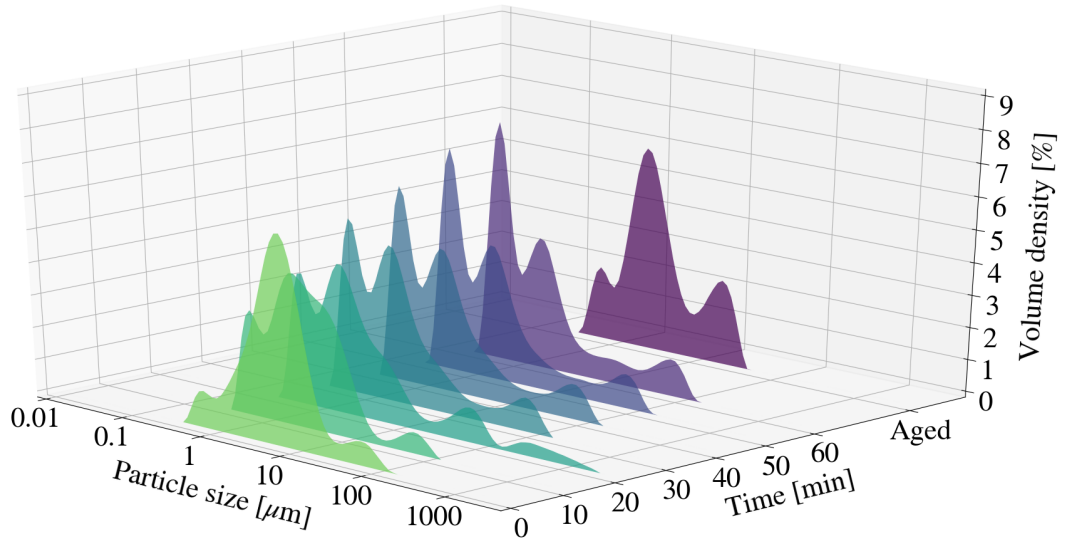


**Figure 66:** Particle size distribution with a change in time for Ca-Al LDH sample, before and after ageing, synthesised with the addition of $CaCO_3$ using a $M^{2+}$:$M^{3+}$ ratio of 2:1.

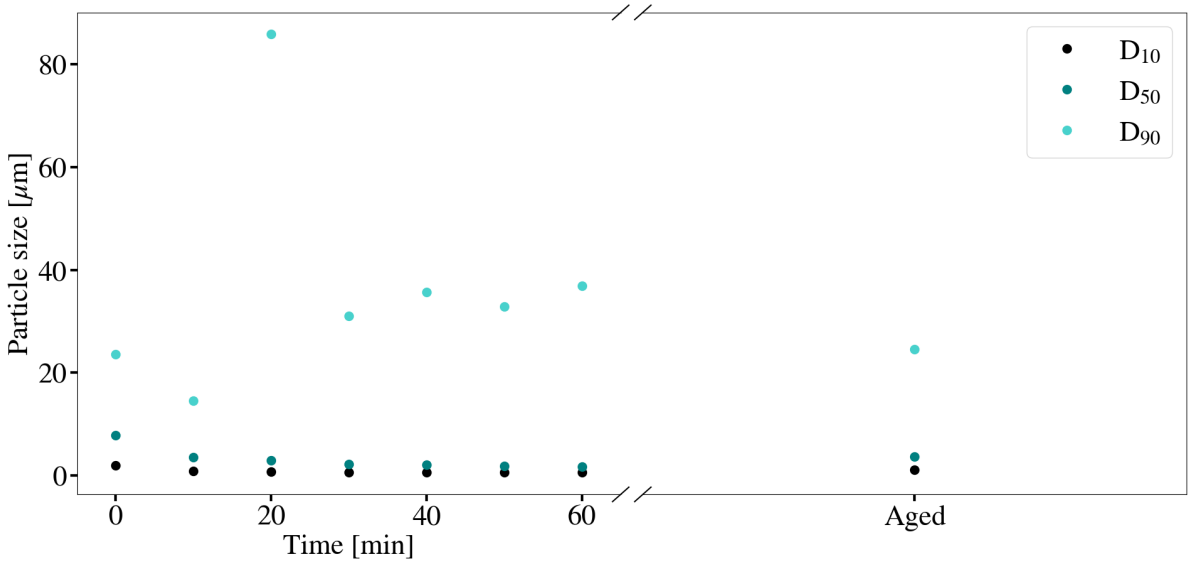


**Figure 67:** The change in particle size with time for Ca-Al LDH sample, before and after ageing, synthesised with the addition of $CaCO_3$ using a $M^{2+}$:$M^{3+}$ ratio of 2:1.

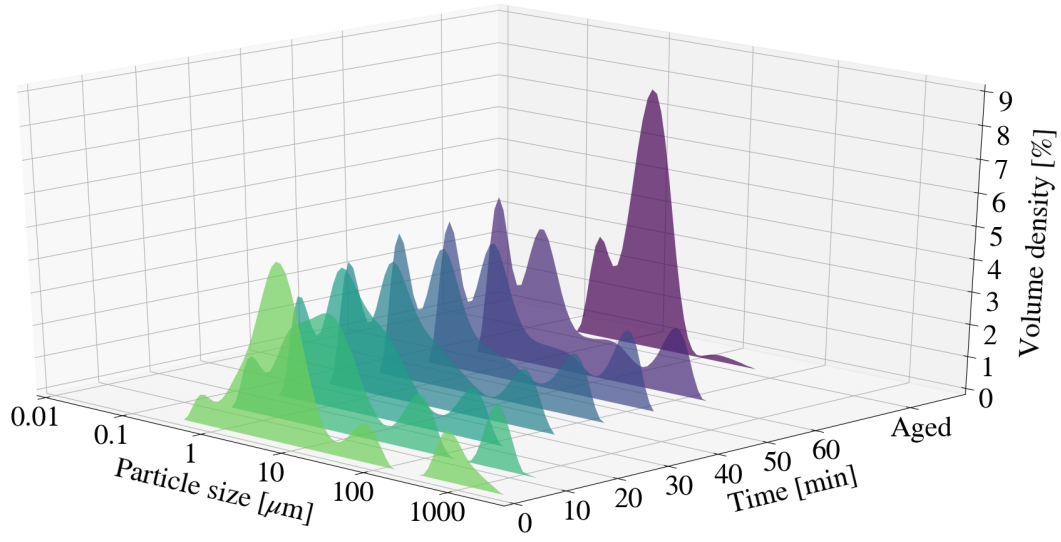


**Figure 68:** Particle size distribution with a change in time for Ca-Al LDH sample, before and after ageing, synthesised without the addition of $CaCO_3$ using a $M^{2+}$:$M^{3+}$ ratio of 2:1.

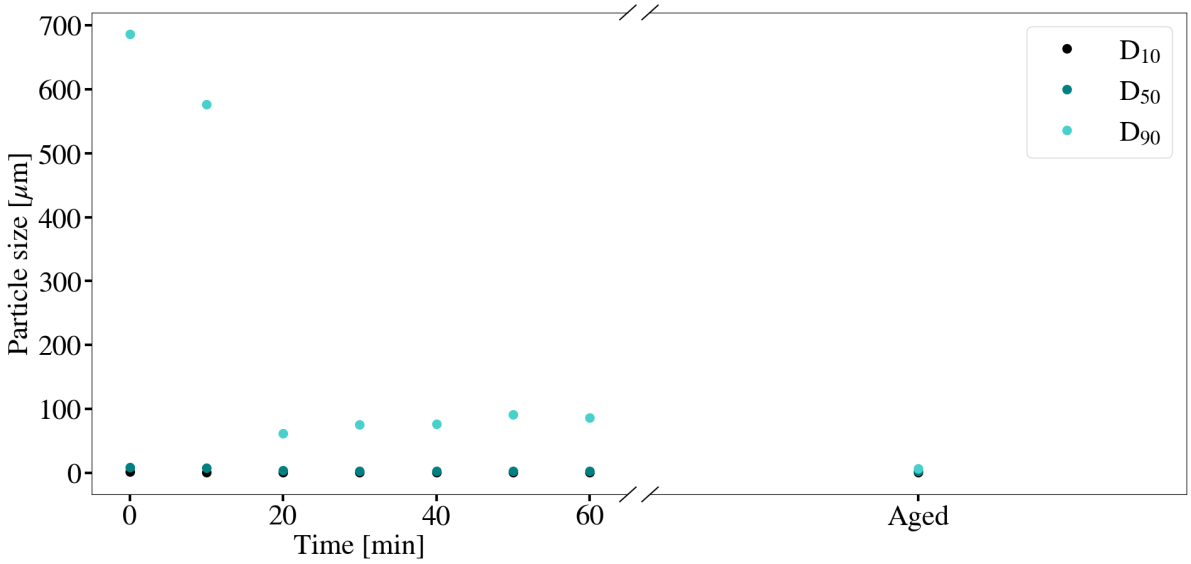


**Figure 69:** The change in particle size with time for Ca-Al LDH sample, before and after ageing, synthesised without the addition of $CaCO_3$ using a $M^{2+}$:$M^{3+}$ ratio of 2:1.

**XRF analysis** Table A.38 depicts a summary of components obtained through XRF analysis for samples S18 and S19. The ratio of $Ca^{2+}$:$Al^{3+}$ for S18 and S19 were calculated to be 2.00:1.09 and 2.00:0.94 respectively. This was found to correlate with the selected theoretical ratios and therefore calculated masses depicted in Table 6.

Impurities such as $SiO_2$, MgO, BaO and $P_2O_5$ were likely a result of retained chemical species within the mill. Whereas $Fe_2O_3$, $Cr_2O_3$, NiO, $ZrO_2$ and $Y_2O_3$ could once again be attributed to mill and milling media degradation. Differences in the LOI value could once again be attributed to the structural differences of the products. XRF analysis was conducted prior to ageing as the concentration of the non-volatile components was not expected to change. Both samples exhibited the presence of LDH, with the conversion for S18 seemingly more complete. This implies more LDH product within the measured sample and therefore a higher concentration of bonded water and interlayer $OH^-$ groups that are lost upon heating.

**SEM imaging** SEM images of S18 and S19, before and after ageing, are indicated in Figures 70 through to 77. Images were varied such that the overall sample, along with the individual particle morphology could be studied. Prior to aging both samples exhibited platelet like structures, however no deductions could be made regarding whether or not they were LDH. Ageing of the samples resulted in clear crystalline platelets for S18. Comparatively S19 exhibited crystals that resemble those of calcite and katoite as could be seen in Figures 75 and 77.

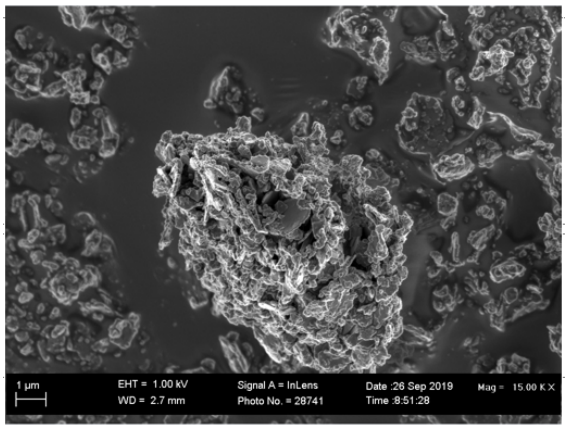


**Figure 70:** SEM imaging of Ca-Al LDH sample, before ageing, synthesised with the addition of $CaCO_3$ using a $M^{2+}$:$M^{3+}$ ratio of 2:1.

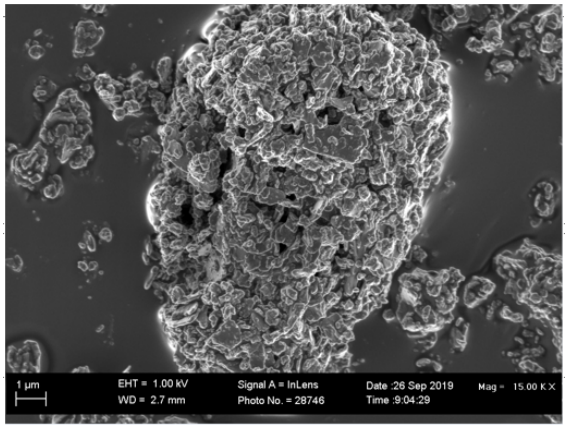


**Figure 71:** SEM imaging of Ca-Al LDH sample, before ageing, synthesised without the addition of $CaCO_3$ using a $M^{2+}$:$M^{3+}$ ratio of 2:1.

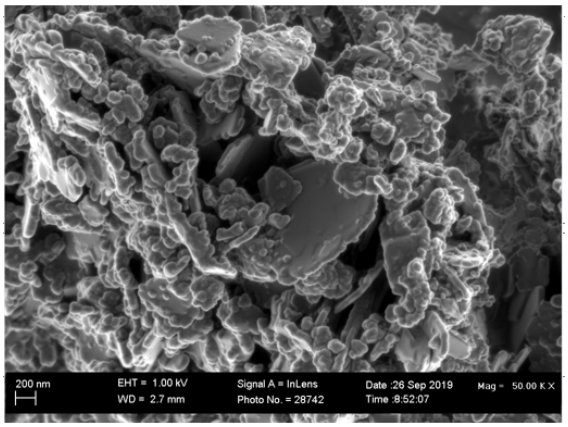


**Figure 72:** SEM imaging of Ca-Al LDH sample, before ageing, synthesised with the addition of $CaCO_3$ using a $M^{2+}$:$M^{3+}$ ratio of 2:1.

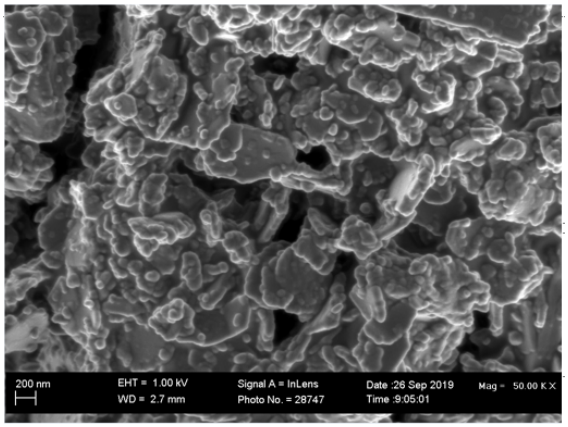


**Figure 73:** SEM imaging of Ca-Al LDH sample, before ageing, synthesised without the addition of $CaCO_3$ using a $M^{2+}$:$M^{3+}$ ratio of 2:1.

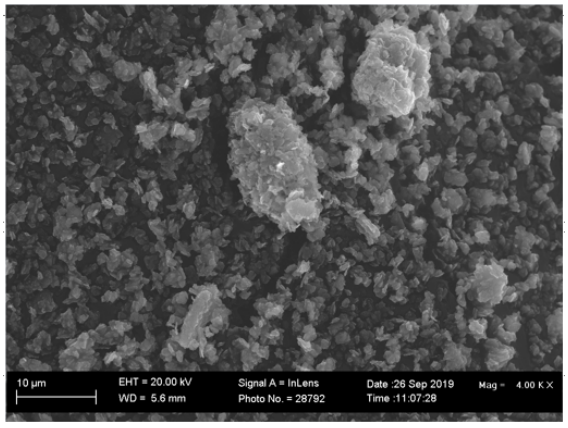


**Figure 74:** SEM imaging of Ca-Al LDH sample synthesised, after ageing, with the addition of $CaCO_3$ using a $M^{2+}$:$M^{3+}$ ratio of 2:1.

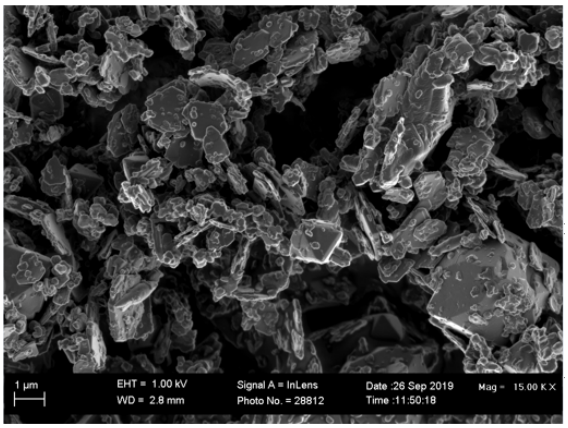


**Figure 75:** SEM imaging of Ca-Al LDH sample synthesised, after ageing, without the addition of $CaCO_3$ using a $M^{2+}$:$M^{3+}$ ratio of 2:1.

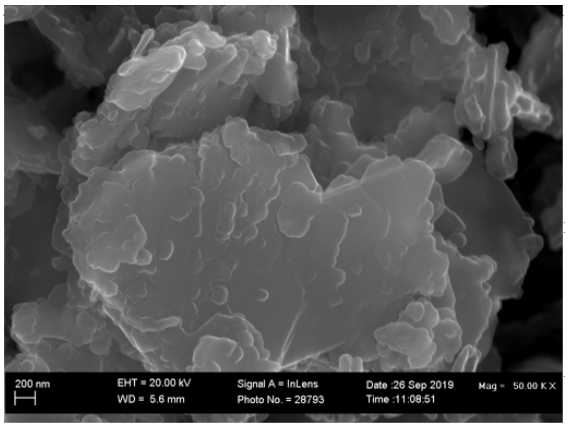


**Figure 76:** SEM imaging of Ca-Al LDH sample synthesised, after ageing, with the addition of $CaCO_3$ using a $M^{2+}$:$M^{3+}$ ratio of 2:1.

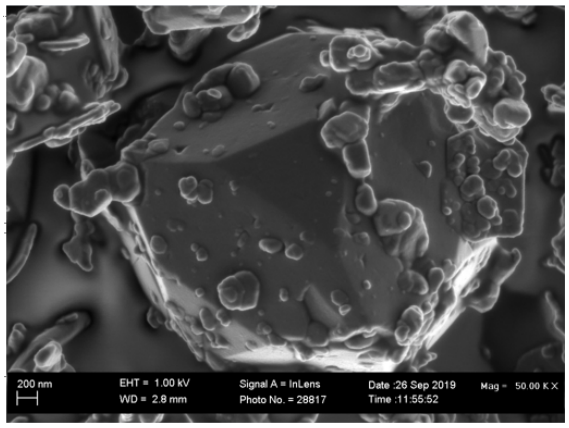


**Figure 77:** SEM imaging of Ca-Al LDH sample synthesised, after ageing, without the addition of $CaCO_3$ using a $M^{2+}$:$M^{3+}$ ratio of 2:1.

### 6.2.3 Zn-Al LDH

**XRD analysis** The synthesis of Zn-Al LDH was conducted making use of two different zinc sources, namely zinc basic carbonate ($Zn_5(CO_3)_2(OH)_6$) and zinc oxide (ZnO). The synthesised samples will be further referred to as S20 and S21 respectively. Ageing was conducted at 80 °C for 24 h after milling was completed.

XRD spectra associated with S20 is as depicted in Figure 79. A primary LDH peak was prominent at a $2\theta$ value of 13.86°, corresponding to a d-spacing of 0.749 nm. Conversion, prior to ageing was incomplete with $Zn_5(CO_3)_2(OH)_6$ and $Al(OH)_3$ peaks visible at $2\theta$ values of 15.08°and 21.31°. Comparatively the peak intensity of the selected raw materials

after ageing were reduced, however still present. A prominent primary LDH peak was observed at a $2\theta$ value of 13.70°, corresponding to a calculated d-spacing of 0.748 nm. The LDH peak intensity increased drastically and could be due to an increase in crystallinity and increase in conversion of raw materials to product. Synthesis with a 1:1 $M^{2+}$:$M^{3+}$ ratio is considered unconventional for LDH synthesis (Forano et al., 2006). It should however be noted that (Qu, He, M Chen, Huang, et al., 2017) tested the effect of $M^{2+}$:$M^{3+}$ ratio on Zn-Al LDH formation and the XRD spectra exhibited no raw material peaks.

Comparatively Figure 78 depicts the spectra for S21. LDH peaks were observed to be present after milling, however conversion was mostly incomplete. Ageing of the sample did not seem to influence the conversion of raw materials to LDH product, with peaks remaining fairly constant. The d-spacing values before and after ageing were calculated to be 0.751 nm at 13.65°and 0.753 nm at 13.62°respectively. ZnO is available in more or less active forms and depends on the method with which it is synthesised. The most inactive form results upon calcination of Zn hydroxide or carbonate (Pourbaix, 1974). The selected ZnO was prepared through vaporizing Zn metal. When exposed to air, the Zn vapour reacts with $O_2$ to form ZnO. This could possibly be a contributing factor to the observed stability of the ZnO. Similarly according to (Pourbaix, 1974) Zn oxides and hydroxides pass through a minimum in solubility at a pH of 9.4. Investigation of the effect of pH on the Zn-Al LDH formation system, would therefore be of interest for future studies.

Additionally the lack of a carbonate source should be further considered. It could be possible that, due to the synthesis not being conducted in an inert environment, atmospheric carbonate contamination contributed to the formation of the LDH product observed. No direct carbonate source prevents further reaction to a stable LDH phase as could be seen in Section 6.2.2.

The average temperatures for both samples are as summarised in Table 28. The total energy removed from the system by the cooling water was determined to be 0.44 kW and 0.55 kW for S20 and S21 respectively.

**Table 27:** Summary of calculated parameters associated with the heat removed by jacket water for samples synthesised with the use of ZnO or $Zn_5(CO_3)_2(OH)_6$, using a $M^{2+}$:$M^{3+}$ ratio of 1:1.

| Zinc Source | T1 [K] | T2 [K] | Molar Flow [kmol·h$^{-1}$] | Cp [J·kmol$^{-1}$·K$^{-1}$] | Cp [kJ·kmol$^{-1}$·K$^{-1}$] | Q [kJ·h$^{-1}$] | Q [kJ·s$^{-1}$] |
|---|---|---|---|---|---|---|---|
| $Zn_5(CO_3)_2(OH)_6$ | 302.63 | 303.35 | 29.29 | 75321.08 | 75.32 | 1588.70 | 0.44 |
| ZnO | 301.87 | 302.78 | 29.26 | 75330.45 | 75.33 | 2005.60 | 0.55 |

**Table 28:** Average temperature and flowrate measurements obtained for Zn-Al LDH samples synthesised with the use of ZnO or $Zn_5(CO_3)_2(OH)_6$, using a $M^{2+}$:$M^{3+}$ ratio of 1:1.

| Zinc source | Flow rate [L·h$^{-1}$] | Inlet [°C] | Outlet [°C] | Reactor [°C] |
|---|---|---|---|---|
| $Zn_5(CO_3)_2(OH)_6$ | 527.31 | 29.48 | 30.20 | 32.47 |
| ZnO | 526.63 | 28.72 | 29.63 | 31.55 |

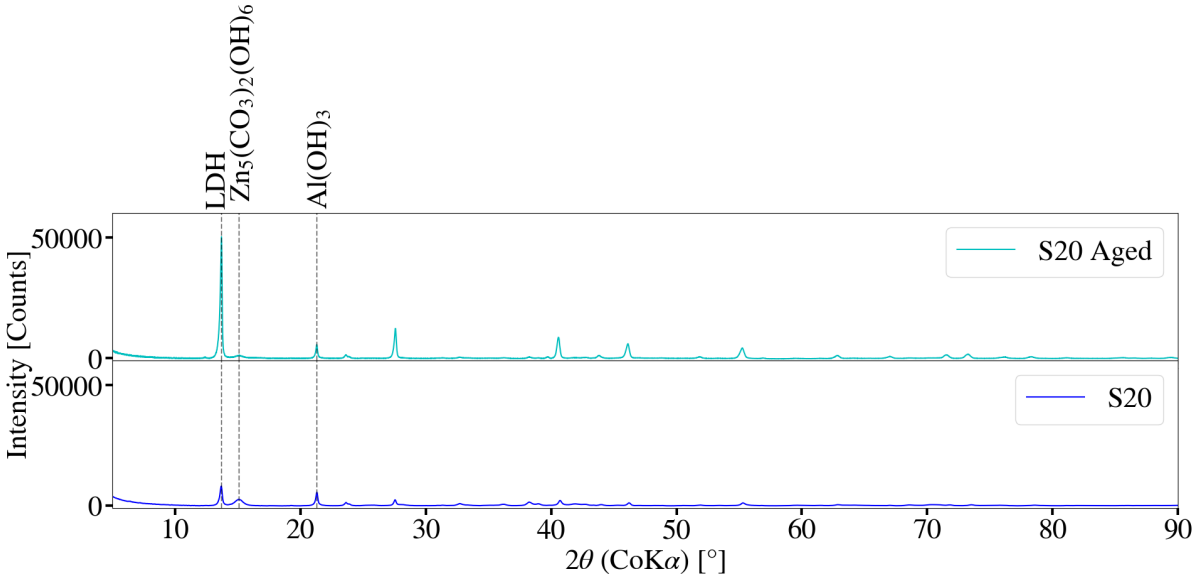


**Figure 78:** XRD spectra for Zn-Al LDH sample, before and after ageing, synthesised making use of $Zn_5(CO_3)_2(OH)_6$, with a $M^{2+}$:$M^{3+}$ ratio of 1:1.

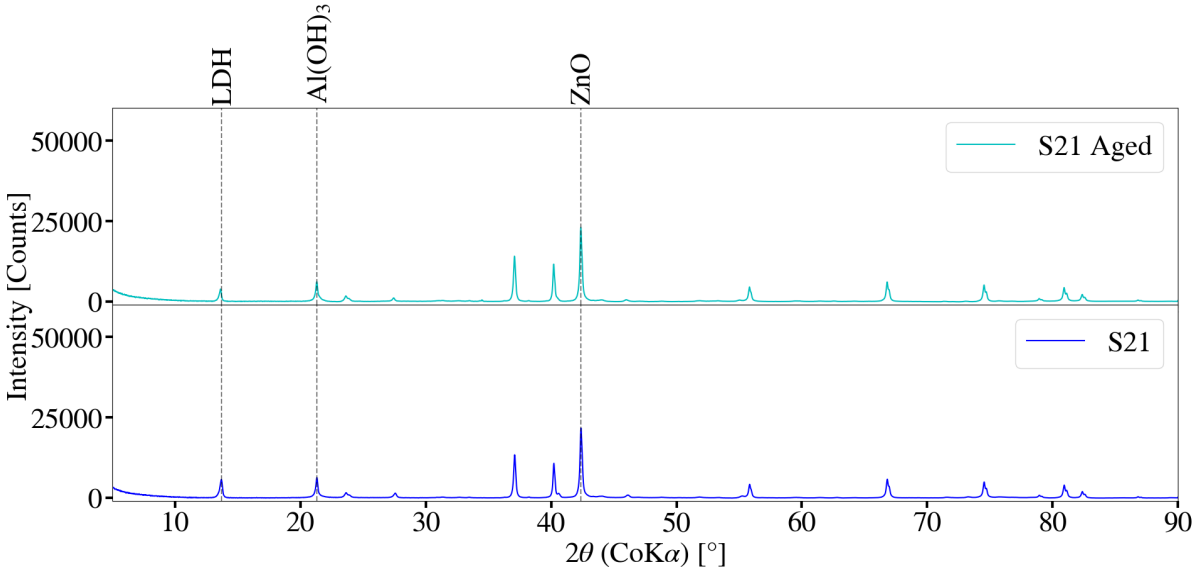


**Figure 79:** XRD spectra for Zn-Al LDH sample, before and after ageing, synthesised making use of ZnO, with a $M^{2+}$:$M^{3+}$ ratio of 1:1.

**FT-IR analysis** The FT-IR spectra for sample S20 is depicted in Figure 80. The peaks observed at and before 3465 $cm^{-1}$ can be attributed to the stretching vibrations of bonded –OH groups (Qu, He, M Chen, Huang, et al., 2017) (Nicolet, 2019). The peaks located between 3500 $cm^{-1}$ and 3700 $cm^{-1}$, specifically 3525 $cm^{-1}$, are likely due to the free –OH groups located within the sample (Qu, He, M Chen, Huang, et al., 2017) (Nicolet, 2019). Minor differences were observed between the spectra of the $Zn_5(CO_3)_2(OH)_6$ and S20. This could largely be due to unreacted $Zn_5(CO_3)_2(OH)_6$ within the sample. Ageing of the sample resulted in the formation of broad peaks between 3000 $cm^{-1}$ and $3700^{-1}$. This

could once-again be attributed to bonded and free -OH within the sample. A prominant peak at approximately 1355 $cm^{-1}$ and 1019 $cm^{-1}$ was observed to form. This is likely due to the carbonate interactions within the interlayer of the LDH (Socrates, 2001).

Figure 81 depicts the FT-IR spectra for S21. Little difference was observed between spectra obtained prior to ageing and that after ageing. Peaks were observed to occur from 3300 $cm^{-1}$ to 3700 $cm^{-1}$. This is likely due to bonded and free -OH within the sample due to the formation of LDH as seen by the XRD spectra for S21 (Nicolet, 2019). Similarly a peak at 1356 $cm^{-1}$ was observed. This is indicative of carbonate contamination within the system as it is likely due to carbonate interactions within the sample (Socrates, 2001).

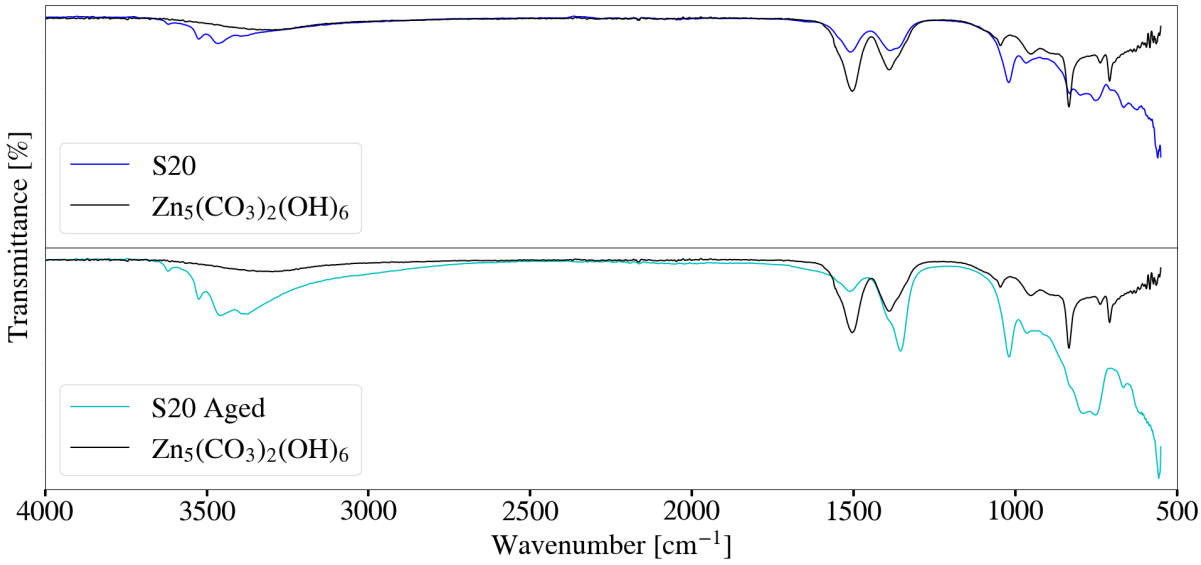


**Figure 80:** FT-IR spectra for Zn-Al LDH sample, before and after ageing, synthesised making use of $Zn_5(CO_3)_2(OH)_6$, with a $M^{2+}$:$M^{3+}$ ratio of 1:1.

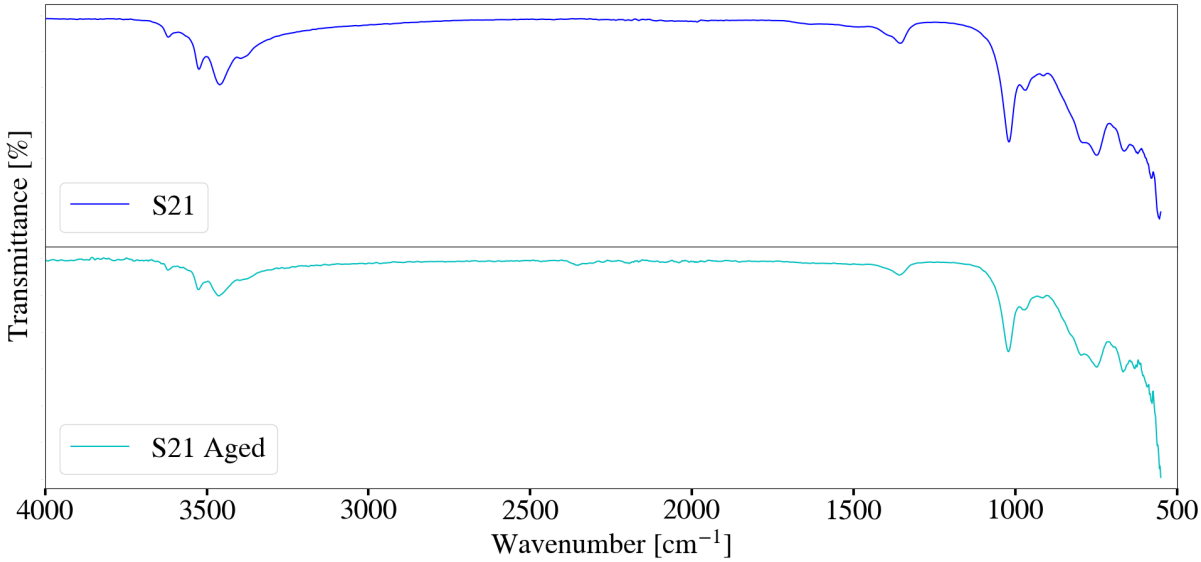


**Figure 81:** FT-IR spectra for Zn-Al LDH sample, before and after ageing, synthesised making use of ZnO, with a $M^{2+}$:$M^{3+}$ ratio of 1:1.

**Particle size analysis** Figure 82 depicts the change in particle size with time for S20. The original mixture of $Zn_5(CO_3)_2(OH)_6$ and $Al(OH)_3$ contained measured $D_{90}$, $D_{50}$ and $D_{10}$ values of 10.5 $\mu$m, 4.13 $\mu$m and 1.71 $\mu$m prior to milling. A decreasing trend was observed for each of the measured particle sizes throughout the milling period, resulting in final values of 4.83 $\mu$m , 2.51 $\mu$m and 0.77 $\mu$m respectively, after 60 min of milling. Ageing of the sample resulted in final $D_{90}$, $D_{50}$ and $D_{10}$ values of 16.80 $\mu$m , 2.74 $\mu$m and 0.668 $\mu$m.

The change in the particle size distribution with time for S20 is depicted in Figure 83. Minor changes were observed in the overall shape of the bi-modal distributions observed. It was noted that despite minor changes observed, LDH formation and reaction does occur during the milling process as supported by the XRD spectra in Figure 79. Aeging of the sample resulted in a multi-modal distribution. Conversion of raw material to LDH product as well as a change in the crystallinity of the sample could have contributed to the difference in distributions observed.

Comparatively Figures 84 and 85 depict the change in particle size and distribution of sample S21. The mixture of raw materials initially exhibited $D_{90}$, $D_{50}$ and $D_{10}$ values of 11.50 $\mu$m, 5.45 $\mu$m and 1.67 $\mu$m respectively. This decreased steadily until final values of 5.68 $\mu$m, 3.02 $\mu$m and 0.837 $\mu$m were reached. Ageing of the sample resulted in the overall increase in these values to 6.34 $\mu$m, 3.83 $\mu$m and 1.9 $\mu$m respectively. This could be due to possible crystallite growth and further reaction occurring during the ageing step. The overall distribution exhibited was bi-modal with the distribution narrowing gradually with an increase in milling time. Ageing, however, resulted in a very narrow

bi-modal peaks. This could be further attributed to a change in crystallite size or the present reaction scheme. It should be noted however that the XRD spectra indicated very little change between the milled sample and the aged sample.

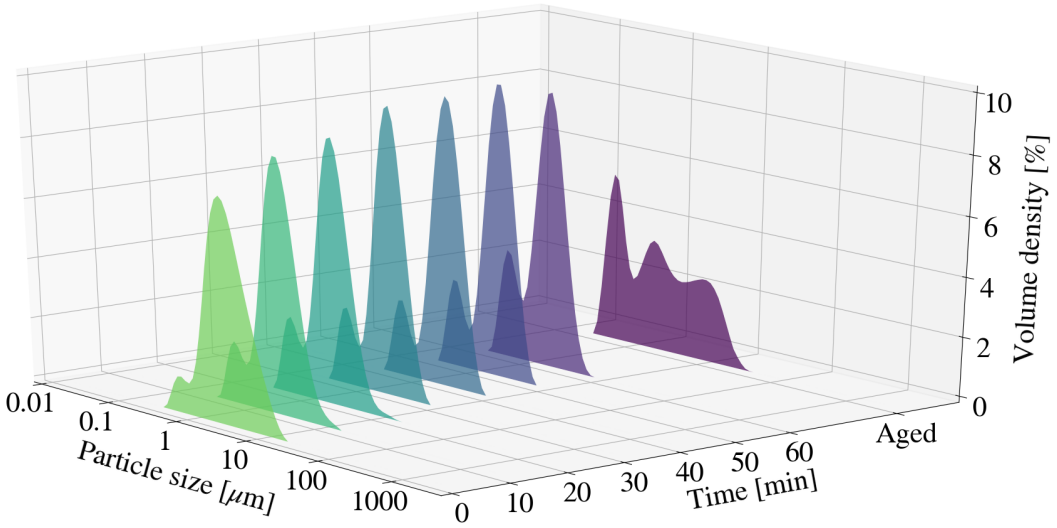


**Figure 82:** Particle size distribution with a change in time for Zn-Al LDH sample, before and after ageing, synthesised with the use of $Zn_5(CO_3)_2(OH)_6$, with a $M^{2+}$:$M^{3+}$ ratio of 1:1.

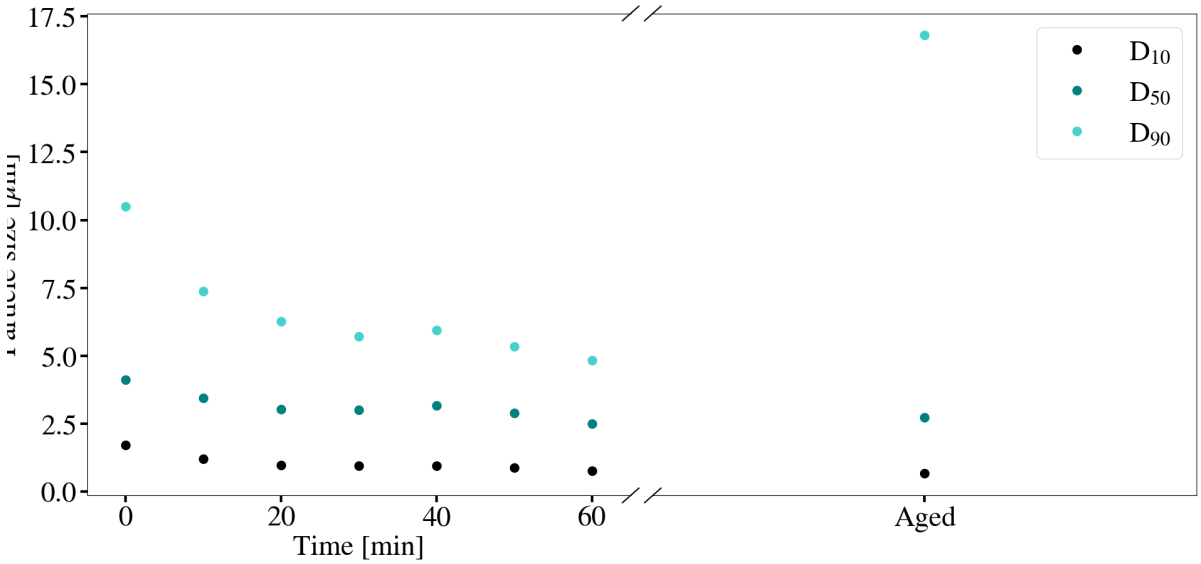


**Figure 83:** The change in particle size with time for Zn-Al LDH sample, before and after ageing, synthesised with the use of $Zn_5(CO_3)_2(OH)_6$, with a $M^{2+}$:$M^{3+}$ ratio of 1:1.

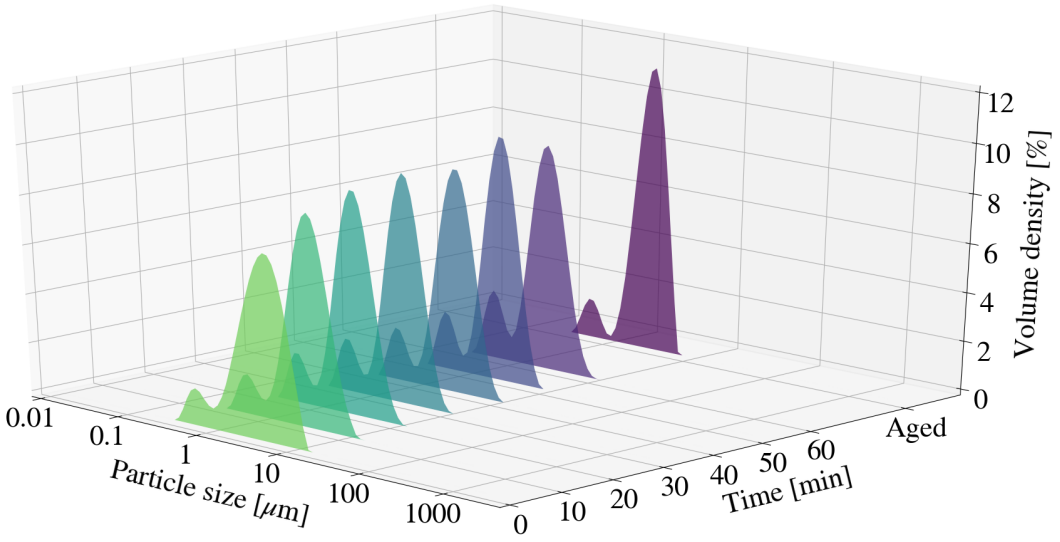


**Figure 84:** Particle size distribution with a change in time for Zn-Al LDH sample, before and after ageing, synthesised with the use of ZnO, with a $M^{2+}$:$M^{3+}$ ratio of 1:1.

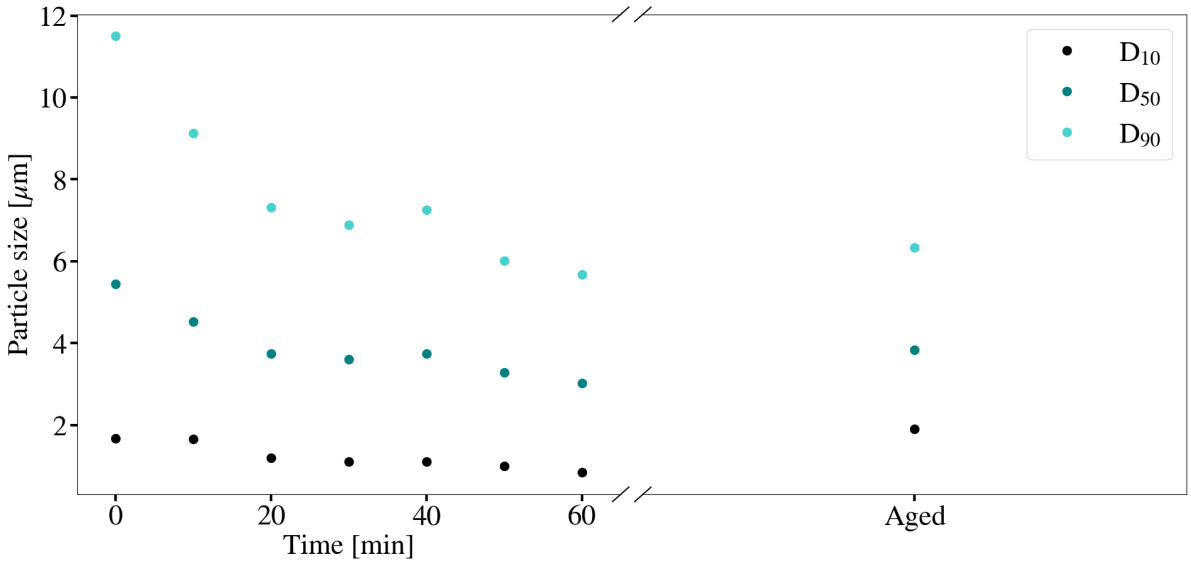


**Figure 85:** The change in particle size with time for Zn-Al LDH sample, before and after ageing, synthesised with the use of ZnO, with a $M^{2+}$:$M^{3+}$ ratio of 1:1.

**XRF analysis** Table A.39 depicts the chemical species obtained for S20 and S21 from XRF analysis. The synthesis of Zn-Al LDH was attempted making use a 1.00:1.00 $M^{2+}$:$M^{3+}$ metal ratio. The calculated ratios were determined to be 1.00:1.01 and 1.00:1.18 for S20 and S21 respectively. The calculated masses depicted in Table 6 were therefore an accurate representation of the selected molar ratios.

Each sample exhibited impurities such as CaO, MgO, CuO, $SiO_2$ and BaO that could

be attributed to retained chemical species within the milling chamber and system. The degradation of milling media along with the milling chamber could once again be the cause of impurities such as $Fe_2O_3$, $Cr_2O_3$, NiO, $ZrO_2$ and $MoO_3$. It was noted that impurities not associated with mill degradation were inconsistent when looking at the different samples obtained.

The formation of LDH was observed to occur more readily for S20 when compared to S21. The differences observed in the LOI values could be attributed to the difference in structure of compounds present within each sample. S20 contained a mixture of LDH, as well as the selected raw materials. Comparitively, S21 consisted of a mixture of ZnO, $Al(OH)_3$ and LDH.

**SEM imaging** SEM imaging for sample S21, before and after ageing, is depicted in Figures 86 and 88. It was noted that the sample exhibited more platelet type structures after ageing. Comparitively the SEM imaging for S20 is as depicted in Figures 87 and 89. Prior to ageing of the sample, LDH-like hexagonal platelets were dispersed throughout the sample. Such platelets were observed to be less common after ageing, however were still identified.

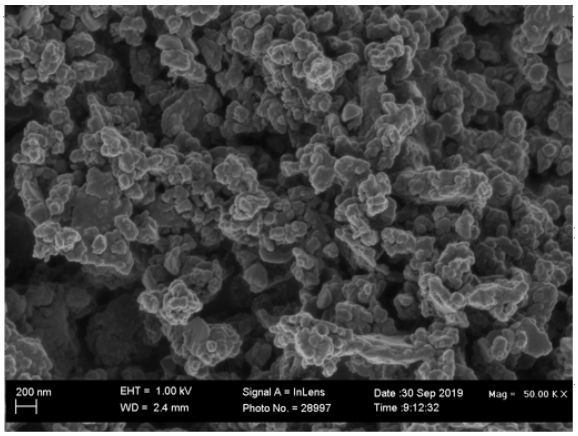


**Figure 86:** SEM imaging of Zn-Al LDH sample synthesised with the use of $Zn_5(CO_3)_2(OH)_6$ prior to ageing.

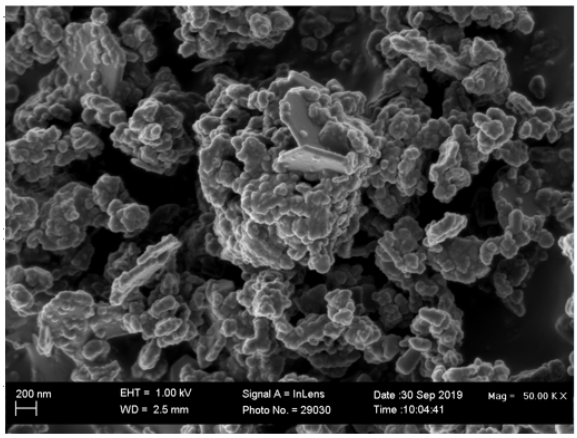


**Figure 87:** SEM imaging of Zn-Al LDH sample synthesised with the use of ZnO prior to ageing.

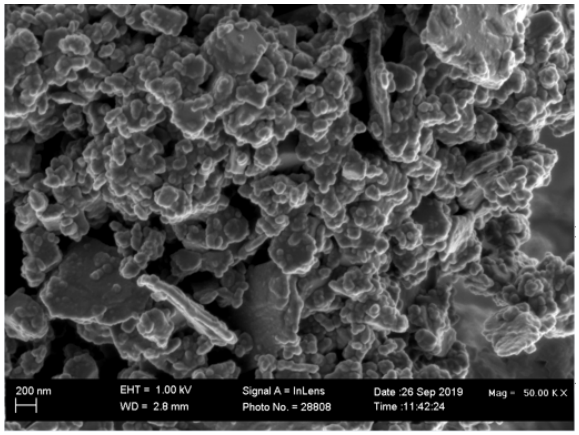


**Figure 88:** SEM imaging of Zn-Al LDH sample synthesised with the use of $Zn_5(CO_3)_2(OH)_6$ after ageing.

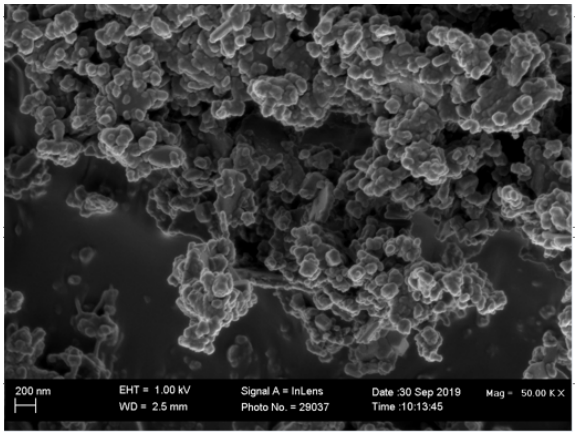


**Figure 89:** SEM imaging of Zn-Al LDH sample synthesised with the use of ZnO after ageing.

### 6.2.4 Cu-Al LDH

**XRD analysis** The synthesis of Cu-Al LDH was attempted making use of commercial grade $Cu_2(OH)_2CO_3$ and $Al(OH)_3$. The synthesis was conducted making use of a 2:1 and 4:1 $M^{2+}$:$M^{3+}$ metal ratio. The samples were labelled S22 and S23 accordingly. Ageing was conducted at 80 °C for a period of 24 h under atmospheric conditions. The respective XRD spectra for each sample, along with that of $Cu_2(OH)_2CO_3$ is depicted in Figures 90 and 91.

The XRD spectra for $Cu_2(OH)_2CO_3$ was found to be dominant, overlapping that of other components present. The presence of LDH was therefore difficult to confirm through XRD spectra alone for both samples.

The spectra for S22, before ageing, indicated a minor primary LDH peak at a $2\theta$ value of 13.82°. This was found to correspond to a calculated d-spacing of approximately 0.742 nm. The peak associated with $Cu_2(OH)_2CO_3$ was found to slightly overlap this primary LDH peak at 13.89°. No other LDH peaks were obvious. Comparatively ageing of the sample resulted in a more prominent primary peak, at 13.74°, with a calculated d-spacing of 0.746 nm. It was noted that a secondary peak was present at 27.76°. Conversion was incomplete despite the incorporated of an ageing step. A decrease in the respective $Al(OH)_3$ and $Cu_2(OH)_2CO_3$ peaks were however observed.

The XRD spectra for S23 indicate the presence of a small primary peak located at a $2\theta$ value of 13.79°, corresponding to a d-spacing of approximately 0.743 nm. The peak was found to closely coincide with a $Cu_2(OH)_2CO_3$ peak located at a $2\theta$ value of 13.89°. Conversion was incomplete with the presence of both $Cu_2(OH)_2CO_3$ and $Al(OH)_3$ peaks.

Comparatively once ageing was complete, the primary LDH peak, located at a $2\theta$ value of 13.7°, was found to be more prominent. This peak intensity was found to correspond with a d-spacing of 0.748 nm. A secondary LDH peak was observed at 27.64°, the rest of the LDH spectra was however not visible due to the presence of $Cu_2(OH)_2CO_3$ and $Al(OH)_3$.A reduction in the $Al(OH)_3$ peak was noted, however little change was observed for the $Cu_2(OH)_2CO_3$ and $Al(OH)_3$ peaks. Conversion was not complete despite the ageing process.

Table 30 summarises the average temperatures and flowrates measured for samples S22 and S23. The total energy removed with the use of cooling water was estimated to be 0.34 kW and 0.32 kW respectively. The calculated parameters associated with the heat transferred to the jacket water is summarised in Table 29.

**Table 29:** Summary of calculated parameters associated with the heat removed by jacket water for Cu-Al samples synthesised with a change in $M^{2+}$:$M^{3+}$ ratio.

| $M^{2+}$:$M^{3+}$ | T1 [K] | T2 [K] | Molar Flow [kmol·h$^{-1}$] | Cp [J·kmol$^{-1}$·K$^{-1}$] | Cp [kJ·kmol$^{-1}$·K$^{-1}$] | Q [kJ·h$^{-1}$] | Q [kJ·s$^{-1}$] |
|---|---|---|---|---|---|---|---|
| 2:1 | 304.21 | 304.77 | 29.18 | 75303.28 | 75.30 | 1230.63 | 0.34 |
| 4:1 | 303.34 | 303.87 | 29.11 | 75312.80 | 75.31 | 1162.01 | 0.32 |

**Table 30:** Average temperature and flowrate measurements obtained for Cu-Al LDH samples synthesised with a change in $M^{2+}$:$M^{3+}$ ratio.

| Sample | Flow rate [L·h$^{-1}$] | Inlet [°C] | Outlet [°C] | Reactor [°C] |
|---|---|---|---|---|
| S7 | 525.29 | 31.06 | 31.62 | 33.56 |
| S8 | 524.01 | 30.19 | 30.72 | 32.14 |

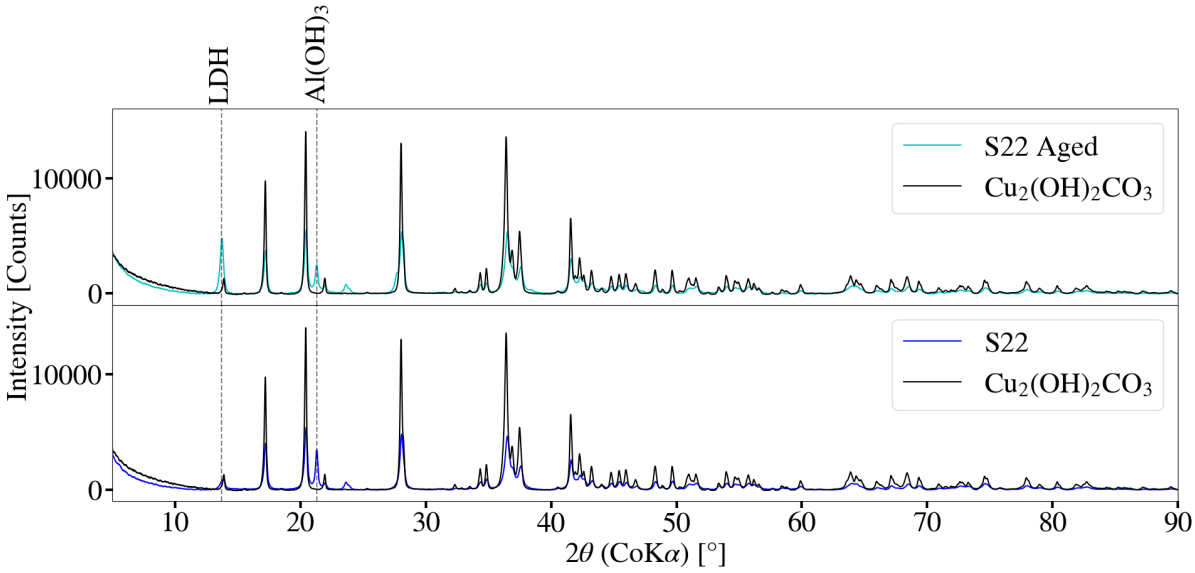


**Figure 90:** XRD spectra for Cu-Al LDH sample, before and after ageing, synthesised making use of a $M^{2+}$:$M^{3+}$ ratio of 2:1.

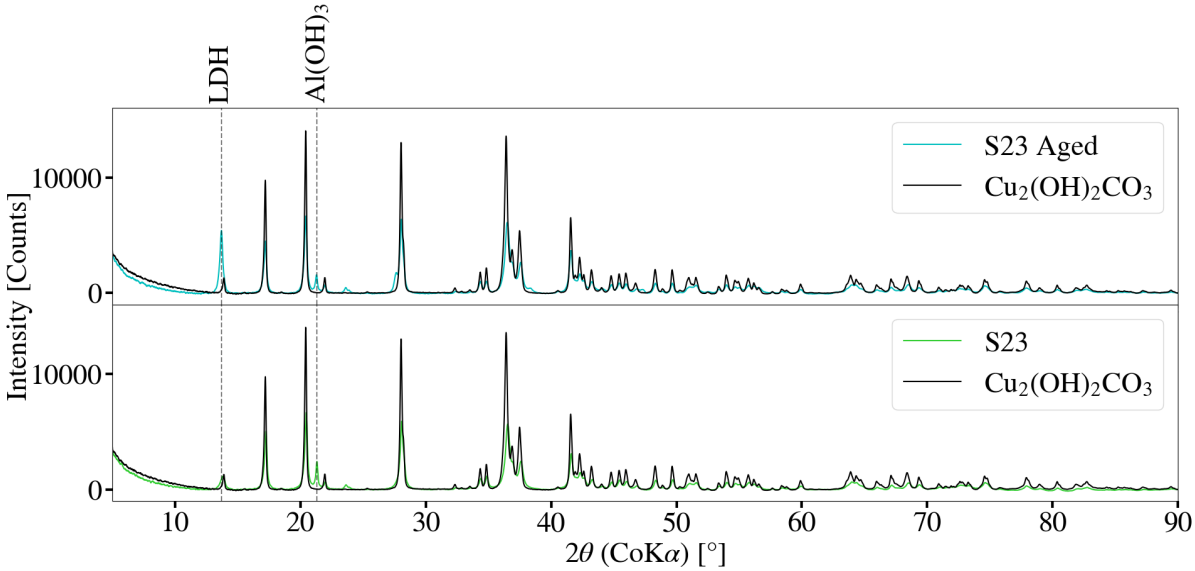


**Figure 91:** XRD spectra for Cu-Al LDH sample, before and after ageing, synthesised making use of a $M^{2+}$:$M^{3+}$ ratio of 4:1.

**FT-IR analysis** The FT-IR spectra for samples S22 and S23, before and after ageing is depicted in Figures 92 and 93. The spectra for $Cu_2(OH)_2CO_3$ was plotted alongside each sample. All 4 samples depicted similar spectra to that of the $Cu_2(OH)_2CO_3$. Identification of bonds that are associated with the LDH was therefore difficult and inconclusive. It was however noted that additional peaks were observed to occur between 3300 $cm^{-1}$ and 3700 $cm^{-1}$ and could possibly be the result of LDH formation. Aeging resulted in a broader, higher intensity peaks in this region. This is likely due to bonded and free -OH within the sample (Nicolet, 2019). This could possibly e related to the formation of LDH

within the system. Ageing resulted in minor peaks at 1632 $cm^{-1}$ (S22) and 1628 $cm^{-1}$ (S23) which were not present in the spectra for $Cu_2(OH)_2CO_3$, this however correlated to Cu-Al LDH spectra in literature (Qu, He, M Chen, Q Zhang, et al., 2017) and could possibly be due to the formation of LDH as seen by XRD spectra obtained.

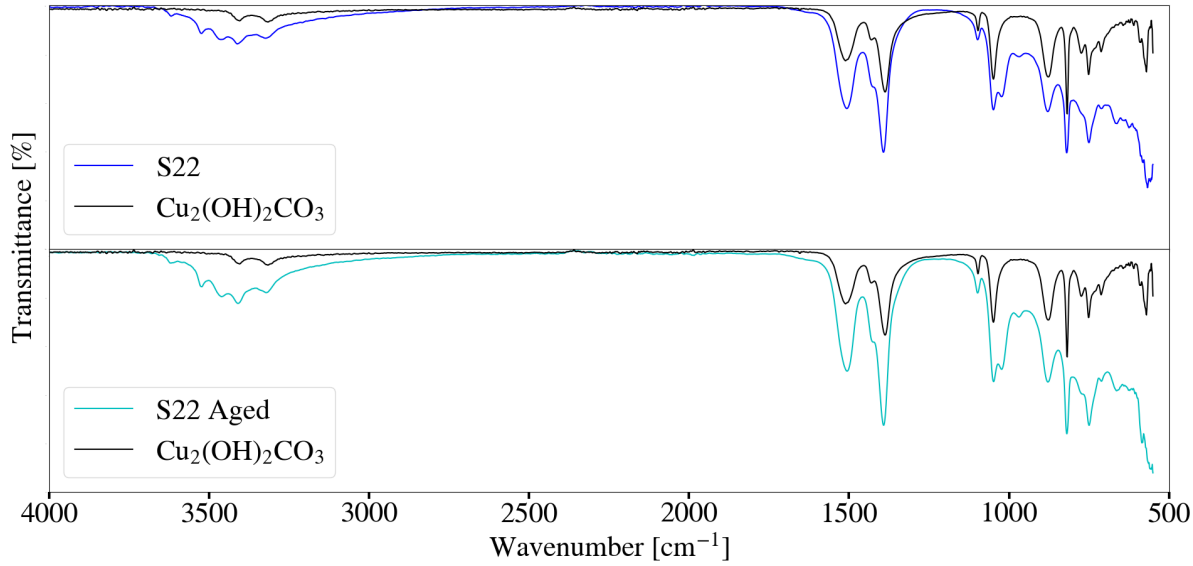


**Figure 92:** FT-IR spectra for Cu-Al LDH sample, before and after ageing, synthesised making use of a $M^{2+}$:$M^{3+}$ ratio of 2:1.

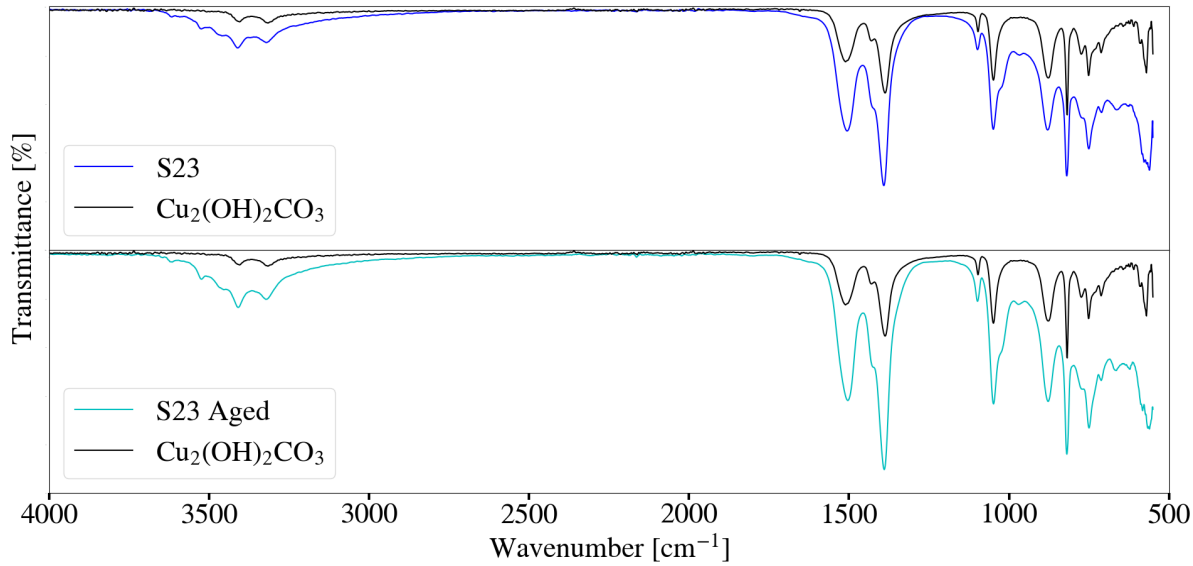


**Figure 93:** FT-IR spectra for Cu-Al LDH sample, before and after ageing, synthesised making use of a $M^{2+}$:$M^{3+}$ ratio of 4:1.

**Particle size analysis** The change in the particle size for S22 and S23 are as indicated in Figures 95 and 97. The raw material mixture for S22 depicted $D_{90}$, $D_{50}$ and $D_{10}$ values of 15.6 $\mu$m, 5.55 $\mu$m and 1.34 $\mu$m. Decreasing trends were observed for the measured $D_{90}$

and $D_{10}$ distributions to final values of 4.93 $\mu$m and 0.764 $\mu$m. The average particle size continued to decrease only slightly after 10 min of milling, to a final value of 2.43 $\mu$m.

Minor changes were observed for the shape of the bi-modal distributions in Figure 94 after approximately 20 min of milling activity. It was unclear whether LDH formation occurred during the milling process, as peaks were not present prior to ageing as seen by the XRD spectra in Figure 90. Ageing of the S22 resulted in a complete shift in the bi-modal distribution as can be seen in Figure 94. The final $D_{90}$, $D_{50}$ and $D_{10}$ values obtained were thus 7.82 $\mu$m, 1.81 $\mu$m and 0.6 $\mu$m. The change in the distribution and particle size could be attributed to the further conversion of raw materials to LDH product as seen by the XRD spectra obtained in Figure 90, as well as potential crystal growth. SEM imaging is required to determine the extent at which the sample morphology has changed compared to the milled sample obtained prior to ageing. This is further discussed in Section 6.2.4.

Figure 97 refers to the change in particle size with milling time for S23. The selected raw material mixture, consisting of an excess of $Cu_2(OH)_2CO_3$, resulted in initial $D_{90}$, $D_{50}$ and $D_{10}$ values of 17 $\mu$m, 5.45 $\mu$m and 1.29 $\mu$m respectively. This was observed to differ from that of S22 and is likely due to the greater concentration of $Cu_2(OH)_2CO_3$ present within sample S23 prior to milling. Particle size reduction occurs, with slight fluctuations occurring in the relevant $D_{90}$, $D_{50}$ and $D_{10}$ values throughout the milling process. The average particle size was determined to decrease to approximately 3 $\mu$m after 10 min of milling, exhibiting a final value of 3.01 $\mu$m after 60 min of milling. Similarly the $D_{90}$ and $D_{10}$ values reduced to that of 5.61 $\mu$m and 0.889 $\mu$m at the end of the 1 h milling process.

The change in particle size distribution with time, exhibited in Figure 96, was similar to that of S22. Minor differences between each sampling interval were observed after approximately 20 min of milling. Ageing of the sample resulted in $D_{90}$, $D_{50}$ and $D_{10}$ values of 11.2 $\mu$m, 2.58 $\mu$m and 0.672 $\mu$m respectively. A shift in the particle size distribution could once again be observed. The distribution was observed to have a similar shape to that of S22, however likely differ due to the difference in $M^{2+}$:$M^{3+}$ ratio. The conversion to LDH material as well as potential crystallite growth could further be a contributing factor to the observed change in distribution.

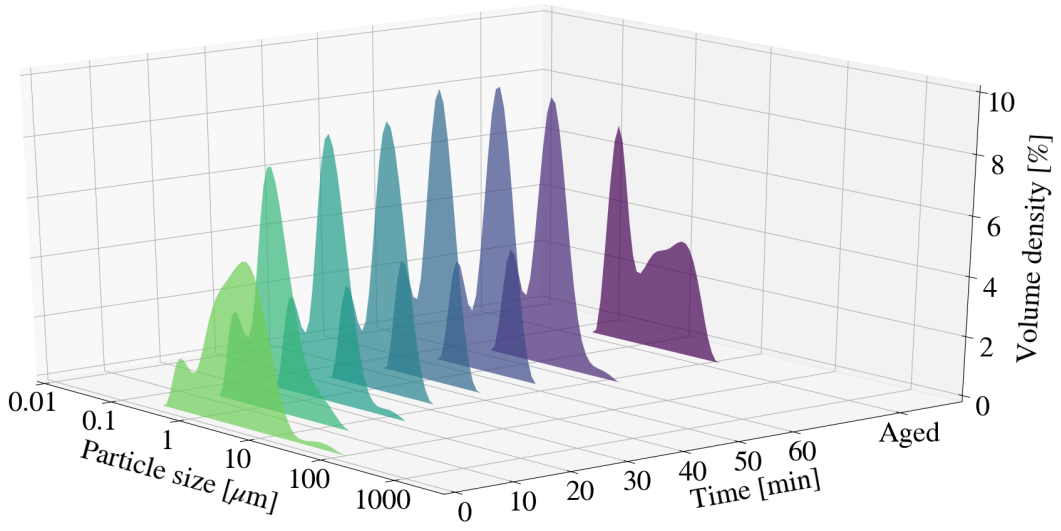


**Figure 94:** Particle size distribution with a change in time for Cu-Al LDH sample synthesised with the use of a $M^{2+}$:$M^{3+}$ ratio of 2:1.

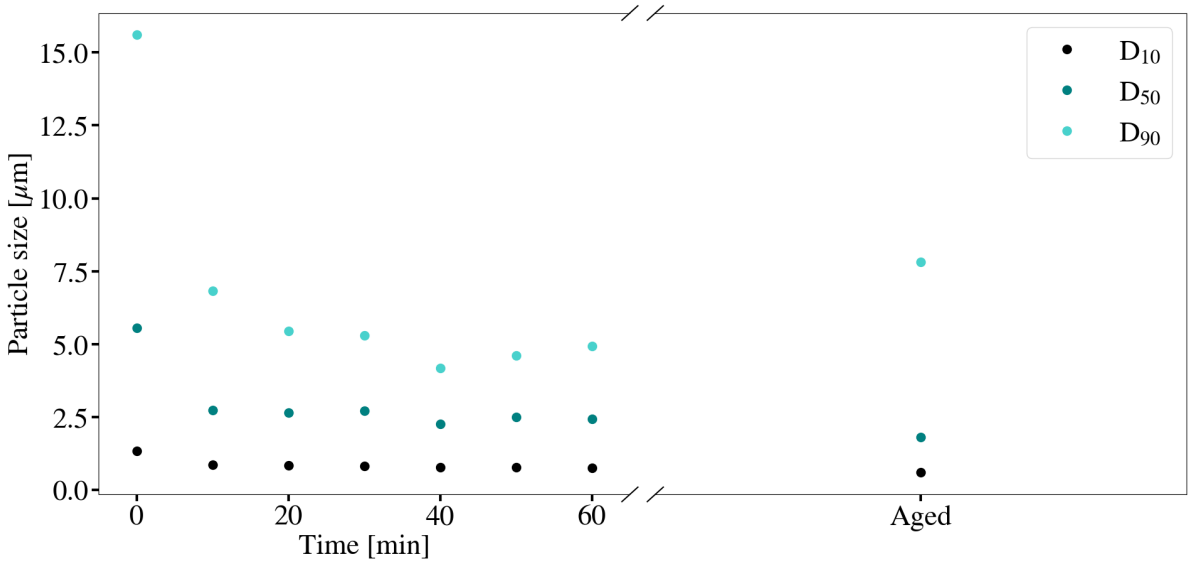


**Figure 95:** The change in particle size with time for Cu-Al LDH sample synthesised with the use of a $M^{2+}$:$M^{3+}$ ratio of 2:1

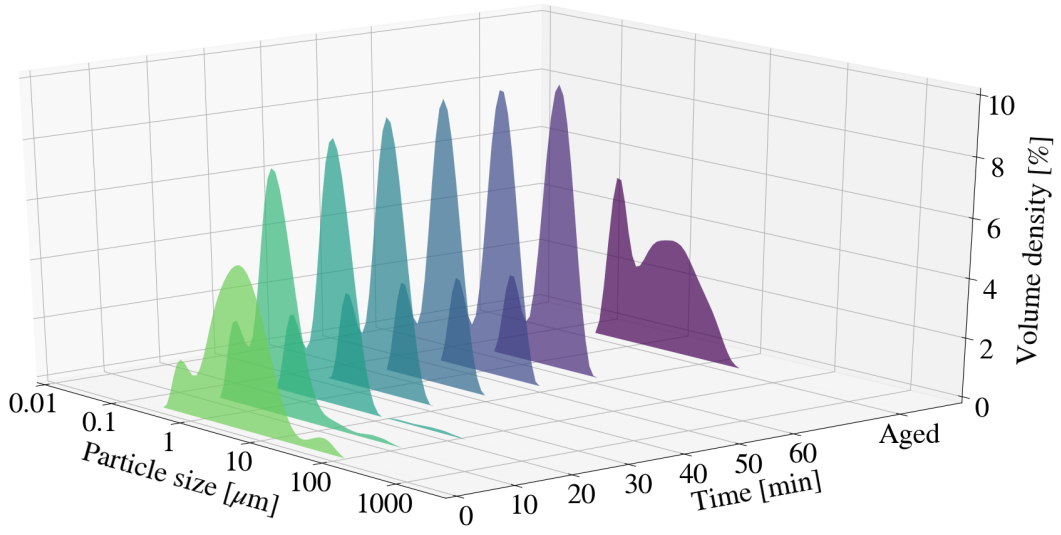


**Figure 96:** Particle size distribution with a change in time for Cu-Al LDH sample synthesised with the use of a $M^{2+}$:$M^{3+}$ ratio of 4:1.

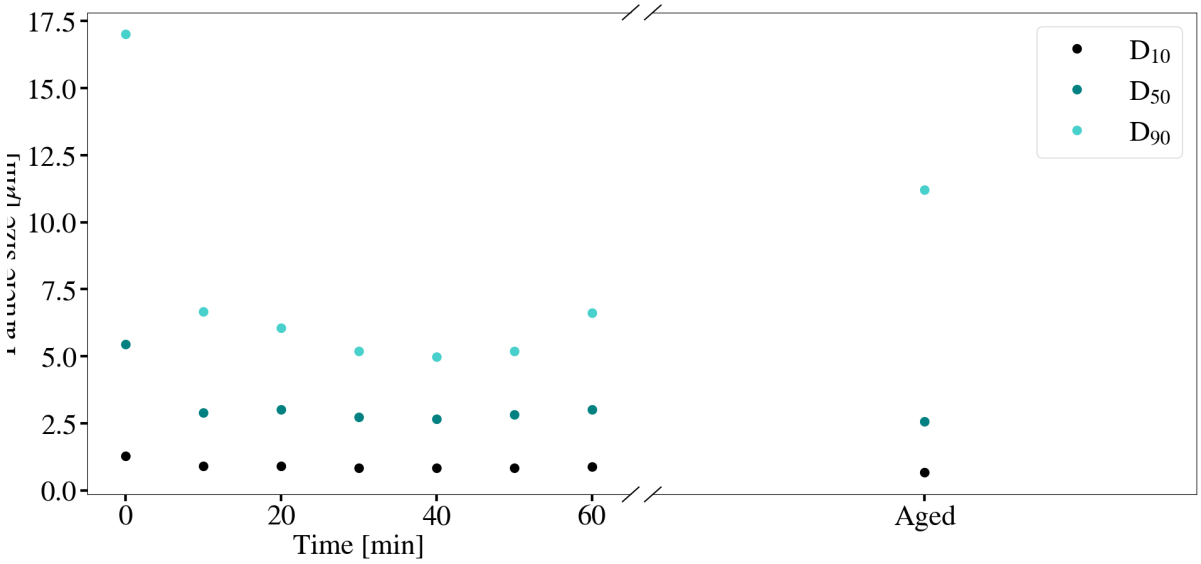


**Figure 97:** The change in particle size with time for Cu-Al LDH sample synthesised with the use of a $M^{2+}$:$M^{3+}$ ratio of 4:1.

**XRF analysis** All samples were prepared as pressed powder pellets when conducting XRF analysis. No Loss upon ignition (LOI) values were therefore available for either S22 and S23. Table A.40 summarises the XRF data obtained through this method of analysis. The $Cu^{2+}$ to $Al^{3+}$ ratios were calculated to be 2.00:0.996 and 4.00:1.06 respectively, correlating to selected masses listed in Table 6.

The chemical species $SiO_2$, MgO, $P_2O_3$, CaO and ZnO could once again be the result of

retained impurities despite washing of the mill and selected media. Similarly mill degradation and bead degradation likely resulted in the presence of $Fe_2O_3$, $Cr_2O_3$, NiO, $ZrO_2$ and $MoO_3$. Concentrations of components associated with mill and media degradation were observed to be similar between each run.

**SEM imaging** Figures 98 and 100 depict the SEM imaging for sample S22, before and after ageing. Similarly the imaging for S23 is depicted in Figures 99 and 101. No obvious differences were observed for the morphology of both samples prior to ageing. This was found to be further true once ageing was complete. The rectangular crystallite structures of the $Cu_2(OH)_2CO_3$ were no longer obvious once milling was complete in either sample.

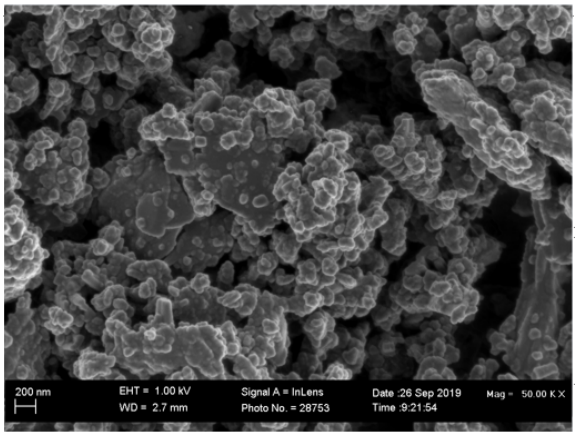


**Figure 98:** SEM imaging of Cu-Al LDH sample synthesised with the use of a $M^{2+}$:$M^{3+}$ ratio of 2:1 prior to ageing.

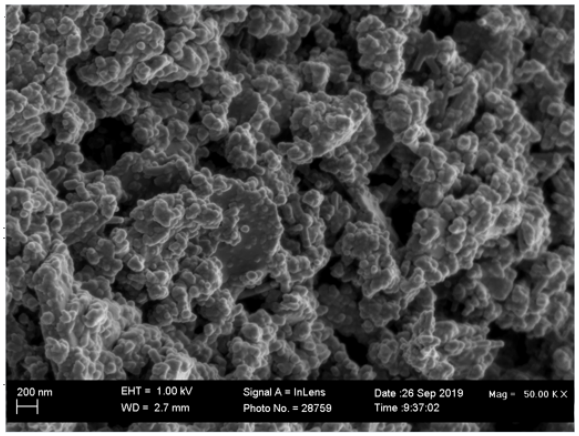


**Figure 99:** SEM imaging of Cu-Al LDH sample synthesised with the use of a $M^{2+}$:$M^{3+}$ ratio of 4:1 prior to ageing.

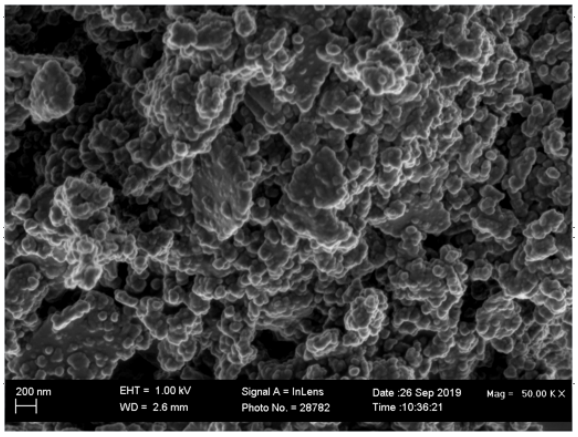


**Figure 100:** SEM imaging of Cu-Al LDH sample synthesised with the use of a $M^{2+}$:$M^{3+}$ ratio of 2:1 after ageing.

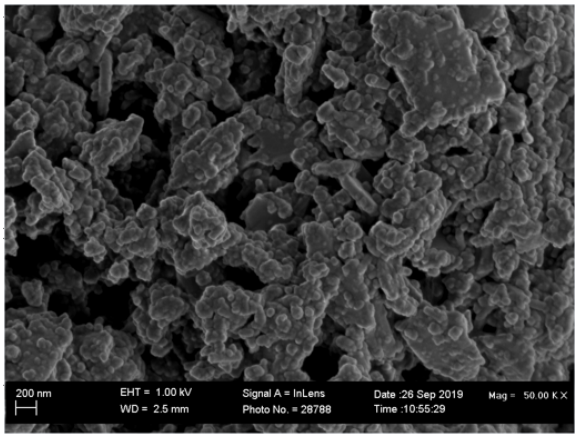


**Figure 101:** SEM imaging of Cu-Al LDH sample synthesised with the use of a $M^{2+}$:$M^{3+}$ ratio of 4:1 after ageing.

# 7 Conclusion and Recommendations

The need for 'green' synthesis methods of LDH material have prompted the exploration of mechanochemistry as a alternative to existing methods. Primary methods of synthesis include urea hydrolysis, co-precipitation, sol-gel and hydrothermal methods. These have proven to be successful, however are either energy intensive, result in environmentally unfriendly by-products, require strict inert environments or are costly to replicate on a large scale. Mechanochemistry offers a more robust, versatile and 'green' solution to these existing methods, with many successful studies conducted. Research indicated that raw materials selected could vary from metallic salts to potentially more environmentally friendly oxides, hydroxides and basic carbonates. Although many successful studies have been conducted, limited research on single-step wet grinding exists. This was primarily due to the difficulties associated with wet grinding, raw materials selected, morphological imperfections and possible lack of mechanochemical activation. Studies conducted have indicated low conversion rates and therefore further exploration is warranted. Similarly synthesis of LDH with the use of oxides, hydroxides and basic carbonates have proven to be difficult. Literature research indicated that the most common methods of mechanochemistry make use of ball mills, mixer mills or manual grinding as the method of mechanical energy addition to a system.

The study therefore aims to expand on one-step wet mechanochemical synthesis of LDHs, from oxides, hydroxides and basic carbonates, by making use of a Netzsch LME 1 horizontal bead mill. To the best of the authors knowledge this method of mechanochemical activation has not yet been explored.The selected mill allows for the continuous, semi batch or batch synthesis of LDH materials. The process could therefore be easily upscaled to produce large volumes of consistent and commercially viable LDH product. This method of synthesis further allows for the control of particle size. The use of LDH materials could therefore be expanded to suit fine-particle application.

The investigation included exploring the synthesis of Mg-Al LDH with a change in milling and experimental parameters such as rotational speed, retention time, solids loading, bead size and jacket water inlet temperature. Additionally the synthesis of Mg-Al, Ca-Al, Zn-Al and Cu-Al LDH was further explored by making use of existing synthesis conditions and adapting them to the selected method of milling. This was specifically in relation to $M^{2+}$:$M^{3+}$ ratio and selected starting materials.

## 7.1 Parameter study

The synthesis of layered double hydroxides with the use of a Netzsch LME 1 horizontal bead mill was deemed successful. Changes in parameters such a rotational speed, retention time, bead size, jacket water inlet temperature and solids loading, provided insight on the synthesis of Mg-Al LDH from MgO and $Al(OH)_3$. An increase in rotational speed resulted in an increase in the degree of amorphitisation of raw materials, with possible LDH decomposition at 3000 rpm. This was true for both selected temperatures of 30 °C and 50 °C. A retention time of 1 h was deemed too short to determine the true effects of the rotational speed on the formation and destruction of LDH. An increase in solids loading resulted in the decrease in grinding activity, with the optimal solids loading likely between that of 10 % and 20 %, with a high viscosity slurry and little grinding observed at 30 %.

A decrease in the bead size (0.25 mm) resulted in an increase in conversion of the selected raw materials to LDH. This was likely a result of an increase in the total amount of reactive surface area. Particle size was observed to be lower than those obtained with 2 mm beads. An increase in retention time for a jacket water inlet temperature of 30 °C resulted in minor quantities of LDH present, with raw material peaks present within XRD spectra obtained. Amorphitisation was observed to increase with an increase in retention time, leading to possible degradation of the LDH structure. Comparatively an inlet temperature of 50 °C drastically improved the conversion of raw materials to LDH, with the XRD spectra for LDH clearly visible after 3 h. Peaks were, however, observed to be broad and low in intensity, implying poor morphology and crystallinity.

It was noted that no $Mg(OH)_2$ peaks were observed for any of the samples synthesised. MgO was however largely present despite suspension in water. The decrease in XRD peak intensity was observed to be greater when at elevated jacket water temperatures (50 °C), when compared to lower temperatures (30 °C). A proposed reasoning could be that the hydration rate of MgO to $Mg(OH)_2$ is greater at elevated temperatures as described by (Rocha et al., 2004). Upon formation of $Mg(OH)_2$, LDH/LDH precursor formation occurs rapidly resulting in no observable $Mg(OH)_2$ peaks in XRD spectra obtained. The hydration is not prevented with the formation of an outer layer of $Mg(OH)_2$/LDH as the grinding activity due to the additional milling media would remove the outer layer. This would allow for further hydration to occur. More research should be conducted through pH measurement to determine the influence of the selected paramters on the solubility and therefore phases present within the sample.

Comparatively $Al(OH)_3$ peaks were mostly observed to decrease at a rate greater than that of MgO. The reactivity of MgO is further influenced by factors such as calination

temperature and time, further influencing the hydration rate. At high alkalinity Al is present as $Al(OH)_4^-$ (Zorn & Kaminski, 2015) and could wash out of the system if no LDH or precursor formation occurs. System pH should therefore be further studied. The effects of factors such as the hardness of the raw materials as well as mixing kinetics should be further considered in future studies. Future studies should further attempt to incorporate an energy or scientific model to better quantify results.

## 7.2 Versatility study

The synthesis of LDH was observed to occur for all samples prior to ageing with the exception of all Cu-Al samples and the Mg-Al sample synthesised with a 2:1 $M^{2+}$:$M^{3+}$ ratio. Conversion was observed to be incomplete for all samples with raw material peaks present in XRD spectra obtained. The influence of parameters on the synthesis of these LDH materials should be further investigated. Ageing of the samples allowes for an alternative two step commercial process through wet milling rather than a one-step process. Aeging further resulted in the increase in particle size of samples obtained. More research should be conducted to allow for particle size control when making use of an additional ageing step.

The formation of Mg-Al LDH occured more readily when making use of a 3:1 $M^{2+}$:$M^{3+}$ ratio when compared to that of a 2:1 $M^{2+}$:$M^{3+}$ ratio. This was attributed to the stablility of Mg-Al LDH synthesised at a 3:1 $M^{2+}$:$M^{3+}$ ratio as it occurs naturally in this state (Forano et al., 2006). Ageing of the samples resulted in a dratic increase in conversion of raw materials to LDH, with no MgO peaks observed in the XRD spectra obtained. Higher temperatures (80 °C) were expected to increase the rate of hydration and LDH formation, as well as sample crystallinity.

The formation of Ca-Al LDH was observed to occur for both samples synthesised. The addition of a carbonate source ($CaCO_3$) resulted in LDH formation occuring more readily, with increased conversion upon ageing. Comparitively, no carbonate source, did result in some LDH formation, however the formation of katoite occured upon ageing. The formation of LDH could be due to the synthesis and drying being conducted under atmospheric conditions, despite no direct carbonate source being present. The addition of a third phase, containing the selected anion for intercalation, is therefore nescessary (Qu, Zhong, et al., 2016).

The use of ZnO and $Zn_5(CO_3)_2(OH)_6$ in combination with $Al(OH)_3$ both yielded LDH with incomplete conversion prior to ageing with raw material peaks observable in XRD spectra obtained. It was noted that no difference was observed for samples synthesised

with ZnO before and after ageing. This could be attributed to the chemical stability of ZnO as well as the lack of carbonate source. The LDH was therefore likely a result of carbonate contamination due to the synthesis being conducted under atmospheric conditions. Comparatively LDH formation was observed to occur more readily when making use of $Zn_5(CO_3)_2(OH)_6$, with ageing drastically increasing the XRD peak intensity of the sample as well as improving the conversion.

The synthesis of Cu-Al LDH was deemed difficult with no LDH peaks observed prior to ageing for both samples synthesised. Initially when no LDH was observed for a selected 2:1 $M^{2+}$:$M^{3+}$ ratio, a ratio of 4:1 was selected to determine how an excess of Cu may influence the synthesis and if it may improve. No noticable difference was observed prior to ageing, with $Cu_2(OH)_2CO_3$ largely present within the XRD spectra obtained. Differences in FT-IR spectra for the sample and that of pure $Cu_2(OH)_2CO_3$ may suggest that LDH formation occured, however it was unclear. Ageing of both samples resulted in minor observable peaks in the XRD spectra obtained, however conversion was mostly incomplete. Longer ageing and milling times should be investigated to determine if the conversion will improve.

# 8 References


Aisawa, S, Hirahara, H, Uchiyama, H, Takahashi, S and Narita, E (2002) "Synthesis and Thermal Decomposition of Mn Al Layered Double Hydroxides" *J. Solid State Chem.*, 167 (1), 152-159.

Bester, K (2016) *Mechanochemical Synthesis of LDH compounds*, technical report, Dept Chem Eng, University of Pretoria.

Boclair, JW and Braterman, PS (1999) "Layered Double Hydroxide Stability.1.Relative Stabilities of Layered Double Hydroxides and Their Simple Counterparts" *J. Chem. Mater.*, 11 (2), 298-302.

Boclair, JW, Braterman, PS, Jiang, J, Lou, S and Yarberry, F (1999) "Layered Double Hydroxide Stability.2.Formation of Cr(III)-Containing Layered Double Hydroxides Directly from Solution" *J. Chem. Mater.*, 11 (2), 303-307.

Cavani, F, Trifiro, F and Vaccari, A (1991) "Hydrotalcite-type anionic clays: Preparation, properties and applications" *J. Catal. Today*, 11, 173-301.

Chamotte (2019) "Caustic Magnesium Oxide", https://www.chamotte.co.za/images /Documents/MgOChammox.pdf.[2019, November 5].

Connoly, J (2019) "Introduction Quantitative X-ray Diffraction Methods" *Prepared for EPS400-001*, -, -.

Conterosito, E, Van Beek, W, Palin, L, Croce, G, Perioli, L, Viterbo, D, Gatti, G and Milanesio, M (2013) "Development of a fast and clean intercalation method for organic molecules into layered double hydroxides" *J. Cryst. Growth Des.*, 13 (3), 1162-1169.

Cullity, B (1956) *Elements of X-ray Diffraction*, Adison-Wesley Publishing Company, Massachuetts.

Davor, M and Vjekoslav, S (2016) *Mechanochemical Organic Synthesis*, Elsevier, Cambridge.

Du, W, Zheng, L, Li, X, Fu, J, Lu, X and Hou, Z (2016) "Plate like Ni-Mg-Al layered double hydroxides synthesised via a solvent free approach and it's application in hydrogenolysis of D sorbitol" *J. App. Clay Sci.*, 123 (1), 166-172.

Dudeka, B, Kustrowski, P, Bialas, A, Natkanski, P, Piwowarskaa, Z, Chmielarz, L, Kozak, M and Michalik, M (2012) "Influence of textural and structural properties of Mg Al and

Mg Zn Al containing hydrotalcite derived oxides on Cr(VI) adsorption capacity" *J. Mater. Chem. Phys.*, 132 (2), 929-936.

Eliseev, AA, Lukashin, AV, Vertegel, AA, Tarasov, VP and Tret'yakov, YD (2002) "A Study of Crystallization of Mg-Al Double Hydroxides" *J. Dokl. Chem.*, 387 (4), 339-343.

Fahami, A, Duraia, EM. Beal, GW and Fahami, M (2017) "Facile synthesis and structural insight of chloride intercalated Ca-Al layered double hydroxide nanopowders" *J. Alloys Compd.*, 727 (1), 970-977.

Fahami, A, Beall, GW, Enayatpour, S, Tavangarian, F and Fahami, M (2016) "Rapid preparation of nano-hexagonal-shaped hydrocalumite via one-pot mechanochemistry method" *J. App. Clay Sci.*, 136 (1), 90-95.

Ferencz, Z, Kukovecz, A, Konya, Z, Sipos, P and Palinko, I (2015) "Optimisation of the synthesis parameters of mechanochemically prepared CaAl-layered double hydroxide" *J. Appl. Clay Sci.*, 112, 94-99.

Ferencz, Z, Szabados, M, Adok-Sipiczki, M, Kukovecz, A, Konya, Z, Sipos, P and Palinko, I (2014) "Mechanichemical assisted synthesis of pristine Ca(II)Sn(IV)-layered double hydroxides and their amino acid intercalated composites *J. Mater. Sci.*, 49 (24), 8479-8486.

Ferencz, ZS, Szabados, M, Varga, G, Csendes, Z, Kukovecz, A, Konya, Z, Carlson, S, Sipos, P and Palinko, I (2016) "Mechanochemical synthesis and intercalation of Ca(II)Fe(III)-layered double hydroxides" *J. Solid State Chem.*, 233 (1), 236-234.

Forano, C, Hibino, T, Leroux, F and Taviot, C (2006) *Developments in Clay Science*, Elsevier, Amsterdam.

Harding (2019) "Infrared Spectroscopy", https://www.chem.ucla.edu/ harding/notes/notes 14CIR:pdf [2019, December 6].

Hare, DO (2001) "Mechanochemical synthesis and intercalation of Ca(II)Fe(III)-layered double hydroxides" *J. Solid State Chem.*, 233 (1), 236-234

khoriba Scientific (2019) "A guidebook to particle size analysis", https://www.horiba.com/fileadmin/upl

Insta-ard, SG, Imwiset, KJ, Bureekaew, S and Ogawa, M (2018) "Mechanochemical way for the preparation of intercalation compounds from intercalation to the formation of layered double hydroxides" *RSC* 1(9), 1-21.

Iwasaki, T, Shimizu, K, Nakamura, H and Watano S (2012) "Novel mechanochemical process for facile and rapid synthesis of Co-Fe layered double hydroxide" *J. Mater. Lett.*,

65, 406-408.

Iwasaki T, Yoshii, H, Nakamura, H and Watano, S (2012) "Simple and rapid synthesis of Ni-Fe Layered double hydroxide by a new mechanochemical method" *J. App. Clay Sci.*, 58, 120-124.

Khusnutdinov, VR and Isupoc, VP (2007) "Mechanochemical synthesis of Layered double Mg-Al Hydroxides" *J. of Chem, Sust. Dev.*, 15, 367-372.

Kuramoto, K, Intasa-ard, S, Bureekaew, S and Ogawa, M (2017) "Mechanochemical synthesis of finite particles of layered double hydroxide-acetate intercalation compound: Swellin, Thin film and ion exchange" *J. Sol. State Chem.*, 253, 147.

Labushchagne, FJWJ, Molefe, DM, Focke, WW, Westhuizen, I, van der Wright, HC and Royeppen, MD (2015) "Heat stabilising flexible PVC with layered double hydroxide derivatives" *J. Polym. degrad. stabil.*, 113, 46-54.

Landge, S, Ghosh, D and Aiken, K (2018) "Chapter 3.17 - Solvent-Free Synthesis of Nanoparticles" *J. Green Chem. stabil.*, 609-646.

Li, Z, Chen, M, Ai, Z, Wu, L and Zhang, Q (2018) "Mechanochemical synthesis of CdS/MgAl LDH-precursor as improved visible-light driven photocatalyst for organic dye" *J. App. Clay Sci.*, 163, 265-272.

Li, Z, Zhang, Q, He, X and Chen, M (2017) "Enhanced visible light photocatalytic activity of mechanochemically prepared nanosized ZnxCd—(1-x)S/Zn-Al Layered double hydroxide precursor heterojunctions" *App. Clay Sci.*,-,-.

Li, Z, Zhang, Q, Liu, X, Chen, M and Ai, Z (2018) "Mechanochemical synthesis of novel heterostructured $Bi_2S_3$/Zn-Al layered double hydroxide nano-particles as efficient visible light reactive Z-scheme photocatalysts" *J. App Surface Sci.*, 452, 123-133.

Li, Z, Zhang, Q, Liu, X, Wu, L, Hu, H and Zhao, Y (2018) "One-step mechanochemical synthesis of plasmonic Ag/Zn-Al LDH with excellent photocatalytic activity" *J. Mater. Sci.*,-,-.

Lopez, T, Ramos, E, Bosch, P, Asomoza, M and Gomez, R (1997) 'DTA and TGA characterization of sol-gel hydrotalcites" *J. Mater. Lett.*, 30, 279-289.

Malvern Panalytical (2019) "Mastersizer 3000", https://www.malvernpanalytical.com/en/products/product-range/mastersizer-range/mastersizer-3000 [2018, August 3]

Manahan, SE (2006) *Green chemistry and the ten commandments of sustainbility*, ChemChar research Inc publishers, Columbia.

Mckay, RB (1994) *Technological applications of dispersions*, New York, CRC Press.

McLaughlin, WJ, White, JL and Hem, SL (1994) "Influence of Heterocoagulation on the Formation of Hydrotalcite in Mixed Suspensions of Magnesium Hydroxide and Aluminium Hydroxycarbonate" *J. Colloid Interf. Sci.*, 165, 41-52.

Milanesio, M, Conterosito, E, Viterbo, D, Perioli, L and Croce, G (2010) "New efficient intercalation of bioactive molecules into layered double hydroxide materials by solid state exchange: An in Situ XRPD study" *J. Cryst. Growth. Des.*, 10, 4710-4712.

Mindat (2019a) "Gibbsite", https://www.mindat.org/min-1689.html. [2019, December 1].

Mindat (2019b) "Periclase", https://www.mindat.org/min-3161.html. [2019, December 1].

NanoScience (2019) "Scanning electron microscopy", https://www.nanoscience.com/techniques/scanning-electron-microscopy/ [2019, December 3]

Nass, LI (1992) *Encyclopedia of PVC, Second Edition: Compounding*, CRC Press, New York.

Nicolet (2019) "Infrared Correlation Chart", http//ftirsearch.com/.[2019, December 4]

O'Hare, D (2001) "Hydrothermal Synthesis" *Encyclopedia of Materials: Science and Technology*, 2 (1), 3989-3992.

Ogawa, M, Kaiho, H. Homogeneous precipitation of uniform hydrotalcite particles. Langmuir 2002, 18, 4240–4242.

Pagano, C, Marmottini, F, Nocchetti, M, Ramella, D and Perioli, L (2018) "Effects of different milling techniques on the layered double hydroxides final properties " *J. Appl. Clay Sci.*, 151, 124-133.

Pathak, S (2017) "Mortar and Pestle" *Arch. Med.*, 9, -.

Pecharsky, V and Zavalij, P (2009) *Fundamentals of Powder differaction*, Springer, New York.

Perry, HR and Green, DW (2008) *Perry's Chemical Engineers' Handbook*, McGraw-Hill, New York.

Pourbaix, M (1974) *Atlas of electrochemical equilibria in aqueous solutions*, Pergamon press, Brussels.

Qi, F, Zhang, X and SLi (2012) "A novel method to get methotrexatum layered double hydroxides intercalation compounds and their release properties" *J. Phys. Chem. Solids*, 74, 1101-1108.

Qu, J, He, X, Chen, M, Huang, P, Zhang, Q and Liu, X (2017) "A facile mechanochemical approach to synthesize Zn-Al layered double hydroxide" *J. Solid State Sci.*, 250, 143.

Qu, J, He, X, Chen, M, Zhang, Q and Liu, X (2017) "Mechanochemical synthesis of Cu-Al and methyl orange intercalated Cu-Al layered double hydroxides" *J. Mater. Chem. Phys.*, 191, 173-180.

Qu, J, He, X, Lei, Z, Zhang, Q and Liu, X (2017) "Mechanochemical synthesis of dodecyl sulfate anion intercalated Cu-Al layered double hydroxide" *J. Solid State Sci.*, 74, 125-130.

Qu, J, He, X, Wang, B, Zhong, L, Wan, L, Li, X, Song, S and Zhang, Q (2016) "Synthesis of Li-Al layered double hydroxides via a mechanochemical route" *J. Appl. Clay Sci.*, 120, 24-27.

Qu, J, Li, X, Lei, Z, Li, Z, Chen, M and Zhang, Q (2016) "Mechano-Hydrothermal synthesis of tetraborate pillared Li-Al layered double hydroxide" *J. Am Ceram. Soc.*, 99, 1151-1154.

Qu, J, Zhang, Q, Li, X, He, X and Song, S (2015a) "Mechanochemical approaches to synthesize layered double hydroxides: a review" *J. Appl. Clay Sci.*, 119, 185-192.

Qu, J, Zhong, L, Li, Z, Chen, M, Zhang, Q and Liu, Z (2016) "Effect of anion addition on the synthesis of Ca-Al layered double hydroxide via a two-step mechanochemical process" *J. Appl. Clay Sci.*, 124, 267-270.

Ranu, B and Stolle, A (2015) *Ball milling towards green synthesis Applications*, RSC, United Kingdom.

Retsch (2018) "Size reduction with knife and cutting mills", http://iris.fishersci.ca/Lit Repo.nsf/0/7B939679DCB937628525711C00690D28/$file/KnifeMills.pdf.[2018, July 7].

Rives, V (2001) *Layered double hydroxides: Present and Future*, Nova Science, Publisher, New York.

Rocha, SDF, Mansur, MB and Ciminelli, VST (2004) "Kinetics and mechanistic analysis of caustic magnesia hydration" *J. Chem. Technol. Biotechnol.*, 79, 816-821.

Ropp, RC (2013) *Encyclopedia of alkaline earth compounds*, Elsevier, UK.

Schmidt, MJ (2016) *Synthesis of modified hydrocalumite: A novel Katoite portlandite precursor method*, technical report, Dept Chem Eng, University of Pretoria.

Socrates, George (2001) *Infrared and Ramen Charecteristic Group Frequencies: Tables and Charts*, John Wiley and Sons, England.

Szabados, M, Bus, CS, Adok-Sipiczki, M, Konya, Z, Kukovecz, A and Sipos, P (2016) "Ultrasound-enhanced milling in the synthesis of phase-pure, highly crystalline ZnAllayered double hydroxide of low Zn(II) content" *J. React. Kinet. Mech. Cat.*, 2, -.

Szabados, M, Meszaros, R, Erdei, S, Konya, Z, Kuvovecz, A and Sipos, P (2016) Ültrasonically enhanced mechanochemical synthesis of Ca-Al-layered double hydroxides intercalated by a variety of inorganic anions" *J. Ultrason. Sonochem.*, 31, 409-416.

Szabados, M, Pasztor, K, Csendes, Z, Murath, S, Konya, Z, Kukovecz, A, Carlson, S, Sipos, P and Palnko, I (2016) "Synthesis of high-quality, well-characterised CaAlFe layered triple hydroxide with the combination of dry-milling and ultrasinuc urradiation in aqueous solution at elevated temperature" *J. Ultrason. Sonochem.*, 32, 173-180.

Szabados, M, Varga, G, Konya, Z, Kukovecz, A, Carlson, S, Sipos, P and Palinko, I (2018) "Ultrasonically-enhanced preparation, characterization of Ca-Fe-layered double hydroxides with various interlayer halide, azide and oxo anions" *J. Ultrason. Sonochem*, 40, 853-860.

Takacs, L (2014) "What Is Unique About Mechanochemical Reactions" *J. Acta Phys. Pol. A*, 126, 1040-1043.

ThermoFischer (2019) "XRF Technology", https://www.thermofisher.com/za/en/home/industrial/spectroscopy-elemental-isotope-analysis/spectroscopy-elemental-isotope-analysis-learning-center/elemental-analysis-information/xrf-technology.html [2019 December 3].

Tongamp, W, Zhang, Q and Saito, F (2006a) "Mechanochemical synthesis of Mg-Al-OH hydrotalcite" *The 38th Fall Meeting of The Chemical Society of Japan.*

Tongamp, W, Zhang, Q and Saito, F (2006b) "Preparation of meixnerite (Mg-Al-OH) type layered double hydroxide by a mechanochemical route", *J. Mater. Sci.*, 42, 9210-9215.

Tongamp, W, Zhang, Q and Saito, F (2008) "Mechanochemical route for synthesizing nitrate form layered double hydroxide" *J. Powder Technol.*, 185, 43-48.

Vanderlaan, RK, White, JL and Hem, SL (1982) "Formation of Hydrotalcite in Mixtures of Aluminium Hydroxycarbonate and Magnesium Hydroxide Gels" *J. Pharm. Sci.*, 71, 780.

Varga, G, Murath, S, Bajcsi, A, Kukovecsz, A, Konya, Z, Sipos, P and Palinko, I (2017) "Borate-containing layered double hydroxide composites: synthesis, characterisation and application as catalysts in the Beckmann rearrangement reaction of cyclohexanone oxime" *J. React. Kinet. Mech. Cat.*,-,-.

Wijitwongwan RP, Intasa-ard SG and Ogawa M (2019) "Preparation of Layered Double Hydroxides toward Precisely Designed Hierarchical Organization" *J. Chem. Engineering*, 3, 158-163. 7.

Williams, RO, Watts, AB and Miller, DA (2012) *Formulating poorly water soluble drugs*, Springer Nature, Switzerland.

Wills, BA and Finch, JA (2016) *Wills' Mineral Processing Technology: An introduction to the Practial Aspects of Ore Treatment and Mineral Recovery*, Elsevier, Massachusetts.

Xu, S, Yang, Y, Xu, T, Kuang, Y, Dong, M, Zhang, F, Besenbacher, F and DG Evans (2011) "Engineered morphologies of layered double hydroxide nanoarchitectured shell microspheres and their calcined products" *J. Chem. Eng. Sci.*, 66, 2157-2163.

Xu, ZP and Lu, GQ (2005) "Hydrothermal synthesis of Layered double hydroxides (LDHs) from mixed MgO and $Al_2O_3$: LDH Formation Mechanism" *J. Chem. Mater.*, 5, 1055-1062.

Zhang, F, Du, N, Song, S and Hou, W (2015) "Mechano-hydrothermal synthesis of SDS intercalated LDH nanohybrids and their removal efficiency for 2,4-dichlorophenoxyacetic acid from aqueous solution" *J. Mater. Chem. Phys.*, 152, 95-103.

Zhang, F, Du, N, Song, S, Liu, J and Hou, W (2013) "Mechano-hydrothermal synthesis of $Mg_2Al$-$NO_3$ layered double hydroxides" *J. Solid State Chem.*, 206, 45-50.

Zhang, F, Du, N, Zhang, R and Hou, W (2012) "Mechanochemical synthesis of $Fe_3O_4$(Mg-Al-OH LDH) magnetic composite" *J. Powder Technol.*, 228, 250-253.

Zhang, F and Hou, W (2018) "Mechano-hydrothermal preparation of Li-Al-OH layered double hydroxides" *J. Solid State Chem.*, 93, 1151-1154.

Zhang, X, Qi, F, Li, S, Wei, S and Zhou, J (2012) "A mechanochemical approach to get stunningly uniform magnesium aluminium layered double hydroxides" *J. Appl. Surf. Sci.*, 259, 245-251.

Zhang, Y and Chen, Y (2018) "Preparation of polypropylene/Mg-Al layered double hydroxides nanocomposites through wet pan milling: non-isothermal crystallisation behaviour" *RSC: Open Sci.*,-,-.

Zhong, L, He, X, Qu, J, Li, X, Lei, Z, Zhang, Q and Liu, X (2017) "Precursor preparation for Ca-Al layered double hydroxide to remove hexavalent chromium coexisting with calcium and magnesium chloride" *J. Solid State Chem.*, 245, 200-206.

Zorn, C and Kaminski, N (2015) "Temperature-humidity-bias testing on insulated-gate bipolartransistor modules - failure modes and acceleration due to high voltage" *Special Issue on ISPS*, 1, 2329-2335.

Zhang X and Li, S (2013) "Mechanochemical approach for synthesis of Layered double hydroxides" *J. Appl. Surf. Sci.*, 274, 158-163.

Cengel, YA and Ghajar, AJ (2015) *Heat and Mass Transfer: Fundamentals and Applications*, McGraw-Hill, New York.

Bunte, K and Abt, SR (2001) *Sampling Surface and Subsurface Particle-size Distributions in Wadable Gravel- and Cobble-bed Streams for Analyses in Sediment Transport, Hydraulics, and Streambed Monitoring*, U.S. Department of Agriculture, Forest Service, Rocky Mountain Research Station, USA.

Agitator Bead Mills for Dispersing and Comminution - Application for Ceramic Processing. Available online: https://d2brmtk65c6t
yc.cloudfront.net/fileadmin/www.netzsch.com/Storage/Press/10_pdf_de.pdf?1422883163 (accessed on 20/01/2021).

Venter, HP. Optimisation of the synthesis of Mg-Al-$CO_3$ LDH and partial substitution of Mg/Ca-Based LDHs. Masters Dissertation, University of Pretoria, Hatfield, 2014.

Fuerstenau, DW and Abouzeid, AZM. (2002) "The energy efficiency of ball milling in communition" *J. Miner. Process.*, 67, 161-185.

Agitator Bead Mills for Dispersing and Comminution - Application for Ceramic Processing. Available online: https://d2brmtk65c6tyc.cloudfront.net/fileadmin/www.netzsch.com/Storage/Press/10_pdf_de.pdf?1422883163, (accessed on 20/01/2021).

# Appendix A XRF results

**Table A.31:** Mass percentages for chemical components and impurities present within Mg-Al LDH samples synthesised with a change in rotational speed, at a cooling water inlet temperature of 30°C.

| Component [mass %] | Rotational Speed [rpm] | | |
|---|---|---|---|
| | 1000 | 2000 | 3000 |
| $SiO_2$ | 9.23 ± 0.14 | 9.02 ± 0.14 | 9.02 ± 0.14 |
| $Al_2O_3$ | 25.85 ± 0.22 | 26.06 ± 0.22 | 24.77 ± 0.22 |
| MgO | 40.82 ± 0.25 | 39.86 ± 0.24 | 39.28 ± 0.24 |
| $Fe_2O_3$ | 0.3 ± 0.015 | 0.49 ± 0.024 | 1.10 ± 0.05 |
| $K_2O$ | 0.01 ± 0.001 | 0.01 ± 0.0011 | 0.01 ± 0.001 |
| CaO | 0.34 ± 0.017 | 0.39 ± 0.02 | 0.38 ± 0.019 |
| $Cr_2O_3$ | 0.07 ± 0.0032 | 0.15 ± 0.0065 | 0.34 ± 0.017 |
| MnO | 0.01 ± 0.0007 | 0.01 ± 0.0007 | 0.02 ± 0.0007 |
| NiO | 0.09 ± 0.0045 | 0.1 ± 0.0049 | 0.02 ± 0.0074 |
| CuO | 0.01 ± 0.0009 | 0.01 ± 0.0009 | 0.01 ± 0.0009 |
| $ZrO_2$ | 1.96 ± 0.07 | 1.47 ± 0.06 | 2.48 ± 0.08 |
| $MoO_3$ | 0.01 ± 0.0066 | 0.03 ± 0.0063 | 0.03 ± 0.0067 |
| $Y_2O_3$ | 0.11 ± 0.0052 | 0.08 ± 0.0039 | 0.13 ± 0.0067 |
| LOI | 21.15 | 22.33 | 22.15 |

**Table A.32:** Mass percentages for chemical components and impurities present within Mg-Al LDH samples synthesised with a change in retention time, at a cooling water inlet temperature of 30 °C.

| Component [mass %] | Residence Time [h] | | |
|---|---|---|---|
| | 1 | 2 | 3 |
| $SiO_2$ | 9.25 ± 0.14 | 9.60 ± 0.15 | 8.06 ± 0.14 |
| $Al_2O_3$ | 25.50 ± 0.22 | 26.47 ± 0.22 | 23.18 ± 0.21 |
| MgO | 35.46 ± 0.24 | 36.99 ± 0.24 | 35.08 ± 0.24 |
| $Fe_2O_3$ | 0.59 ± 0.029 | 0.95 ± 0.048 | 1.06 ± 0.05 |
| $K_2O$ | 0.04 ± 0.0031 | 0.02 ± 0.0025 | 0.01 ± 0.001 |
| CaO | 0.40 ± 0.02 | 0.43 ± 0.022 | 0.38 ± 0.019 |
| $Cr_2O_3$ | 0.16 ± 0.0079 | 0.27 ± 0.014 | 0.31 ± 0.015 |
| MnO | 0.01 ± 0.0018 | 0.02 ± 0.0016 | 0.02 ± 0.0009 |
| NiO | 0.12 ± 0.0058 | 0.14 ± 0.0069 | 0.14 ± 0.0068 |
| CuO | 0.03 ± 0.0029 | 0.03 ± 0.0023 | 0.03 ± 0.0016 |
| $ZrO_2$ | 1.45 ± 0.06 | 0.95 ± 0.047 | 3.13 ± 0.09 |
| ZnO | 0.94 ± 0.046 | 0.88 ± 0.044 | 0.71 ± 0.035 |
| $MoO_3$ | 0.01 ± 0.018 | 0.01 ± 0.0033 | 0.05 ± 0.0067 |
| $Y_2O_3$ | 0.07 ± 0.012 | 0.06 ± 0.0037 | 0.17 ± 0.0083 |
| LOI | 25.96 | 23.14 | 27.63 |

**Table A.33:** Mass percentages for chemical components and impurities present within Mg-Al LDH samples synthesised with a change in solids loading, at a cooling water inlet temperature of 30 °C

| Component [mass %] | Solids Loading [%] | | |
|---|---|---|---|
| | 10 | 20 | 30 |
| $SiO_2$ | 9.02 ± 0.14 | 9.11 ± 0.14 | 9.24 ± 0.14 |
| $Al_2O_3$ | 26.06 ± 0.22 | 25.43 ± 0.22 | 25.78 ± 0.22 |
| MgO | 39.86 ± 0.24 | 38.40 ± 0.24 | 38.81 ± 0.24 |
| $P_2O_5$ | 0.01 ± 0.0016 | 0.01 ± 0.0025 | 0.01 ± 0.0025 |
| $Fe_2O_3$ | 0.49 ± 0.024 | 0.38 ± 0.019 | 0.30 ± 0.015 |
| $K_2O$ | 0.01 ± 0.0011 | 0.00 ± 0.0011 | 0.00 ± 0.001 |
| CaO | 0.39 ± 0.02 | 0.34 ± 0.017 | 0.35 ± 0.017 |
| $Cr_2O_3$ | 0.15 ± 0.0065 | 0.10 ± 0.005 | 0.07 ± 0.0036 |
| MnO | 0.01 ± 0.0007 | 0.01 ± 0.0007 | 0.01 ± 0.0006 |
| NiO | 0.1 ± 0.0049 | 0.09 ± 0.0044 | 0.09 ± 0.0043 |
| $ZrO_2$ | 1.47 ± 0.06 | 1.19 ± 0.05 | 0.76 ± 0.038 |
| $Y_2O_3$ | 0.08 ± 00039 | 0.06 ± 0.0037 | 0.04 ± 0.0037 |
| $MoO_3$ | 0.03 ± 0.0063 | 0.00 ± 0.0059 | 0.00 ± 0065 |
| LOI | 22.33 | 24.82 | 24.49 |

**Table A.34:** Mass percentages for chemical components and impurities present within Mg-Al LDH samples synthesised with a change in bead size to 0.25 mm, at a cooling water inlet temperature of 30 °C

| Component [mass %] | Milling Media Size [mm] |
|---|---|
| | 0.25 |
| $SiO_2$ | 5.36 ± 0.11 |
| $Al_2O_3$ | 22.83 ± 0.21 |
| MgO | 31.81 ± 0.23 |
| $Fe_2O_3$ | 0.39 ± 0.019 |
| $K_2O$ | 0.05 ± 0.0023 |
| CaO | 0.43 ± 0.021 |
| $Cr_2O_3$ | 0.14 ± 0.0067 |
| MnO | 0.01 ± 0.0008 |
| NiO | 0.09 ± 0.0043 |
| $ZrO_2$ | 4.69 ± 0.11 |
| $Y_2O_3$ | 0.27 ± 0.013 |
| $MoO_3$ | 0.03 ± 0.011 |
| $SO_3$ | 0.04 ± 0.0024 |
| CuO | 0.01 ± 0.0013 |
| SrO | 0.01 ± 0.005 |
| LOI | 32.71 |

**Table A.35:** Mass percentages for chemical components and impurities present within Mg-Al LDH samples synthesised with a change in retention time, at a cooling water inlet temperature of 50 °C.

| Component [mass %] | Retention Time [h] | | |
|---|---|---|---|
| | 1 | 2 | 3 |
| $SiO_2$ | 8.54 ± 0.14 | 7.88 ± 0.13 | 6.81 ± 0.12 |
| $Al_2O_3$ | 24.04 ± 0.21 | 22.60 ± 0.21 | 20.20 ± 0.21 |
| MgO | 33.80 ± 0.24 | 33.31 ± 0.24 | 30.88 ± 0.23 |
| $Fe_2O_3$ | 0,54 ± 0.027 | 0.77 ± 0.038 | 0.87 ± 0.053 |
| $K_2O$ | 0.02 ± 0.0024 | 0.02 ± 0.0014 | 0.01 ± 0,0009 |
| CaO | 0.35 ± 0.018 | 0.33 ± 0.017 | 0.30 ± 0.015 |
| $Cr_2O_3$ | 0.14 ± 0.007 | 0.22 ± 0.011 | 0.26 ± 0.013 |
| MnO | 0.01 ± 0.0015 | 0.01 ± 0.0009 | 0.02 ± 0.0008 |
| NiO | 0.11 ± 0.0054 | 0.12 ± 0.0058 | 0.11 ± 0.0057 |
| $ZrO_2$ | 1.96 ± 0.07 | 2.97 ± 0.08 | 3.54 ± 0.09 |
| $Y_2O_3$ | 0.10 ± 0.0097 | 0.16 ± 0.0079 | 0.19 ± 0.0094 |
| $MoO_3$ | 0.00 ± 0.015 | 0.03 ± 0.0078 | 0.05 ± 0.0094 |
| ZnO | 0.02 ± 0.002 | 0.02 ± 0.001 | 0.02 ± 0.001 |
| CuO | 0.02 ± 0.0023 | 0.02 ± 0.0012 | 0.02 ± 0.0009 |
| LOI | 30.33 | 31.52 | 36.68 |

**Table A.36:** Mass percentages for chemical components and impurities present within Mg-Al LDH samples synthesised with a change in rotational speed, at a cooling water inlet temperature of 50 °C.

| Component [mass %] | Rotational Speed [rpm] | | |
|---|---|---|---|
| | 1000 | 2000 | 3000 |
| $SiO_2$ | 8.97 ± 0.14 | 9.07 ± 0.14 | 8.69 ± 0.14 |
| $Al_2O_3$ | 25.20 ± 0.22 | 24.80 ± 0.22 | 23.77 ± 0.21 |
| MgO | 39.91 ± 0.24 | 39.25 ± 0.24 | 37.71 ± 0.24 |
| $Fe_2O_3$ | 0.28 ± 0.014 | 0.49 ± 0.025 | 0.93 ± 0.046 |
| $K_2O$ | 0.01 ± 0.001 | 0.01 ± 0.001 | 0.01 ± 0.001 |
| CaO | 0.34 ± 0.017 | 0.37 ± 0.018 | 0.33 ± 0.017 |
| $Cr_2O_3$ | 0.06 ± 0.0031 | 0.14 ± 0.007 | 0.29 ± 0.015 |
| MnO | 0.01 ± 0.0007 | 0.01 ± 0.0007 | 0.02 ± 0.0008 |
| NiO | 0.09 ± 0.0043 | 0.10 ± 0.005 | 0.13 ± 0.0063 |
| $ZrO_2$ | 1.80 ± 0.07 | 1.97 ± 0.07 | 2.88 ± 0.08 |
| $Y_2O_3$ | 0.10 ± 0.0048 | 0.11 ± 0.0053 | 0.05 ± 0.0077 |
| $MoO_3$ | 0.01 ± 0.0064 | 0.02 ± 0.0059 | 0.04 ± 0.006 |
| CuO | 0.00 | 0.01 ± 0.0009 | 0.01 ± 0.0009 |
| LOI | 23.20 | 23.65 | 24.95 |

**Table A.37:** Mass percentages for chemical components and impurities present within Mg-Al LDH samples synthesised with a change in $M^{2+}$:$M^{3+}$ ratio.

| Component [mass %] | Reference | |
|---|---|---|
| | S16 | S17 |
| $SiO_2$ | 9.02 ± 0.14 | 9.13 ± 0.14 |
| $Al_2O_3$ | 26.06 ± 0.22 | 18.03 ± 0.19 |
| MgO | 39.86 ± 0.24 | 41.01 ± 0.25 |
| $Fe_2O_3$ | 0.49 ± 0.024 | 0.41 ± 0.02 |
| $K_2O$ | 0.01 ± 0.0011 | 0.00 |
| CaO | 0.39 ± 0.02 | 0.35 ± 0.017 |
| $Cr_2O_3$ | 0.13 ± 0.0065 | 0.11 ± 0.0054 |
| MnO | 0.01 ± 0.0007 | 0.01 ± 0.0006 |
| NiO | 0.1 ± 0.0049 | 0.1 ± 0.0048 |
| $ZrO_2$ | 1.47 ± 0.06 | 1.59 ± 0.06 |
| $Y_2O_3$ | 0.08 ± 0.0039 | 0.08 ± 0.0042 |
| $MoO_3$ | 0.03 ± 0.0063 | 0.02 ± 0.006 |
| ZnO | 0.01 ± 0.0009 | 0.01 ± 0.0007 |
| CuO | 0.01 ± 0.0009 | 0.01 ± 0.0008 |
| LOI | 22.33 | 29.12 |

**Table A.38:** Mass percentages for chemical components and impurities present within Ca-Al LDH samples with and without the addition of $CaCO_3$ using a Ca:Al ratio of 2:1.

| Component [mass %] | Reference | |
|---|---|---|
| | S18 | S19 |
| $SiO_2$ | 0.65 ± 0.032 | 0.92 ± 0.046 |
| $Al_2O_3$ | 19.45 ± 0.2 | 18.44 ± 0.19 |
| MgO | 1.31 ± 0.06 | 1.49 ± 0.06 |
| $P_2O_5$ | 0.044 ± 0.0024 | 0.049 ± 0.0025 |
| $Fe_2O_3$ | 0.19 ± 0.0095 | 0.20 ± 0.01 |
| CaO | 39.14 ± 0.24 | 43.00 ± 0.25 |
| $Cr_2O_3$ | 0.047 ± 0.0023 | 0.047 ± 0.0023 |
| NiO | 0.013 ± 0.0007 | 0.012 ± 0.0008 |
| $ZrO_2$ | 0.40 ± 0.02 | 0.37 ± 0.018 |
| $SO_3$ | 0.20 ± 0.0024 | 0.19 ± 0.0024 |
| $Y_2O_3$ | 0.020 ± 0.0023 | 0.020 ± 0.0023 |
| BaO | 0.16 ± 0.07 | 0.15 ± 0.07 |
| LOI | 38.16 | 34.99 |

**Table A.39:** Mass percentages for chemical components and impurities present within Zn-Al LDH samples synthesised with the use of ZnO or $Zn_5(CO_3)_2(OH)_6$ with a $M^{2+}$:$M^{3+}$ ratio of 1:1.

| Component [mass %] | Reference | |
|---|---|---|
| | S20 | S21 |
| $SiO_2$ | 0.01 ± 0.0055 | 0.04 ± 0.012 |
| $Al_2O_3$ | 26.62 ± 0.23 | 33.00 ± 0.23 |
| MgO | 0.20 ± 0.0024 | 0.00 |
| $Fe_2O_3$ | 0.13 ± 0.0069 | 0.20 ± 0.011 |
| CaO | 0.05 ± 0.0046 | 0.32 ± 0.0049 |
| $Cr_2O_3$ | 0.04 ± 0.0018 | 0.06 ± 0.0028 |
| NiO | 0.01 ± 0.0013 | 0.01 ± 0.0015 |
| CuO | 0.81 ± 0.0025 | 0.64 ± 0.0025 |
| $ZrO_2$ | 0.03 ± 0.002 | 0.01 ± 0.006 |
| ZnO | 42.21 ± 0.24 | 44.29 ± 0.25 |
| $MoO_3$ | 0.02 ± 0.0062 | 0.01 ± 0.0064 |
| BaO | 0.01 ± 0.05 | 0.17 ± 0.06 |
| LOI | 29.80 | 21.11 |

**Table A.40:** Mass percentages for chemical components and impurities present within Cu-Al LDH samples synthesised with a change in $M^{2+}$:$M^{3+}$ ratio.

| Component [mass %] | Reference | |
|---|---|---|
| | S22 | S23 |
| $SiO_2$ | 0.16 ± 0.0073 | 0.17 ± 0.0062 |
| $Al_2O_3$ | 23.94 ± 0.24 | 14.25 ± 0.23 |
| MgO | 0.10 ± 0.016 | 0.19 ± 0.016 |
| $P_2O_5$ | 0.16 ± 0.0031 | 0.04 ± 0.0031 |
| $Fe_2O_3$ | 0.29 ± 0.014 | 0.21 ± 0.0097 |
| CaO | 0.16 ± 0.0076 | 0.56 ± 0.016 |
| $Cr_2O_3$ | 0.08 ± 0.0039 | 0.07 ± 0.0027 |
| NiO | 0.02 ± 0.0021 | 0.02 ± 0.0015 |
| CuO | 75.02 ± 0.42 | 84.21 ± 0.032 |
| $ZrO_2$ | 0.04 ± 0.0017 | 0.12 ± 0.0025 |
| ZnO | 0.11 ± 0.0053 | 0.12 ± 0.25 |
| $MoO_3$ | 0.02 ± 0.0033 | 0.02 ± 0.007 |